CENTRALE LILLE

THÈSE

Présentée en vue d'obtenir le grade de

DOCTEUR

En spécialité : **Génie civil**

Par

Xingxing Qi

DOCTORAT DÉLIVRÉ PAR CENTRALE LILLE

Titre de la thèse :

Étude expérimentale et numérique du comportement hydromécanique couplé des interfaces des géomatériaux

Titre de la thèse en anglais:

Experimental and Numerical Investigation of Coupled Hydro-mechanical Behavior of Geomaterials Interfaces

Soutenue le **13 octobre 2025** devant le jury d'examen

Président :

M. **Farid BENBOUDJEMA**, Professeur, ENS Paris-Saclay

Thèse dirigée par :

M. **Matthieu BRIFFAUT**, Professeur, Centrale Lille Institut
Mme. **Yun JIA**, Maître de Conférences – HDR, Université de Lille
M. **Nicolas GAY**, RI (Co-encadrant), Centrale Lille Institut
M. **Jean-Philippe CARLIER**, Maître de Conférences, Université de Lille

Rapporteurs :

Mme. **Stéphanie BONNET**, Professeure, Université de Nantes
M. **Luc COURARD**, Professeur, Université de Liège

Examinateur :

M. **Menes BADIKA KYEDI**, Dr. Ing., ASNR

Thèse préparée au Laboratoire de Mécanique, Multiphysique, Multi-échelle (LaMcube)

École Doctorale ENGSYS Sciences de l'ingénierie et des systèmes - N°632

RÉSUMÉ

Les structures en béton armé vieillissantes nécessitent aujourd'hui des solutions de réparation plus durables, plus compatibles et moins carbonées que les matériaux cimentaires traditionnels. Dans ce contexte, les mortiers géopolymères suscitent un intérêt croissant en raison de leur faible empreinte environnementale, de leur microstructure dense et de leurs propriétés mécaniques élevées. Toutefois, pour garantir une réhabilitation durable, la compréhension précise du comportement hydromécanique aux interfaces – en particulier entre un mortier géopolymère et les substrats en béton et en acier – reste un enjeu scientifique majeur. Les interfaces étant souvent les zones critiques de transfert d'efforts, de concentration de contraintes et d'initiation de fissures, l'étude intégrée de leur comportement mécanique et de leur perméabilité apparaît indispensable. La présente thèse vise ainsi à développer une compréhension multi-échelle et multi-physique du comportement hydromécanique couplé de ces interfaces, depuis la caractérisation du matériau géopolymère jusqu'à la validation structurale sur poutres en béton armé.

La première partie de ce travail consiste à caractériser le mortier géopolymère étudié. Les essais à l'état frais démontrent une bonne ouvrabilité et une cohésion suffisante pour un emploi sur chantier. Les propriétés à l'état durci révèlent une résistance à la compression atteignant 49,8 MPa à 14 jours, une faible perméabilité intrinsèque au gaz et une microstructure homogène mettant en évidence une densification progressive du réseau poreux. L'un des aspects essentiels est l'étude du retrait précoce, investiguée par corrélation d'images numériques (DIC). Les champs de déformation montrent que plus de 70 % du retrait se produit dans les premières 24 heures, ce qui peut engendrer des contraintes initiales importantes au niveau des interfaces. Ces résultats constituent une base essentielle pour comprendre l'évolution des interactions mécaniques durant les premières heures de cure, période critique pour la cohésion initiale entre géopolymère et béton.

Une revue de littérature approfondie a ensuite mis en lumière plusieurs lacunes dans l'état de l'art : d'une part, la majorité des études se concentrent sur des essais de cisaillement simples (slant shear, push-off, bi-matériaux inclinés) ne permettant pas d'isoler correctement la contribution propre de l'interface ; d'autre part, très peu de travaux se sont intéressés au couplage entre cisaillement et perméabilité sous confinement. De plus, la rugosité de surface, pourtant reconnue comme paramètre déterminant dans les systèmes béton–béton et béton–roche, n'est que rarement quantifiée dans les systèmes géopolymère–béton. Enfin, les interfaces géopolymère–acier demeurent encore peu documentées, en particulier sous sollicitations hydromécaniques. Ces constats ont guidé la conception d'un programme expérimental complet.

La partie centrale de la thèse présente un dispositif expérimental original permettant de mesurer simultanément la résistance au cisaillement et la perméabilité sous pression de confinement constante (3 MPa). Ce dispositif a permis de reproduire des conditions proches du terrain où l'interface est soumise à la fois à une contrainte normale, à un cisaillement progressif et à un gradient hydraulique. Différentes rugosités de surface ont été étudiées : surface lisse (L0), surfaces sablées d'intensités variables (L1, L2), et sur-

face fortement rugueuse (L3). Les résultats montrent que la résistance au cisaillement augmente de manière significative avec la rugosité, passant de 5–6 MPa pour les surfaces lisses jusqu'à 12 MPa pour les surfaces fortement rugueuses. Les courbes cisaillement–déplacement révèlent trois phases successives : (i) une phase élastique contrôlée par l'adhérence chimique, (ii) une phase de dégradation progressive marquée par la diminution de la cohésion et l'activation du frottement, et (iii) une phase résiduelle dominée par le glissement frictionnel.

Le comportement de perméabilité est étroitement couplé au comportement mécanique. Pour les surfaces lisses, la perméabilité augmente précocement avant même l'atteinte du pic, signe d'une initiation rapide de microfissures interfaciales. Pour les surfaces rugueuses, la perméabilité reste faible jusqu'en post-pic, indiquant un réseau de fissures plus tardif et un meilleur engagement du mécanisme d'interverrouillage. L'analyse quantitative met en évidence une relation entre rugosité Sa, résistance maximale et perméabilité en post-pic, démontrant que l'amélioration de la rugosité ralentit la formation des chemins préférentiels de transport hydrique.

Un ensemble de tests comparatifs a également été conduit sur des éprouvettes monolithiques en béton à granulats fins (F-CON), béton à gros granulats (C-CON) et mortier géopolymère (G-GEO). Les résultats montrent que : (i) le béton à gros granulats présente les résistances maximales les plus élevées mais une augmentation rapide de perméabilité en post-pic due à sa structure hétérogène ; (ii) le géopolymère présente un comportement plus stable avec une progression régulière de la perméabilité ; (iii) les interfaces géopolymère–béton se situent entre les deux en termes de capacité portante mais présentent une évolution hydromécanique fortement dépendante de la rugosité. Ces observations permettent de situer objectivement la performance du géopolymère par rapport aux matériaux conventionnels et d'établir une base de comparaison pour les modèles numériques.

La thèse s'intéresse également aux interfaces géopolymère–acier, particulièrement critiques dans les zones où les armatures sont exposées ou requièrent une adhérence parfaite. Les premiers essais ont révélé un décollement prématuré dû à l'absence d'interverrouillage mécanique et à la différence marquée de rigidité. Pour y faire face, un dispositif concentrique symétrique a été développé afin d'assurer une distribution uniforme des efforts de cisaillement. Parallèlement, l'ajout d'additifs phosphatés dans le géopolymère a permis d'améliorer la réaction chimique avec la surface de l'acier. Les essais montrent une amélioration substantielle de la résistance interfaciale et une réduction nette de la perméabilité, confirmant que le géopolymère modifié peut assurer une adhérence fiable avec l'acier.

La partie numérique repose sur un modèle d'interface cohésif–frottant implémenté dans Abaqus/Standard à l'aide d'éléments cohésifs tridimensionnels. Le modèle intègre une loi traction–séparation avec dégradation progressive de la cohésion, un critère de rupture basé sur l'énergie de fissuration, ainsi qu'un terme frictionnel permettant de simuler le glissement résiduel. Les paramètres du modèle ont été calibrés à partir des

essais expérimentaux et permettent de reproduire fidèlement les trois phases d'évolution du cisaillement. Les simulations montrent une très bonne concordance avec les courbes charge–déplacement expérimentales, ainsi qu'une représentation réaliste de l'initiation et de la propagation des fissures. Ce modèle offre un outil robuste pour prédire la performance des interfaces en conditions réelles et pour optimiser les traitements de surface.

Enfin, une validation à l'échelle réelle a été réalisée par des essais de flexion en quatre points sur des poutres en béton armé réparées avec le géopolymère. Les poutres réparées présentent une charge ultime supérieure, une ductilité améliorée et une fissuration plus uniforme par rapport aux poutres réparées à l'aide d'un mortier cimentaire commercial. Ces résultats démontrent que l'amélioration des propriétés interfaciales se traduit directement par une meilleure performance structurale.

En conclusion, cette thèse démontre que le mortier géopolymère étudié présente une excellente compatibilité hydromécanique avec le béton et l'acier, une forte résistance interfaciale et une stabilité de transport favorable. La combinaison d'essais multi-échelles, de mesures couplées cisaillement–perméabilité, de caractérisations fines de la rugosité et de modélisations numériques cohésives–frottantes offre une compréhension complète des mécanismes de transfert à l'interface. Les résultats positionnent les géopolymères parmi les matériaux les plus prometteurs pour la réparation durable et performante des structures en béton armé soumises à des sollicitations complexes. Des perspectives sont ouvertes, notamment en matière d'optimisation des formulations, de traitement des surfaces, de réduction des retraits précoces et d'intégration de ces matériaux dans des applications de grande échelle.

Mots-clés : Mortier géopolymère, Réparation du béton armé, Interface béton–géopolymère, Interface acier–géopolymère, Comportement hydromécanique, Modélisation par éléments finis

ACKONWLEDGEMENTS

It has been a remarkable journey pursuing my doctoral studies at the Laboratoire de Mécanique, Multiphysique et Multiéchelle (LaMcube). At this special moment of completion, I would like to express my sincere gratitude to everyone who has supported me throughout the past three years.

First and foremost, I would like to express my heartfelt thanks to my supervisor, **Prof. Matthieu Briffaut**, for his continuous guidance, encouragement, and patience during the entire course of this research. His rigorous attitude, constructive advice, and generous support were invaluable to the success of this work.

I am deeply grateful to **Prof. Yun Jia**, whose support made it possible for me to come to Lille. Her trust and encouragement opened the door to this research journey, and I remain sincerely thankful for her mentorship.

My appreciation also extends to my co-supervisors, **Dr. Nicolas Gay** and **Prof. Jean-Philippe Carlier**, for their technical insights, critical discussions, and kind involvement throughout the thesis.

I would also like to sincerely thank **Mr. Thierry Dubois** and **Mr. Ludovic Potier**, whose help during the experimental phase was indispensable. I greatly appreciate their availability, experience, and generosity. A special word of thanks to **Mr. Zhibo Duan**, for his friendship, technical suggestions, and the many inspiring conversations that made difficult moments easier to bear. I warmly thank **Mr. Laurent Coustenoble**, who provided valuable technical support and conducted the scanning of my specimens.

I also wish to thank the entire team at **LaMcube** for creating a professional and supportive environment that fostered both personal and academic development. I also wish to thank all the colleagues who helped me with the preparation and testing of the reinforced concrete beams. Your teamwork, dedication, and patience made the large-scale experiments possible.

Last but not least, I am deeply thankful to my family and friends for their love, understanding, and constant encouragement throughout this journey. Your presence was my strongest source of motivation and strength.

This thesis is dedicated to those who repair, connect, and support—both in concrete and in life.

CONTENTS

Résumé i

Ackonwledgements v

Contents xii

List of Figures xiii

List of Tables xix

General Introduction 1

CHAPTER 1: State of the Art 3

1 Background and motivations 3
2 OPC and geopolymer 4
2.1 Carbon dioxide equivalent 4
2.2 Challenges of OPC and advancements in geopolymer technology 7
2.3 Summary 8
3 Repair materials for reinforced concrete 8
3.1 Typical deterioration mechanisms 9
3.2 International standards for repair materials: EN 1504 framework 9
3.3 Categories of repair materials 10
3.4 Need for improved interface performance 13
3.5 Geopolymer mortar as repair material 13
3.5.1 General application of geopolymers in structural engineering 13
3.5.2 Precursors of geopolymer as repair material 14
3.6 Summary 17
4 Properties of geopolymer mortars as repair materials 17
4.1 Geopolymerization 17
4.2 Fresh geopolymer mortar 19
4.2.1 Setting time of geopolymer mortars 19
4.2.2 Flowability of geopolymer mortars 20
4.3 Hardened geopolymer mortar 21
4.3.1 Compressive strength of geopolymer mortars 21
4.3.2 Shrinkage of geopolymer mortars 25
4.4 Summary 29
5 Hydro-mechanical behavior research on geomaterials interfaces 29
5.1 Testing method 30

5.2 Geopolymer-concrete interfaces 30
5.3 Geopolymer-steel interfaces 33
5.4 Shear evolution 35
5.4.1 Failure criterion 35
5.4.2 Geopolymer-concrete interfaces 37
5.4.3 Geopolymer-steel interfaces 38
5.5 Influence of roughness on geomaterials interfaces 40
5.5.1 Characterization of roughness 40
5.5.2 Influence of roughness on geomaterials interfaces 41
5.6 Numerical modeling of shear evolution 45
5.6.1 Numerical modeling of bonded interfaces 45
5.6.2 FEM Methods on geo–con interfaces 46
5.7 Summary 48
6 Conclusion 49

CHAPTER 2: Physical-mechanical properties of geopolymer mortar as repair materials 51

1 Introduction 51
2 Materials and mix design 52
2.1 Geopolymer mortar and substrate 52
2.2 Mix proportion and furmula design 53
3 Fresh-state properties of geopolymer mortar 55
3.1 Setting time assessment 55
3.2 Flowability evaluation 56
4 Hardened-state properties of geopolymer mortar 57
4.1 Mechanical performance evaluation 57
4.1.1 Flexural and compressive strength 57
4.1.2 Uniaxial compressive behavior of geopolymer mortar and concrete substrate 60
4.2 Durability-related characteristics 68
4.2.1 Gas permeability 68
4.2.2 Pore structure and porosity analysis 76
4.3 Shrinkage behavior of geopolymer mortar 80
4.3.1 Experimental methods and measurement setup 81
4.3.2 Long-term shrinkage of geopolymer mortar 86
4.3.3 Early-age (7 Days) shrinkage 89
4.3.4 Plastic shrinkage at initial setting phase 96
5 Conclusion 99

CHAPTER 3: Experimental Investigation of Geopolymer-Concrete Interfaces **101**

1 Introduction 101
2 Preliminary tests and methods 102
2.1 Preparation of Geo-con samples 102
2.2 Shear testing of the interface 103
2.3 Results and discussion 104
2.4 Conclusion and adjustments 106
3 Hydro-mechanical behaviour under shear loading 106
3.1 Materials and Methods 107
3.1.1 Materials 107
3.1.2 Roughness and quantification 109
3.1.3 Experimental setup 112
3.1.4 Shear stress and permeability calculation 114
3.1.5 Testing program 116
3.2 Results 118
3.2.1 Surface roughness characterization 118
3.2.2 Interface shear and permeability response 119
3.2.3 Monolithic specimen comparison 126
3.2.4 Summarizes the results 130
3.3 Discussion 132
3.3.1 Hydro-mechanical performance of geopolymer-concrete interfaces under shear loading 132
3.3.2 Description of the shear evolution 133
3.3.3 Shear strength components 134
3.3.4 Hydro-mechanical coupling shear stages 137
3.3.5 Comparative evaluation of the peak shear strength at geopolymer–concrete interfaces with fine and coarse aggregate concrete 138
3.3.6 Influence of roughness on geopolymer-concrete interface hydro-mechanical behavior 139
3.4 Roughness before shear tests and after shear tests 141
4 Conclusion 142

CHAPTER 4: Numerical simulations **145**

1 Introduction 145
2 Construction of numerical model 146
2.1 Software Selection and Justification 146
2.2 Model geometry and mesh sensitivity 147
2.3 Constitutive models for studied materials 148

2.4 Constitutive models for studied materials 149
2.4.1 Concrete and geopolymer: Mohr–Coulomb model 150
2.4.2 Rubber layer: Mooney–Rivlin hyperelastic model 151
2.4.3 Geo–con interface: Cohesive–Frictional model 152
3 Simulation of interface behavior 155
3.1 Boundary conditions and loading steps 156
3.2 Incorporation of surface roughness 157
3.3 Model calibration and parameter validation 159
3.3.1 Smooth Interface (L0) 159
3.3.2 Rough Interfaces (L1, L2, L3) 161
4 Numerical results and analysis 165
4.1 Stages of shear behavior 165
4.2 Parametric studies with interface roughness 171
4.3 Prediction of the shear response of concentric cell shear 173
4.3.1 Influence of confining pressure 174
4.3.2 Influence of cell diameter 175
4.3.3 Influence of roughness 175
4.4 Evolution of displacement and strain fields 176
5 Conclusion 178

CHAPTER 5: Experimental investigation of Geopolymer-steel Interfaces 181
1 Introduction 181
2 Trial tests on geopolymer-steel specimens 182
2.1 Specimen preparation for geopolymer-steel interface testing 182
2.2 Specimen behavior after curing 183
2.3 Discussion and adjustment 184
3 Methods to improve geo-steel binder 184
3.1 Surface treatments 185
3.2 Using phosphatic additive 186
3.3 Using silicon-rich MK 188
3.4 Conclusion and adjustments 190
4 Concentric cell testing 191
4.1 Test design and cell setup 192
4.2 Shear test with permeability measure of geopolymer-steel interface 193
4.3 Using phosphatic additive to improve geopolymer-steel bonding 195
4.3.1 Compressive and flexural strength of phosphatic geopolymer mortar 195
4.3.2 Shear test with permeability measure of phosphatic geo-steel interface 196

5 Conclusion 198

CHAPTER 6: Large-Scale Validation: Application on Repaired Beams 201
1 Introduction 201
2 Design and fabrication of damaged beams 202
2.1 Reinforced concrete beams geometry 202
2.2 Materials and repair materials properties 205
2.2.1 Concrete 205
2.2.2 Repair materials: geopolymer mortar and commercial repair product 206
2.3 Specimens fabrication and repair 206
2.3.1 Rebar cages fabrication 207
2.3.2 Fabrication of complete reinforced concrete beams and reinforced concrete beams for repair 208
2.3.3 Rough concrete surface treatment 209
2.3.4 Repairing smooth and rough concrete beams with geopolymer mortar 210
2.3.5 Repairing smooth concrete beams with commercial products 211
3 Testing setup and methods 213
3.1 Loading method 213
3.2 Measurement items and methods 214
3.2.1 DIC set up 215
3.3 Experimental procedure 217
4 Results and discussion 217
4.1 Failure modes based on full-field strain visualization 217
4.1.1 Unrepaired concrete beams (CON) 218
4.1.2 Geopolymer-repaired beams with smooth interfaces (GEO-S) 220
4.1.3 Geopolymer-repaired beams with rough interfaces (GEO-R) 221
4.1.4 Commercial repair beams with smooth interfaces (P-S) 223
4.1.5 Comparative discussion of observed failure patterns 225
4.2 Force–displacement response of the tested beams 226
4.2.1 Unrepaired concrete beams (CON) 226
4.2.2 Geopolymer-repaired beams with smooth interfaces (GEO-S) 227
4.2.3 Geopolymer-repaired beams with rough interfaces (GEO-R) 229
4.2.4 Commercial repair beams (P-S) 229
4.2.5 Summary comparison across all beams 230
4.2.6 CON: Crack evolution and failure behavior 232
4.2.7 GEO-S: Crack evolution and patterns 234
4.2.8 GEO-R: Crack evolution and patterns 236

4.2.9 P-S: Crack evolution and patterns 238
4.2.10 Comparison of crack numbers across groups 240
5 Conclusion 241

Conclusions and perspectives **243**

References **247**

LIST OF FIGURES

1.1 CO_2 emissions system for production of 1 m^3 of concrete/geopolymer (Turner and Collins, 2013) 5
1.2 CO_2 emissions system for production of geopolymer alkali activators (Turner and Collins, 2013) 6
1.3 Advantages of utilizing geopolymers in infrastructure construction (Almutairi et al., 2021) 8
1.4 Conceptual model for geopolymerization (Duxson et al., 2007a) 18
1.5 The effect of metakaolin replacement ratio of GBFS on setting time (Huseien et al., 2018) 19
1.6 The flowability of geopolymer mortars (Adapted from Zhong et al. (2023)) 21
1.7 Development of compressive and flexural strength of metakaolin-based geopolymer mortar (Adapted from Rovnaník (2010)) 22
1.8 Impact of MK substituted GBFS on the early compressive strength of GPMs. (Adapted from Huseien et al. (2018)) 23
1.9 Development in compressive strength of GPMs vs. sodium hydroxide concentration for various curing days in the presence of different sand to binder mass ratios. (Adapted from Vasconcelos et al. (2013)) 24
1.10 Autogenous and drying shrinkage of the geopolymer pastes and mortars with different S/B (Adapted from Yang et al. (2017a)) 27
1.11 Slant shear test setup for composite concrete interface (Ekaputri et al., 2022) 30
1.12 Photo and schematic of the direct shear apparatus (El Dandachy et al., 2024a) 31
1.13 Push-out test setup for composite concrete interface (Ekaputri et al., 2022) 32
1.14 Z-shaped specimen shear test setup for composite concrete interface. (Adapted from Ekaputri et al. (2022)) 33
1.15 Direct pull-out test setup for evaluating bond performance at the geopolymer–steel interface (Peng et al., 2022b) 34
1.16 Mohr-Coulomb failure criterion for interfaces 35
1.17 Typical shear process of HDG Overlay on Concrete Substrate (Li et al., 2024) 37
1.18 Shear stress distribution and debonding process of double-interfaced shear specimen (Gao et al., 2022) 38
1.19 Relationship between compressive strength and ultimate bond strength for geopolymer–steel interfaces. 39
1.20 Shear mechanism of interface: (a) Exposed aggregate type; (b) Shear key type (Bai et al., 2024) 42
1.21 Minimum bond strength of various binder systems under different substrate conditions. (Adapted from Ariyadasa et al. (2024)) 43

1.22 Failure patterns of slant shear test composites (Ariyadasa et al., 2024) . . 44
1.23 The boundary conditions and interface geometry. (Adapted from Badika et al. (2024)) 47

2.1 Schematic presentation of regularized crack topology 52
2.2 Automatic Vicat apparatus used for setting time determination 55
2.3 Flowability evaluation of geopolymer mortar under different drop counts . 56
2.4 Flexural strength evaluation setup 58
2.5 Compressive strength evaluation setup 60
2.6 Schematic of uniaxial compression test setup 61
2.7 Representative stress–strain response of a geopolymer mortar specimen under uniaxial compression. 62
2.8 Failed specimens after uniaxial compression tests 64
2.9 Uniaxial compressive stress–strain responses of geopolymer mortar specimens GM1, GM2, and GM3 65
2.10 Uniaxial compressive stress–strain responses of traditional Portland Concrete specimens OPC1, OPC2, and OPC3 66
2.11 Permeability testing apparatus (actual laboratory configuration) 70
2.12 Schematic diagram of the permeability apparatus (Quelennec et al., 2023) 70
2.13 Gas permeability of geopolymer mortar under two conditions: (a) confining pressure variation; (b) gas pressure variation 74
2.14 Klinkenberg correction: linear fitting of dry-state apparent permeability versus $1/P_{\mathrm{mean}}$ 75
2.15 Porosity testing apparatus 77
2.16 Schematic diagram of the porosity apparatus 77
2.17 Vacuum drainage apparatus 80
2.18 Shrinkage specimens preparation procedure: (a) Shrinkage test mold; (b) Specimens after casting; (c) Specimens after demolding 81
2.19 Shrinkage test setup using vertical deformation meter 82
2.20 Illustration of 3D printing mould for plastic shrinkage test (Chen et al., 2018) 83
2.21 Grid division for DIC analysis of geopolymer mortar shrinkage 84
2.22 Digital Image Correlation (DIC) Shrinkage testing setup 84
2.23 Custom-designed mold for plastic shrinkage test (Chen et al., 2018) . . . 85
2.24 Shrinkage specimens preparation procedure 85
2.25 Long-term drying shrinkage of geopolymer mortar 87
2.26 Long-term drying shrinkage mass loss ratio of geopolymer mortar 87
2.27 Long-term autogenous shrinkage of geopolymer mortar 88
2.28 Long-term autogenous shrinkage mass loss ratio of geopolymer mortar . . 89
2.29 DIC camera view at different test stages 90

2.30 Comparison of short-term drying shrinkage measured by LVDT and DIC 91
2.31 Discrete and continuous DIC monitoring of early-age drying shrinkage . . 92
2.32 ε_{xx} shrinkage strain distribution of geopolymer mortar from Day 1 to Day 7 93
2.33 Continuous shrinkage monitoring of geopolymer mortar from casting vs. after demolding using DIC 95
2.34 Strain vector distribution of specimens DS-D and PS-E analyzed by DIC . 96
2.35 Plastic shrinkage evolution and setting time measured by Vicat needle penetration (EN 196-3, 2016) 97
2.36 Plastic shrinkage under different wind speeds 98

3.1 Geo-con samples after preparation 103
3.2 Shear test setup and schematic of geo–con interface 104
3.3 Shear strength preliminary test shear displacement curve of geo-con interface 105
3.4 Photographs of geo-con specimens with cracks on concrete part following shear testing 106
3.5 Preparation of cylindrical and half-cylindrical concrete specimens from large cast blocks 107
3.6 Concrete specimens for shear strength and permeability tests 108
3.7 Geopolymer specimens for shear and permeability test 109
3.8 Processes involved in preparing concrete specimens 109
3.9 Fine aggregate concrete half-cylinder specimens with different roughness 110
3.10 Coarse aggregate concrete half-cylinder specimens with different roughness 111
3.11 Concrete surface: texture and 3D topographical visualization 111
3.12 Photograph of the shear strength and permeability test apparatus 112
3.13 Schematic diagram of the shear cell under confining pressure 113
3.14 3D roughness scans of smooth coarse aggregate concrete surfaces (L0) . . 118
3.15 3D roughness scans of sandblasted concrete surfaces (L1 and L2) 118
3.16 3D roughness scans of shear-fractured concrete surfaces (L3) 119
3.17 Coupled evolution of shear stress and permeability for fine aggregate geo-con interfaces with different surface roughness levels 121
3.18 Coupled shear stress and permeability responses of C-L0 coarse aggregate geo-con smooth interfaces 123
3.19 Coupled shear stress and permeability responses of C-L1 coarse aggregate geo-con interfaces 124
3.20 Coupled shear stress and permeability responses of C-L2 coarse aggregate geo-con interfaces 125
3.21 Coupled shear stress and permeability responses of C-L3 coarse aggregate geo-con interfaces 126
3.22 Coupled shear stress and permeability responses of F-CON whole specimen 127

3.23 Coupled shear stress and permeability responses of C-CON whole specimens . . . 128
3.24 Coupled shear stress and permeability responses of G-GEO whole specimens . . . 129
3.25 Initial and final permeability (K) results for concrete, geopolymer, and geo-con interface . . . 130
3.26 Typical shear load-displacement characteristic curves (Yang et al., 2024) . 133
3.27 Mechanism of relative sliding of the geopolymer and concrete specimen. . 134
3.28 Typical shear permeability-displacement characteristic curves . . . 137
3.29 Scatter plot of shear modulus (MPa) and Sa (um) . . . 139
3.30 Scatter plot of shear stress (MPa) and Sa (um) . . . 141
3.31 Roughness scanning images and results after shear tests . . . 142

4.1 Main stages of the shear evolution of interfaces under low normal loading. (Badika et al., 2022) . . . 146
4.2 2D schematic view of the direct shear test configuration. . . . 147
4.3 Structured mesh distribution used in the geopolymer–concrete model. . . 148
4.4 Boundary conditions and loading steps . . . 156
4.5 Configuration of interfaces in the geopolymer–concrete model . . . 158
4.6 Model prediction and experimental results for smooth interface (L0) . . . 160
4.7 Model prediction and experimental results for rough interface L1 . . . 162
4.8 Model prediction and experimental results for rough interface L2 . . . 163
4.9 Model prediction and experimental results for rough interface L3 . . . 163
4.10 Normal contact stress (CPRESS) distribution on the geopolymer side at different loading stages . . . 167
4.11 Normal contact stress (CPRESS) distribution on the concrete side at different loading stages . . . 168
4.12 Evolution of displacement and interfacial shear strain (geopolymer side) in the numerical simulation of smooth geo–con interface under shear loading 169
4.13 Shear strain evolution on the concrete side in the numerical simulation of smooth geo–con interface under shear loading . . . 170
4.14 Correlation between interface parameters and interface roughness(Sa) . . 172
4.15 Boundary condition of the shear response of concentric cell shear . . . 173
4.16 Shear stress–displacement response of the concentric geo–con interface under different confining pressures . . . 174
4.17 Shear stress–displacement response of geo–con interfaces with various concrete core diameters under 30 bar confinement . . . 175
4.18 Shear stress–displacement response of geo-con interfaces with various roughness under 30 bar confinement . . . 176

4.19 Evolution of displacement and shear strain fields in the concentric cell shear numerical simulation of smooth geo–con interface 177

5.1 Steel substrates with varying surface roughness for Geo-steel interface preparation 182
5.2 Cylindrical geo-Steel specimens after demolding 183
5.3 Geo-steel interface specimens after curing, showing different steel surface roughness levels 183
5.4 Debonded geo-steel interface specimens after curing 184
5.5 Debonded geo-steel specimens with different steel surface treatments . . 185
5.6 Debonding behavior of geo-steel specimens with 2% phosphatic additive . 187
5.7 Shear test performance of geo-steel specimens made with silicon-rich MK 189
5.8 Shear stress and permeability results of new MK geopolymer 190
5.9 Load transfer interfaces in the shear testing setup 191
5.10 Schematic diagram cell under press for concentric cell shear and permeability test 192
5.11 Post-test appearance of geo-steel specimen showing no visible cracks, confirming the validity of shear strength results 193
5.12 Shear stress and permeability results of geo-steel specimen concentric cell testing 194
5.13 Post-test appearance of phosphatic geo-steel specimen showing no visible cracks, confirming the validity of shear strength results 196
5.14 Shear stress and permeability results of geo-steel specimen concentric cell testing 197

6.1 Stereoscopic image of a beam 203
6.2 Concrete beam reinforcement details (Unit:mm) 204
6.3 Concrete beam reinforcement details with repair materials (Unit:mm) . . 204
6.4 The particle size distribution for sand and coarse aggregate 205
6.5 Rebar cages fabrication progress 207
6.6 Fabrication of complete reinforced concrete beams 208
6.7 Fabrication of reinforced concrete beams for repair 209
6.8 Fabrication of reinforced concrete beams with rough surface for repair . . 210
6.9 Fabrication of beams repaired with geopolymer mortar 211
6.10 Fabrication of beams repaired with commercial products 212
6.11 Diagram of the beam subjected to four-point bending test 213
6.12 Loading apparatus 214
6.13 Digital Image Correlation (DIC) configuration and observation zones . . . 215
6.14 Surface preparation procedure for DIC measurement 217

6.15 Full-field maximum principal strain (ε_1) distribution of reinforced concrete beams at final loading stage (CON-1 to CON-3) 219
6.16 Full-field maximum principal strain (ε_1) distribution of beams repaired with geopolymer mortar on smooth interfaces 220
6.17 Full-field maximum principal strain (ε_1) distribution of beams repaired with geopolymer mortar on rough interfaces 222
6.18 Full-field maximum principal strain (ε_1) distribution of beams repaired with commercial repair mortar on smooth interfaces 224
6.19 Force–displacement (F–δ) response curves of unrepaired reinforced concrete beams (CON-1 to CON-3) 226
6.20 Force–displacement (F–δ) response curves of reinforced concrete beams repaired with geopolymer mortar (GEO-S and GEO-R) 228
6.21 Force–displacement (F–δ) response curves of reinforced concrete beams repaired with commercial repair products (P-S-1 to P-S-3) 230
6.22 Comparative force–displacement (F–δ) curves of all beam specimens, including unrepaired, geopolymer-repaired, and commercially repaired groups 231
6.23 Crack patterns and evolution curves of unrepaired reinforced concrete beams (CON-1 to CON-3) 233
6.24 Crack patterns and evolution curves of beams repaired with geopolymer mortar on smooth interfaces (GEO-S-1 to GEO-S-3) 235
6.25 Crack patterns and evolution curves of beams repaired with geopolymer mortar on rough interfaces (GEO-R-1 to GEO-R-3) 237
6.26 Crack patterns and evolution curves of beams repaired with commercial repair materials (P-S-1 to P-S-3) 239

List of Tables

1.1 Detailed comparison of reinforced concrete repair materials (compiled by the author) . . . 12
1.2 Comparison of common geopolymer precursors for repair applications (Swathi and Vidjeapriya, 2023) . . . 16
1.3 Calibrated parameters for cohesive–frictional interface model (Badika et al., 2024) . . . 48

2.1 Chemical Composition of Metakaolin Powder (by weight) . . . 53
2.2 Chemical composition of Betol K 5020 T® (by mass) . . . 53
2.3 Compressive properties of geopolymer mortar specimens . . . 67
2.4 Elastic Modulus and Poisson's ratio of OPC . . . 67
2.5 Comparison of compressive responses between geopolymer mortar and OPC . . . 68
2.6 Comparison between conventional shrinkage measurement and DIC method 86

3.1 Experimental matrix for shear and permeability tests at geopolymer–concrete interfaces . . . 117
3.2 Summary of interface roughness, peak shear strength, and deformation characteristics of all specimens . . . 131
3.3 Characteristic values from the shear stress displacement curves . . . 136

4.1 Linear elastic properties of geopolymer and concrete used for Mohr–Coulomb model . . . 151
4.2 Mooney–Rivlin hyperelastic parameters for rubber material . . . 152
4.3 Calibrated parameters for smooth interface and rubber interfaces . . . 161
4.4 Interface model parameters for the geo–con interface under different roughness levels . . . 164

5.1 Chemical composition of the silicon-rich metakaolin . . . 188

6.1 Flexural stiffness and peak load results from four-point bending tests on all beam specimens . . . 232
6.2 Observed number of cracks in each beam specimen after testing . . . 241

General Introduction

In the face of growing environmental concerns and the aging of infrastructure worldwide, the durability and sustainability of repair materials have become critical challenges in civil engineering. Reinforced concrete, widely used in transportation, marine, and industrial facilities, is prone to degradation due to mechanical fatigue, environmental attacks, and material aging. Typical symptoms include cracking, reinforcement corrosion, and surface spalling, all of which threaten the serviceability and safety of structures.

Traditionally, Ordinary Portland Cement (OPC)-based materials have served as the main binder in concrete repair systems. Despite their widespread use, OPC binders suffer from significant drawbacks including high carbon emissions, poor acid resistance, and vulnerability to shrinkage and microcracking. These limitations hinder their performance in aggressive service environments and motivate the development of alternative repair technologies.

Geopolymers, first conceptualized by Davidovits in the late 1970s, are aluminosilicate binders formed through alkaline activation of materials such as metakaolin or fly ash. With their low carbon footprint, high chemical stability, and favorable mechanical performance, geopolymers have attracted increasing attention as a promising candidate for sustainable repair. In particular, their intrinsic compatibility with existing concrete due to similar mechanical properties and enhanced bond strength opens new opportunities for infrastructure rehabilitation.

However, despite these promising characteristics, several gaps remain in the understanding of geopolymer-based repair systems, especially concerning their interface performance with traditional concrete and steel substrates. The mechanical integrity and long-term durability of such systems are largely governed by the behavior of the repair–substrate interface under combined mechanical and hydraulic actions. Moreover, shrinkage-induced stresses and the role of surface roughness at the interface have not been fully quantified in existing literature.

To address these challenges, this thesis aims to investigate the potential of potassium-based geopolymer mortars for repairing reinforced concrete structures. The study encompasses multiscale experimental and numerical approaches, focusing on:

- Physical and mechanical characterization of geopolymer mortars, including shrink-

age evolution and permeability.

- Hydro-mechanical behavior of geopolymer–concrete and geopolymer–steel interfaces under confining shear.
- Development and calibration of finite element models for simulating interfacial damage mechanisms.
- Structural-scale validation through four-point bending tests on geopolymer-repaired reinforced concrete beams.

This thesis is organized as follows:

- **Chapter 1** reviews the state of the art in repair materials, compares OPC and geopolymer systems, and identifies current research gaps.
- **Chapter 2** presents the formulation, shrinkage performance, and mechanical properties of the potassium-based geopolymer mortars.
- **Chapter 3** investigates the shear strength and permeability of geopolymer–concrete interfaces, with emphasis on roughness effects and hydro-mechanical coupling.
- **Chapter 4** develops a numerical simulation framework for the interfacial response under confinement, incorporating cohesive-frictional behavior laws.
- **Chapter 5** explores the bonding performance of geopolymer–steel interfaces and assesses the effects of phosphatic additives.
- **Chapter 6** validates the proposed repair approach on structural-scale specimens, comparing geopolymer repairs to commercial products through full-field DIC measurements and flexural testing.

By integrating material-level understanding with structural-scale verification, this work contributes to the advancement of geopolymer-based repair strategies, providing a scientific basis for their application in sustainable infrastructure renewal.

CHAPTER 1

State of the Art

1 Background and motivations

In response to the growing global demand for infrastructure repair, the development of effective and sustainable repair materials has become increasingly urgent. Among aging reinforced concrete structures, typical deterioration mechanisms include cracking, rebar corrosion, and concrete spalling, which critically compromise structural integrity and safety (Huang et al., 2017; Aldahdooh et al., 2016; Fu et al., 2016; Tennakoon et al., 2017; Shaheen and Pradhan, 2017; Grengg et al., 2019; Markandeya et al., 2019; Aggelis, 2011; Wu et al., 2017; Andrade et al., 1993; Li, 2003, 2005; Otsuki et al., 2000; Tepfers, 1973; Prieto et al., 2011; Pantazopoulou and Papoulia, 2001; Moccia et al., 2021). Ordinary Portland Cement (OPC) remains the dominant binder in repair mortars, but its environmental impact and limited durability in aggressive environments have prompted the search for alternative materials.

Geopolymers have emerged as a promising class of binder materials for repair applications, owing to their favorable early-age properties, such as high strength, low shrinkage, and excellent chemical durability (Zhang et al., 2014; Xie and Ozbakkaloglu, 2015). Originally introduced by Davidovits in the late 1970s (Davidovits, 1991a), geopolymers are inorganic aluminosilicate binders activated by alkaline solutions. Their mechanical compatibility with OPC—particularly similar elastic modulus and tensile strength—makes them especially suitable for hybrid or composite repair systems (Deb et al., 2014; Nath and Sarker, 2014, 2015).

In the context of structural repair, two key challenges arise: (1) mitigating early shrinkage to reduce stress accumulation and cracking at the interface, and (2) ensuring durable bonding between the repair material and the substrate, particularly at the geopolymer–concrete and geopolymer–steel interfaces. Addressing these issues requires a thorough understanding of hydro-mechanical behavior at the interface, influenced by shrinkage development, surface roughness, confinement, and permeability.

This chapter introduces the potential of geopolymers to replace OPC-based repair systems and discusses the experimental and numerical approaches used in this thesis to investigate early shrinkage and interface bonding mechanisms. In particular, the mechanical and transport behavior of the geo-con and geo-steel interfaces is examined through shear–permeability tests. The impact of surface roughness on adhesion and durability is emphasized, alongside the application of Finite Element Analysis (FEA) for simulating interface evolution and long-term repair performance.

2 OPC and geopolymer

2.1 Carbon dioxide equivalent

Widely utilized in infrastructure projects, OPC is, however, implicated as a significant contributor to CO_2 emissions (Zhang et al., 2018; Cong et al., 2024; Karadumpa and Pancharathi, 2024; Nie et al., 2022), accounting for approximately 8% of global emissions (Andrew, 2018). This underscores the environmental impact associated with its use in the construction industry. The International Energy Agency (IEA) mandates that global energy-related CO_2 emissions reach net zero by the year 2050 (International Energy Agency (IEA), 2021). In alignment with this goal, and to meet the climate targets established by the Paris Agreement, global greenhouse gas (GHG) emissions must reach net-zero—and likely become net-negative—between 2055 and 2080 (Bataille et al., 2018).

However, OPC is a fundamental component in the construction sector, produced by calcining limestone or chalk mixed with clay at high temperatures around 1450° C within rotary kilns. This process generates solid nodules that are subsequently ground with a minor addition of gypsum through ball milling. The manufacturing process is energy-intensive, primarily utilizing coal or petroleum coke as a fuel source (Hashmi et al., 2022;

Karadumpa and Pancharathi, 2024). It has been reported that the production of one ton of OPC emits approximately 0.73 to 0.85 tons of CO_2 (Hasanbeigi et al., 2012; Hills et al., 2016). However, more recent estimates by the International Energy Agency (IEA) suggest a slightly lower average direct emission intensity—just under 0.6 t CO_2 per ton of cement—based on data stabilized since 2018 (International Energy Agency, 2024).

Unlike traditional Portland cement, which is based on calcium silicate hydrates, geopolymers derive their strength from networks of aluminum and silicon oxides (Karuppaiyan and Jeyalakshmi, 2024; Vanitha et al., 2022). Geopolymers offer a compelling alternative to cementitious materials (McLellan et al., 2011; Duxson et al., 2007b; Aleem and Arumairaj, 2012). Research shows that replacing OPC with geopolymers can reduce carbon emissions by about 25-80% (van Deventer et al., 2010; Duxson et al., 2007b; Stengel et al., 2009; Witherspoon et al., 2009; Habert et al., 2011; McLellan et al., 2011), depending on the precursors and alkaline activators used (Tayeh et al., 2021).

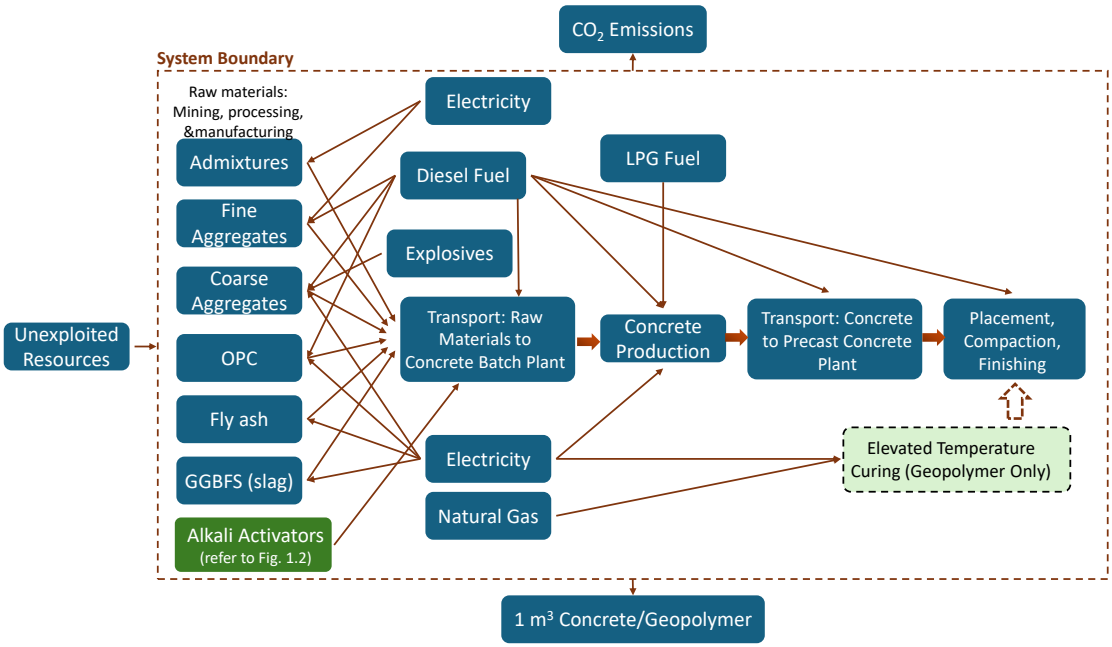

Figure 1.1: CO_2 emissions system for production of 1 m^3 of concrete/geopolymer (Turner and Collins, 2013)

Australian researchers (Turner and Collins, 2013) have conducted comprehensive analyses comparing the carbon dioxide emissions associated with the production of concrete and geopolymer materials on a per-unit-volume basis. Their studies encompass the entire life cycle—from raw material extraction to manufacturing processes—providing a holistic

assessment of the environmental impacts of each binder system. Figure 1.1 illustrates the CO_2 emission activities associated with the production of 1 m^3 of concrete or geopolymer. It includes a breakdown of the major energy inputs required for each activity throughout the production chain. Furthermore, Figure 1.2 provides a detailed summary of the CO_2 emission contributions specifically related to the synthesis of alkaline activators used in geopolymer production.

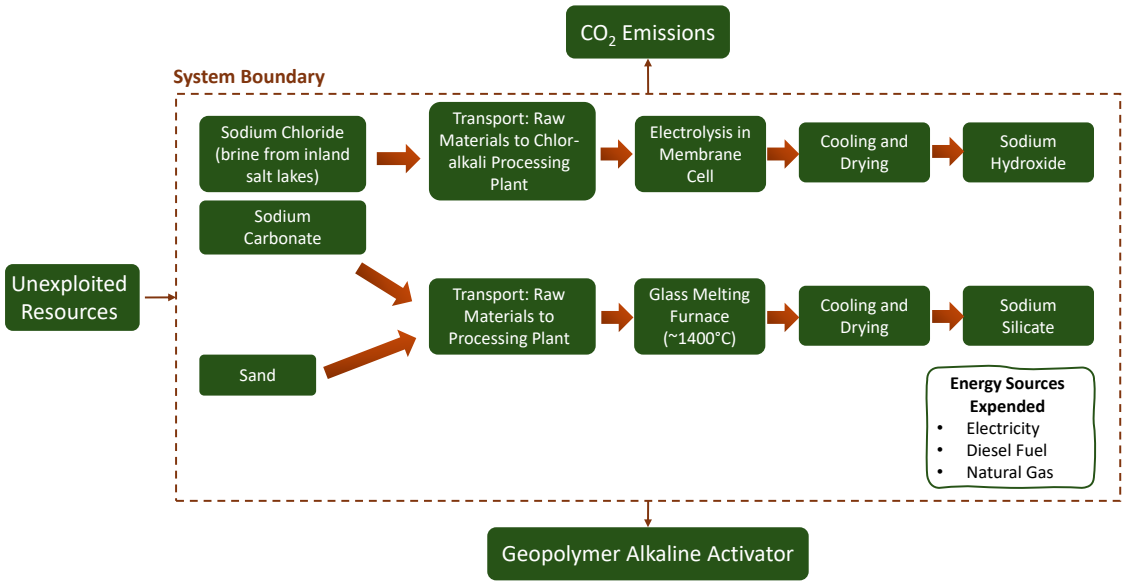

Figure 1.2: CO_2 emissions system for production of geopolymer alkali activators (Turner and Collins, 2013)

According to Turner and Collins (2013), the CO_2 equivalent (CO_2-e) emissions are estimated by considering the total emissions of CO_2, CH_4, N_2O, and synthetic gases released during fuel combustion. The calculation takes into account the fuel's energy content, the types of greenhouse gases generated, and their associated global warming potential (GWP).

$$CO_2\text{-e} = Q \times EC \times GWP \tag{1.1}$$

where Q represents the mass of fuel consumed for a specific process (in kg); EC denotes the energy content of the given fuel type used for the activity (in J/kg); and GWP indicates the global warming potential associated with the specific fuel, accounting for the combined effect of greenhouse gases such as CO_2, CH_4, N_2O, and synthetic gases

(expressed in kg CO_2-e/J).

The results indicate that the CO_2-e emissions associated with geopolymer production are approximately 9% lower than those of ordinary Portland cement (OPC). However, elevated temperature curing leads to a 12.4% increase in CO_2 emissions compared to ambient curing conditions. These discrepancies with previous studies are primarily attributed to the substantial variation in transportation-related emissions. In contrast to earlier assessments, the present study incorporates the energy consumption involved in the sourcing and delivery of both raw materials and alkaline activators, providing a more comprehensive estimation of environmental impact.

It is worth noting that the situation in Europe is relatively complex, making it challenging to accurately quantify emissions related to transportation and material procurement. Nevertheless, the findings presented in this study offer valuable insights and serve as a useful reference for understanding the environmental implications of geopolymer production under varying regional conditions.

2.2 Challenges of OPC and advancements in geopolymer technology

Ordinary Portland Cement (OPC) has exhibited compromised performance in acidic or sulfate-rich environments, particularly concerning marine infrastructure. The presence of calcium compounds in OPC makes it non-resistant to acid attack. This leads to an easy dissolution of these compounds, increased porosity, and accelerated degradation of the structure as detailed in recent studies (Chindaprasirt and Rattanasak, 2016). Over the years, structures made from OPC have shown significant signs of deterioration, impacting their integrity and longevity (Hossain et al., 2015). The inherent composition of OPC includes approximately 60–65% calcium oxide (CaO) and 25% calcium hydroxide ($Ca(OH)_2$), which reacts negatively in acidic conditions. The interaction between carbon dioxide (CO_2) and calcium hydroxide ($Ca(OH)_2$) within these environments accelerates the degradation process, leading to the rapid erosion and reduced lifespan of concrete structures (Hossain et al., 2015). Additionally, such vulnerabilities in OPC highlight its limitations in terms of durability, safety, and environmental sustainability.

Geopolymer materials not only contribute to the reduction of greenhouse gas emissions but also provide superior performance in terms of resistance to chemicals (Bakharev, 2005; Tomkins, 2011; Hassan et al., 2020; Sikora et al., 2018), heat (Luhar et al., 2021b;

Lahoti et al., 2019; Amran et al., 2022), and mechanical stress (Ahmed et al., 2021, 2023; Vora and Dave, 2013; Ng et al., 2018; Wang et al., 2021a).

2.3 Summary

The literature review indicates that geopolymers exhibit excellent mechanical properties and superior durability performance. Figure 1.3 illustrates the advantages of utilizing geopolymers in infrastructure construction, making them promising candidates for long-term structural applications, especially for repair using.

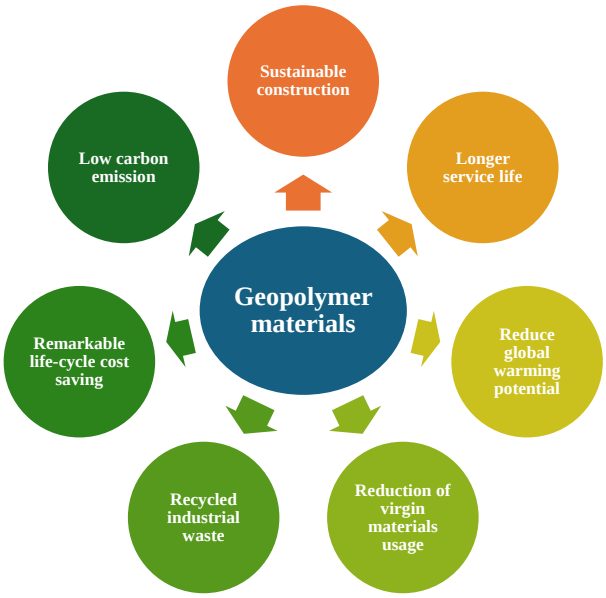

Figure 1.3: Advantages of utilizing geopolymers in infrastructure construction (Almutairi et al., 2021)

3 Repair materials for reinforced concrete

Reinforced concrete (RC) structures worldwide are experiencing progressive deterioration driven by aging, increased service loads, carbonation, chloride ingress, and insufficient maintenance. As a consequence, the global market for concrete repair materials has expanded rapidly, exceeding €20 billion per year (Markets and Markets, 2021; Research, 2023). Forecasts up to 2030 indicate a sustained rise in demand across all major regions, including North America, Europe, Asia-Pacific, Latin America, and the Middle

East, confirming the strategic importance of durable repair systems in civil infrastructure management.

3.1 Typical deterioration mechanisms

RC elements, both cast-in-place and prestressed, commonly suffer from multiple forms of degradation, often occurring simultaneously and accelerating structural decline. Typical damage includes:

- cracking induced by mechanical loads, shrinkage, thermal gradients or restrained movements,
- corrosion of reinforcing steel triggered by carbonation or chloride penetration,
- delamination and loss of adhesion between concrete layers,
- leakage and localized permeability defects, particularly in hydraulic infrastructures.

These mechanisms weaken the composite action of concrete and steel, reduce serviceability, and compromise structural safety. As a result, the selection of appropriate repair materials is critical for restoring load-bearing capacity and ensuring long-term durability.

3.2 International standards for repair materials: EN 1504 framework

The European standard EN 1504 provides a comprehensive framework for the protection and repair of concrete structures. The ten-part standard defines terminology, required performance, testing procedures, product classification, and conformity assessment. Within this framework, Part 3(EN 1504-3) specifies the performance criteria for structural and non-structural repair materials, which include:

Physical requirements dimensional stability (restrained shrinkage/expansion), compatibility with the substrate, and adequate thermal behavior.

Mechanical requirements compressive strength, adhesive bond, and elastic modulus appropriate for structural repair applications.

Chemical requirements resistance to carbonation, chloride ingress, and chemical attack in aggressive environments.

Durability requirements low capillary absorption, low permeability, adequate freeze–thaw resistance, and stable long-term volume change.

These criteria highlight that a repair material must restore structural integrity while simultaneously providing durable protection against environmental actions.

3.3 Categories of repair materials

Typically, the requirements for reinforced concrete repair materials encompass both superior bond strength and mechanical properties, while also taking into consideration porosity and permeability (Cabrera and Al-Hasan, 1997; Morgan, 1996; Song et al., 2022; Minoru et al., 2001).

In the field of reinforced concrete rehabilitation, the selection of appropriate repair materials is crucial to ensure mechanical restoration, long-term durability, and interfacial compatibility with the existing substrate. Conventional repair materials include polymer-modified mortars, epoxy composites, fiber-reinforced mortars, micro-expansive cements, and quick-setting binders (Ahmad et al., 2012; Guo et al., 2020; Zhang et al., 2024a; Bhutta et al., 2019; Yang et al., 2016). While each system offers specific advantages, their widespread use remains challenged by several performance limitations.

Among these, shrinkage-induced stress is one of the most prevalent and critical issues. Early-age autogenous and drying shrinkage can generate tensile stresses exceeding the interfacial bond strength, particularly at the transition zone between new and existing materials, leading to interfacial cracking and eventual delamination (Morgan, 1996; Rudnicki et al., 2023). This phenomenon is exacerbated under restrained conditions typical of patch repairs, where volumetric deformation cannot be freely accommodated.

Other drawbacks include moisture sensitivity, thermal incompatibility, elevated cost, and limited chemical resistance under aggressive environmental exposures (Hassan et al., 2001; Jumaat et al., 2006). Additionally, the mismatch in mechanical and thermal properties between repair and substrate materials can accelerate differential movement and premature failure.

Given these challenges, there is increasing interest in alternative binder systems with

improved dimensional stability, interfacial performance, and durability. A wide range of materials has been developed to meet EN 1504 requirements. Common categories are summarized in Table 1.1

Table 1.1
Detailed comparison of reinforced concrete repair materials (compiled by the author)

Material Type	Advantages	Disadvantages	Special Applications
Geopolymer (Huseien et al., 2017; Maras, 2021; Wasim et al., 2021; Wazien et al., 2016; Cong and Cheng, 2021; Shahedan et al., 2024; Luhar et al., 2021a)	• Low CO2 emissions during production • High resistance to acids and sulfates • Excellent thermal stability	• Relatively high initial costs • Limited large-scale commercial availability	• Ideal for aggressive chemical environments • Suitable for fire-damaged structure repair
Portland Cement (Shahi et al., 2022; Morgan, 1996; Conde Silva and Serra, 2022)	• Economically viable • Readily available • Well-researched	• High greenhouse gas emissions • Potential for shrinkage and microcracking	• Used in residential/commercial building repairs • Suitable for superficial repairs
Polymer-modified Materials (Ahmad et al., 2012; Ohama and Ramachandran, 1996; Zhang et al., 2021; Assaad, 2018)	• Excellent adhesion • Rapid curing times • High tensile and flexural strengths	• Costly for large-scale applications • Potential environmental hazards	• Used in roads and bridges repair • Effective in sealing hydraulic structures
Calcium Magnesium Phosphate Cement (Yang et al., 2016; Gelli and Ridi, 2023; Ostrowski et al., 2016; Haque and Chen, 2019; Arora et al., 2019)	• Sets and hardens quickly • Good for cold weather applications	• Less durable long-term • Can be more expensive	• Useful for emergency repairs in colder climates • Fast track constructions
Epoxy Resin Mortars (Guo et al., 2020; Rahman and Akhtarul Islam, 2022; Xia et al., 2021)	• Strong mechanical properties • Resistant to chemicals • Customizable	• Sensitive to application conditions • More expensive	• Ideal for structural component repairs • Used for steel reinforcement bonding

Among these, geopolymer mortars have gained particular interest in recent years due to their reduced CO_2 footprint and their favorable performance in aggressive environments. Nevertheless, their performance in *interface-dominated* processes—such as adhesion to aged concrete, compatibility under restrained shrinkage, permeability control, and shear transfer under confinement—remains insufficiently documented.

3.4 Need for improved interface performance

Field experience and repair standards consistently highlight that the success of RC repair systems largely depends on the behavior of the interface between the repair material and the substrate. Interface-related failures—such as premature debonding, crack reopening, or permeability increase—are frequently observed in practice. Therefore, modern repair strategies increasingly focus on:

- optimizing surface roughness to promote mechanical interlocking,
- reducing restrained shrinkage of the repair mortar,
- enhancing adhesion to both concrete and reinforcement steel,
- improving resistance to permeability and aggressive agents.

These considerations form the scientific motivation of the present thesis, which investigates the **coupled hydro-mechanical behavior of geopolymer–concrete and geopolymer–steel interfaces** through a multi-scale experimental program and numerical modeling.

3.5 Geopolymer mortar as repair material

3.5.1 General application of geopolymers in structural engineering

Geopolymer materials have gained increasing attention as environmentally friendly alternatives to Ordinary Portland Cement (OPC) in various specialized structural applications. Their favorable properties—including high early strength, chemical resistance, low shrinkage, and thermal stability—have enabled their use in diverse domains such as fire-resistant coatings (Wang and Le, 2023; Temuujin et al., 2011b; Abdul Rashid et al., 2020), fiber-reinforced composite matrices (Natali et al., 2011; Farhan et al., 2021), and

immobilization of hazardous wastes through encapsulation technologies (Williams et al., 2016; Guzmán-Carrillo et al., 2021; Rooses et al., 2013).

Beyond these niche applications, geopolymers have shown growing potential in civil infrastructure, particularly in surface protection and structural rehabilitation. As protective coatings, geopolymer mortars have demonstrated outstanding performance in resisting chloride ingress and corrosion propagation in reinforced concrete elements, especially in marine or deicing salt–exposed environments (Aguirre-Guerrero et al., 2017). Their high chemical stability and low permeability make them effective barriers against aggressive ions.

In the domain of structural strengthening, geopolymer-based bonding agents have been successfully used in composite systems such as CFRP-strengthened beams, showing comparable or improved performance relative to conventional epoxy systems (Peng et al., 2022a). Similarly, textile-reinforced geopolymer mortars (TRGM) have proven effective in enhancing the shear and flexural capacity of RC elements, while offering intrinsic advantages such as fire and corrosion resistance (Zhang et al., 2019b).

Despite these promising developments, it is noteworthy that the application of geopolymer mortars specifically for repairing deteriorated reinforced concrete remains comparatively underexplored. Only in recent years has research begun to systematically investigate their use in patch repairs and interfacial bonding scenarios (Huseien et al., 2017; Tan et al., 2022). These studies highlight the need for tailored formulations and performance evaluation under realistic service conditions.

Overall, while geopolymer technology has found a firm footing in specialized construction sectors, its extension to structural repair—particularly involving bond-critical applications—represents a compelling and timely area for further research and development.

3.5.2 Precursors of geopolymer as repair material

The performance of geopolymer repair mortars is significantly governed by the type of aluminosilicate precursor used during synthesis. Among the commonly adopted precursors are fly ash (FA), ground granulated blast furnace slag (GGBFS), and metakaolin (MK), each exhibiting distinct physicochemical characteristics that influence setting behavior, workability, and durability (Provis and Bernal, 2014; Duxson et al., 2007a).

Fly ash is a low-calcium industrial by-product rich in reactive silica and alumina. While Class F FA is widely utilized due to its availability and low environmental impact, the high variability in composition across sources and the requirement of thermal curing often limit its applicability in on-site repair scenarios (Duxson et al., 2007a). **GGBFS**, on the other hand, is calcium-rich and exhibits rapid reactivity under ambient conditions, making it suitable for applications requiring high early strength. However, its high CaO content contributes to shrinkage cracking, poor chemical durability in acidic or sulfate environments, and susceptibility to efflorescence (Temuujin et al., 2009). **Metakaolin (MK)**, a dehydroxylated form of kaolinite obtained via thermal activation, offers a high-purity, highly reactive, and compositionally consistent alternative. It contains a well-balanced ratio of amorphous silica and alumina and is free of calcium phases, making it dimensionally stable and chemically durable. As such, MK-based geopolymers have demonstrated excellent resistance to chloride penetration, acid and sulfate attack, and carbonation, making them highly suitable for the rehabilitation of RC structures exposed to aggressive environments (Bakharev, 2005; Swathi and Vidjeapriya, 2023). In addition, MK-based mortars have been shown to achieve strong interfacial bonding with OPC substrates and maintain good long-term mechanical integrity even under ambient curing conditions (Temuujin et al., 2011a). These characteristics address many of the incompatibility issues associated with traditional OPC- or slag-based repair systems.

Table 1.2
Comparison of common geopolymer precursors for repair applications (Swathi and Vidjeapriya, 2023)

Property	**Metakaolin (MK)**	**Fly Ash (FA)**	**GGBFS**
Origin	Calcined kaolinite clay	Coal combustion by-product	Steel industry by-product
Calcium content	Low (Ca-free)	Variable (often low)	High
Amorphous content	High	Moderate to high	Moderate
Chemical consistency	High	Variable (site-dependent)	Variable
Setting behavior	Slow but controllable	Slow (needs heat)	Rapid (fast hardening)
Early strength	Moderate	Low	High
Shrinkage	Low	Moderate	High (with risk of cracking)
Curing conditions	Ambient (suitable for field repair)	Often requires thermal curing	Ambient or slightly elevated
Durability (acid/sulfate)	Excellent	Good	Moderate to poor
Environmental impact	Moderate (not a by-product)	Very low (recycled waste)	Low to moderate
Commercial availability	Moderate	High in some regions	High

Despite these advantages, MK systems are not without limitations. Their slower setting behavior and reduced early-age strength, relative to slag-based mixes, can pose challenges in fast-track repair projects (Temuujin et al., 2009; Khale and Chaudhary, 2007; Zhang et al., 2012). Furthermore, they often require careful tailoring of the activator composition—particularly the silicate modulus and alkali concentration—to balance flowability and reactivity (Temuujin et al., 2009; Swathi and Vidjeapriya, 2023).

Overall, metakaolin represents a technically robust and environmentally sustainable precursor for geopolymer repair mortars. Its superior durability, chemical stability, and interfacial compatibility make it a preferred candidate for long-term reinforced concrete rehabilitation applications (Swathi and Vidjeapriya, 2023).

3.6 Summary

This section reviewed key materials used in reinforced concrete repair, highlighting both conventional and emerging systems. While traditional materials such as polymer-modified mortars, epoxy composites, and expansive cements offer good adhesion and rapid strength gain, they often suffer from shrinkage, poor durability in aggressive environments, and incompatibility with existing substrates.

Geopolymer mortars, particularly those based on metakaolin, offer a promising alternative due to their low shrinkage, excellent chemical resistance, and strong interfacial bonding. MK-based systems are especially suited for ambient-cured, durable repair applications, although careful mix design is required to address slower setting and lower early strength. Overall, geopolymers represent a sustainable and technically sound option for long-term rehabilitation of reinforced concrete structures.

4 Properties of geopolymer mortars as repair materials

4.1 Geopolymerization

Figure 1.4 illustrates a highly simplified mechanism of the geopolymerization reaction. This schematic provides an overview of the essential processes involved during the transformation of solid aluminosilicate sources into synthetic alkaline aluminosilicate compounds (Duxson et al., 2007a).

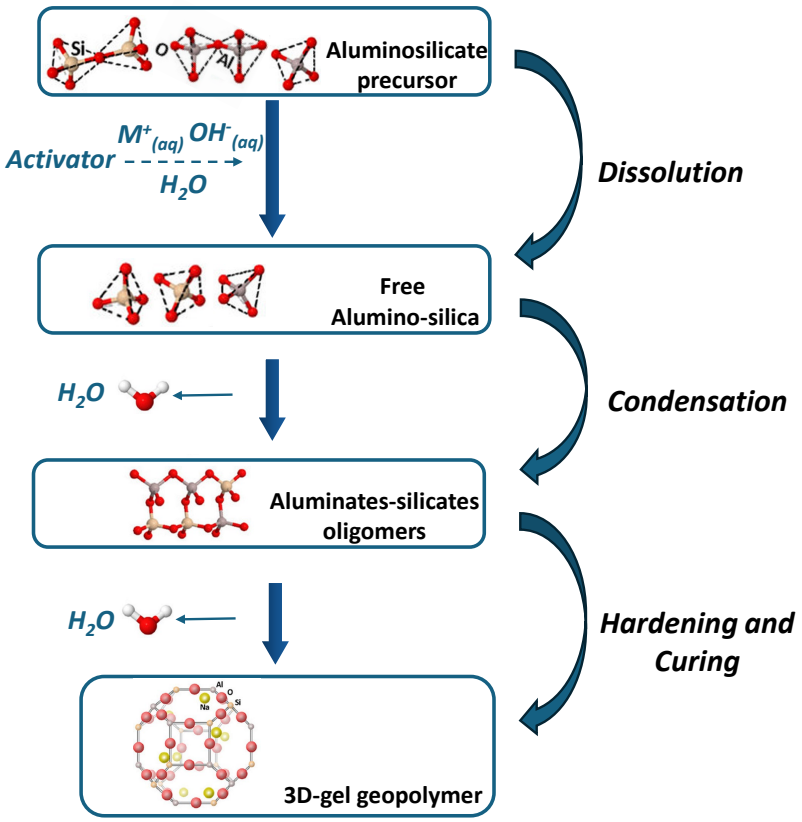

Figure 1.4: Conceptual model for geopolymerization (Duxson et al., 2007a)

A conceptual model outlining the geopolymerization process is presented, which is characterized by three primary stages: dissolution, condensation, and hardening and curing. Initially, solid aluminosilicate precursors undergo dissolution upon interaction with an alkaline activator (typically containing alkali cations and hydroxide ions), forming free alumina and silica species. Subsequently, these dissolved species polymerize through condensation reactions, resulting in the formation of aluminosilicate oligomers. Finally, the continued polymerization leads to the creation of a three-dimensional aluminosilicate gel structure (Blum et al., 1988; Walther, 1996; Oelkers, 2001; Walther, 1996; Khale and Chaudhary, 2007; Duxson et al., 2007a). The strength of geopolymers primarily originates from the development and maturity of this interconnected three-dimensional aluminosilicate network, whose integrity and robustness define the resulting mechanical properties (Majidi, 2009; Muñiz-Villarreal et al., 2011).

4.2 Fresh geopolymer mortar

Setting time and flowability are critical factors influencing the performance of repair materials (Dan et al., 2023; Huseien et al., 2017; Wu and An, 2014). A suitable setting time ensures sufficient workability during application while enabling rapid strength gain, thus minimizing downtime of infrastructure. Optimal flowability facilitates proper filling and bonding at the geopolymer-concrete interface, enhancing bond strength and reducing void formation.

4.2.1 Setting time of geopolymer mortars

The setting time of geopolymers is influenced by several factors, including alkali solution concentration, solid-to-liquid ratio, curing conditions, and precursor properties (Davidovits, 1991b; Temuujin et al., 2009; Duxson et al., 2007b). The setting time of geopolymer mortar was determined in accordance with EN 196-3 (2016), which specifies methods for assessing the initial and final setting time using the Vicat apparatus.

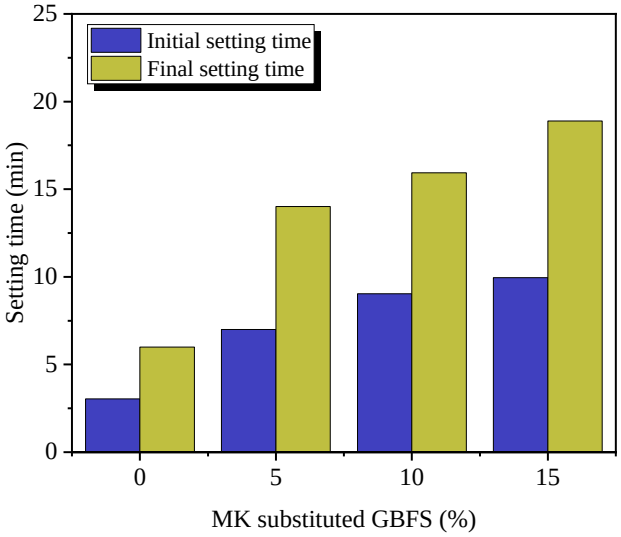

Figure 1.5: The effect of metakaolin replacement ratio of GBFS on setting time (Huseien et al., 2018)

Based on previous studies, it has been observed that in geopolymer systems using metakaolin (MK) and ground granulated blast furnace slag (GGBFS) as precursors, a reduction in calcium content leads to an increase in both initial and final setting times (Phoo-ngernkham et al., 2015; Lee et al., 2016; Sofi et al., 2007). Since increasing the

MK content significantly reduces the overall calcium concentration in the system, it consequently results in prolonged setting. As illustrated in Figure 1.5, the effect of MK replacing GGBFS on the setting time of geopolymer paste (GPP) is clearly demonstrated by Huseien et al. (2018). It can be concluded that MK, as a component of the binary blended binder, effectively delays the setting process of GPM under ambient conditions (Huseien et al., 2018).

Generally, increasing the concentration of alkali activator (e.g., KOH or NaOH) or using higher silicate modulus tends to accelerate the geopolymerization process and shorten the setting time (Khale and Chaudhary, 2007; Al Bakri et al., 2011; Ghosh and Ghosh, 2012). As the liquid-to-solid ratio increases, both the initial and final setting times of the geopolymer tend to increase (Yang et al., 2012). Moreover, higher curing temperatures are known to significantly reduce setting time by enhancing reaction kinetics (Temuujin et al., 2009; Al-Majidi et al., 2016).

4.2.2 Flowability of geopolymer mortars

Flowability is primarily influenced by the liquid-to-solid (L/S) ratio , the viscosity and composition of the alkaline activator, the type and fineness of the precursor, and the presence of additives such as superplasticizers or fine fillers (Pacheco-Torgal et al., 2014). Zhong et al. (2023) prepared MK-GGBFS geopolymer mortars with liquid-to-solid (L/S) ratios of 1.1 and 1.3, respectively and different modules. For each mixture, sand was incorporated at varying volume fractions of 0.35, 0.40, 0.45, 0.50, and 0.55. The flowability of these mixtures was evaluated, and the results are presented in Figure 1.6, demonstrating the influence of both L/S ratio and sand content on the workability of the geopolymer mortar system. An increase in the L/S ratio generally enhances workability due to the reduction in mixture viscosity. The results indicate that the flowability decreases with increasing sand volume fraction. This reduction can be attributed to the decreased paste content, which leads to thinner paste films surrounding the sand particles and increases the likelihood of particle-to-particle contact, thereby hindering the overall mobility of the mixture. The flowability of fresh geopolymer mortar was evaluated based on EN 1015-3 (2007), which defines a standard method using the flow table test for consistency measurement of mortars.

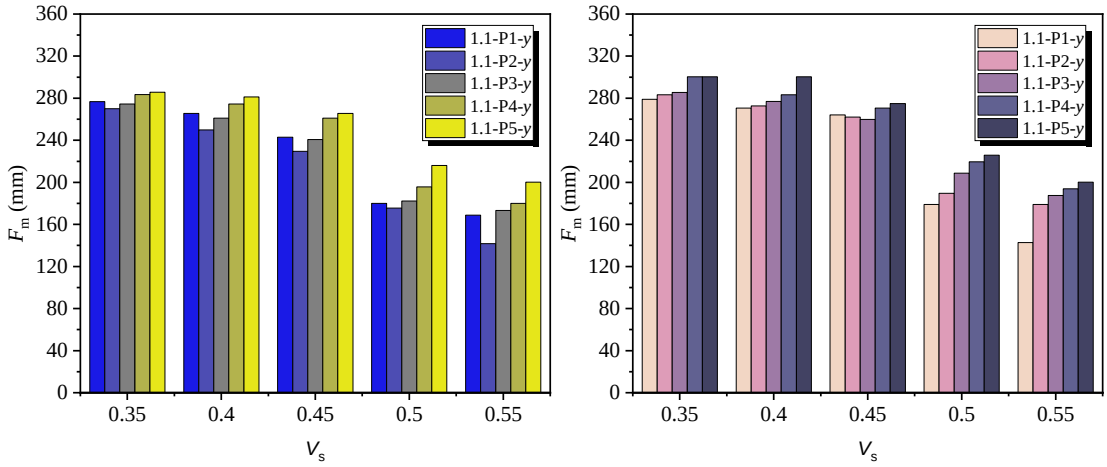

(a) *L/S*=1.1 **(b)** *L/S*=1.3

Figure 1.6: The flowability of geopolymer mortars (Adapted from Zhong et al. (2023))

Note: P1 to P5 represent different silicate moduli (the molar ratio of SiO_2 to Na_2O in the alkaline activator), corresponding to 1.0, 1.2, 1.4, 1.6, and 1.8, respectively.

The use of higher silicate modulus in the activator solution (e.g., higher SiO_2/Na_2O or SiO_2/K_2O) typically results in more viscous systems, thereby reducing the spread diameter and overall flowability (Varga, 2015; Yang and Song, 2009; Yang et al., 2008; Palacios and Puertas, 2005). In contrast, metakaolin-based systems often exhibit lower flow compared to fly ash- or slag-based systems due to the plate-like morphology and higher surface area of MK particles, which increase water demand (Rashad, 2013).

4.3 Hardened geopolymer mortar

4.3.1 Compressive strength of geopolymer mortars

The compressive strength of geopolymer materials is one of the most critical mechanical properties for structural and repair applications. It is influenced by various factors (Huseien et al., 2017). Mechanical properties such as tensile strength, flexural strength, and elastic modulus are strongly correlated with compressive strength. These parameters are often derived or validated through experimental procedures compliant with relevant European standards, including EN 12390-3 (2019) for compressive strength, EN 12390-5 (2019) for flexural strength. Rovnaník (2010) investigated the effect of curing temperature on the mechanical performance of metakaolin-based geopolymer mortars, as shown

in Figure 1.7. The results confirmed the early strength development characteristics of geopolymers, with elevated curing temperatures significantly accelerating both compressive and flexural strength gains within the first few days.

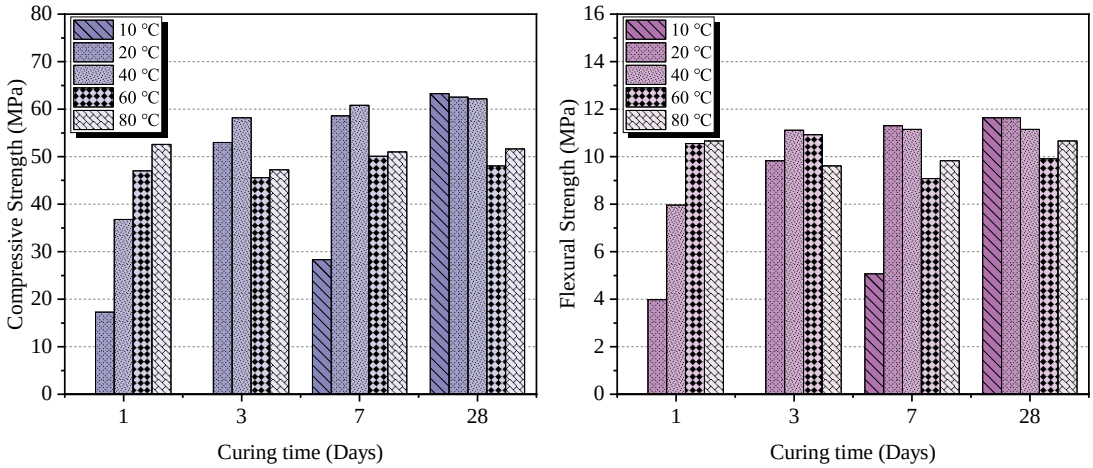

(a) Compressive strength **(b)** Flexural strength

Figure 1.7: Development of compressive and flexural strength of metakaolin-based geopolymer mortar (Adapted from Rovnaník (2010))

Note: Curing at 40, 60 and 80 °C was carried out for initial 4 h.

Precursor type. The nature of the precursor significantly influences the compressive strength of geopolymer binders (Qaidi et al., 2022; Duxson and Provis, 2008; Anburuvel, 2023). Calcium-rich precursors such as GGBFS tend to enhance early-age strength due to the formation of C–(A)–S–H gels alongside geopolymeric gels, whereas low-calcium precursors like metakaolin (MK) usually result in slower strength development but improved long-term stability (Luo et al., 2023; Zhong et al., 2022; Samson et al., 2017; Wu et al., 2024; Pradhan et al., 2024). Huseien et al. (2018) investigated the early-age compressive strength of GPMs with partial MK replacement of GBFS. As shown in Figure 1.8, 5–15% MK substitution improved strength within the first 3 days, indicating a synergistic effect between MK and GBFS.

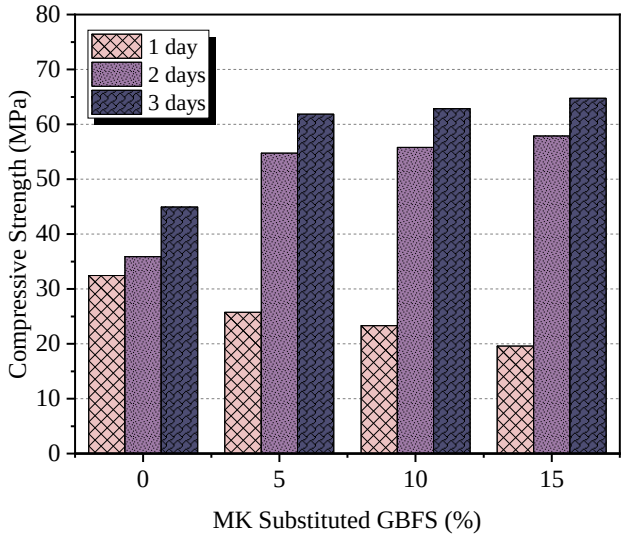

Figure 1.8: Impact of MK substituted GBFS on the early compressive strength of GPMs. (Adapted from Huseien et al. (2018))

Alkali concentration. Higher concentrations of alkali activator generally promote more extensive dissolution of aluminosilicate species, thereby accelerating geopolymerization and increasing compressive strength (Ahmed et al., 2021; Chithambaram et al., 2018; Hadi et al., 2018). However, excessive alkalinity may lead to efflorescence or microcracking, which can negatively impact strength (Castillo et al., 2021).

Silicate modulus. The silicate modulus (SiO_2/Na_2O) of the alkaline activator has a notable effect on strength development. A moderate increase in silicate modulus (typically in the range of 1.2 to 1.6) improves the degree of polymerization and densifies the gel structure, enhancing compressive strength. However, an excessively high modulus (e.g., above 1.8) significantly increases the viscosity of the activator, reducing workability and potentially entrapping air voids, which weaken the hardened matrix (Yadollahi et al., 2015; Kaze et al., 2018; Firdous and Stephan, 2019; Sivasakthi et al., 2021; Guo et al., 2010).

Sand-to-binder ratio. Increasing sand content in geopolymer mortars tends to reduce compressive strength due to reduced paste content and weaker interfacial bonding. An optimal sand volume fraction must balance strength with workability and dimensional stability (Khan et al., 2018; Alnahhal et al., 2022; Kim et al., 2023; Prusty and Pradhan, 2022). Vasconcelos et al. (2013) examined the influence of sodium hydroxide molarity

and sand-to-binder (S/B) ratio on the compressive strength development of geopolymer mortars (GPMs). As shown in Figure 1.9, increasing the alkali concentration from 12 M to 16 M generally enhanced the strength across all curing ages, particularly at lower S/B ratios. However, when the S/B ratio reached 0.9, the effect of molarity became less pronounced, likely due to reduced paste content and insufficient binder availability. These results indicate that the optimal alkaline concentration must be considered alongside aggregate content to ensure sufficient polymerization and mechanical performance.

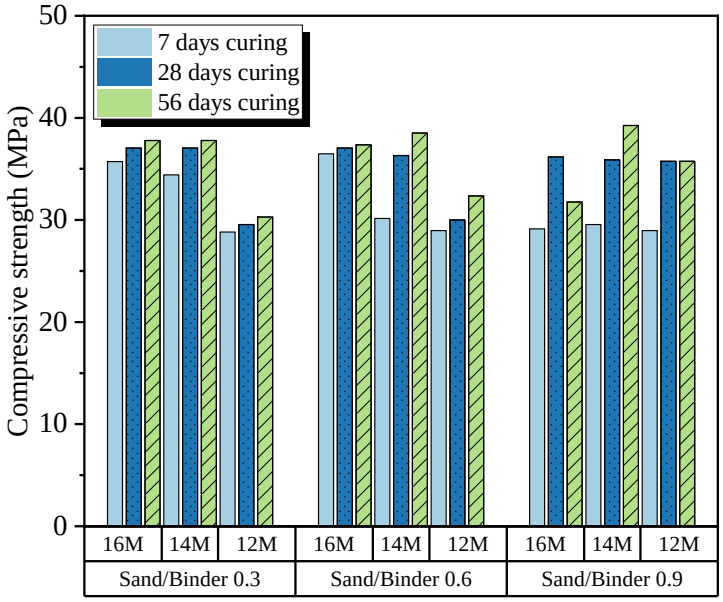

Figure 1.9: Development in compressive strength of GPMs vs. sodium hydroxide concentration for various curing days in the presence of different sand to binder mass ratios. (Adapted from Vasconcelos et al. (2013))

Liquid-to-solid (L/S) ratio. Lower L/S ratios usually result in higher compressive strength due to the formation of a denser matrix (Chen et al., 2024; Maaze and Shrivastava, 2023; Mohammed and Géber, 2025). Conversely, higher L/S ratios increase porosity and reduce strength, despite improving workability.

Curing temperature. Elevated curing temperatures (e.g., 60–90 °C) significantly accelerate the geopolymerization process and promote early strength development. Ambient temperature curing is more convenient for practical use but generally requires longer

time to achieve comparable strength (Rovnaník, 2010; Satpute Manesh et al., 2012; Nasvi et al., 2012; Verma et al., 2022). However, for repair applications, controlling the curing temperature on-site is often impractical, especially under variable environmental conditions (Bernal and Provis, 2014).

Alkali activator type. Common activators include sodium hydroxide (NaOH), potassium hydroxide (KOH), and silicate solutions (Na_2SiO_3 or K_2SiO_3). Generally, activators containing soluble silicates result in higher compressive strength due to enhanced polymerization and the formation of a denser aluminosilicate network. Between Na-based and K-based activators, K-based systems are often reported to form more compact micro structures and achieve comparable or higher strength, possibly due to differences in ion mobility and gel morphology (Leong et al., 2016; Xin et al., 2014; Hadi et al., 2018; Kaur et al., 2018; Bondar et al., 2011).

4.3.2 Shrinkage of geopolymer mortars

The dimensional stability of geopolymer mortars plays a critical role in the performance of composite systems, particularly in the context of interfacial bonding with substrates such as OPC-based concrete. Among the various deformation mechanisms, shrinkage — both autogenous and drying — can induce tensile stresses at the geopolymer–concrete interface, leading to microcracking, debonding, or long-term degradation of the bond strength (Chen et al., 2021a; Zheng et al., 2023; Mastali et al., 2018; Collins and Sanjayan, 2000). Not only do these cracks compromise the integrity and strength of the components, but they also potentially create pathways for the infiltration of harmful substances. Such infiltration can induce corrosion of the internal reinforcement bars in reinforced concrete structures (Zhang et al., 2019a), subsequently reducing their load-bearing capacity. This degradation affects both the usability and durability of the structure. This is also an important consideration when contemplating the use of geopolymer materials applications (Khan et al., 2019; Archez et al., 2021).

Existing research indicates that geopolymer concrete exhibits a higher drying shrinkage rate compared to traditional Portland cement concrete (Collins and Sanjayan, 1999; Mastali et al., 2018; Duran Atiş et al., 2009; Krizan and Zivanovic, 2002). However, the tendency to crack in geopolymers is lower than in traditional concretes (Ling et al., 2019).

The factors influencing the shrinkage of geopolymers are numerous, such as the mod-

ulus and concentration of the alkali-activating solution, pore size distribution, curing conditions, etc (Haha et al., 2011; Bakharev et al., 1999; Chen et al., 2021b). In general, The shrinkage of geopolymer mortar exhibits less than that of paste (Yang et al., 2017b). Higher sand content has been reported to reduce both autogenous and drying shrinkage (Wang et al., 2021b; Nematollahi et al., 2016), as well as to increase the elastic modulus of the mixture (Li et al., 1995; Nematollahi et al., 2016). However, the incorporation of sand as an inert filler also leads to a reduction in the overall volume of binder and alkaline activator per unit volume of mixture, which may adversely affect the geopolymerization process and the resulting mechanical properties. Yang et al. (2017a) investigated the influence of fly ash content (0-30%) and sand-to-binder ratio (S/B = 0, 0.5, 1.0) on the autogenous and drying shrinkage of metakaolin-based geopolymer pastes and mortars. The shrinkage was measured over 50 days under controlled temperature and humidity, with autogenous shrinkage isolated using polyethylene film. Their results (as shown in Figure 1.10) showed that increasing fly ash content significantly increased autogenous shrinkage due to pore refinement and capillary tension, while simultaneously reducing drying shrinkage by limiting moisture loss. Furthermore, the inclusion of sand (higher S/B) effectively reduced both shrinkage types. The mix with 30% fly ash and S/B = 1.0 achieved the lowest total shrinkage and highest compressive strength, suggesting an optimal balance between dimensional stability and mechanical performance.

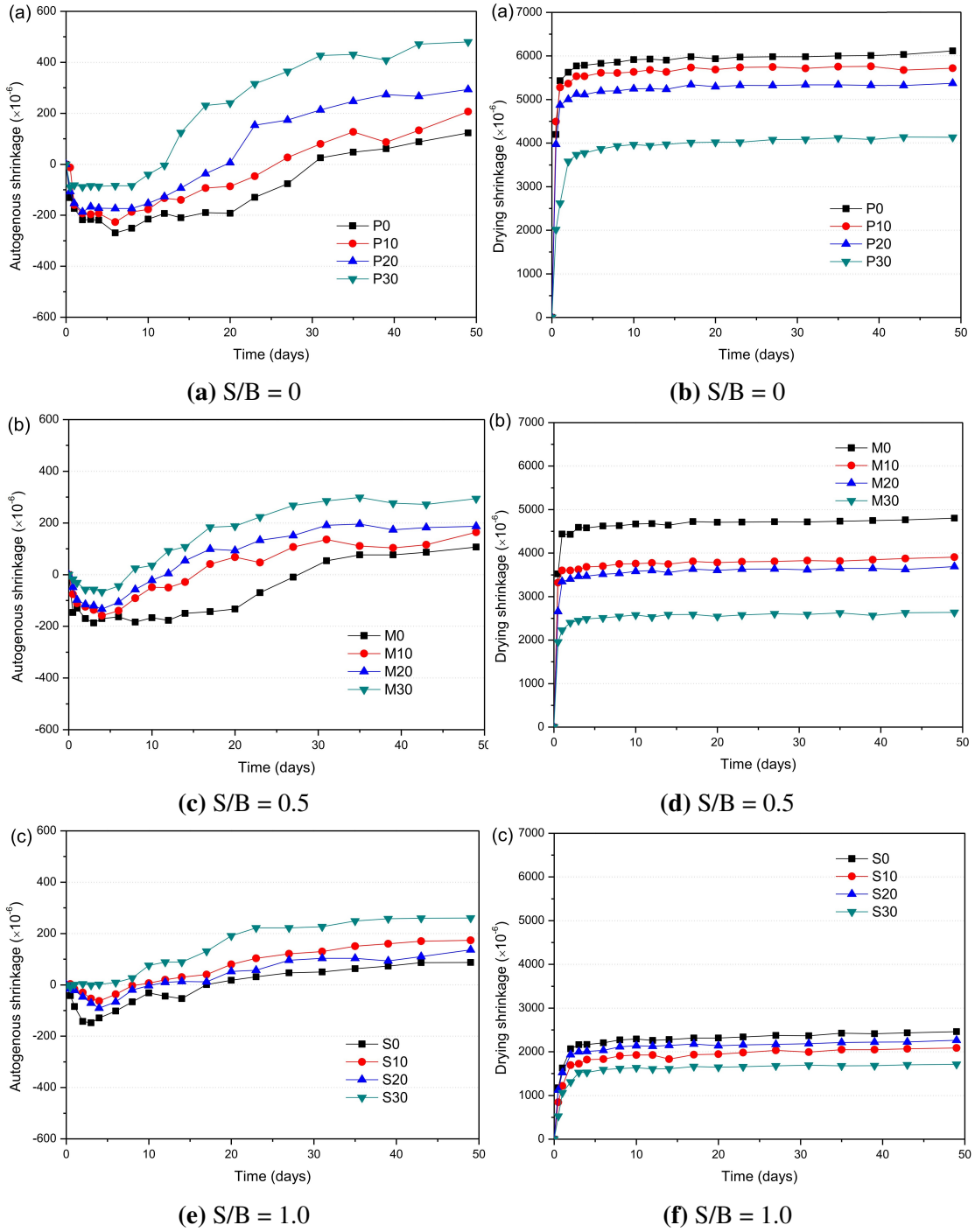

(a) S/B = 0 **(b)** S/B = 0

(c) S/B = 0.5 **(d)** S/B = 0.5

(e) S/B = 1.0 **(f)** S/B = 1.0

Figure 1.10: Autogenous and drying shrinkage of the geopolymer pastes and mortars with different S/B (Adapted from Yang et al. (2017a))

In academic research on concrete shrinkage, shrinkage is typically categorized into three types based on different underlying principles. When studying geopolymers, a sim-

ilar approach is often adopted, examining plastic shrinkage, drying shrinkage, and autogenous shrinkage (Mastali et al., 2018; Huang et al., 2024).

- **Plastic Shrinkage:** Plastic shrinkage occurs during the initial setting phase of cementitious materials when environmental conditions (such as high temperature, high wind speed, and low humidity) cause rapid evaporation of water from the surface before it can be replenished from within, leading to volume reduction and cracking.
- **Drying Shrinkage:** Drying shrinkage happens after the cementitious materials have hardened, as moisture evaporates from the material, causing a reduction in volume. This type of shrinkage is driven by the loss of water from the capillary pores within the cement matrix and is related to the external relative humidity.
- **Autogenous Shrinkage:** Autogenous shrinkage refers to the volume reduction that occurs even in a sealed condition, where there is no loss of moisture to the external environment. It is primarily due to chemical shrinkage associated with the hydration of cement, and is more pronounced in high-performance cementitious materials with low water-to-cement ratios.

It is important to acknowledge that shrinkage in geopolymers predominantly occurs during the curing phase. However, the measurement of this shrinkage typically commences after curing has completed, and may extend over a prolonged period. (Cai et al., 2019; Huang et al., 2024). To measure the shrinkage of geopolymer specimens, the most conventional method involves using a vertical mortar shrinkage meter to observe changes in strain (Zhang et al., 2024c). The advantage of this method is its convenience and low cost, making it suitable for long-term testing. However, the drawbacks include the inability to monitor deformations before demolding and limited precision in the measurements. Ring specimens and strain gauges are utilized to perform restrained shrinkage tests, ingeniously measuring both shrinkage and tensile stress concurrently (Ling et al., 2019). However, the primary limitation of this method is that it only captures data after full consolidation, and the indirectly measured shrinkage values lack precision. Additionally, it only observes local deformations of the specimens. Some researchers adopt microscopy to monitor the changes in deformations and cracks, which allows for a more detailed observation of microscopic changes. Nonetheless, accurately measuring the shrinkage values of specimens of certain sizes remains challenging. Digital Image Correlation (DIC) is

an innovative method used to observe shrinkage in materials (Zhang et al., 2024c; **?**). This technique involves capturing a series of images of the specimen surface as it deforms and then analyzing these images to measure displacements and strains with high accuracy.

4.4 Summary

The fresh and hardened properties of geopolymer mortars have been systematically examined, with particular focus on setting time, flowability, compressive strength, and shrinkage behavior. The results confirm that the studied geopolymer formulations offer satisfactory workability in the fresh state and favorable mechanical performance after hardening. Moreover, the relatively low shrinkage observed in optimized mixtures suggests good dimensional stability. Overall, these characteristics align well with the functional requirements of repair materials, particularly in applications demanding durability, compatibility, and ease of placement.

5 Hydro-mechanical behavior research on geomaterials interfaces

Hydro-mechanical coupling at geomaterial interfaces (including geopolymer–concrete interface and geopolymer and steel interface) refers to the interaction between moisture transport and mechanical response, which is particularly critical in repair systems where a new material is bonded to an existing substrate. In such systems, especially those involving geopolymer mortars and OPC-based concrete, the interface often governs the overall structural performance due to its role in stress transfer, crack initiation, and fluid movement (Hu et al., 2012; Qi et al., 2024; Huseien et al., 2017).

Although various experimental studies have explored the effects of moisture gradients, shrinkage, and substrate surface conditions on interfacial performance (Xia et al., 2023; Sekkal et al., 2023), very few have specifically addressed transport through the interface under mechanical loading. This knowledge gap is particularly evident in studies involving alkali-activated materials and geopolymer systems, where the distinct pore structure and moisture sensitivity could lead to unique coupling mechanisms.

5.1 Testing method

5.2 Geopolymer-concrete interfaces

Recognizing the critical role of interfacial bond strength in the performance of composite systems, numerous experimental approaches have been developed to characterize the shear-bond behavior at the interface between geopolymer and concrete substrates. These methods have been widely adopted in the literature, each offering distinct advantages and limitations.

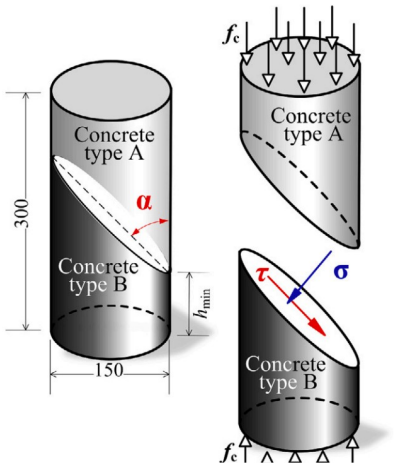

Figure 1.11: Slant shear test setup for composite concrete interface (Ekaputri et al., 2022)

Slant shear test is one of the most commonly adopted due to its relatively simple setup and its ability to simulate combined shear and compressive stresses along the interface (Hachem et al., 2024; Ariyadasa et al., 2024; Zanotti et al., 2017; Alanazi et al., 2016; Ahmad Zailani et al., 2020; Ariyadasa et al., 2024). In this method, a composite specimen — typically composed of geopolymer and concrete segments — is cast with an inclined bonding interface, often at a 30° or 45° angle, as shown in Figure 1.11. Compressive load is then applied axially, inducing a combination of normal and shear stresses across the interface. Despite its widespread use, the slant shear test presents several limitations. The stress distribution along the interface is inherently non-uniform, as the inclined geometry introduces a coupled shear-compression stress state that varies along the bonding plane, making it difficult to isolate and quantify a pure shear response. Additionally, the

measured bond strength is influenced not only by the shear resistance but also by the compressive strength of the constituent materials, which may lead to an overestimation of the true interfacial bond performance. These complexities complicate the interpretation of results, particularly when aiming to understand the intrinsic bond behavior of geopolymer–concrete interfaces under realistic service conditions.

Direct shear test offers a simple and targeted approach for evaluating interfacial bond strength between composite layers (Li et al., 2024, 2025; Badika et al., 2022), as illustrated in Figure 1.12. In this method, a composite specimen with a planar interface is subjected to shear loading, while confinement is theoretically applied in the orthogonal direction to ensure lateral stability. Depending on the test configuration, the shear load may be applied vertically with horizontal confinement, or vice versa. The test is intended to generate pure shear stresses along the bonded surface, theoretically isolating the interface shear response from other stress components. However, confinement is not always clearly implemented or visualized in published setups, potentially resulting in non-uniform stress distribution. This limitation, together with the possibility of misalignment during loading, may introduce unintended tensile or compressive stresses that interfere with accurate bond strength evaluation. Therefore, while this method remains widely used due to its simplicity, caution must be exercised in interpreting the results, particularly for complex composite interfaces involving heterogeneous materials such as geopolymer and concrete.

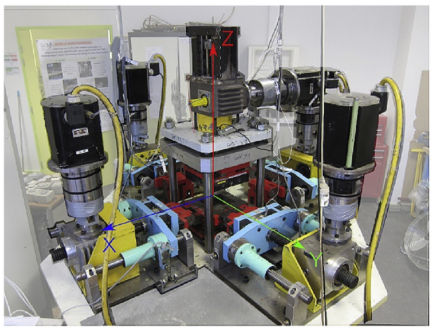

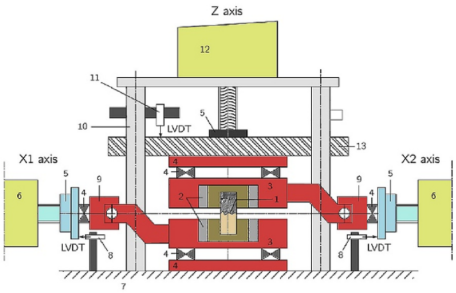

1: Specimen under test
2: Internal removable shear boxes
3: External fixed boxes
4: Rail allowing translation of the boxes
5: Load cells
6: Horizontal actuators
7: Rigid base
8: LVDTs measuring dX1 and dX2
9: Kneecaps
10: Rigid fixed columns
11: LVDT measuring dZ
12: Vertical actuator
13: Rigid vertical plate free to move along Z-axis

Figure 1.12: Photo and schematic of the direct shear apparatus (El Dandachy et al., 2024a)

The push-out test is particularly effective in assessing the behavior across dual bonded surfaces (Peng et al., 2022b; Castel, 2016; Sarker, 2011; Mirza et al., 2014). In this configuration, a central concrete (or geopolymer) element is cast between two external blocks, creating two parallel interfaces subjected to shear during testing. Vertical compressive loads are applied to the outer blocks, generating shear forces at both bonded surfaces simultaneously, as shown in Figure 1.13. An important advantage of this method lies in its ability to evaluate bond performance under symmetric confinement, simulating realistic restraint conditions often encountered in structural elements. However, the presence of two interfaces complicates the interpretation of results, especially when debonding or failure occurs asymmetrically. Additionally, confinement effects can significantly influence shear resistance, and careful design of loading and support conditions is necessary to isolate the pure bond response.

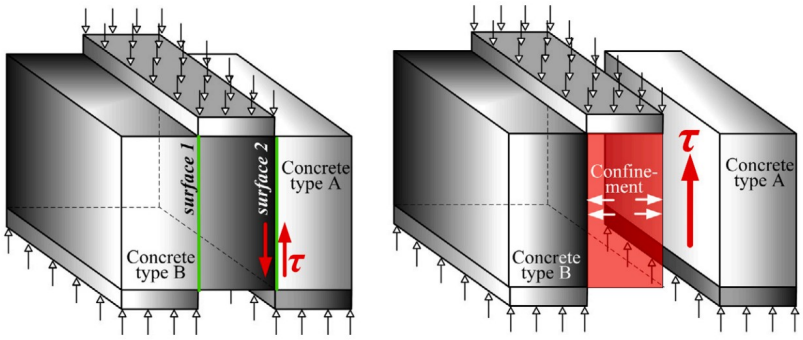

Figure 1.13: Push-out test setup for composite concrete interface (Ekaputri et al., 2022)

Z-shaped specimen shear test is designed to generate a relatively pure shear stress state at the interface between two bonded materials. The specimen interface is shaped in a "Z" form, where the two bonded materials — typically geopolymer and concrete — are arranged in an interlocking manner. The axial compressive load applied to the top and bottom of the specimen induces a direct shear transfer through the bonded interface, as shown in Figure 1.14. A key advantage of the Z-method is its ability to minimize bending or eccentric effects, thus allowing a more reliable assessment of the true shear bond strength (Ganeshan and Venkataraman, 2022; Ekaputri et al., 2022). Moreover, the test setup requires no lateral confinement and offers easier alignment compared to push-out or slant shear tests. However, manufacturing the Z-shaped specimen demands higher precision, and the stress distribution may still be affected by the specimen geometry or

boundary friction.

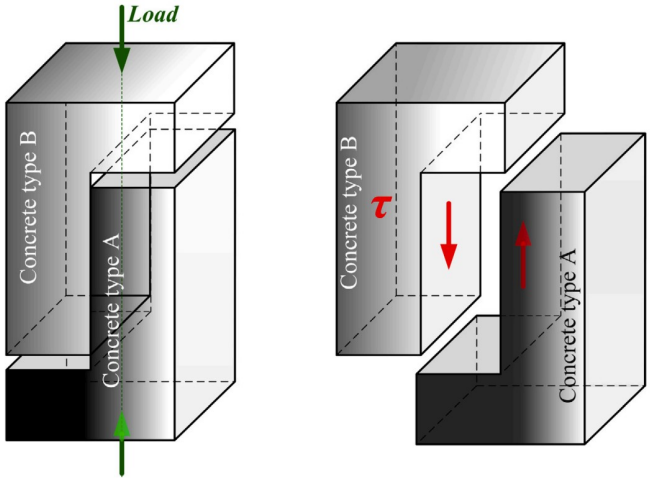

Figure 1.14: Z-shaped specimen shear test setup for composite concrete interface. (Adapted from Ekaputri et al. (2022))

The experimental assessment of interfacial shear bond strength is essential for understanding the mechanical integrity of geopolymer-concrete composite systems. Each method provides unique advantages: for instance, slant shear tests simulate combined stress states, direct shear allows for targeted loading, push-out tests incorporate confinement effects, and the Z-method minimizes bending and eccentricity.

Conventional shear tests are generally designed for mechanical evaluation alone and do not consider the influence of concurrent fluid flow through the interface, which can significantly alter the mechanical response of geopolymer materials—particularly in repair or underground applications.

5.3 Geopolymer-steel interfaces

The direct pull-out test has long been regarded as a standard method for assessing the bond behavior between reinforcing bars and cementitious matrices, including geopolymers (Peng et al., 2022b; Sarker, 2011; Castel and Foster, 2015; Dahou et al., 2016; Bhutta et al., 2017). This method involves embedding a steel rebar into the geopolymer matrix and applying axial tensile force to evaluate the bond strength and slip characteristics along the embedded length, as illustrated in Figure 1.15. Its simplicity, reproducibility, and capacity to deliver quantitative insights into bond strength and stiffness have contributed to

its widespread use.

However, recent studies have underscored the limitations of this method, particularly when evaluating the complex stress transfer mechanisms and post-debonding behavior at the steel–geopolymer interface. El Dandachy et al. (2024b) emphasized that axial pull-out tests may not accurately reflect the true interfacial mechanics under realistic loading conditions. Their findings highlight that such tests are dominated by axial stress fields and fail to capture the influence of radial confinement, transverse cracking, and shear-dominated failure modes, all of which are critical in service conditions involving flexure or combined loading.

Moreover, conventional pull-out configurations often disregard the effects of bar geometry (e.g., ribbed vs. smooth rebars), interface degradation after unloading, and the redistribution of bond stresses along the embedded length. These issues are particularly relevant for geopolymer matrices, which exhibit distinct interfacial microstructures and failure mechanisms compared to OPC systems. Therefore, while the pull-out test remains useful for preliminary bond assessments, more sophisticated experimental protocols (e.g., direct shear or beam-end tests) may be required to comprehensively characterize the bond durability and transfer properties of geopolymer–steel systems under practical scenarios.

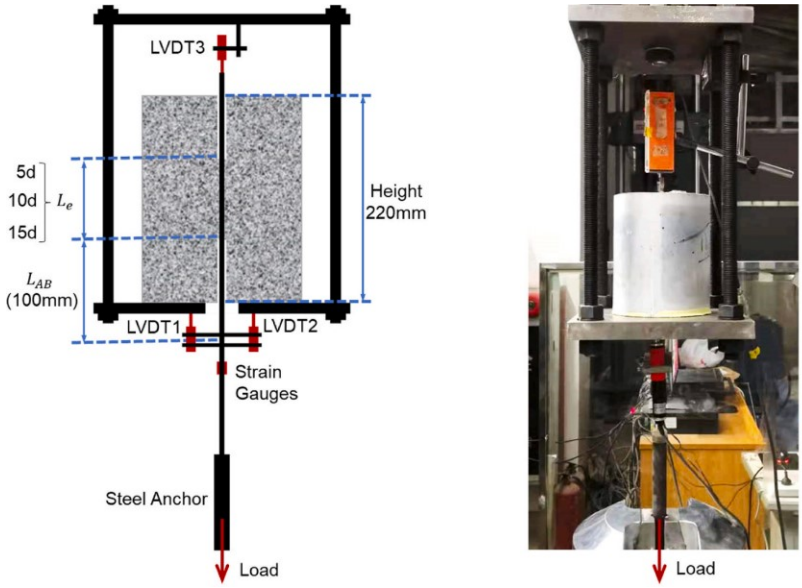

(a) Schematic diagram **(b)** Photograph of the experimental setup

Figure 1.15: Direct pull-out test setup for evaluating bond performance at the geopolymer–steel interface (Peng et al., 2022b)

5.4 Shear evolution

5.4.1 Failure criterion

The shear behavior of geomaterial interfaces—such as those between concrete and geopolymer repair materials—exhibits a combination of adhesion, frictional sliding, interlocking due to surface roughness, and progressive damage. To describe these complex mechanisms, various theoretical models have been proposed, ranging from classical empirical laws to more advanced cohesive–frictional constitutive frameworks (Menes Badika Kiyedi, 2023).

The Mohr–Coulomb criterion is widely adopted due to its conceptual clarity and ease of application, as shown in Figure 1.16. It assumes a linear relationship between shear strength τ and normal stress σ_n:

$$\tau = c + \sigma_n \tan \phi \tag{1.2}$$

where c is the cohesive strength and ϕ is the internal friction angle. This model is useful for soil–structure and rock–concrete interfaces (Ariyadasa et al., 2024; Hachem et al., 2024), but it fails to capture post-peak softening and progressive failure commonly observed in quasi-brittle interfaces like those formed between geopolymer mortars and existing concrete (Zhang et al., 2020; Ueng et al., 2012).

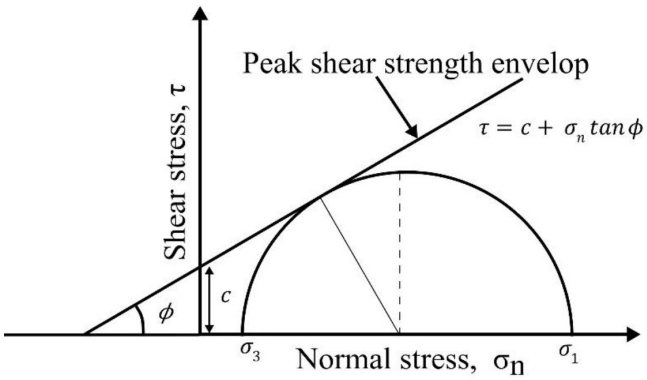

Figure 1.16: Mohr-Coulomb failure criterion for interfaces

To account for interface morphology, the **Patton model** introduces surface roughness effects by modifying the effective friction angle based on asperity inclination. This model better reflects dilatant behavior and stepped failure patterns in rough joints (Menes

Badika Kiyedi, 2023).

Cohesive zone models (CZMs) offer a more robust framework for modeling bond degradation. These models define a traction–separation relationship with softening behavior, often described by linear, bilinear, or exponential laws (Volokh, 2004; Chandra et al., 2002; Li and Chandra, 2003; Roe and Siegmund, 2003). The cohesive strength decreases with increasing relative displacement, governed by a damage variable $D \in [0, 1]$. CZMs are particularly suitable for simulating the failure of geopolymer–concrete interfaces, where debonding is progressive.

Frictional contact laws, such as the classical Coulomb friction model, describe the residual shear behavior after complete bond failure. These models relate shear stress to normal contact pressure via a friction coefficient μ (Nian et al., 2018; Immel et al., 2020). However, they lack the capacity to simulate the pre-peak adhesive behavior.

To address this limitation, **combined cohesive–frictional models** have been introduced, integrating both adhesive and frictional mechanisms in a unified formulation. Notable examples include the works by Alfano and Sacco (2006), Zhong et al. (2014), and Serpieri et al. (2015), which incorporate traction–separation relations coupled with frictional slip laws.

BADIKA (2023) further proposed a strength criterion tailored for bonded interfaces under low confinement, where roughness and adhesion significantly influence shear resistance. The peak shear strength is expressed as:

$$\tau_p = \sigma_n \tan\left[\phi_b + \left(\frac{\theta^*_{\max}}{C+1}\right)^{1.8}\right] + c \tag{1.3}$$

where ϕ_b is the basic friction angle, $\theta^*_{\max}$ is the maximum interface slope, and C is a roughness-dependent constant.

In summary, while the Mohr–Coulomb model provides a foundational tool, cohesive–frictional approaches are more capable of representing the shear behavior of geopolymer–concrete interfaces across the full bond–slip spectrum. These models are essential for accurate simulation of delamination, slip, and interfacial degradation in composite systems.

5.4.2 Geopolymer-concrete interfaces

To investigate the shear bond performance between high ductility geopolymer (HDG) overlays and existing concrete substrates, Li et al. (2024) conducted a series of direct shear tests. Figure 1.17 shows the representative load–slip (P–S) curve of specimen C30–2.0%-M, where the horizontal axis S represents the interface slip in millimeters, and the vertical axis P denotes the applied shear force in kilonewtons. Four critical points (A to D) are selected to characterize the progressive interface failure, with Digital Image Correlation (DIC)-based strain fields illustrating the corresponding deformation states.

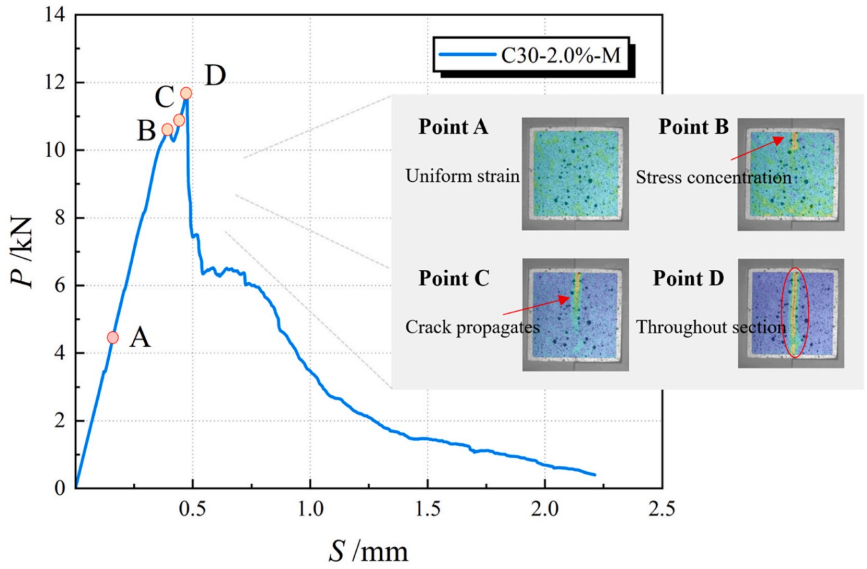

Figure 1.17: Typical shear process of HDG Overlay on Concrete Substrate (Li et al., 2024)

- **Point A:** The strain is uniformly distributed over the interface, indicating that the bonded system remains in the elastic range with effective stress transfer across the geopolymer–concrete interface.
- **Point B:** A localized high-strain zone emerges at the upper edge of the bonding interface, indicating the onset of microcracking. The local strain exceeds the cracking threshold of concrete, marking the initiation of interfacial failure.
- **Point C:** As the load increases, the crack begins to propagate downward. The strain field reveals a distinct damage zone along the interface, signaling progressive debonding and localized fracture development.

- **Point D:** The crack reaches the bottom of the bonded section, resulting in complete interfacial debonding. The strain becomes highly concentrated along the crack path, while surrounding regions remain under compressive stress. This indicates the presence of a macro-interlocking effect, which contributes to residual load-bearing capacity beyond peak load.

This strain evolution highlights the transition from elastic adhesion to full interface separation, governed by the interaction of mechanical interlocking, crack development, and residual frictional resistance.

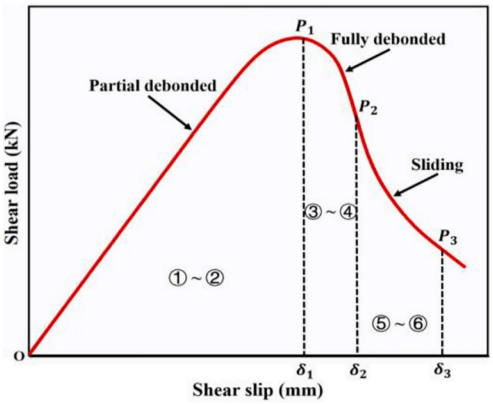

Figure 1.18: Shear stress distribution and debonding process of double-interfaced shear specimen (Gao et al., 2022)

In the context of geopolymer–concrete interfaces, Gao et al. (2022) conducted numerical simulations on the shear behavior of geopolymer mortar–concrete interfaces based on double-interfaced shear test, and identified the damage evolution of the specimens as a three-stage process comprising elastic deformation, plastic development, and interface debonding. The use of surface-based cohesive contact models enabled an accurate representation of the bond characteristics observed in bi-material shear specimens, capturing both the initiation and propagation of damage along the interface.

5.4.3 Geopolymer-steel interfaces

The interaction between geopolymer matrices and steel reinforcement is a fundamental issue in the design of structural and repair systems using alkali-activated materials. While early research mostly focused on the compressive behavior and durability of

geopolymer binders, the bond performance at the steel interface has received increasing attention in recent years.

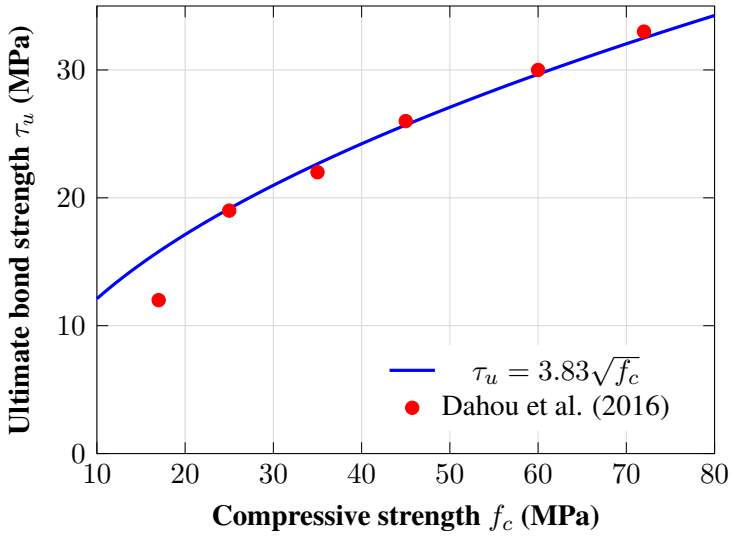

Figure 1.19: Relationship between compressive strength and ultimate bond strength for geopolymer–steel interfaces.

Experimental studies have shown that geopolymer concretes can develop effective mechanical interlock and chemical adhesion with steel bars, provided that appropriate curing and mix design are ensured. Dahou et al. (2016) conducted an extensive experimental program consisting of 260 pull-out tests to evaluate the bond behavior of geopolymer concretes with different compressive strengths and steel bar parameters such as diameter and rib geometry. Their results demonstrated that geopolymer concretes can achieve high bond strengths ranging from 12 MPa to 33 MPa, with a clear dependence on the compressive strength of the matrix. A regression model was proposed in the form $\tau_u = 3.83\sqrt{f_c}$, where τ_u is the ultimate bond strength and f_c is the compressive strength of the geopolymer matrix (in MPa). This relationship is illustrated in Figure 1.19, showing a strong correlation between matrix strength and bond capacity.

In addition, Castel and Foster (2015) evaluated the bond behavior of geopolymer concretes containing slag and low-calcium fly ash under elevated temperature curing. Their study showed that ribbed bars embedded in geopolymer matrices exhibited bond stress–slip curves and failure modes comparable to those of OPC-based systems. They also observed that adequate early-age curing (e.g., 48 hours at 80°C) was essential to achieve reliable bond performance, especially under long-term exposure or aggressive

environments.

Sarker (2011) further confirmed that the bond strength of geopolymer repair mortars with embedded steel bars can meet the requirements of structural rehabilitation. The dominant failure modes were attributed not to adhesive failure at the interface, but to bar pull-out and matrix cracking induced by mechanical interaction at the steel rib zone. These findings highlight that the bonding mechanism is primarily governed by mechanical anchorage rather than interfacial debonding, consistent with observations in both geopolymer and OPC systems.

In summary, existing evidence indicates that geopolymer binders—when properly activated and cured—can provide adequate or even superior bonding with steel reinforcement compared to traditional OPC-based materials.

5.5 Influence of roughness on geomaterials interfaces

Roughness is a critical factor influencing both the bond strength at the interface and permeability in composite materials (Shen et al., 2019; Valikhani et al., 2020; He et al., 2017). Generally, surface roughness impacts the adhesive bond, particularly in terms of cohesive forces at the interface (Li et al., 2024). Additionally, as the roughness index increases, it can alter the location and morphology of the failure plane at the interface (Shen et al., 2019; Hong et al., 2014; Saiang et al., 2005).

5.5.1 Characterization of roughness

The characterization of interface roughness is essential for understanding the mechanical behavior between dissimilar geomaterials, such as concrete, rock, or geopolymer-based matrices. Roughness governs the degree of mechanical interlocking, influences frictional resistance, and contributes significantly to bond strength across interfaces.

Sand patch method was one of the earliest approaches to evaluating roughness, commonly used for concrete surfaces (China and James, 2012; Santos and Júlio, 2013). In this test, a known volume of standard sand is spread on the surface until it forms a circular patch.

Line-based profilometer allowed more detailed measurement of surface profiles, including both contact (stylus-type) and non-contact (optical) systems. These systems provide a 2D trace of vertical displacement $z(x)$ over a sampling length L, from which the following parameters are commonly derived:

$$R_a = \frac{1}{L}\int_0^L |z(x)|\,dx \tag{1.4}$$

$$R_q = \sqrt{\frac{1}{L}\int_0^L z(x)^2\,dx} \tag{1.5}$$

Optical scanning technologies. Advanced precision measurement techniques, such as 3D scanner (Hong et al., 2014), Scanning Electron Microscopy (SEM) (Panda et al., 2018), the ATOS Compact Scan system (Mouzannar et al., 2017), have been employed to assess and describe surface roughness parameters, including peak-to-valley depth, wavelength, and amplitude variations. These systems output spatially continuous surface data, allowing for the calculation of area-based roughness parameters:

$$S_a = \frac{1}{A}\iint_A |z(x,y)|\,dx\,dy \tag{1.6}$$

$$S_q = \sqrt{\frac{1}{A}\iint_A z(x,y)^2\,dx\,dy} \tag{1.7}$$

5.5.2 Influence of roughness on geomaterials interfaces

In bonded interfaces such as geopolymer-to-concrete systems and concrete-to-rock systems, roughness directly affects the interfacial bond strength, the shear resistance, and the failure mechanisms under both monotonic and cyclic loading (Hong et al., 2014; Saiang et al., 2005; Chen et al., 2015; Caliskan et al., 2002; Valikhani et al., 2020; Seidel and Haberfield, 2002; Mouzannar et al., 2017). Li et al. (2024) conducted a experimental study on the interfacial shear behavior between high ductility geopolymer (HDG) and normal concrete (NC), and found that surface roughness was the most significant factor influencing the peak shear strength, with improvements ranging from 185% to 343% as the roughness increased.

Surface roughness at the geo–con interface significantly governs the mobilization of shear resistance by affecting both adhesive and mechanical interlocking mechanisms. As illustrated in Figure 1.20, Bai et al. (Bai et al., 2024) identified two typical shear mechanisms based on interface morphology: the exposed aggregate type and the shear key type. In both cases, shear transfer is governed by two main components—adhesive bonding force (V_{ad}) and interlocking force (V_{co})—which act sequentially during loading. Initially, V_{ad} dominates the response through chemical adhesion, but degrades rapidly under small slip. As loading progresses, V_{co} becomes active via mechanical interlocking and frictional resistance, delaying total debonding.

Compared to smooth interfaces, rough interfaces require larger displacement to reach peak shear strength due to enhanced engagement of surface asperities. Moreover, after the breakdown of cohesive bonds, residual shear strength remains higher in rough surfaces owing to friction and dilatancy effects. These mechanisms are illustrated schematically in Figure 1.20, providing a conceptual framework for understanding the progressive mobilization of interfacial shear resistance in geopolymer–concrete systems.

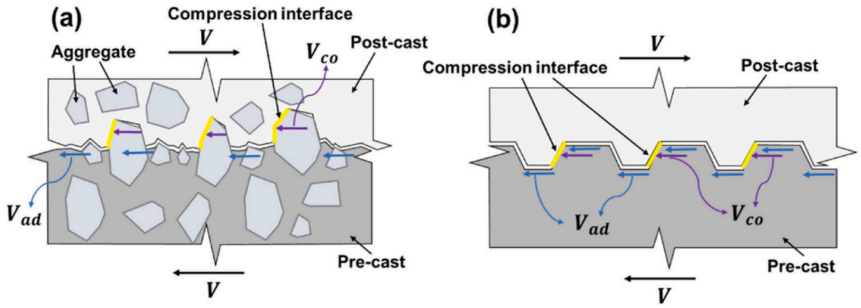

Figure 1.20: Shear mechanism of interface: (a) Exposed aggregate type; (b) Shear key type (Bai et al., 2024)

Recent findings by El Dandachy et al. (2024a) using a novel 3D direct shear apparatus further validated the critical influence of interface roughness on the shear bond performance of concrete–concrete joints. By systematically varying surface profiles (Smooth, VLowSR, LowSR, InterSR, HighSR), the study revealed that peak shear strength ($\tau_{\max}$) increased significantly—from 1.5 MPa for untreated smooth surfaces to 4.9 MPa for substrates roughened via high-pressure water jet. Notably, specimens with high surface roughness exhibited shear behavior and fracture energy comparable to monolithic concrete specimens, indicating effective mechanical interlocking. The fracture energy in-

creased proportionally with roughness, from 0.6 to 2.7 N/mm, while residual shear stress remained largely constant (1 MPa), determined primarily by applied normal stress rather than surface preparation. This work also highlighted that dilative normal displacement is a strong indicator of interlocking, reaching values up to 1.69 mm for monolithic and highly roughened specimens. These results emphasize the importance of surface engineering in achieving durable and high-performance repair joints under combined shear and normal loading.

The influence of roughness is also evident in the observed shear failure modes. Smooth interfaces tend to fail in a brittle, adhesive mode with localized slip, while roughened interfaces exhibit a more progressive debonding process characterized by dilatancy, microcrack development, and frictional sliding. These mechanisms are strongly influenced by the geometric interlocking and surface morphology parameters (e.g., S_a, S_q), which correlate with residual shear strength and energy dissipation during interface separation (Li et al., 2025; Ekaputri et al., 2022).

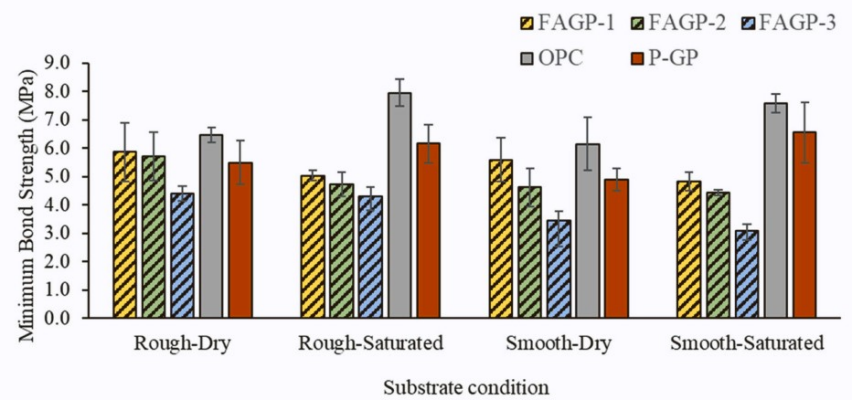

Figure 1.21: Minimum bond strength of various binder systems under different substrate conditions. (Adapted from Ariyadasa et al. (2024))

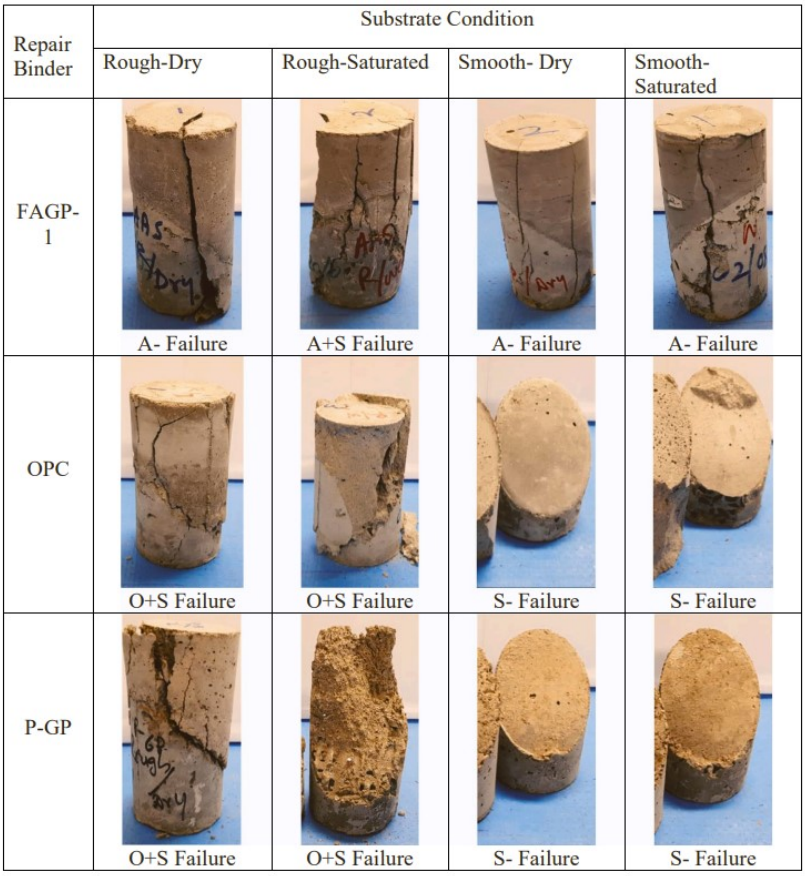

Figure 1.22: Failure patterns of slant shear test composites (Ariyadasa et al., 2024)

In a recent study by Ariyadasa et al. (2024), the bond behavior of fly ash-based geopolymer mortars was evaluated using slant shear tests under various substrate conditions, simulating concrete sewer environments. The experimental program involved multiple repair binders (FAGP-1, FAGP-2, FAGP-3, OPC, and P-GP) applied to concrete substrates with different surface textures (rough vs. smooth) and moisture states (dry vs. saturated). As shown in Figure 1.21, the geopolymer systems exhibited varied bond strengths depending on the interface condition, with rough and saturated surfaces generally providing higher shear resistance. The failure mechanisms were further characterized, revealing that geopolymer-based repairs often exhibited axial splitting and mixed-mode failure, while OPC and P-GP interfaces were more likely to fail in shear, particularly on smooth substrates. These observations are illustrated inFigure 1.22.

Additionally, in hydro-mechanical contexts, rough interfaces influence pore water distribution and flow paths along the interface, leading to local variations in effective stress

and shear strength. This is particularly important in saturated conditions or in interfaces subject to hydraulic gradients, where interface permeability is roughness-dependent (Muthu and Sadowski, 2023; Xu et al., 2022).

5.6 Numerical modeling of shear evolution

5.6.1 Numerical modeling of bonded interfaces

The numerical modeling of shear behavior at bonded interfaces has evolved considerably in recent decades, with applications spanning rock mechanics, concrete repair systems, and geotechnical composites. Earlier studies have largely focused on unbonded or weakly bonded interfaces, such as rock–rock or concrete–rock contacts, where frictional behavior and asperity degradation govern the interface response (Karami and Stead, 2008; Park and Song, 2009). These works often employed Discrete Element Models (DEM), such as the Bonded Particle Model (BPM) or Smooth Joint Contact Model (SJCM), to capture progressive failure and contact dilation.

More recent developments have extended to bonded interfaces, where cohesive behavior and surface interlocking dominate the shear resistance. Tian et al. (2018) introduced a cohesive–frictional interface model to simulate the shear evolution of concrete–rock interfaces using cohesive elements implemented in FEM. Their model defined three typical stages: pre-peak elastic response driven by bond stiffness, a softening phase involving bond degradation and frictional mobilization, and a residual phase governed by interfacial friction. This concept was further applied and extended to simulate foamed concrete interfaces and bonded rock–mortar systems Zhao et al. (2018); Dong et al. (2020); Murali et al. (2022).

Among the numerical methods employed, Finite Element Analysis (FEA) has been widely adopted to model the mechanical behavior at interfaces due to its robustness and flexibility in dealing with heterogeneous materials (Badika et al., 2022, 2024; Çelik et al., 2022; Ekaputri et al., 2022). More advanced approaches such as the Discrete Element Method (DEM) are also gaining attention for capturing discontinuities and particle-scale interactions (Gutiérrez-Ch et al., 2018; Wang et al., 2022; Gao and Zhai, 2022).

5.6.2 FEM Methods on geo–con interfaces

Despite the increasing use of geopolymer binders in structural repair systems, finite element modeling (FEM) studies that explicitly address the shear behavior of geopolymer–concrete (geo–con) interfaces remain extremely limited. This knowledge gap is mainly due to the complex and heterogeneous nature of alkali-activated materials, as well as the lack of experimentally validated interface models for such systems.

Nevertheless, transferable insights can be drawn from FEM studies on bonded interfaces in more conventional systems. In particular, numerical investigations of concrete–concrete (Al-Fasih et al., 2021; Ding et al., 2022; Dudziak et al., 2021) and concrete–rock interfaces (Renaud et al., 2021; Min et al., 2020) have demonstrated the importance of incorporating surface roughness, interfacial friction, and progressive damage mechanisms when modeling shear transfer behavior. These studies typically adopt cohesive zone models (CZMs) or traction–separation laws to reproduce interface softening, dilatancy, and post-peak degradation.

A representative example is provided by Badika et al. (2024), who performed an integrated experimental and numerical analysis of the shear response at concrete–granite interfaces under varying roughness and normal stress conditions. Although geopolymer-based interfaces may involve different chemical bonding behavior, the cohesive–frictional modeling approach used in their work provides a relevant framework that can be adapted to simulate geo–con interface behavior.

Their work highlights the critical role of both micro- and macro-roughness in influencing interface shear resistance. It was observed that surface roughness alters the bonding mechanism and failure mode along the interface. Under lower normal stress (0.5 MPa), failure was governed primarily by interfacial sliding with minimal damage to the base materials. In contrast, higher normal stresses (1.0–1.5 MPa) induced additional shearing in the concrete near the interface, demonstrating the transition between interface-controlled and matrix-involved failure modes.

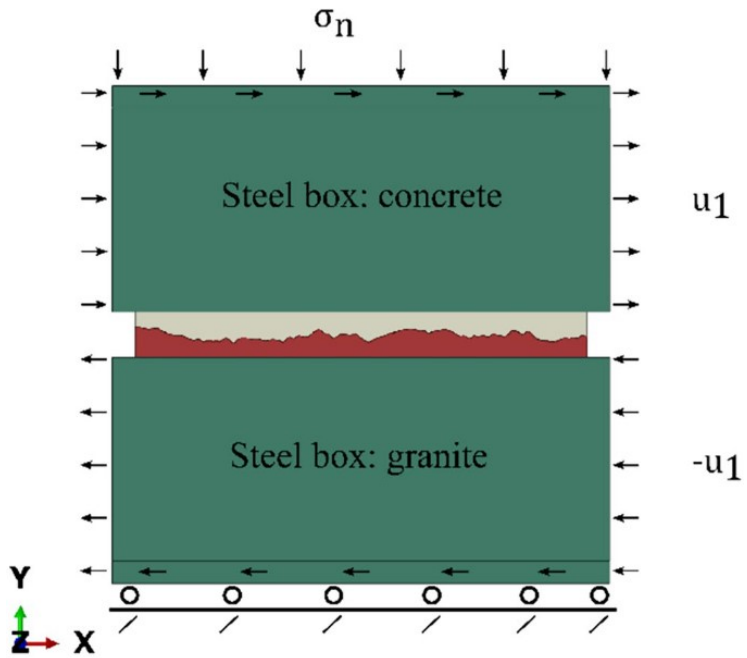

Figure 1.23: The boundary conditions and interface geometry. (Adapted from Badika et al. (2024))

To simulate this progressive behavior, Badika et al. (2024) employed a cohesive–frictional interface model within the FEM framework, initially proposed by Tian et al. (2018). The boundary conditions and interface geometry used in their FEM simulations are illustrated in Figure 1.23, where a steel-constrained concrete–granite specimen is subjected to direct shear under constant normal stress. The model incorporates a three-phase shear stress evolution: an initial elastic response governed by interface bonding, a softening phase due to bond damage, and a frictional residual phase dominated by mechanical interlocking. As shown in Table 1.3, the parameters were calibrated for two distinct failure regimes depending on the applied normal stress.

Table 1.3
Calibrated parameters for cohesive–frictional interface model (Badika et al., 2024)

Model component	Parameter (unit)	0.5 MPa	1.0–1.5 MPa
Cohesive part	Normal stiffness (GPa/m)	15	15
	Shear stiffness (GPa/m)	7.5	4.5
	Normal strength (MPa)	1.0	1.4
	Shear strength (MPa)	1.2	1.6
	Shear displacement (mm)	0.9	2.25
	Rate of damage evolution (–)	4	4
Frictional part	Friction coefficient (–)	0.70	0.65

These findings support the use of cohesive–frictional models for simulating geopolymer–concrete interfaces, particularly where performance depends on surface roughness, bond variability, and brittle matrix behavior.

5.7 Summary

Although direct FEM studies on geopolymer–concrete (geo–con) interfaces are scarce, valuable insights can be drawn from modeling approaches developed for concrete–rock and concrete–concrete systems. Cohesive–frictional interface models have proven effective in capturing progressive shear behavior, including bond degradation and residual friction. As shown by Badika et al. (2024), interface parameters must be calibrated based on surface conditions and loading regimes. This is especially important for geopolymer systems, which often exhibit brittle matrix behavior and high sensitivity to surface preparation and moisture conditions.

Thus, existing modeling strategies for conventional interfaces provide a solid foundation for simulating the hydro-mechanical performance of geo–con systems, as long as key material-specific factors like alkali activation and pore structure are properly accounted for.

6 Conclusion

This chapter has provided a comprehensive review of the current state of knowledge concerning geopolymer mortars and their potential application in the repair of reinforced concrete structures. Starting from the environmental motivations for shifting away from Ordinary Portland Cement (OPC), the chapter outlined the technological advances in alkali-activated materials—particularly potassium-based metakaolin geopolymer systems—and assessed their mechanical, shrinkage, and durability properties.

Special emphasis was placed on the role of shrinkage evolution and interfacial performance, as these aspects critically affect the long-term compatibility and effectiveness of geopolymer-based repairs. Literature on geopolymer–concrete and geopolymer–steel interfaces was reviewed, focusing on the influence of surface roughness, chemical interaction, mechanical interlocking, and hydro-mechanical coupling. Various experimental observations and interface models were introduced to illustrate the complex failure mechanisms that occur at these bonded surfaces under loading.

As a bibliographic foundation for the dissertation, this chapter serves three essential roles:

- It defines the technological and environmental motivations for using geopolymers in structural repair;
- It identifies key knowledge gaps in the understanding of interface behavior, shrinkage effects, and long-term mechanical performance;
- It establishes a conceptual framework and rationale for the experimental and numerical investigations presented in the subsequent chapters.

In response to the gaps identified, the remainder of this thesis is organized around three major themes:

1. **Chapter 2** develops and characterizes potassium-based geopolymer mortars, with a focus on shrinkage evolution and early-age behavior using Digital Image Correlation (DIC).

2. **Chapters 3 to 5** investigate the hydro-mechanical behavior of geopolymer–concrete and geopolymer–steel interfaces through confined shear–permeability testing and finite element simulations.

3. **Chapter 6** validates the material and interface-level findings at the structural scale through full-scale bending tests on geopolymer-repaired beams.

Overall, this chapter provides the scientific context and justification for the integrated experimental–numerical methodology adopted in this research, and supports the central hypothesis that geopolymer-based repairs can offer reliable, durable, and environmentally sustainable solutions for reinforced concrete rehabilitation.

CHAPTER 2

Physical-mechanical properties of geopolymer mortar as repair materials

1 Introduction

As reviewed in Chapter 1, geopolymer mortars have emerged as promising eco-efficient alternatives to Ordinary Portland Cement (OPC) in structural repair applications, offering superior chemical durability and reduced carbon footprint. However, their practical performance depends strongly on key properties such as setting behavior, workability, shrinkage, and mechanical strength, particularly when applied to concrete substrates under variable environmental conditions.

While Chapter 1 provided a broad overview of these requirements, the present chapter focuses on a detailed experimental evaluation of a potassium-activated metakaolin geopolymer mortar specifically developed for structural repair. The selected formulation aims to combine high mechanical performance with controlled shrinkage and good compatibility with existing concrete. This material-level investigation serves as a crucial foundation for subsequent studies on interface behavior and structural performance, as explored in later chapters.

Among the various parameters influencing long-term durability, shrinkage plays a pivotal role due to its potential to cause early-age cracking, debonding at interfaces, and compromised adhesion to the substrate. Despite its importance, shrinkage behavior of geopolymer mortars remains poorly understood, especially under realistic curing and ambient conditions. Existing studies often isolate drying or autogenous shrinkage, lacking a

unified assessment of the total deformation process over different time scales.

To address this gap, this chapter presents a comprehensive experimental program including both standardized tests and advanced Digital Image Correlation (DIC) techniques. DIC allows for continuous, full-field strain monitoring at early ages, providing insight into time-dependent deformation and cracking risk. By quantifying the shrinkage evolution and its variability with environmental conditions, this study provides critical input for interface modeling and durability prediction in geopolymer-based repair systems.

Overall, this chapter establishes the essential material characteristics of the selected geopolymer mortar and lays the groundwork for understanding its interaction with concrete substrates, which will be further examined in interface shear and permeability tests and full-scale repair applications in next chapters.

2 Materials and mix design

2.1 Geopolymer mortar and substrate

In this research, geopolymer mortar was prepared using alkali-activated technology. The process flow diagram for its production is presented in Figure 2.1. The geopolymer was produced by blending, curing, and maintaining the precursor materials, standard sand, and a pre-prepared alkali-activating solution. The precursor employed was metakaolin powder, commercially known as Argicem®, a form of metakaolin developed by Argeco Développement. This was produced through the flash calcination of kaolin clay. The results of the chemical composition tests are presented in Table 2.1.

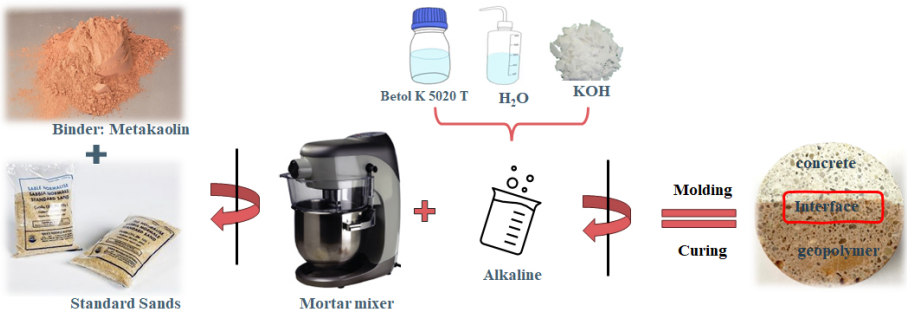

Figure 2.1: Schematic presentation of regularized crack topology

Table 2.1
Chemical Composition of Metakaolin Powder (by weight)

Metakaolin	SiO_2	Al_2O_3	Fe_2O_3	TiO_2	K_2O	CaO	MgO	SO_3	ZrO_2	Fire loss
Argicem (%)	60.53	29.64	4.68	1.72	0.65	1.41	0.95	0	0.15	0.27

* Data obtained from internal laboratory analysis by S. Koubeissy (Centrale Lille, 2022).

The alkaline-activated solution was prepared using Betol K 5020 T® (a commercial potassium silicate solution), flake potassium hydroxide (KOH), and laboratory-grade water. The preparation process involved continuous stirring for 30 minutes, during which a substantial exothermic reaction occurred, releasing a significant amount of heat. To ensure the homogeneity and stability of the solution, it was subsequently sealed and left to settle for over 24 hours before use. The chemical composition of Betol K 5020 T®, as provided by the manufacturer, is presented in Table 2.2.

Table 2.2
Chemical composition of Betol K 5020 T® (by mass)

Product	SiO_2	Na_2O	K_2O	Molar Ratio
Betol K 5020 T (%)	30	0	18.5	2.54

* Data provided by Woellner GmbH (Germany), commercial product datasheet.

2.2 Mix proportion and furmula design

This mix design was optimized for workability, durability, and shrinkage evaluation under both sealed and drying conditions.[1]

The geopolymer mortar was prepared following a controlled laboratory procedure to ensure consistency and minimize material loss during mixing. Initially, the dry components were pre-mixed at a low rotational speed for 30 seconds to prevent airborne dispersion of metakaolin particles. The alkali-activated solution was then gradually added, followed by 60 seconds of continued low-speed mixing to allow wetting and initial dissolution. Subsequently, a high-speed mixing phase lasting 30 seconds was applied to

[1] Data adapted from unpublished internal experiments conducted by S. Koubeissy (Centrale Lille, 2023).

promote homogeneous dispersion and reaction initiation. After a 90-second rest period to reduce air entrapment, the paste was subjected to a final 60-second high-speed mixing phase to ensure uniformity.

While the specific rotation speed values were not displayed on the equipment panel, the mixing regime was operated according to predefined low- and high-speed sequences commonly adopted in mortar preparation protocols. After casting, all specimens were cured under sealed conditions in a humidity-controlled chamber maintained at $20\,^{\circ}\mathrm{C}$ and 90% relative humidity (RH).

The mix design adopted in this research is based on the preliminary, unpublished experimental work of Sara Koubeissy from our laboratory team in the framework of Europe PREDIS. The alkali-activated solution consisted of 39 wt% BETOL K5020T, 7 wt% potassium hydroxide (KOH), and 6 wt% deionized water. The solid precursor was metakaolin, accounting for 48 wt% of the total paste mass. The molar ratios were adjusted as follows: SiO_2/K_2O = 3.40, H_2O/K_2O = 11.0, and K_2O/Al_2O_3 = 1.0. To prepare the mortar, standard sand was added at a mass ratio of 65.31% relative to the paste mass.The mix design adopted in this research is based on the preliminary, unpublished experimental work of Sara Koubeissy from our laboratory team in the framework of the European project PREDIS. The alkali-activated paste was formulated using an activator solution composed of 39 wt% BETOL K5020T, 7 wt% potassium hydroxide (KOH), and 6 wt% deionized water, while metakaolin accounted for 48 wt% of the total paste mass as the solid precursor. The molar ratios were adjusted to obtain a stable and reactive geopolymer network, with SiO_2/K_2O = 3.40, H_2O/K_2O = 11.0, and K_2O/Al_2O_3 = 1.0.

To produce the mortar, standard sand was incorporated at 65.31% of the paste mass. For practical application and large-scale preparation, the mix proportions were also defined for 1 m^3 of mortar, resulting in the following quantities: approximately 1503 kg of sand, 311 kg of BETOL 5020T activator, 382 kg of metakaolin, 56 kg of KOH pellets, and 50 kg of deionized water. These proportions ensure adequate workability, homogeneous dispersion of the activator within the metakaolin matrix, and a consistent geopolymerization process suitable for both laboratory-scale and structural-scale casting.

All experimental investigations were conducted at the mortar level, which is more representative of practical applications in repair engineering. This mix design was optimized for workability, durability, and shrinkage evaluation under both sealed and drying conditions.

3 Fresh-state properties of geopolymer mortar

Considering that setting time and flowability are key indicators for evaluating the workability and application potential of geopolymer mortar in repair scenarios (Dan et al., 2023; Huseien et al., 2017; Wu and An, 2014), this study experimentally investigates these properties to establish a fundamental understanding of the fresh behavior of the formulated potassium-based geopolymer system.

3.1 Setting time assessment

The setting time of the geopolymer mortar was assessed using an automatic Vicat apparatus (Vicatronic, E2ME), shown in Figure 2.2. The procedure followed the specifications outlined in EN 196-3 (2016). This standard defines the initial setting time as the time elapsed from the zero point until the needle penetration reaches 6 ± 3 mm, and the final setting time as the point when the needle penetrates only 0.5 mm into the specimen.

To ensure precision and consistency, the Vicat apparatus was programmed to perform automatic penetration tests at 10-minute intervals. Throughout the test, the depth of needle penetration was continuously recorded and plotted as a function of time. This enabled the clear identification of setting thresholds based on standardized criteria.



Figure 2.2: Automatic Vicat apparatus used for setting time determination

According to the experimental data, the initial setting time of the potassium-based

geopolymer mortar was determined to be approximately **380 minutes**, while the final setting time was recorded at **570 minutes**. These results reflect the extended reaction kinetics and delayed stiffening behavior characteristic of metakaolin-activated systems. Such prolonged setting duration is particularly relevant when designing casting schedules, early-age shrinkage monitoring, and field placement strategies for repair applications.

3.2 Flowability evaluation

The flowability of the geopolymer mortar was evaluated using the flow table method as specified in EN 1015-3 (2007). A standardized truncated cone mold (Ø100 mm bottom, Ø70 mm top, 60 mm height) was placed at the center of a flow table. Fresh mortar was filled into the mold in two equal layers, each tamped 10 times. After carefully lifting the mold vertically, the table was dropped 15 times within 15 seconds. The resulting spread diameter was measured in two perpendicular directions and averaged. The mean spread diameter after 15 drops was **123.5 mm**.

To further explore the influence of additional agitation, a second test was conducted in reference to ASTM International (2020), in which the same specimen was subjected to 25 drops instead of 15. The resulting average flow diameter increased significantly to **175.0 mm**, indicating enhanced flow potential under extended mechanical vibration.



(a) Flow table setup **(b)** After 15 drops **(c)** After 25 drops

Figure 2.3: Flowability evaluation of geopolymer mortar under different drop counts

The results indicate that the potassium-based geopolymer mortar exhibited satisfactory flowability under standard agitation, achieving an average spread diameter of over 120 mm after 15 drops. When subjected to extended mechanical vibration (25 drops), the flow diameter increased significantly to approximately 175 mm, demonstrating the material's excellent dispersion and lubricity. This high deformability suggests that the

formulated geopolymer system is well-suited for repair applications, particularly where substrate conformity, gap filling, and surface encapsulation are essential for performance and durability.

4 Hardened-state properties of geopolymer mortar

In the context of repair materials, previous studies have consistently highlighted the critical importance of mechanical properties, durability indicators, and volumetric stability in evaluating structural compatibility and long-term performance (Al-Zahrani et al., 2003; Mangat and Limbachiya, 1997; Huang et al., 2014; Shi et al., 2020; Pawelec et al., 2019). Sufficient mechanical strength is essential to ensure that the repair material can withstand service loads and integrate structurally with the substrate. Meanwhile, low permeability and refined pore structure are widely recognized as key contributors to durability by mitigating ingress of aggressive agents. Additionally, shrinkage behavior significantly influences dimensional compatibility at the interface between the repair material and the host structure, particularly in early-age stages where differential deformation may lead to interfacial cracking or delamination. Therefore, this chapter provides a comprehensive assessment of hardened geopolymer mortar, with emphasis placed on its mechanical strength, permeability and porosity, and shrinkage behavior.

4.1 Mechanical performance evaluation

4.1.1 Flexural and compressive strength

To investigate the mechanical behavior of geopolymer mortar as a potential substitute for conventional cementitious repair materials, standardized testing methods commonly used for ordinary concrete mortar were adopted. In particular, flexural and compressive strengths were evaluated based on procedures outlined in EN 12390-5 (2019) and EN 12390-3 (2019), respectively.

Prismatic geopolymer mortar specimens with dimensions of $40\,\mathrm{mm}\times40\,\mathrm{mm}\times160\,\mathrm{mm}$ were prepared and subjected to curing at $20\,^{\circ}\mathrm{C}$ and 90% relative humidity for 14 days. The selection of a 14-day curing age is widely employed in the characterization of alkali-activated materials, as it enables reliable early-age mechanical performance assessment

while ensuring a stable reaction environment (Ding et al., 2016; Gebregziabiher et al., 2015).

Flexural strength evaluation

Flexural strength was measured using a three-point bending configuration with center-point loading, as schematically shown in Figure 2.4(a), and physically implemented on a universal testing machine in Figure 2.4(b). The loading rate was fixed at $3000\,\mathrm{N/min}$. The flexural strength $f_{\mathrm{ct,fl}}$ was calculated according to the following formula from EN 12390-5 (2019):

$$f_{\mathrm{ct,fl}} = \frac{3Fl}{2d_1 d_2^2} \tag{2.1}$$

where:

- $f_{\mathrm{ct,fl}}$ is the flexural strength in MPa,
- F is the maximum load in N,
- l is the span between the supporting rollers in mm,
- d_1 and d_2 are the lateral dimensions of the cross-section in mm.

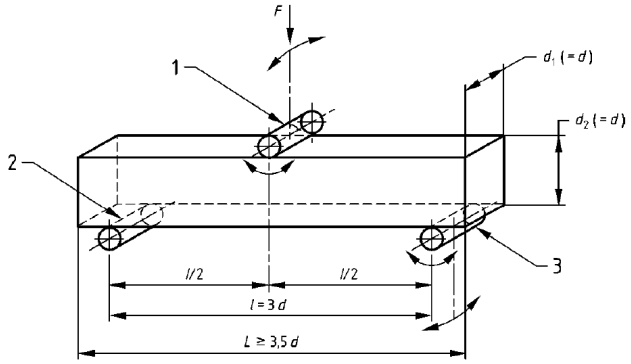

Key

1 Loading roller (capable of rotation and of being inclined)
2 Supporting roller
3 Supporting roller (capable of rotation and of being inclined)

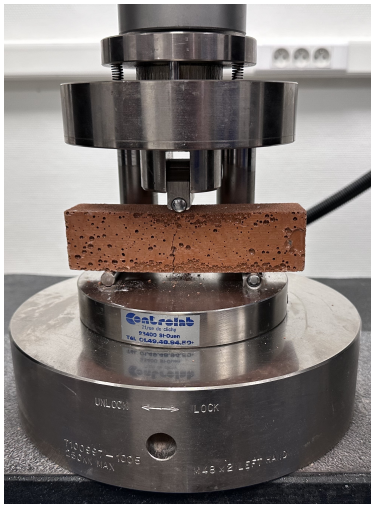

(a) Arrangement of loading of test specimen (EN 12390-3, 2019) **(b)** Flexural tests

Figure 2.4: Flexural strength evaluation setup

Three prismatic specimens with dimensions of $160\,\mathrm{mm} \times 40\,\mathrm{mm} \times 40\,\mathrm{mm}$ were prepared to evaluate the flexural strength of the geopolymer mortar. The test results yielded flexural strength values of $7.83\,\mathrm{MPa}$, $8.57\,\mathrm{MPa}$, and $7.17\,\mathrm{MPa}$, respectively. The corresponding average flexural strength was calculated to be approximately $7.86\,\mathrm{MPa}$.

According to the comparative results reported by Nath and Sarker (2017), two OPC-based mortars with different mix designs—referred to as OPC1 and OPC2—achieved 28-day flexural strengths of $3.68\,\mathrm{MPa}$ and $5.26\,\mathrm{MPa}$, respectively. In comparison, the geopolymer mortar developed in this study reached an average flexural strength of $7.86\,\mathrm{MPa}$ after only 14 days of ambient curing, outperforming OPC1 and approaching or even surpassing OPC2.

This superior early-age flexural strength highlights the potential of geopolymer mortars to match or exceed the mechanical performance of conventional OPC systems, even under less aggressive curing conditions. The enhancement may be attributed to the high pozzolanic reactivity of metakaolin and the optimized alkali-activation formulation employed in this research.

Compressive strength evaluation

Following the flexural strength tests, the fractured halves of each prism specimen were subjected to compressive testing in accordance with the EN 12390-3 (2019). Each half prism was positioned with its largest cross-sectional face perpendicular to the loading direction, as illustrated in Figure 2.5, to ensure a uniform stress distribution and comparability across samples.

The compressive load was applied using an Instron testing machine at a constant rate of $144\,\mathrm{kN/min}$, in line with the standard's recommendation. The compressive strength, f_c, was calculated as:

$$f_c = \frac{F}{A} \tag{2.2}$$

where:

- f_c is the compressive strength in MPa,
- F is the peak load at failure in N,
- A is the bearing area of the specimen in mm^2.

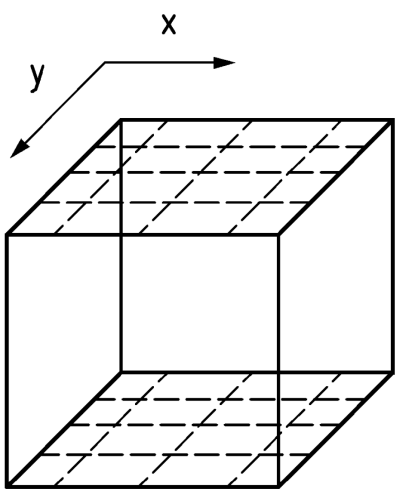

(a) Loading face schematic (EN 12390-3, 2019)



(b) Compressive test

Figure 2.5: Compressive strength evaluation setup

The visual representation of the loading configuration and test setup is provided in Figure 2.5, where the specimen is compressed along the vertical axis after being sectioned from the original prism.

A total of six compressive strength measurements were obtained for the geopolymer mortar: 49.57 , 51.30 , 50.70 , 49.87 , 49.67 , and $47.80\,\mathrm{MPa}$, resulting in an average value of $49.82\,\mathrm{MPa}$.

To contextualize this performance, Nath and Sarker (2017) reported 28-day compressive strengths of $41.6\,\mathrm{MPa}$ and $53.6\,\mathrm{MPa}$ for two OPC mortars with different mix proportions, denoted as OPC1 and OPC2. The geopolymer mortar investigated in the present study thus exhibits a comparable level of compressive strength—exceeding OPC1 and approaching OPC2—despite being cured under ambient conditions.

These results highlight the mechanical competitiveness of geopolymer systems relative to conventional OPC-based materials.

4.1.2 Uniaxial compressive behavior of geopolymer mortar and concrete substrate

To investigate the fundamental mechanical performance of the geopolymer mortar and its compatibility with conventional concrete, uniaxial compression tests were performed on both geopolymer mortar and OPC specimens. This test provides essential input for understanding material stiffness, deformation characteristics, and volumetric

response, which are crucial for evaluating hydro-mechanical coupling behavior at the geopolymer–concrete interface.

Specimen preparation and test setup

Figure 2.6 shows the schematic configuration of the test setup and strain gauge layout. All specimens were cylindrical, with a diameter of $37\,\mathrm{mm}$ and a height of $74\,\mathrm{mm}$, following a standard aspect ratio of 1:2. This geometry was selected to ensure a uniform stress field in the central zone of the specimen while minimizing end friction effects and lateral confinement from the platens. The geopolymer mortar samples were cast and cured under controlled conditions at $20\,^{\circ}\mathrm{C}$ and $90\,\%$ relative humidity for 14 days to simulate ambient curing and reflect practical repair scenarios. For comparison, OPC specimens with identical dimensions were extracted from cured concrete blocks by core drilling.

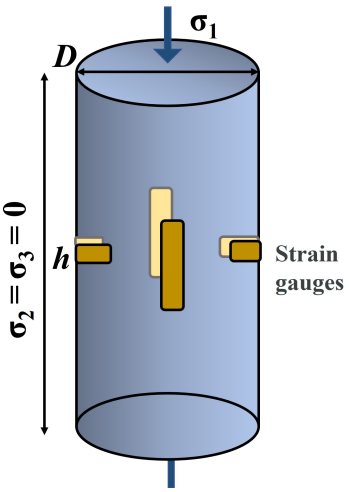

Figure 2.6: Schematic of uniaxial compression test setup

To monitor the deformation accurately, four strain gauges were attached to each specimen—two aligned vertically to measure axial strain and two placed horizontally at mid-height to capture transverse deformation. The instrumentation enabled simultaneous acquisition of both axial and lateral strains, which were used to determine the elastic modulus and Poisson's ratio. In this study, uniaxial compression tests were performed using an Instron testing machine.

Stress–strain response and deformation stages

To better capture the elastic properties and transverse deformation behavior, a partial unloading cycle was incorporated after reaching the peak axial stress ($\sigma_{\max}$). This unloading phase is crucial for minimizing the influence of plastic deformation and internal damage on the measurement of material constants. The nearly linear unloading path along the axial direction provides a reliable basis for calculating both the elastic modulus and Poisson's ratio.

Figure 2.7 presents the typical uniaxial compressive stress–strain response of a geopolymer mortar specimen, where both axial strain (ε_a) and transverse strain (ε_t) were recorded. This representative curve serves to illustrate the deformation characteristics and key mechanical parameters extracted from the test.

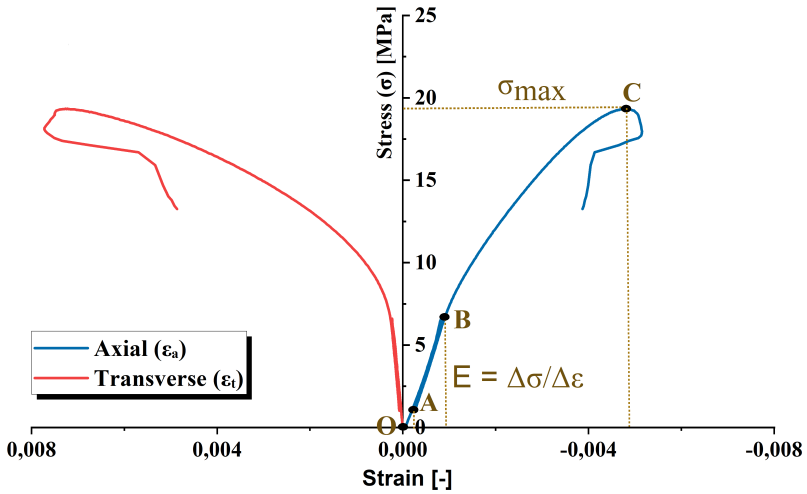

Figure 2.7: Representative stress–strain response of a geopolymer mortar specimen under uniaxial compression.

Note: Axial and transverse strains are illustrated, with key stages labeled: O–A (Initial seating phase), A–B (Elastic stage), B–C (Nonlinear hardening), C–End (Post-peak softening)

- **O–A: Initial seating phase** — This initial segment corresponds to specimen–platen adjustment, including seating imperfections and friction effects. The axial stress increases slightly with negligible strain accuracy; this region is excluded from modulus evaluation due to its nonlinearity and setup influence.

- **A–B: Elastic stage** — This stage exhibits a clear linear relationship between axial stress σ and axial strain ε_a. The elastic modulus E is determined from this segment

using:

$$E = \frac{\sigma_B - \sigma_A}{\varepsilon_B - \varepsilon_A}$$

where σ_A and σ_B are measured in MPa, and ε_A, ε_B are dimensionless axial strains.

The Poisson's ratio ν was determined based on the unloading segment following peak stress, where the stress–strain relationship is approximately linear. The ratio was computed using the incremental transverse-to-axial strain relationship, as follows:

$$\nu = -\frac{\Delta\varepsilon_{\mathrm{t}}}{\Delta\varepsilon_{\mathrm{a}}}$$

where $\Delta\varepsilon_{\mathrm{t}}$ and $\Delta\varepsilon_{\mathrm{a}}$ are the transverse and axial strain increments during elastic unloading. Both are dimensionless quantities.

- **B–C: Nonlinear hardening** — Beyond the elastic region, the material continues to carry load, but the stress–strain curve deviates from linearity. This region is attributed to the initiation and stable propagation of microcracks within the geopolymer matrix, leading to gradual stiffness reduction.

- **C–End: Post-peak softening** — Point C corresponds to the peak compressive strength $\sigma_{\max}$ of the material. Following this, stress decreases with further axial deformation, indicating unstable crack coalescence and material failure. This softening behavior is critical for characterizing the ductility and energy absorption capacity of the material.

This staged interpretation provides a comprehensive understanding of the deformation characteristics of geopolymer mortar under compressive loads. The calculated mechanical parameters—elastic modulus E, peak stress $\sigma_{\max}$, and Poisson's ratio ν—form the basis for evaluating material performance and are summarized in the next section.

Failure observations and characteristic behavior

Failure observations further support this distinction in material response. As shown in Figure 2.8, the geopolymer mortar specimens exhibited distributed cracking, edge spalling, and gradual degradation. In contrast, the OPC concrete specimens failed explosively, with wide through-thickness cracks and brittle fragmentation.

It is acknowledged that this comparison involves two different material classes—mortar and concrete—which naturally exhibit distinct failure characteristics due to differences in composition, heterogeneity, and aggregate structure. Nevertheless, this contrast is still relevant in the context of repair applications, where geopolymer mortar is typically applied onto OPC concrete substrates. Understanding their respective failure modes helps to anticipate potential incompatibilities at the repair interface and highlights the importance of selecting materials with compatible deformation behaviors.

The relatively gradual failure process in geopolymer mortar offers a beneficial deformation buffer, which may help reduce stress concentrations and delay interfacial delamination when bonded to stiffer concrete substrates.

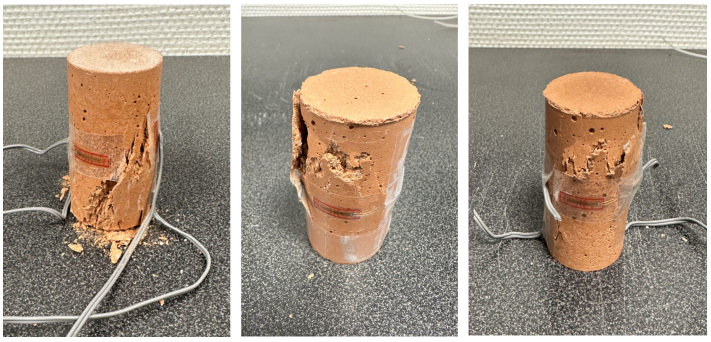

(a) Failed geopolymer mortar specimens

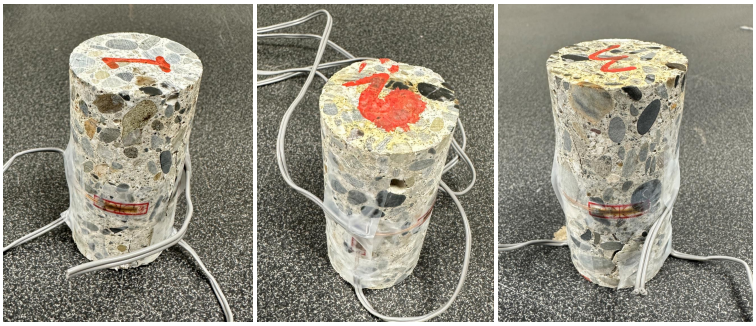

(b) Failed OPC specimens

Figure 2.8: Failed specimens after uniaxial compression tests

Mechanical parameters of geopolymer mortar and OPC

The uniaxial compressive stress–strain responses of geopolymer mortar specimens GM1, GM2, and GM3 are presented in Figure 2.9. These curves consistently exhibit four characteristic stages: initial linear elasticity, nonlinear hardening, a peak stress point, and

a post-peak softening response. The axial strain (ε_a) at peak stress exceeded -0.004 in all specimens, while transverse strain (ε_t) progressively increased throughout loading, particularly after the elastic limit. This indicates a quasi-ductile behavior marked by lateral dilation and internal damage accumulation. Such deformation capacity is essential for repair materials, which must accommodate inelastic strains and maintain integrity at the interface with the existing substrate.

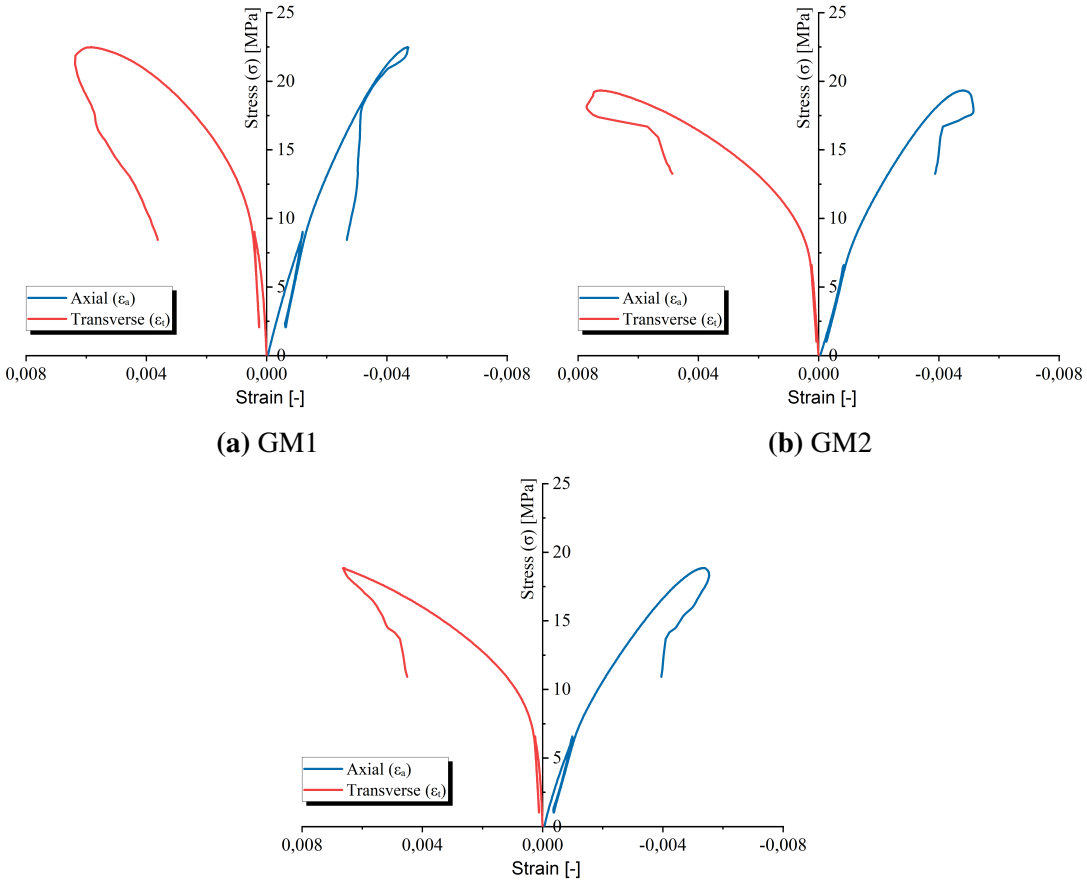

(a) GM1 **(b)** GM2

(c) GM3

Figure 2.9: Uniaxial compressive stress–strain responses of geopolymer mortar specimens GM1, GM2, and GM3

Although this study is not intended as a direct comparison between different binders, reference tests were also performed on OPC concrete specimens (see Figure 2.10) to characterize the behavior of the target substrate material. The OPC samples showed much higher compressive strength (average $35.30\,\mathrm{MPa}$) and a significantly steeper elastic slope, with a corresponding axial strain at peak of only -0.0018. Post-peak behavior was brittle,

with minimal deformability and abrupt load drop. Transverse strain remained negligible until fracture, highlighting the limited lateral extensibility of the material.

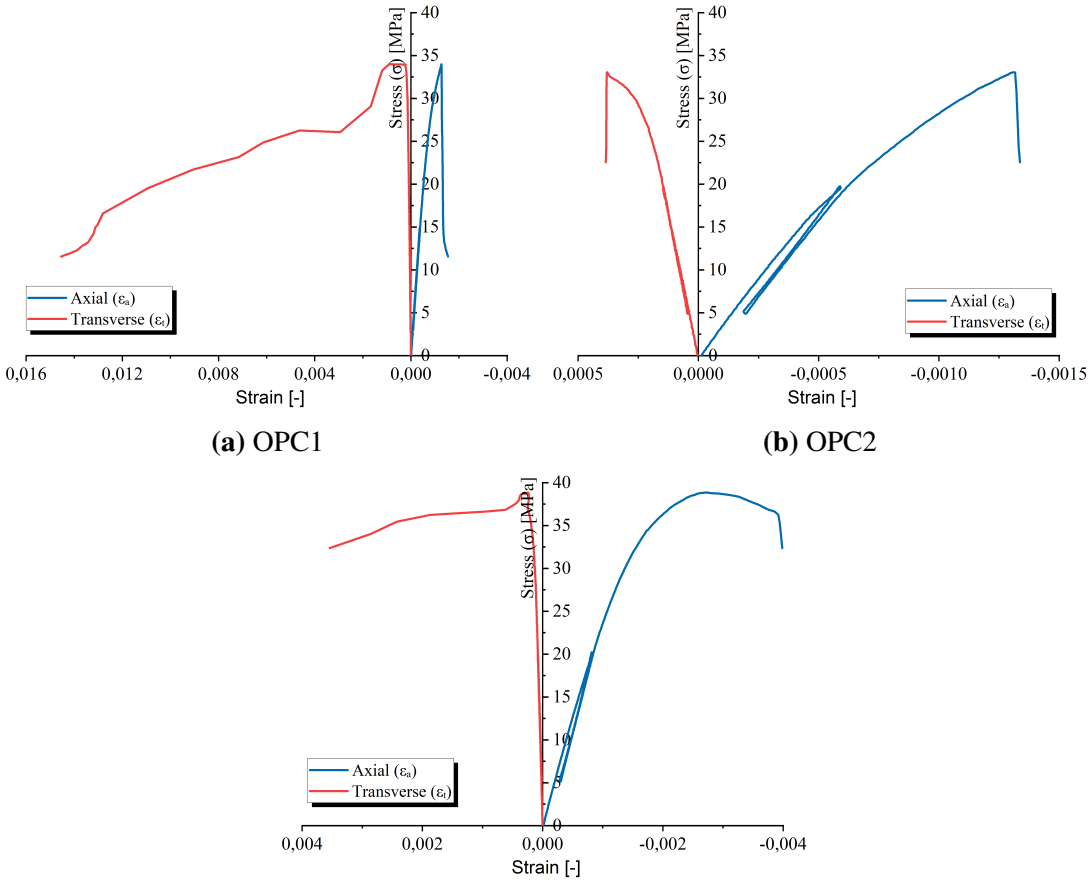

(a) OPC1 **(b)** OPC2

(c) OPC3

Figure 2.10: Uniaxial compressive stress–strain responses of traditional Portland Concrete specimens OPC1, OPC2, and OPC3

The quantitative properties extracted from both materials are summarized in Table 2.3 and Table 2.4. The geopolymer mortar displayed a lower average elastic modulus (9.80 GPa) and a higher Poisson's ratio (0.25), reflecting reduced stiffness but greater lateral compliance. In contrast, the OPC substrate exhibited higher stiffness (35.50 GPa) but lower lateral deformability ($\nu = 0.18$). These differences are not intended for material ranking, but rather for understanding compatibility: effective repair requires that the repair material not only bond well but also deform compatibly with the substrate under mechanical loads.

Table 2.3
Compressive properties of geopolymer mortar specimens

	MG-1	MG-2	MG-3	Average
σ_{max} (MPa)	22.50	19.33	18.86	21.26
$\varepsilon_{a,\sigma_{max}}$ (-)	-0.0047	-0.0048	-0.0053	-0.0049
$\varepsilon_{t,\sigma_{max}}$ (-)	0.0058	0.0072	0.0066	0.0065
E (GPa)	11.59	9.27	8.53	9.80
ν	0.28	0.27	0.21	0.25

Table 2.4
Elastic Modulus and Poisson's ratio of OPC

	CON-1	CON-2	CON-3	Average
σ_{max} (MPa)	33.99	33.06	38.85	35.30
$\varepsilon_{a,\sigma_{max}}$ (-)	-0.0013	-0.0013	-0.0027	-0.0018
$\varepsilon_{t,\sigma_{max}}$ (-)	0.0009	0.0009	0.0002	0.0006
E (GPa)	41.79	36.60	28.12	35.50
ν	0.15	0.26	0.12	0.18

Implications for repair compatibility

These differences are summarized in Table 2.5. While OPC concrete delivers superior strength and stiffness, it suffers from abrupt, brittle failure. In contrast, the geopolymer mortar exhibits a more gradual post-peak response and higher strain capacity, suggesting improved toughness and energy dissipation potential. Such characteristics are highly desirable for repair applications and interface zones where compatibility with surrounding deformation is critical.

Table 2.5
Comparison of compressive responses between geopolymer mortar and OPC

Material	$\sigma_{\max}$ (MPa)	E (GPa), ν	Mechanical implication
Geopolymer mortar	21.26	9.80, 0.25	Moderate stiffness, good ductility, progressive failure
OPC	35.30	35.50, 0.18	High stiffness, brittle fracture, low energy absorption

In this context, understanding the standalone compressive behavior of geopolymer mortar is essential. It establishes the mechanical foundation for subsequent investigation of geopolymer–concrete interfaces, especially under shear or coupled hydro-mechanical conditions. The deformability and energy dissipation capacity observed in geopolymer mortars highlight their potential to function not only as passive fillers but as active stress-accommodating repair layers.

4.2 Durability-related characteristics

4.2.1 Gas permeability

Gas permeability is a critical parameter for evaluating the durability and serviceability of cementitious and geopolymer-based materials (Abbas et al., 1999; Shi, 1996; Hossain et al., 2015). It reflects the ease with which gases can penetrate through the microstructure, thus providing an indirect measure of porosity, pore connectivity, and the integrity of the material matrix. In practical applications, high gas permeability often correlates with increased vulnerability to ingress of aggressive agents such as carbon dioxide, oxygen, and water vapor, which can accelerate chemical degradation and reduce structural longevity.

In the context of geopolymer-to-concrete repairs, assessing the gas permeability of the geopolymer mortar is particularly important (Provis and Bernal, 2014; Dassekpo et al., 2021; Wasim et al., 2021). Since the geopolymer layer is applied over or bonded to existing OPC substrates, its ability to resist gas and fluid transport not only affects its own durability but also influences the protection it provides to the substrate. Moreover,

permeability characteristics help evaluate the tightness of the interface and the potential for fluid migration along interfacial defects.

To investigate the gas transport behavior of geopolymer mortar under service-relevant conditions, two experimental series were conducted on specimens prepared in distinct moisture states. The first group of specimens was cured at $20\,^{\circ}\mathrm{C}$ and 90% relative humidity (RH) until mass stabilization was achieved, representing the **saturated state**. The second group was subjected to progressive thermal drying in a controlled oven, where the temperature was gradually raised to $105\,^{\circ}\mathrm{C}$ and maintained until no further mass loss was observed. These specimens were defined as being in the **dry state**.

For both saturation conditions, two complementary gas permeability test series were performed. In the first series, the gas injection pressure was fixed at $5\,\mathrm{bar}$, while the confining pressure was incrementally increased. This configuration simulates the influence of increasing external confinement, such as from overburden or lateral structural restraint, on gas permeability. In the second series, the confining pressure was held constant at $30\,\mathrm{bar}$, and the gas pressure was varied to investigate pressure sensitivity and potential slippage effects—especially relevant in dry-state, low-permeability conditions.

Experimental setup and procedure

The gas permeability tests were conducted based on the isobaric method outlined in International Organization for Standardization (2003), which has been widely applied to characterize porous cementitious materials (Hubbert, 1956; Loosveldt et al., 2002; Quelennec et al., 2023). This method evaluates the material's resistance to gas flow under steady or quasi-steady conditions, governed by Darcy's law for compressible fluids.

Figure 2.11 illustrates the actual laboratory configuration of the permeability test system, and a detailed schematic representation is shown in Figure 2.12. Cylindrical specimens of $36\,\mathrm{mm}$ in diameter and height were used. The specimens were inserted into a stainless steel triaxial cell equipped with radial O-ring seals and metal tightening flanges to ensure airtight conditions and uniform confinement.

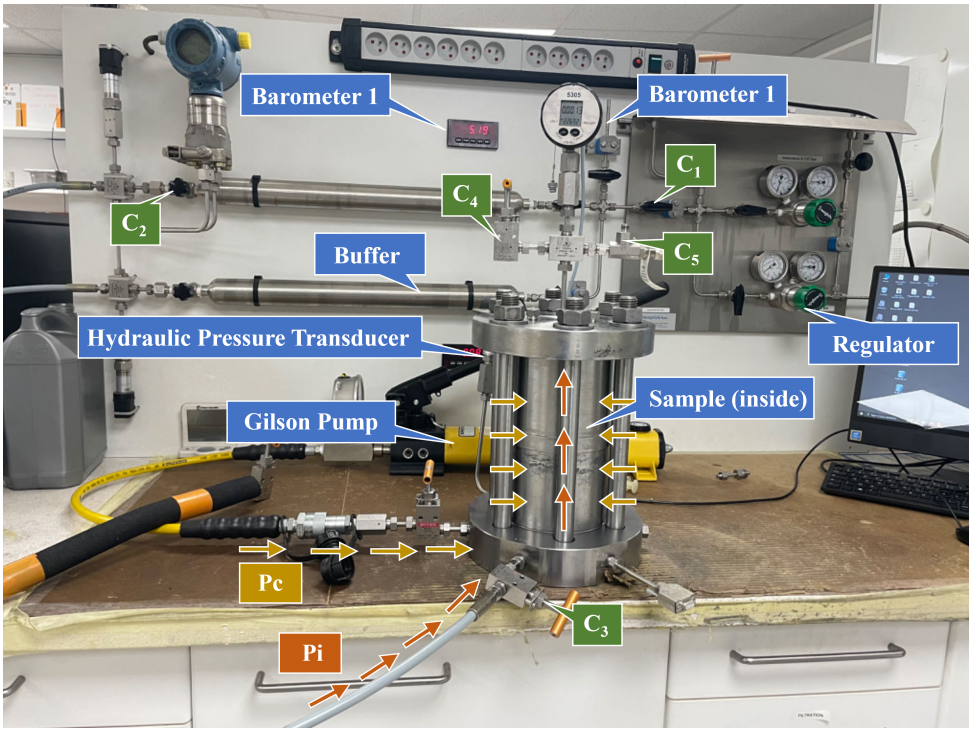

Figure 2.11: Permeability testing apparatus (actual laboratory configuration)

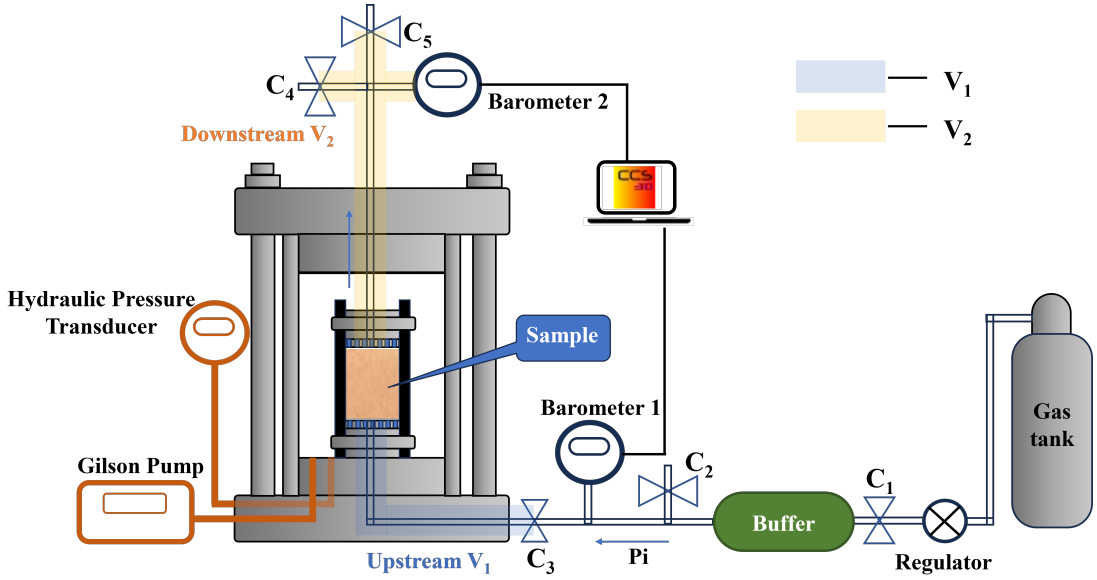

Figure 2.12: Schematic diagram of the permeability apparatus (Quelennec et al., 2023)

Nitrogen gas was used as the injected medium due to its chemical inertness and stable flow behavior. All tests were performed under ambient laboratory conditions, with

temperature maintained at $20\,^{\circ}\mathrm{C}$ and relative humidity below 50%.

The experimental setup comprises five manually operated valves (C_1 to C_5) and multiple pressure monitoring components. Nitrogen gas was supplied from a pressurized tank, regulated by a high-precision controller, and stabilized by a buffer tank to mitigate short-term pressure fluctuations. The upstream injection pressure P_i was continuously monitored by Barometer 1. Confining pressure P_c was applied via a hydraulic oil system and measured using a hydraulic pressure transducer, ensuring a constant lateral stress condition during testing.

The upstream reservoir volume V_1 was defined as the total gas volume extending from the pressure regulator to the base of the specimen, including the internal volume of the buffer tank and the tubing between valve C_3 and the triaxial cell. Likewise, the downstream reservoir volume V_2 corresponds to the gas space extending from the specimen top to valve C_4, including the connecting tubing and pressure sensors. Although C_5 is designed to relieve overpressure in emergency conditions, it was securely shut during all test procedures to maintain a sealed downstream domain.

Prior to testing, the system was leak-tested using a soap-bubble method, and all connections were tightened to ensure complete airtightness. Once the specimen was mounted and the chamber sealed, nitrogen gas was introduced at a constant pressure P_i, and flow was allowed to stabilize under quasi-steady conditions.

Calculation method and data processing

To evaluate the gas permeability of geopolymer mortar specimens, a quasi-steady-state isobaric method was applied, based on Darcy's law under compressible gas flow conditions. The internal gas pressure distribution across the specimen height follows a parabolic profile derived from the steady-state formulation of Darcy's law:

$$\nabla^2 P^2 = 0 \quad \text{and} \quad P(x) = \sqrt{P_1^2 \left(1 - \frac{x}{L}\right) + P_0^2 \frac{x}{L}} \tag{2.3}$$

where:

- $P(x)$ is the gas pressure at a height x [m] within the specimen;
- P_1, P_0 are the absolute upstream and downstream pressures [Pa];
- L is the specimen height [m];

- x is the axial coordinate from the top surface [m].

Average flow rate measurement. The average volumetric flow rate was evaluated by monitoring pressure variations within well-defined reservoir volumes. For the upstream measurement, once a quasi-steady gas flow was established, valve C_1 was closed, while valve C_3 was opened and C_2 was kept closed. This configuration isolated the upstream gas volume V_1, which included the internal capacity of the buffer tank and the connecting tubing from valve C_3 to the base of the specimen. Over a given time interval Δt, the pressure drop ΔP_1 within this volume was used to calculate the average inlet flow rate using the following expression:

$$Q_1^{\text{avg}} = \frac{V_1 \cdot \Delta P_1}{P_1^{\text{avg}} \cdot \Delta t}, \quad P_1^{\text{avg}} = P_1 - \frac{\Delta P_1}{2} \tag{2.4}$$

Similarly, the downstream flow rate was determined by closing valve C_4 while keeping the safety valve C_5 closed. Under this condition, the downstream volume V_2 consisted of the gas space from the specimen outlet up to valve C_4, encompassing all downstream tubing and sensors. The pressure increase ΔP_0 recorded within this closed volume over the same time interval Δt was used to evaluate the average outlet flow rate as:

$$Q_0^{\text{avg}} = \frac{V_2 \cdot \Delta P_0}{P_0^{\text{avg}} \cdot \Delta t}, \quad P_0^{\text{avg}} = P_0 + \frac{\Delta P_0}{2} \tag{2.5}$$

All pressures were recorded as absolute values with respect to vacuum and expressed in pascals (Pa). The resulting flow rates were reported in cubic meters per second (m^3/s), and were subsequently used to determine the intrinsic gas permeability, as detailed in the following section.

Permeability calculation. Gas permeability K is calculated using the compressible form of Darcy's law, taking into account the parabolic pressure profile. For flow through a cylindrical specimen:

$$K_{\text{app}} = \frac{\mu \cdot Q_0^{\text{avg}} \cdot 2L \cdot P_0^{\text{avg}}}{A \cdot ((P_0^{\text{avg}})^2 - P_0^2)} \tag{2.6}$$

where:

- K_{app}: gas permeability obtained from Darcy's law [m^2];

- μ: dynamic viscosity of air, $2.20 \times 10^{-5}\,\mathrm{Pa \cdot s}$;
- Q_0^{avg}: average flow rate downstream [m^3/s];
- L: specimen height [m];
- $A = \pi D^2/4$: cross-sectional area [m^2] with diameter $D = 0.036\,\mathrm{m}$;
- P_0^{avg}, P_0: average and final downstream pressure [Pa].

Klinkenberg correction for gas slippage. At low pressures, gas molecules may exhibit slippage at the pore walls, leading to an overestimation of the intrinsic permeability. To correct this, the Klinkenberg model introduces a pressure-dependent term:

$$K_{\mathrm{app}} = K\left(1 + \frac{b}{P_{\mathrm{mean}}}\right) \tag{2.7}$$

where:

- K_{app} is the apparent gas permeability obtained from Darcy's law [m^2],
- K is the intrinsic (corrected) permeability [m^2],
- b is the Klinkenberg parameter [Pa],
- $P_{\mathrm{mean}} = (P_1 + P_0)/2$ is the mean absolute pressure across the specimen [Pa].

Multiple permeability values were obtained at different test pressures. A plot of K_{app} versus $1/P_{\mathrm{mean}}$ was used to linearly regress the Klinkenberg model, where the intercept gives the intrinsic permeability K, and the slope gives the slippage factor b (Bear, 2013; Tanikawa and Shimamoto, 2009; Al-Jabri et al., 2015).

Results and Discussion

Apparent gas permeability. Gas permeability tests were conducted under two different boundary conditions to characterize the transport behavior of geopolymer mortar in both dry and saturated states. Figure 2.13(a) shows the apparent gas permeability values obtained at different confining pressures (10–50 bar) while maintaining a constant gas injection pressure of 5 bar. Conversely, Figure 2.13(b) presents results under variable gas pressures (3–10 bar) with a fixed confining pressure of 30 bar.

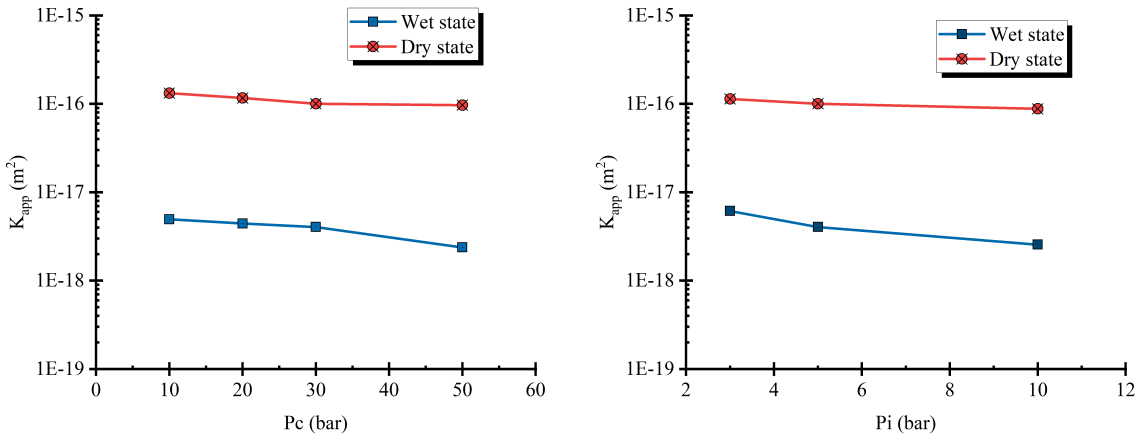

(a) Permeability under different confining pressures at fixed gas pressure of 5 bar

(b) Permeability under different gas pressures at fixed confining pressure of 30 bar

Figure 2.13: Gas permeability of geopolymer mortar under two conditions: (a) confining pressure variation; (b) gas pressure variation

In both cases, the permeability in the dry state was found to be significantly higher than in the saturated state, consistent with the expectation that water-filled pores obstruct gas flow. For instance, at a confining pressure of 10 bar, the dry-state permeability reached 1.324×10^{-16} m^2, compared to 4.95×10^{-18} m^2 in the saturated condition.

The results also reveal a clear decreasing trend in gas permeability with increasing confining pressure. This reduction is primarily attributed to the compaction of pore structures and the progressive closure of microcracks under elevated stress. In geopolymer mortars, particularly in the dry state, microcracks formed during curing or shrinkage may remain open and serve as dominant gas flow paths. Applying higher confinement compresses both the matrix porosity and these micro-defects, significantly limiting gas transport capacity.

In contrast, increasing the gas injection pressure under constant confinement also led to a reduction in measured permeability. This effect is associated with the suppression of gas slippage at higher pressures, as the mean free path of gas molecules decreases and interactions with pore walls become less pronounced. The dry-state results, in particular, display this pressure-dependent behavior more clearly due to the unfilled pore space facilitating boundary layer effects.

These observations highlight the sensitivity of gas permeability to both pore saturation and stress state, which must be considered when evaluating geopolymer materials for

repair applications. The permeability reduction in saturated conditions suggests enhanced sealing performance and reduced susceptibility to external gas ingress.

Corrected gas permeability. As gas permeability measurements are affected by slippage effects under low pressure conditions, the Klinkenberg correction was applied to derive the intrinsic permeability of geopolymer mortar in the dry state.

To perform the correction, a series of permeability tests were conducted under varying inlet gas pressures ($P_i = 3, 5, 10\,\text{bar}$), while maintaining a constant confining pressure of 30 bar. The measured apparent permeability values in the dry state were then plotted against $1/P_{\text{mean}}$ and fitted with a linear function, as shown in Figure 2.14.

The linear regression yielded the following relationship:

$$K_{\text{app}} = 7.32 \times 10^{-17} + \left(8.15 \times 10^{-12}\right) \cdot \left(\frac{1}{P_{\text{mean}}}\right) \tag{2.8}$$

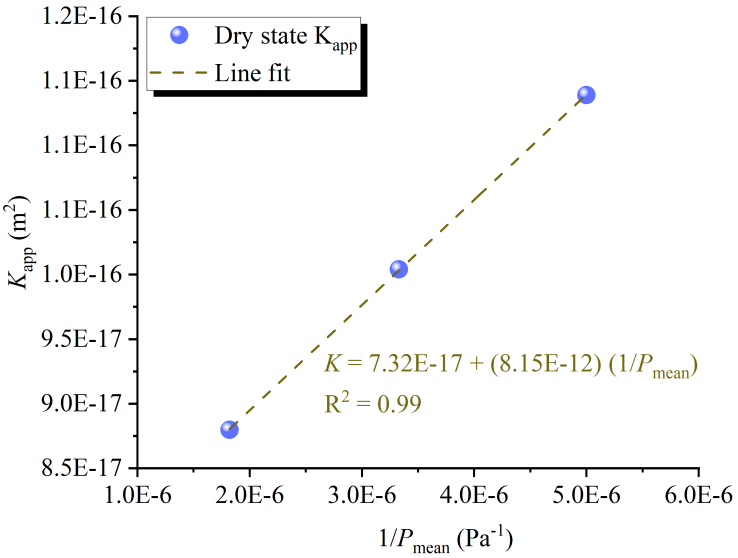

Figure 2.14: Klinkenberg correction: linear fitting of dry-state apparent permeability versus $1/P_{\text{mean}}$

Accordingly, the intrinsic gas permeability of the geopolymer mortar under dry conditions was determined to be:

$$K = 7.32 \times 10^{-17}\ \text{m}^2 \tag{2.9}$$

This corrected value represents the gas permeability of the material excluding the slippage effect, and therefore better reflects the true pore structure of the geopolymer matrix. The comparison between the corrected intrinsic permeability and the average apparent permeability ($K_{\text{app}} \approx 1.00 \times 10^{-16}$ m^2) indicates a considerable overestimation caused by slip flow at lower mean pressures. The obtained Klinkenberg parameter $b = 8.15 \times 10^{-12}$ Pa is within the expected range for low-permeability geomaterials. This result confirms that correction is essential for accurate permeability characterization, especially when assessing durability-related transport behavior in geopolymer repair applications.

This correction was not applied to the saturated condition, as gas slippage effects are less significant due to reduced gas mobility in moisture-filled pores.

4.2.2 Pore structure and porosity analysis

Gas expansion method

To evaluate the effective porosity of geopolymer specimens, a gas expansion technique based on Boyle's law ($P_1V_1 = P_2V_2$) was employed (Washburn and Bunting, 1922; Alekseev et al., 2018). This method allows for the estimation of the connected pore volume by measuring the volume change caused by gas expansion into a previously evacuated system. The test setup is illustrated in Figure 2.15, and a schematic diagram is provided in Figure 2.16.

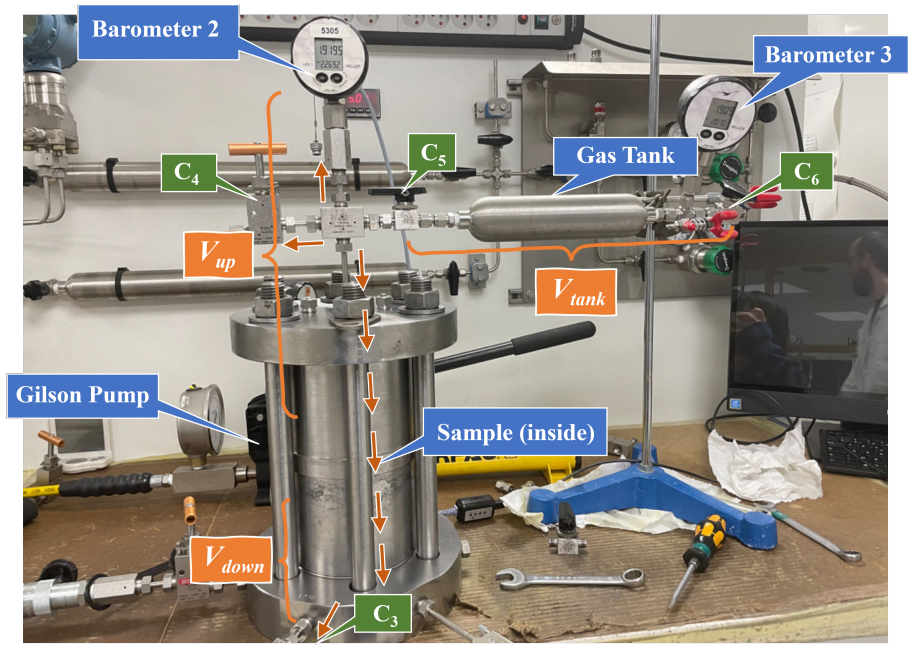

Figure 2.15: Porosity testing apparatus

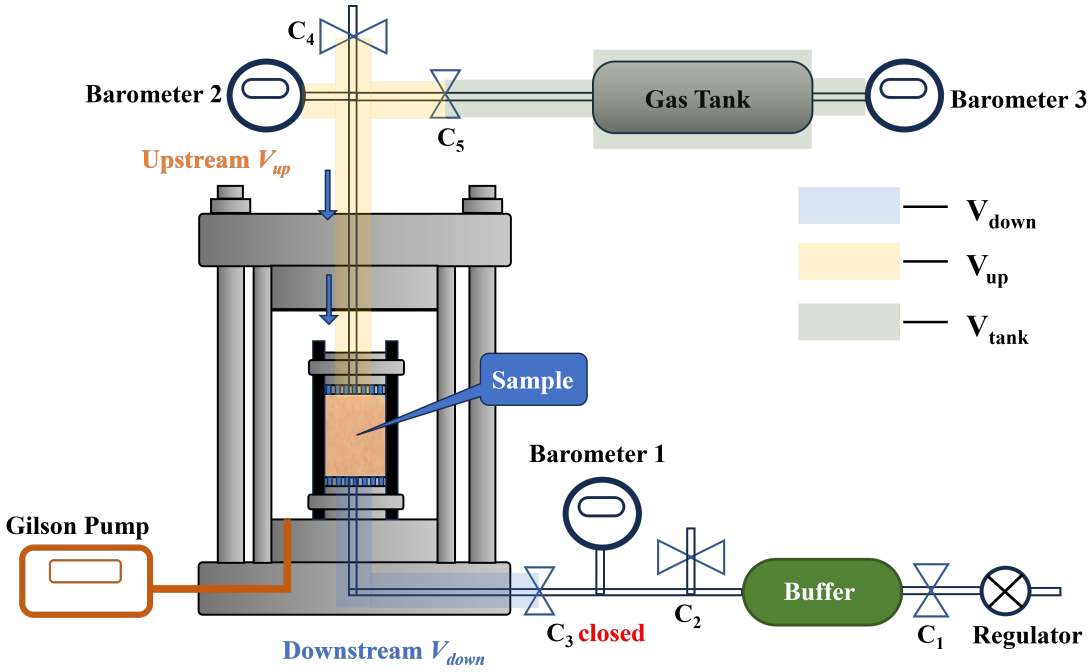

Figure 2.16: Schematic diagram of the porosity apparatus

The test procedure consisted of two steps. First, a known volume of nitrogen gas, confined within the calibrated tank volume V_{tank}, was pressurized to an initial pressure

P_1, recorded by Barometer 3 with valves C_4, C_5, and C_6 all closed. The downstream section of the system (including the sample chamber, upstream pipes, and buffer zone) was initially evacuated or at atmospheric pressure.

Next, valve C_5 was opened to allow the gas to expand from the tank into the test system. After equilibrium was reached, the new pressure P_2 was recorded using Barometer 2. Assuming ideal gas behavior and isothermal conditions, the total volume of the downstream system V_{sys} can be calculated as:

$$V_{\text{sys}} = \frac{P_1 \cdot V_{\text{tank}}}{P_2} - V_{\text{tank}} \tag{2.10}$$

Here, V_{tank} is the known internal volume of the gas tank, and V_{sys} represents the total accessible volume from the gas tank outlet to valve C_3, including all upstream sections.

To isolate the sample's pore space, previously measured system volumes were used: V_{up}, the upstream test configuration volume (as defined in the permeability test), and V_{down}, the known downstream volume (below the specimen). The volume of connected pores within the sample, V_{pore}, is then:

$$V_{\text{pore}} = V_{\text{sys}} - V_{\text{up}} - V_{\text{down}} \tag{2.11}$$

Finally, the porosity ϕ of the sample is calculated by normalizing the pore volume with respect to the specimen's geometric volume V_{geo}:

$$\phi = \frac{V_{\text{pore}}}{V_{\text{geo}}} \tag{2.12}$$

Assuming ideal gas behavior and isothermal conditions, the porosity ϕ of the specimen is determined by quantifying the volume of connected pores through pressure-volume expansion. The final expression is:

$$\phi = \frac{1}{V_{\text{geo}}} \left(\frac{P_1 \cdot V_{\text{tank}}}{P_2} - V_{\text{tank}} - V_{\text{up}} - V_{\text{down}} \right) \tag{2.13}$$

where:

- ϕ: porosity of the specimen [–];
- V_{geo}: geometric volume of the specimen, calculated from its dimensions [m^3];

- V_{tank}: known internal volume of the pressurized gas tank [m^3];
- P_1: initial absolute pressure in the tank before expansion [Pa];
- P_2: equilibrium absolute pressure after expansion into the test system [Pa];
- V_{up}: upstream system volume (from tank outlet to specimen top) [m^3];
- V_{down}: downstream system volume (below specimen) [m^3].

All pressure values were measured as absolute pressures (Pa), and volumes were expressed in cubic meters (m^3). This approach allowed reliable estimation of the open porosity accessible to gas under dry conditions, suitable for evaluating the continuity and connectivity of the pore structure in geopolymer materials. Based on the gas expansion method described above, the connected porosity of the geopolymer specimen was determined to be $26.87 \pm 1.12\%$. This value reflects the proportion of interconnected pore space accessible to gas under dry conditions and provides a quantitative basis for evaluating the internal pore structure of the material (Jaya et al., 2020; Papa et al., 2022; Novais et al., 2020). The relatively high porosity is consistent with the expected microstructure of alkali-activated materials, which are known to possess a continuous capillary pore network formed during polymerization and curing.

Vacuum saturation method

To complement the gas expansion method, a classical vacuum saturation technique was also used to assess the porosity of the geopolymer specimens (Li et al., 2017; Safiuddin and Hearn, 2005; Bu et al., 2014). This method estimates the volume of connected pores by measuring the amount of water absorbed into the dried sample under vacuum conditions. The experimental setup is shown in Figure 2.17, where a vacuum pump was used to evacuate the desiccator containing the dried sample. After maintaining vacuum for at least 3 hours to remove entrapped air, deionized water was introduced to fully saturate the specimen under continued vacuum. The saturated mass was then recorded, and the connected porosity ϕ was calculated using the following relation:

$$\phi = \frac{m_{\text{sat}} - m_{\text{dry}}}{\rho_{\text{water}} \cdot V_{\text{geo}}} \tag{2.14}$$

where m_{sat} and m_{dry} are the saturated and oven-dry masses of the specimen, ρ_{water} is the density of water, and V_{geo} is the geometric volume of the sample.

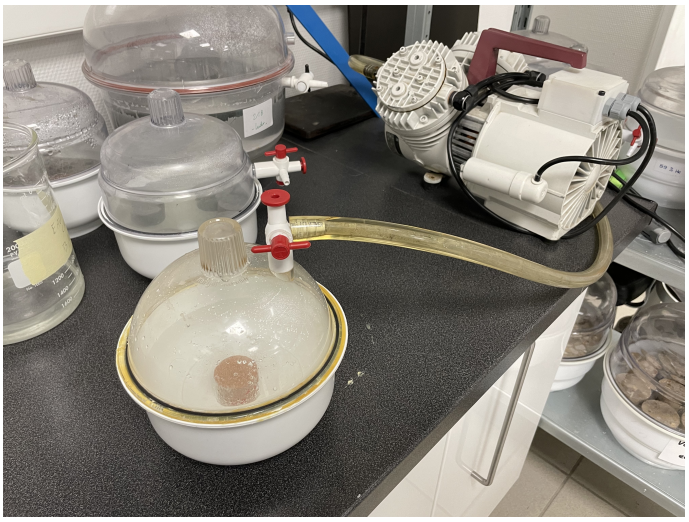

Figure 2.17: Vacuum drainage apparatus

Using this method, the porosity of the tested geopolymer specimen was determined to be 18.54%. This value is notably lower than the result obtained from the gas expansion method (26.87%), which suggests that a portion of the pore network may be inaccessible to water due to disconnected pores or hydrophobic surfaces. In contrast, the gas expansion technique can detect both continuous and partially connected pores accessible to gas molecules. This discrepancy highlights the importance of method selection when evaluating pore structure and transport properties in geopolymer materials.

4.3 Shrinkage behavior of geopolymer mortar

This study aims to investigate the shrinkage properties of geopolymer mortar, a critical factor affecting its suitability as a repair material. By integrating traditional shrinkage measurement methods with innovative approaches, this research measures autogenous shrinkage, drying shrinkage, and plastic shrinkage. It also compares mass change, the setting time of geopolymer mortar and examines the impact of temperature on specimen deformation, exploring the shrinkage behavior of potassium-based geopolymer mortar. Combining the vertical mortar shrinkage meter with Digital Image Correlation (DIC) methods not only validated the feasibility of the DIC observational technique but also

addressed the limitation commonly encountered in shrinkage research, where changes are typically observed only in the horizontal direction without detecting vertical shrinkage.

4.3.1 Experimental methods and measurement setup

(1) Using verticle mortar shrinkage meter (LVDT) observe dry shrinkage and autogenous shrinkage

Figure 2.18 and Figure 2.19 illustrate the preparation and testing procedure for shrinkage and mass variation of geopolymer mortars. After demolding, the specimens were subjected to two distinct curing environments:

Autogenous shrinkage. Specimens were sealed with aluminum foil and placed in a chamber maintained at 20 °C and 90 % RH to eliminate external moisture exchange.

Drying shrinkage. Specimens were left unsealed and stored in another chamber at 20 °C and 50 % RH, allowing free moisture evaporation.

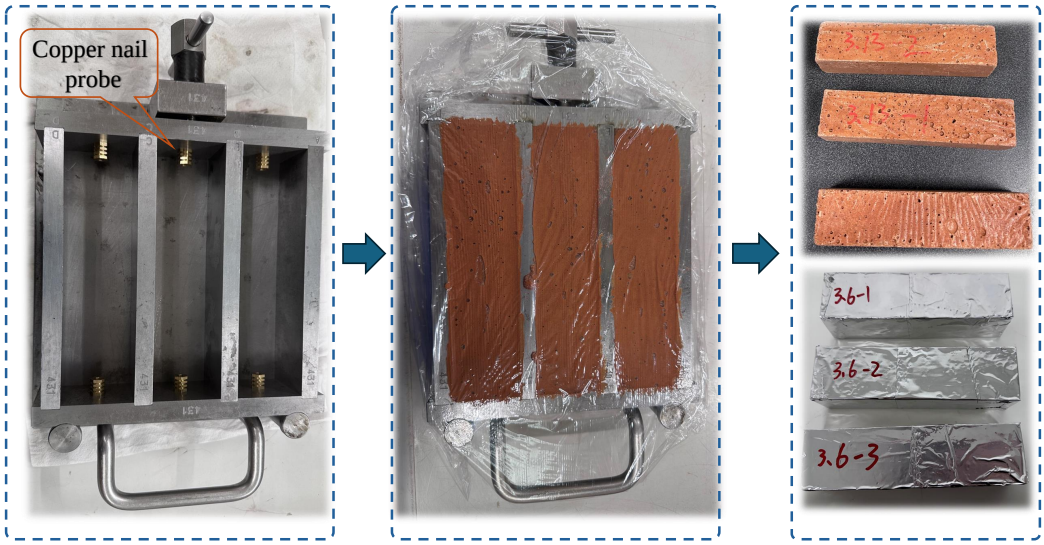

Figure 2.18: Shrinkage specimens preparation procedure: (a) Shrinkage test mold; (b) Specimens after casting; (c) Specimens after demolding

The shrinkage mold was equipped with embedded copper nail probes, and axial deformation was monitored using a vertical shrinkage meter with a digital dial gauge. Tests

were performed according to British Standards Institution (2002). In parallel, specimen mass was recorded periodically using a precision scale to assess moisture loss.



Figure 2.19: Shrinkage test setup using vertical deformation meter

The shrinkage strain at time t was calculated as:

$$\varepsilon(t) = \frac{L_0 - L(t)}{L_0} \times 10^6$$

The corresponding mass loss ratio was computed by:

$$\Delta m(t) = \frac{m_0 - m(t)}{m_0} \times 100\%$$

where:

- $\varepsilon(t)$ is the shrinkage strain at time t (με),
- L_0 and $L(t)$ are the initial and current lengths of the specimen (mm),
- $\Delta m(t)$ is the mass loss ratio at time t (%),
- m_0 and $m(t)$ are the initial and current specimen masses (g).

This combined measurement method enables a coupled assessment of moisture loss and deformation, which is essential for understanding shrinkage behavior in geopolymer mortars.

(2) Using DIC technology to observe specimens deformation

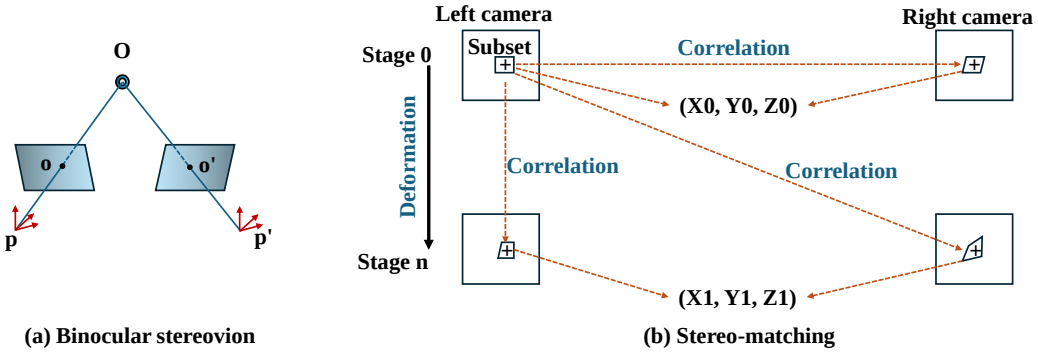

Figure 2.20: Illustration of 3D printing mould for plastic shrinkage test (Chen et al., 2018)

Principle of DIC. The diagram in Figure 2.20 illustrates the principles of 3D Digital Image Correlation (3D-DIC), showcasing the processes of binocular stereo vision and stereo matching for measuring the three-dimensional positioning and deformation of objects. 3D-DIC integrates binocular stereo vision with DIC technology to serve as an optical method for measuring the three-dimensional shapes and displacement fields of both planar and non-planar objects (Orteu, 2009). Binocular stereo vision (Orteu et al., 2007) is a technique used to reconstruct the three-dimensional positions of actual image points. Prior to testing, it is essential to adjust and calibrate both the cameras and lenses. The adjustment of the cameras involves setting the relational angles of the lenses, focal lengths, and apertures (Luo et al., 1994).

The calculation of spatial distances primarily relies on grid division. Initially, it is necessary to select a region of interest (ROI) within the image (indicated by the red area in Figure 2.21). Subsequently, the ROI is divided into a gridded format (depicted as the white grid in Figure 2.21). Over 1200 individual squares were defined within the DIC grid to facilitate a detailed and localized measurement of deformation.

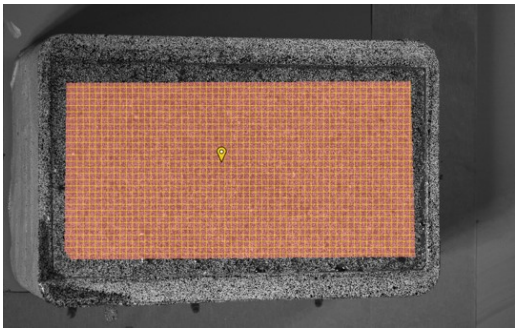

Figure 2.21: Grid division for DIC analysis of geopolymer mortar shrinkage

DIC Shrinkage testing setup. Figure 2.22 shows a typical DIC testing setup we used for shrinkage tests, including camera and lens, lighting equipment, computer and monitoring equipment, specimen and support,and fan for airflow and an anemometer.

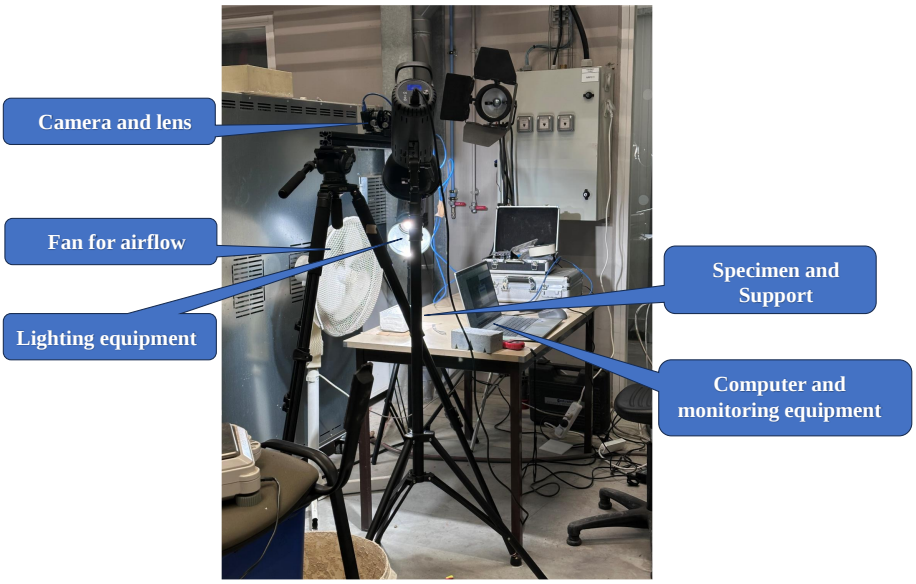

Figure 2.22: Digital Image Correlation (DIC) Shrinkage testing setup

Considering that shrinkage primarily occurred in the early stages, the observation strategy using DIC was structured to capture high-frequency data initially. For the first 24 hours, images were taken every 2 minutes. After the initial 24-hour period, the frequency was reduced, with images being captured every 30 minutes. This schedule optimized the monitoring of the dynamic shrinkage process over time.

(3) Plastic shrinkage based on ASTM International (2021)

To investigate the plastic shrinkage behavior of geopolymer mortar at early age, a custom mold (denoted as **Mould PA**) was developed based on the principles outlined by Yang et al. (2022a) and Meyer and Combrinck (2022), following the methodology specified in ASTM International (2021).

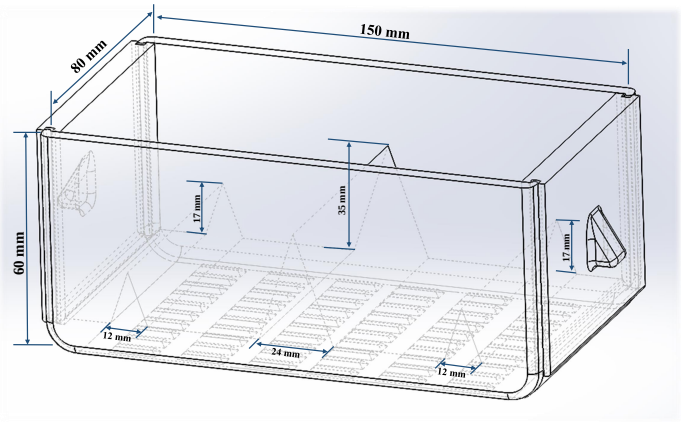

Figure 2.23: Custom-designed mold for plastic shrinkage test (Chen et al., 2018)

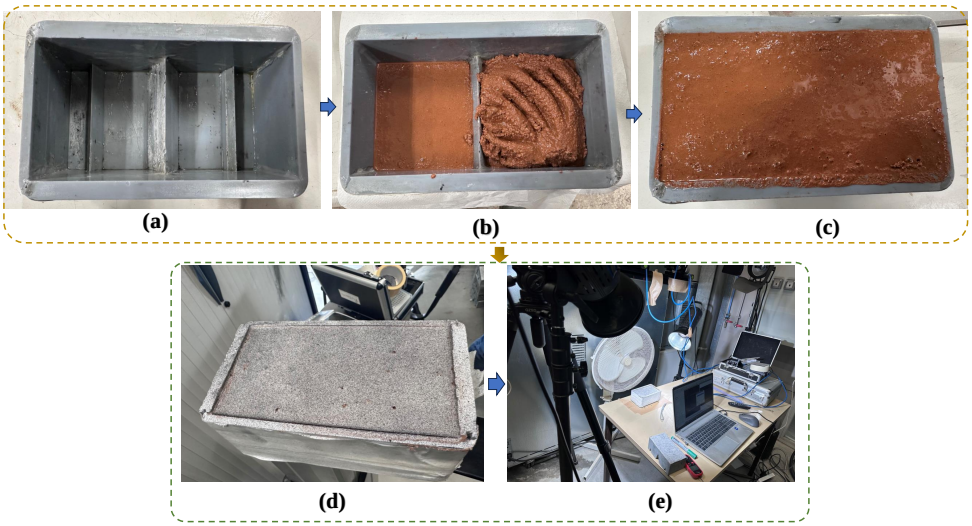

Figure 2.24: Shrinkage specimens preparation procedure

As shown in Figure 2.23, the mold was fabricated using 3D-printed UV-sensitive resin, with internal dimensions of $150\,\mathrm{mm} \times 80\,\mathrm{mm} \times 60\,\mathrm{mm}$. Three triangular notches were

integrated along the mold base to act as stress concentrators. The longer sides of the mold were mechanically restrained, while the shorter sides were left unrestrained, consistent with the partial restraint condition defined in ASTM International (2021). The procedure involved several steps as depicted in Figure 2.24.

After casting, fresh geopolymer mortar was leveled and placed under ambient conditions of 20 °C and 50 % relative humidity. Crack initiation and surface deformation were monitored using both visual inspection and DIC.

(4) Limitation and discussion

As shown in Table 2.6, both the conventional vertical mortar shrinkage meter and the DIC method have their respective advantages and limitations. Instead of relying solely on one approach, combining the traditional and advanced techniques provides a more comprehensive understanding of shrinkage behavior across different time scales.

Table 2.6
Comparison between conventional shrinkage measurement and DIC method

Aspect	Vertical mortar shrinkage meter	DIC
Measurement continuity	Discrete	Continuous
Early-age shrinkage	Misses data within mold	Captures data from casting
Contact requirement	Contact-based	Non-contact, full-field strain
Sensitivity to environment	Less sensitive (specimen stored in controlled chamber)	Highly sensitive; specimen under ambient conditions
Data richness	Single-point deformation data	Full-field deformation data
Applicability to duration	Well-suited for long-term	More suitable for short-term
Surface visibility requirement	Not required (embedded deformation can be measured)	unsuitable for sealed or covered specimens

4.3.2 Long-term shrinkage of geopolymer mortar

(1) Drying shrinkage

The long-term drying shrinkage behavior of geopolymer mortar was evaluated using the conventional vertical mortar shrinkage meter. Three specimens, labeled DS-1, DS-

2, and DS-3, were monitored over a period of 105 days under controlled environmental conditions (20 °C, 50% RH). As shown in Figure 2.25, all specimens exhibited a rapid shrinkage in the first 7 days, followed by a gradual stabilization phase. The final shrinkage values stabilized around -2500 $\mu\varepsilon$ for DS-1 and slightly lower for DS-2 and DS-3.

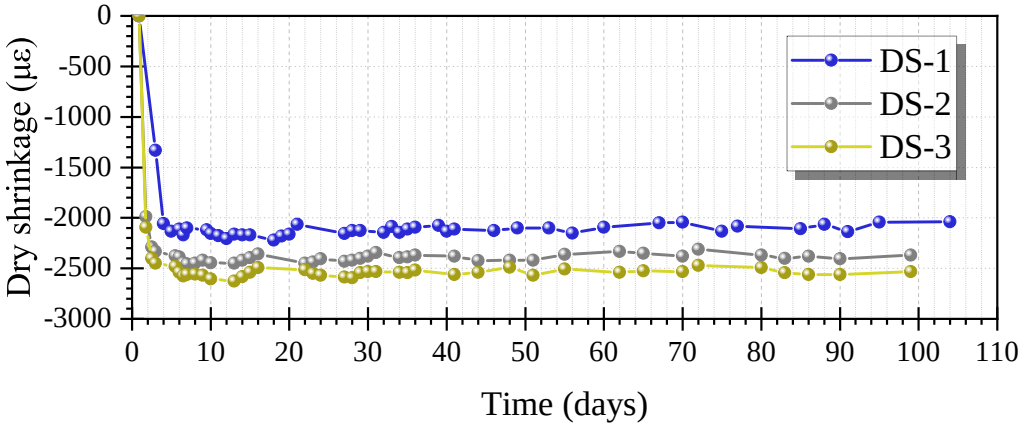

Figure 2.25: Long-term drying shrinkage of geopolymer mortar

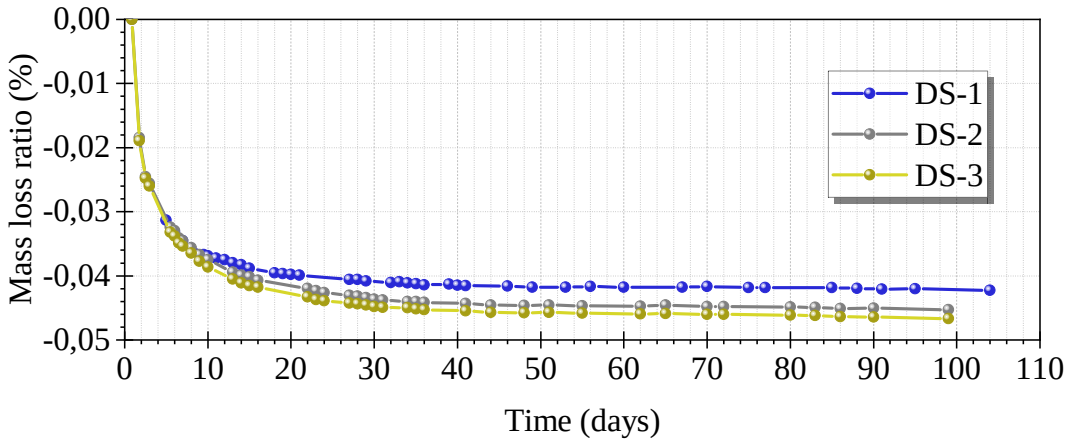

Figure 2.26: Long-term drying shrinkage mass loss ratio of geopolymer mortar

In parallel, mass loss measurements were conducted to assess moisture loss over time. As presented in Figure 2.26, a significant portion of the mass loss occurred within the first two weeks, which corresponds well with the period of rapid shrinkage. The mass loss ratio gradually plateaued after 30 days, indicating that the primary drying process

was complete. The correlation between early-age mass loss and shrinkage confirms that drying is the dominant mechanism driving the deformation in geopolymer mortar under the given curing conditions.

(2) Autogenous shrinkage

Autogenous shrinkage of geopolymer mortar was measured under sealed conditions using a conventional vertical mortar shrinkage meter. As shown in Figure 2.27, three specimens (AS-1, AS-2, and AS-3) were monitored for a period of 126 days. The shrinkage magnitude was relatively low, typically ranging between 200 and 800 $\mu\varepsilon$, with substantial fluctuations observed across all three specimens. These oscillations are largely attributed to the limitations of the conventional method when dealing with low-magnitude deformations, where system sensitivity and mechanical resolution introduce significant noise.

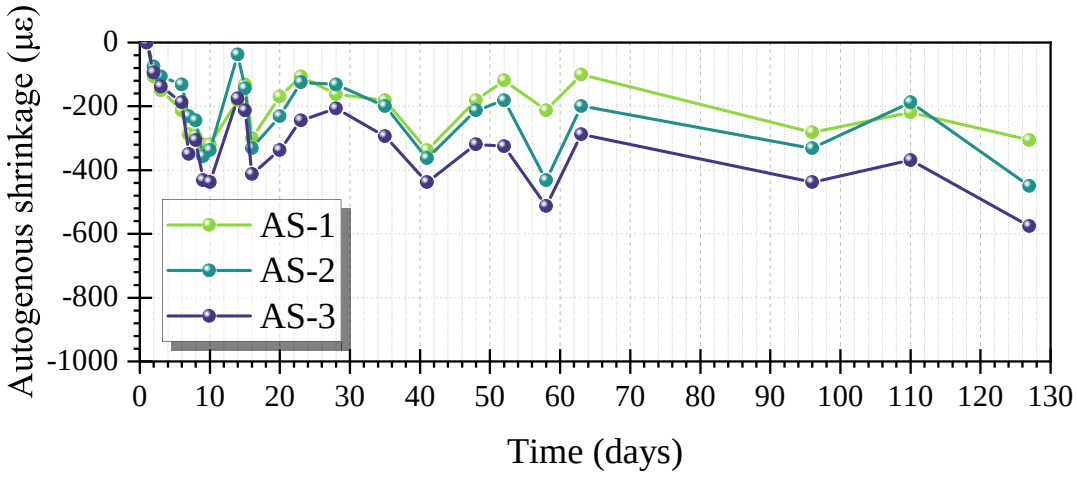

Figure 2.27: Long-term autogenous shrinkage of geopolymer mortar

The corresponding mass loss ratios are presented in Figure 2.28, and remained extremely small throughout the testing period (less than 0.008%). The negligible moisture loss confirms that the deformation observed in sealed specimens is primarily autogenous in nature, driven by internal chemical and physical transformations such as geopolymerization and self-desiccation.

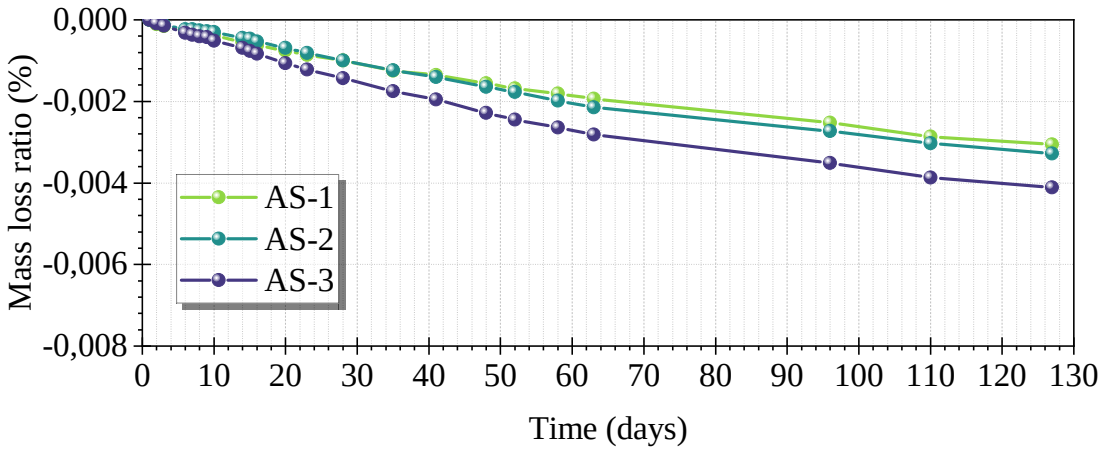

Figure 2.28: Long-term autogenous shrinkage mass loss ratio of geopolymer mortar

(3) Discussion and conclusion

The experimental results clearly demonstrate that drying shrinkage in geopolymer mortar occurs predominantly within the first 7 days after casting. This early-stage deformation is closely associated with rapid moisture loss, as confirmed by the mass loss data. In contrast, autogenous shrinkage evolves more gradually and exhibits a much smaller magnitude. Moreover, the traditional vertical mortar shrinkage meter, while effective for detecting large-scale deformation in drying conditions, shows considerable limitations when used for low-magnitude measurements such as autogenous shrinkage, as evidenced by the data fluctuations.

Given these observations, the application of high-resolution, non-contact techniques like DIC becomes particularly relevant. DIC allows for continuous monitoring from the very early age and can capture both small-scale strain changes and full-field deformation patterns.

4.3.3 Early-age (7 Days) shrinkage

To ensure the reliability of the comparative analysis and to isolate the effects of measurement techniques, all specimens used in the short-term (7 days) shrinkage study were cast from the same batch of geopolymer mortar. This approach minimizes variability due to differences in raw material mixing, curing time, and environmental exposure. By controlling these influencing factors, the differences observed between traditional and

DIC-based measurement results can be attributed primarily to the testing method itself. To investigate the early-age deformation behavior of geopolymer mortar, four prismatic specimens were monitored under different durations and modes using a DIC setup, as illustrated in Figure 2.29.

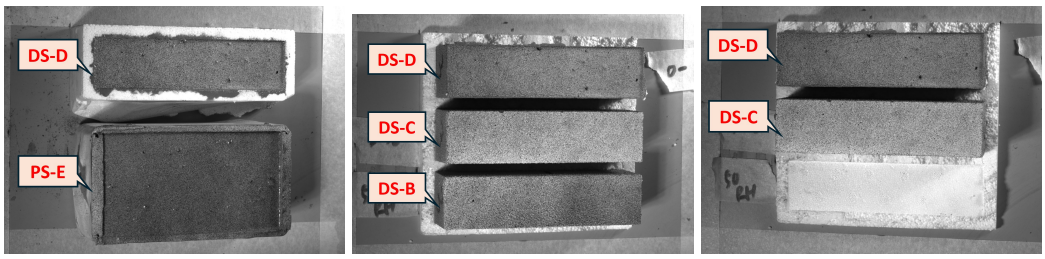

(a) 0-1 day **(b)** 1-7 day (with DS-C) **(c)** 1-7 day (without DS-C)

Figure 2.29: DIC camera view at different test stages

- **PS-E**: Dedicated to plastic shrinkage monitoring within the first 24 hours after casting. This specimen was tested in an unsealed condition from 0 to 1 day, capturing the plastic phase.
- **DS-D**: Used to continuously monitor total shrinkage from 0 to 7 days. The specimen remained in front of the DIC camera throughout the entire duration, from casting to 7 days.
- **DS-C and DS-B**: Both specimens were demolded at 24 hours after casting. DS-C was continuously monitored by DIC between Day 1 and Day 7, while DS-B was measured twice daily under DIC. Outside of DIC measurements, DS-B was stored in a curing chamber at 20 °C and 50% RH when not under observation.

Due to the limited field of view of the DIC camera, the experiment was divided into three successive setups: (a) PS-E and DS-D (0–1 day), (b) DS-C and DS-D (1–7 days, DS-C visible), and (c) DS-C and DS-D (1–7 days, DS-C temporarily removed from view).

(1) Feasibility of using DIC monitor dry shrinkage

To assess the feasibility of DIC in monitoring short-term shrinkage of geopolymer mortar, two identical prismatic specimens were prepared, labeled as DS-A and DS-B. Both specimens had dimensions of 40 mm × 40 mm × 160 mm and were cast from the

same batch of material. DS-A was tested using the traditional LVDT-based vertical mortar shrinkage meter, while DS-B was monitored with the DIC system. All specimens were cured under identical environmental conditions ($20\,^{\circ}\mathrm{C}$, 50% RH) and tested simultaneously to ensure consistency.

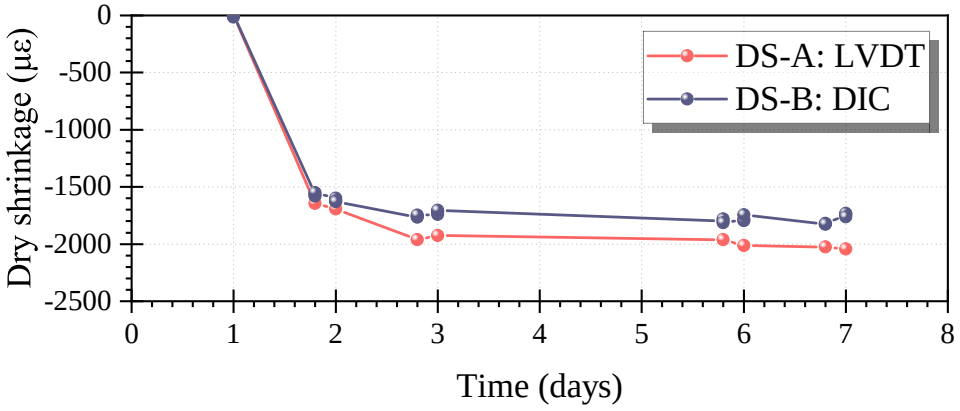

Figure 2.30: Comparison of short-term drying shrinkage measured by LVDT and DIC

Measurements were conducted twice per day for both methods. In this case, DIC virtual extensometers was used to compute the change in distance between two virtual gauge points placed in the mid-span of the specimen, corresponding to the same location as the copper nail probes used in LVDT measurements. This experimental setup allows a direct comparison of the two testing methods under matched conditions, providing insight into the precision and responsiveness of DIC in capturing early-age shrinkage behavior.

As shown in Figure 2.30, both specimens DS-A and DS-B exhibited similar shrinkage trends during the first 7 days, with the majority of deformation occurring within the first 48 hours. The overall magnitude and evolution pattern of shrinkage recorded by the DIC system closely matched those measured by the traditional vertical mortar shrinkage meter. For instance, by day 2, DS-A (LVDT) recorded a shrinkage of approximately $-1900\ \mu\varepsilon$, while DS-B (DIC) recorded $-1850\ \mu\varepsilon$; the difference between the two remained within $\pm 50\ \mu\varepsilon$ throughout the monitoring period.

This good agreement confirms that DIC is capable of reliably capturing early-age shrinkage behavior in geopolymer mortar. Minor differences between the two curves were observed, especially during the early stages. These discrepancies are most likely due to the limited resolution and sensitivity of the LVDT system in detecting rapid, low-magnitude deformation.

(2) Using DIC to continuously monitor dry shrinkage (1-7 day)

To further investigate the capabilities of DIC in capturing the evolution of early-age shrinkage, two monitoring strategies were compared using the same material batch. DS-B, introduced in the previous section, was kept in the curing chamber and measured twice daily using DIC. In contrast, DS-C was continuously monitored under the DIC setup in an ambient environment for the entire duration of the test. Both specimens were subjected to the same temperature and humidity conditions (20 °C, 50% RH), and the results are shown in Figure 2.31.

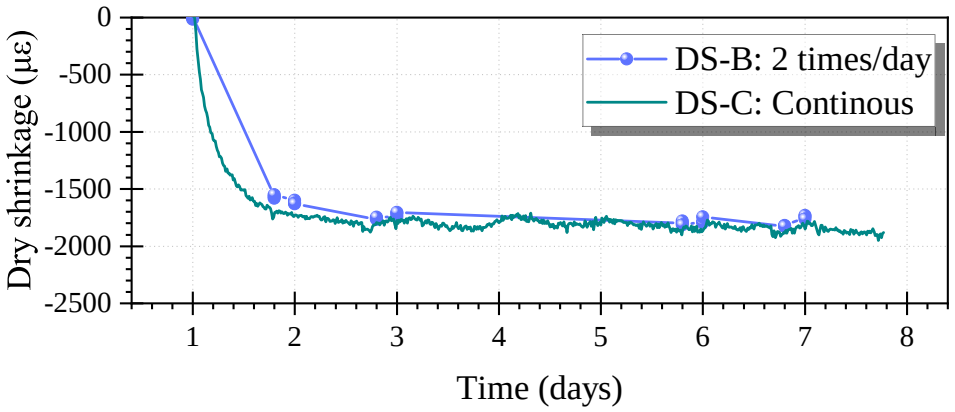

Figure 2.31: Discrete and continuous DIC monitoring of early-age drying shrinkage

The shrinkage trends of both specimens were highly consistent, particularly after the first 48 hours. Although DS-C was exposed to the laboratory environment during the entire monitoring period, the overall shrinkage behavior closely matched that of DS-B, which was stored in the curing chamber when not being measured. This indicates that under controlled ambient conditions, continuous DIC monitoring does not introduce significant deviations in drying shrinkage data.

Moreover, DS-C revealed more detailed shrinkage evolution, including small fluctuations and intermediate stages that were not captured by the discrete sampling of DS-B. These findings not only confirm the accuracy of DIC measurements but also demonstrate that continuous monitoring provides a more comprehensive understanding of the time-dependent deformation characteristics in geopolymer mortar.

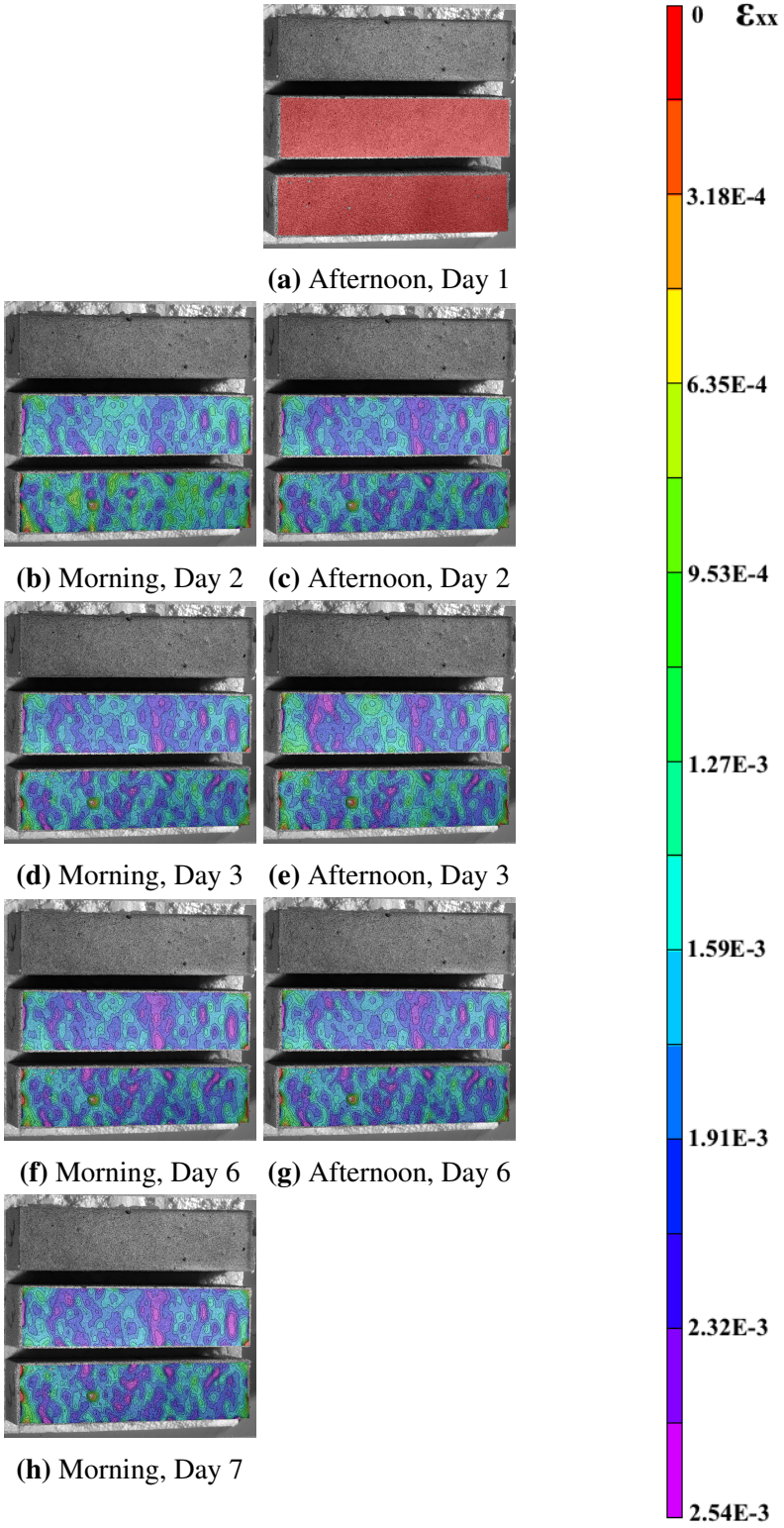

(a) Afternoon, Day 1

(b) Morning, Day 2 **(c)** Afternoon, Day 2

(d) Morning, Day 3 **(e)** Afternoon, Day 3

(f) Morning, Day 6 **(g)** Afternoon, Day 6

(h) Morning, Day 7

Figure 2.32: ε_{xx} shrinkage strain distribution of geopolymer mortar from Day 1 to Day 7

Note: Bottom: DS-B (intermittent monitoring); Middle: DS-C (continuously exposed to DIC).

In this study, the horizontal Lagrangian strain component ε_{xx} was selected as the primary indicator for shrinkage analysis. This direction corresponds to the restrained axis in the specimen setup, and is where shrinkage-induced tensile stress is most likely to accumulate. Moreover, it aligns with the direction in which linear displacement was measured using LVDT method in complementary tests, enabling direct comparison between full-field DIC results and point-based measurements.

Figure 2.32 presents the evolution of ε_{xx} in geopolymer mortar specimens DS-B and DS-C over a 7-day drying period. The strain maps were obtained using DIC and are overlaid on grayscale images of the specimens. Specimen DS-B was exposed intermittently, while DS-C was continuously monitored under ambient conditions. The colorbar on the right encodes the magnitude of ε_{xx}, with warmer colors (e.g., red and orange) corresponding to higher compressive strain, and cooler tones (e.g., blue and violet) indicating zones of lower or neutral deformation. The full strain range spans from 0 to approximately -2.54×10^{-3}, with high-strain zones often localized near exposed surfaces, indicating shrinkage concentration at drying fronts.

Comparing the two specimens, both DS-B and DS-C show consistent trends in shrinkage progression across the monitored days. At each time step, the spatial patterns and strain magnitudes were comparable between the two samples, reflecting the reproducibility of shrinkage behavior under similar drying conditions. Minor differences were noted in the rate of early-age strain development, particularly between Day 1 and Day 2, which may be attributed to slight variations in moisture exposure or air circulation near the specimen surfaces.

Importantly, despite DS-B being cured within a humidity-controlled chamber and DS-C exposed to ambient room conditions, the overall shrinkage distribution and peak strain levels remained similar. This observation suggests that, for geopolymer mortar, the influence of post-curing environmental exposure on early-age shrinkage may be less pronounced than expected—particularly when the material has reached a stable moisture state prior to demolding.

(3) Using DIC to continuously monitor shrinkage behavior (0–7 day)

To evaluate the true early-age shrinkage behavior of geopolymer mortar, two different DIC monitoring strategies were employed. Specimen DS-C was cured in the chamber for

24 hours and then demolded before initiating DIC measurement, representing a conventional shrinkage test approach. However, in practical applications such as repair materials, shrinkage begins immediately after casting, and deformation before demolding can be critical.

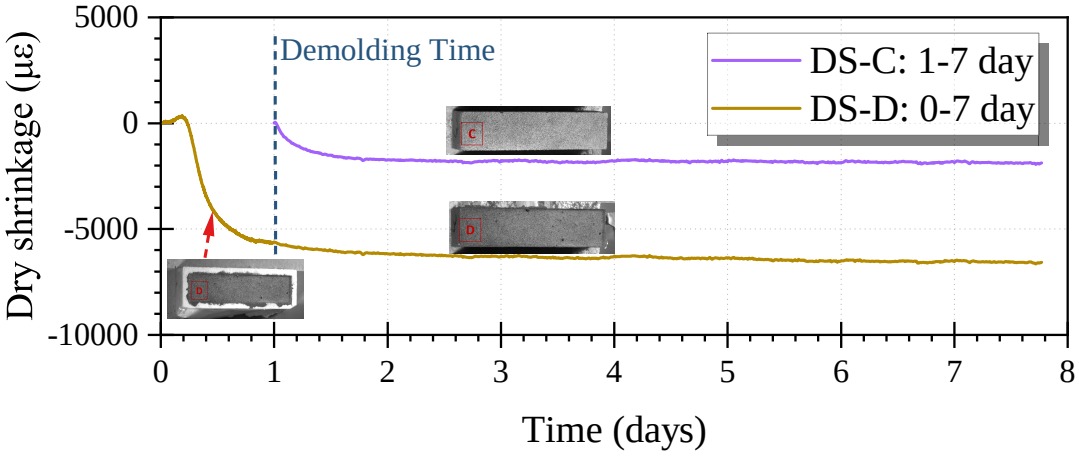

Figure 2.33: Continuous shrinkage monitoring of geopolymer mortar from casting vs. after demolding using DIC

To capture this early behavior, specimen DS-D was monitored continuously by the DIC system starting immediately after casting. It remained under observation during the first 24 hours and continued to be monitored after demolding. The shrinkage results for both DS-C and DS-D are presented in Figure 2.33.

The results reveal a significant difference between the two specimens. At 7 days, DS-C recorded a total shrinkage of approximately $-1850\ \mu\varepsilon$, whereas DS-D exhibited a total shrinkage of about $-6600\ \mu\varepsilon$. This clearly indicates that more than 70% of the total shrinkage occurred prior to demolding. The conventional approach underestimates early shrinkage by a factor of more than 3.5, which may lead to serious misjudgment in practical applications.

Such underestimation is particularly critical for repair mortars or high-performance cementitious systems, where cracking risks are highest within the first hours after casting. These findings demonstrate the necessity of initiating shrinkage monitoring immediately after casting. The DIC technique, with its ability to continuously monitor deformation without disturbing the specimen, offers a powerful and accurate tool for capturing these early, yet crucial, deformation phases.

4.3.4 Plastic shrinkage at initial setting phase

(1) Plastic shrinkage and setting time of geopolymer mortar

To investigate early-age plastic shrinkage behavior, two types of geopolymer mortar specimens were monitored using Digital Image Correlation (DIC) over a 24-hour period. Specimen DS-D (top in Figure 2.34) was cast in a standard prismatic mold ($40\,\mathrm{mm} \times 40\,\mathrm{mm} \times 160\,\mathrm{mm}$), while specimen PS-E (bottom) used a modified ASTM C1579-type mold with triangular notches to promote strain localization and cracking.

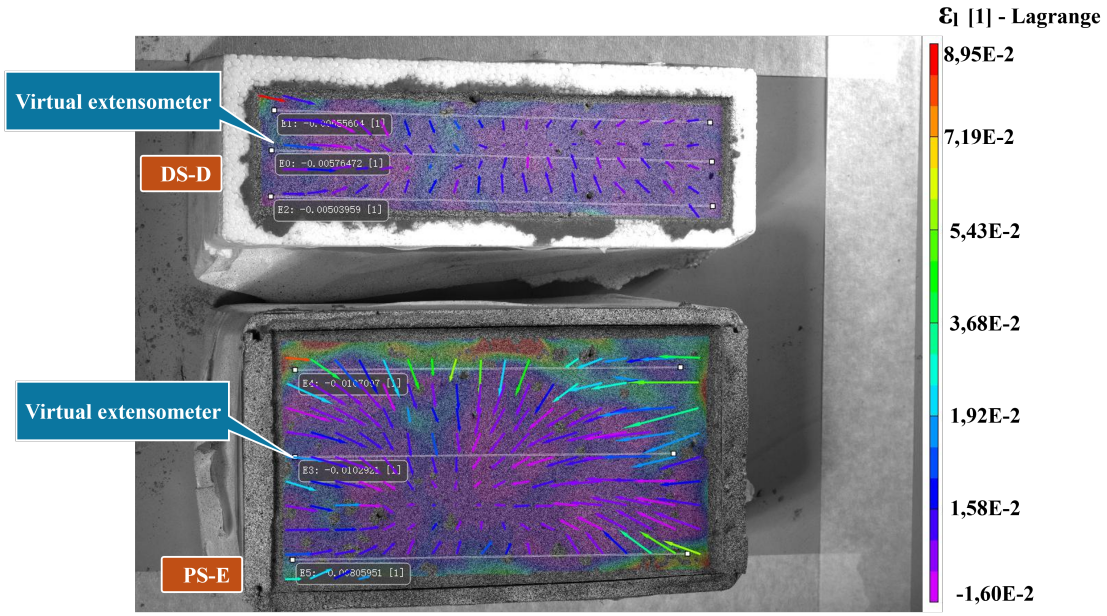

Figure 2.34: Strain vector distribution of specimens DS-D and PS-E analyzed by DIC

The color contours in Figure 2.34 represent the distribution of major principal strains, with warmer colors indicating higher tensile strain. Arrows depict local displacement vectors, providing insight into shrinkage directionality and intensity. While quantitative strain data were derived from virtual extensometers, the full-field DIC images qualitatively reveal the spatial heterogeneity of shrinkage, especially in PS-E.

Figure 2.35 shows the evolution of shrinkage strain alongside Vicat penetration results. The initial and final setting times were determined to be approximately 6.33 hours and 9.5 hours, respectively. By initial setting, DS-D exhibited a shrinkage of approximately $-500\,\mu\varepsilon$, while PS-E showed a much greater deformation of about $-6100\,\mu\varepsilon$. By final setting, PS-E reached approximately $-8000\,\mu\varepsilon$.

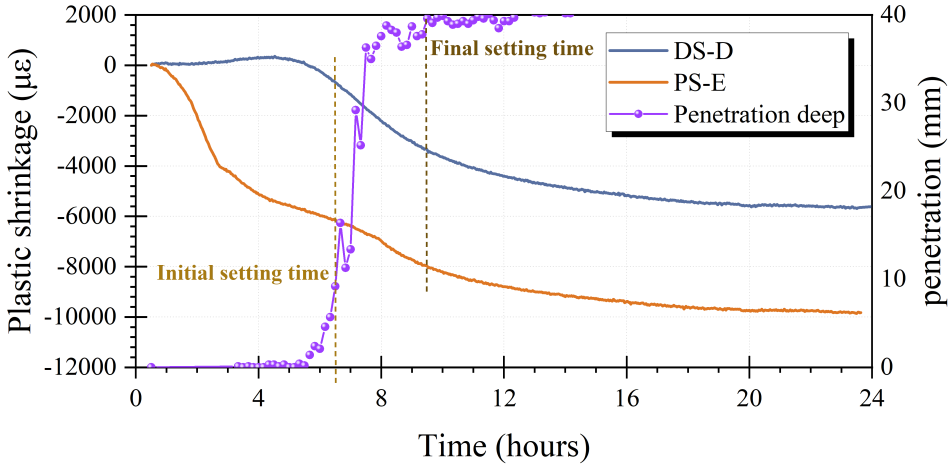

Figure 2.35: Plastic shrinkage evolution and setting time measured by Vicat needle penetration (EN 196-3, 2016)

These results indicate that the majority of shrinkage occurred **before the initial setting time**, when the geopolymer matrix remained fluid-like and exhibited negligible stiffness (i.e., Young's modulus ≈ 0). During this phase, strain accumulates due to particle settlement, water evaporation, and bleeding, but without significant stress development. Nonetheless, DIC measurements captured distinct zones of strain concentration in PS-E, suggesting that geometric features introduced by the mold induced localized deformation patterns.

Although stresses are not expected to develop in the pre-setting phase, the transition from fluid to solid may trap these strain gradients, giving rise to residual stress or microcracking upon early stiffening. This explains why visible cracking was observed in PS-E specimens despite most shrinkage occurring before setting. The ASTM-type mold thus proves more effective at amplifying plastic shrinkage effects and simulating field-relevant cracking scenarios.

Overall, the use of setting time as a reference frame helps isolate the critical shrinkage window, highlighting the importance of controlling deformation before the onset of structural buildup in geopolymer-based repair systems.

(2) Plastic shrinkage under different wind speeds

To evaluate the sensitivity of geopolymer mortar to ambient wind conditions during its plastic phase, shrinkage evolution was compared under three controlled wind speeds: 0, 2.7, and 4.0 $\mathrm{m/s}$, as shown in Figure 2.36. The setting time thresholds (initial setting at 6.33 h and final setting at 9.5 h) were referenced from previous Vicat penetration results.

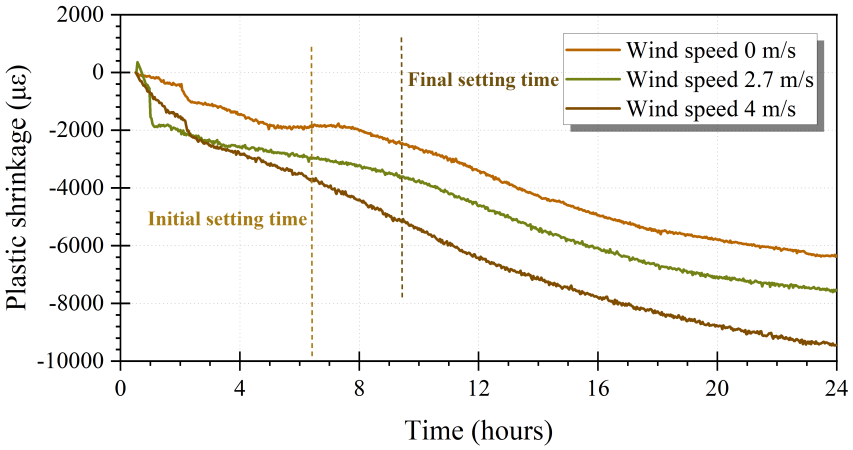

Figure 2.36: Plastic shrinkage under different wind speeds

The shrinkage strain exhibited a clear acceleration as wind speed increased. At the initial setting time, the specimen exposed to 0 $\mathrm{m/s}$ wind had undergone minor shrinkage (around $-1900\,\mu\varepsilon$), while specimens subjected to 2.7 and 4.0 $\mathrm{m/s}$ had already reached significantly higher shrinkage levels, up to approximately -3000 and $-3700\,\mu\varepsilon$, respectively.

This trend became even more pronounced by the final setting time. Specimens under 4.0 $\mathrm{m/s}$ wind experienced nearly double the cumulative shrinkage compared to those in still air. The increased evaporation rate under higher wind speeds likely intensified capillary pressure and surface tensile stress, accelerating deformation before the material gained sufficient rigidity. At the end of the 24-hour monitoring period, the cumulative plastic shrinkage values reached approximately -6000 , -7700 , and $-9500\,\mu\varepsilon$ for wind speeds of 0, 2.7, and 4.0 $\mathrm{m/s}$, respectively. This demonstrates a near-linear correlation between wind intensity and total early-age deformation. The 4.0 $\mathrm{m/s}$ group experienced nearly 60% more shrinkage than the still-air condition, confirming the critical role of evaporation-driven stress in geopolymer mortar settlement.

The results suggest that wind-induced evaporation is a critical factor in triggering plas-

tic shrinkage in geopolymer systems. Wind exposure not only amplifies early shrinkage magnitude but also shifts the shrinkage onset to earlier times. These findings reinforce the importance of environmental controls—especially airflow regulation—during the vulnerable early-age phase of geopolymer casting.

5 Conclusion

This chapter presented a comprehensive evaluation of potassium-activated metakaolin-based geopolymer mortar, focusing on its potential as a repair material for concrete substrates. The study examined fresh properties, mechanical behavior, transport characteristics, shrinkage performance, and the use of advanced monitoring tools. Key conclusions are as follows:

1. Fresh-State Performance

The mortar exhibited good flowability and appropriate setting times (initial: 380 min; final: 570 min), confirming its practical suitability for casting and encapsulation in repair applications.

2. Mechanical Properties

- A 14-day flexural strength of 7.86 MPa exceeded typical OPC values, while compressive strength reached 21.26 MPa with a lower stiffness (9.80 GPa).
- The material displayed ductile, gradual post-peak behavior—advantageous for stress redistribution when bonded to concrete substrates.

3. Transport Characteristics

- Gas permeability decreased significantly under saturation, with intrinsic permeability measured as $7.32 \times 10^{-17}\ \mathrm{m}^2$ (Klinkenberg-corrected).
- Porosity measured by gas expansion averaged $26.87 \pm 1.12\%$, reflecting high pore connectivity typical of alkali-activated materials.

4. Shrinkage Behavior

- Drying shrinkage developed rapidly within the first 7 days (up to $-2500\ \mu\varepsilon$), while early-age deformation exceeded $-6600\ \mu\varepsilon$ as captured by DIC.
- Wind exposure intensified plastic shrinkage (e.g., $-9500\ \mu\varepsilon$ at 4.0 m/s), and notch molds (ASTM C1579-type) effectively amplified localized deformation and cracking.

5. DIC Monitoring

Digital Image Correlation enabled full-field, real-time tracking of shrinkage and strain localization—highlighting behaviors not captured by conventional methods and supporting early cracking assessment.

In summary, the tested geopolymer mortar demonstrated favorable fresh and hardened-state performance, manageable shrinkage, and robust transport resistance. These material-level insights lay the foundation for subsequent analysis of interfacial behavior with concrete substrates.

CHAPTER 3

Experimental Investigation of Geopolymer-Concrete Interfaces

1 Introduction

The experimental investigations presented in Chapter 2 provided a comprehensive characterization of the physical and mechanical properties of geopolymer mortar, establishing its potential as a repair material. However, those tests focused solely on the bulk behavior of the material itself and did not address the performance of the critical interface between geopolymer and concrete substrates. Moreover, the preliminary shear tests conducted without confinement (see Section 2) revealed important limitations: most failures occurred within the concrete substrate rather than along the interface, and no information was obtained regarding the permeability evolution during loading.

These findings highlight the necessity of a more advanced experimental approach capable of capturing the true interfacial behavior under service-like conditions. In practical repair scenarios, interfaces are often subjected to moderate confining pressures and exposed to moisture. Hence, both the shear strength and sealing capacity of the interface are essential to the long-term durability of the repaired system. Yet, existing literature rarely addresses the coupled shear–permeability behavior of geopolymer–concrete interfaces under confinement. Furthermore, the effects of surface roughness and aggregate size on this coupling remain poorly quantified.

To address these gaps, this chapter develops a refined test protocol to assess the hydro-mechanical response of geopolymer–concrete interfaces under constant confining pres-

sure. The specific objectives are: (i) to measure the shear strength and permeability evolution under 3 MPa confinement, (ii) to investigate the influence of surface morphology and aggregate gradation (fine vs. coarse) on the coupled interface behavior, and (iii) to employ standardized 3D roughness characterization (ISO 25178) to link micromechanical morphology with macroscopic hydro-mechanical performance.

The chapter is organized as follows. The next section revisits the unconfined shear test results and motivates the development of the confined experimental program. The following section details the specimen design, surface preparation procedures, and the modified direct shear apparatus. Then, the experimental results on shear strength and permeability evolution are presented and discussed, with a particular focus on the role of surface roughness. Finally, the last section summarizes the key findings of this chapter.

2 Preliminary tests and methods

To evaluate the bonding performance between geopolymer mortar and conventional concrete, a series of preliminary experiments were conducted under unconfined conditions.

2.1 Preparation of Geo-con samples

Six cylindrical concrete specimens, each measuring 30 mm in height and 65 mm in diameter, were prepared for the tests. A central cylindrical cavity with a diameter of 20 mm was drilled longitudinally through each specimen. Rubber pads were positioned at the base of these cavities to provide a consistent interface layer. Geopolymer mortar was then prepared following a standardized mixing procedure and poured into the cavities atop the rubber pads, forming geopolymer cores within the concrete matrix. Two core heights were investigated: 10 mm and 15 mm. For each height, three specimens were produced, as illustrated in Figure 3.1. The specimens with 10 mm geopolymer cores were labeled PS-10 mm-17, PS-10 mm-21, and PS-10 mm-20, while those with 15 mm cores were designated PS-15 mm-23, PS-15 mm-3, and PS-15 mm-16. This configuration was selected to systematically assess the influence of core height on the bonding behavior at the geopolymer-concrete interface.

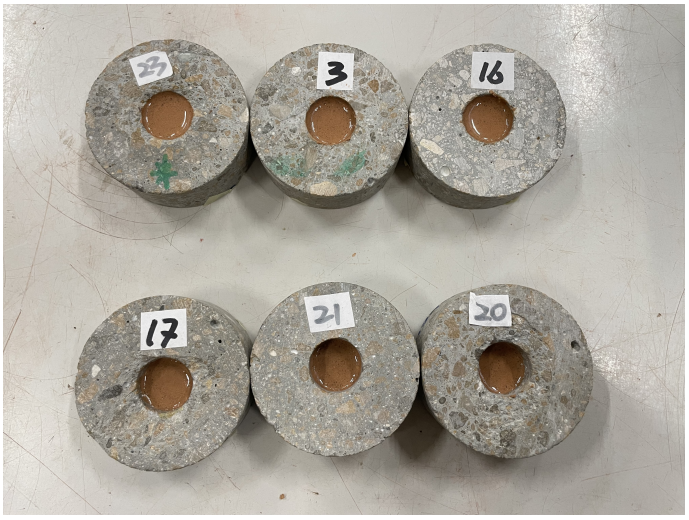

Figure 3.1: Geo-con samples after preparation

After casting, all specimens were cured in a controlled environment at 20°C and 90% relative humidity for seven days to ensure consistent hydration and material properties prior to testing.

2.2 Shear testing of the interface

Interfacial shear strength was measured using a Zwick/Roell Z250 universal testing machine, following the methodology described by Briffaut et al. (2024). A stainless steel piston with a diameter $D = 9.9$ mm was employed to apply an axial load directly to the geopolymer core (see Figure 3.2(a)). The loading rate was maintained at 0.12 mm/min. A steel ring was placed around the specimen to maintain alignment and constrain lateral movement. The test configuration, depicted schematically in Figure 3.2(b), enabled the determination of the shear strength τ at the interface, calculated as follows:

$$\tau = \frac{F_{\text{max}}}{A} \tag{3.1}$$

where A is the interfacial area. The area A is determined by the equation:

$$A = \pi \times D \times H \tag{3.2}$$

Here, D represents the diameter and H the height of the cylindrical interface.

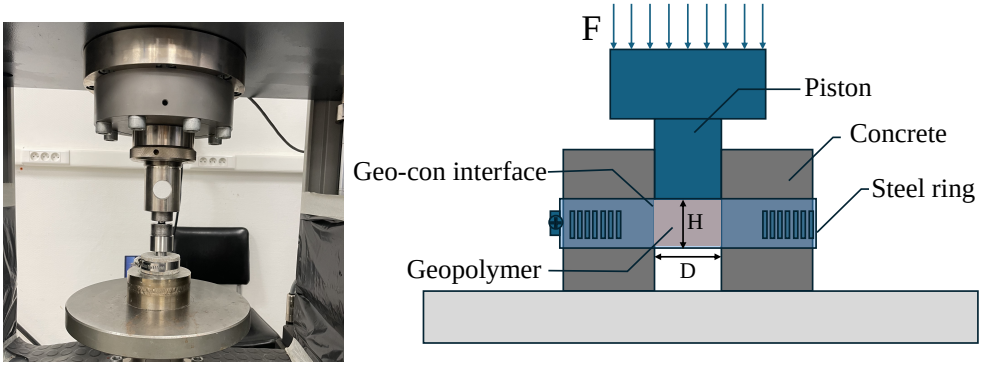

(a) Shear strength test device **(b)** Shear strength test schematic diagram

Figure 3.2: Shear test setup and schematic of geo–con interface

2.3 Results and discussion

Figure 3.3 displays the shear strength profiles for the tested specimens. Panels (a), (b), and (c) correspond to specimens with a 10 mm geopolymer core, while panels (d), (e), and (f) represent specimens with a 15 mm core.

For the 10 mm core specimens, PS-10 mm-17 exhibited the highest peak shear strength at 2.71 MPa, indicative of a strong interfacial bond capable of withstanding significant stress prior to failure. The rapid increase and subsequent abrupt decrease in the load-displacement curve for this specimen suggest brittle failure behavior. In contrast, PS-10 mm-20 and PS-10 mm-21 reached lower peak shear strengths and displayed more gradual post-peak declines, which may reflect either weaker interfacial bonding or the presence of microcracking that initiated at lower stress levels.

For the 15 mm core specimens, PS-15 mm-03 demonstrated a progressive increase in shear strength, attaining a maximum of 2.21 MPa, which reflects robust bonding at the interface. PS-15 mm-16 reached a peak shear strength of 1.78 MPa, with minor fluctuations observed after peak loading, potentially indicating localized yielding or microstructural adjustments. PS-15 mm-23 achieved a peak shear strength of 2.64 MPa, but the curve exhibited significant fluctuations post-peak, suggesting cyclic micro-failures and subsequent redistribution of stresses.

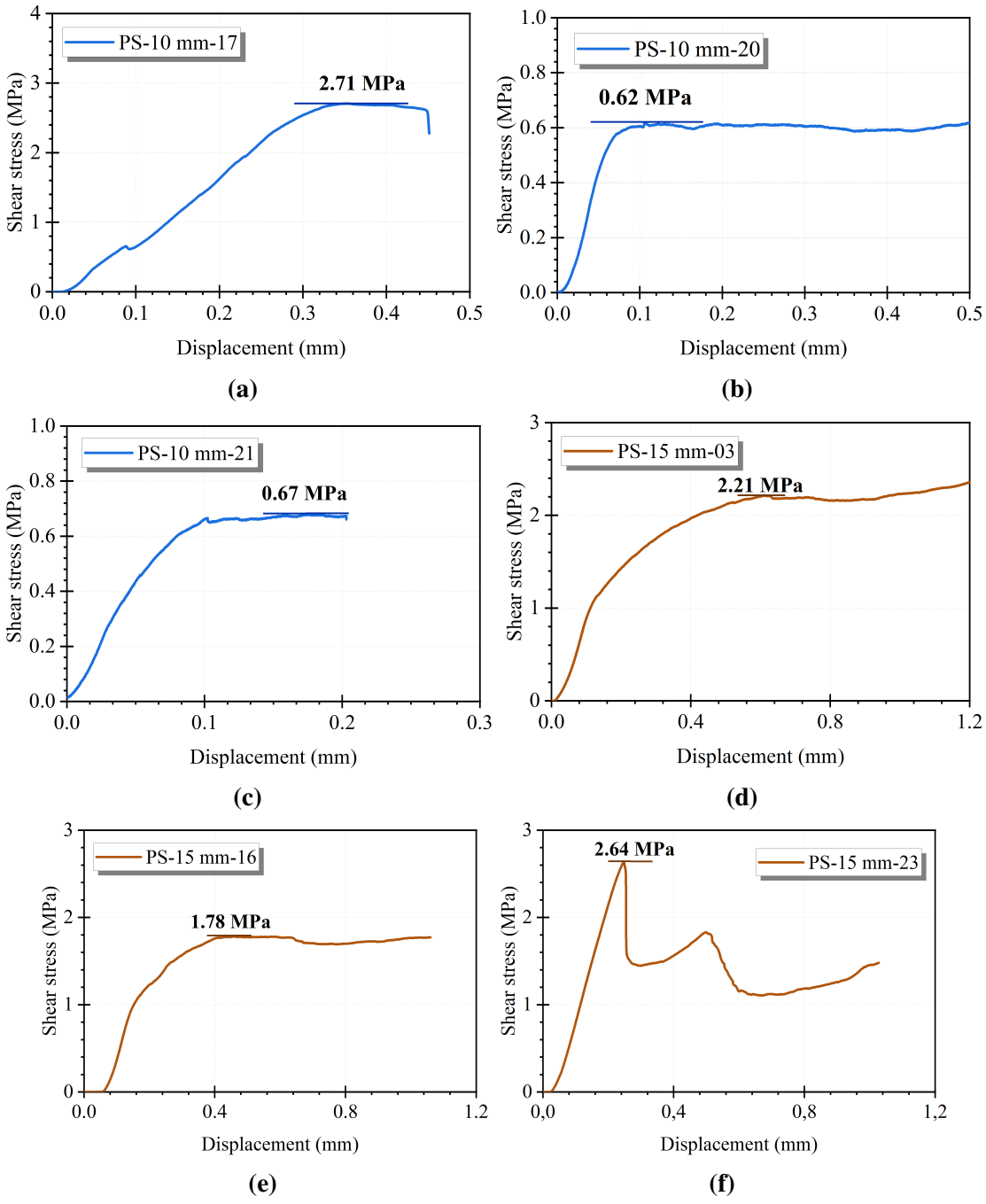

Figure 3.3: Shear strength preliminary test shear displacement curve of geo-con interface

Figure 3.4 shows post-test images of the specimens, highlighting the development of cracks in the concrete following shear loading. During testing, the central piston applies a concentrated axial force to the geopolymer core and the surrounding interface. As the applied shear stress exceeds the bond strength or the intrinsic shear strength of the ma-

terials, cracks initiate either at the interface or within the concrete matrix. The location and propagation of these cracks provide insights into whether the failure is governed by interfacial debonding or by the mechanical properties of the concrete itself.

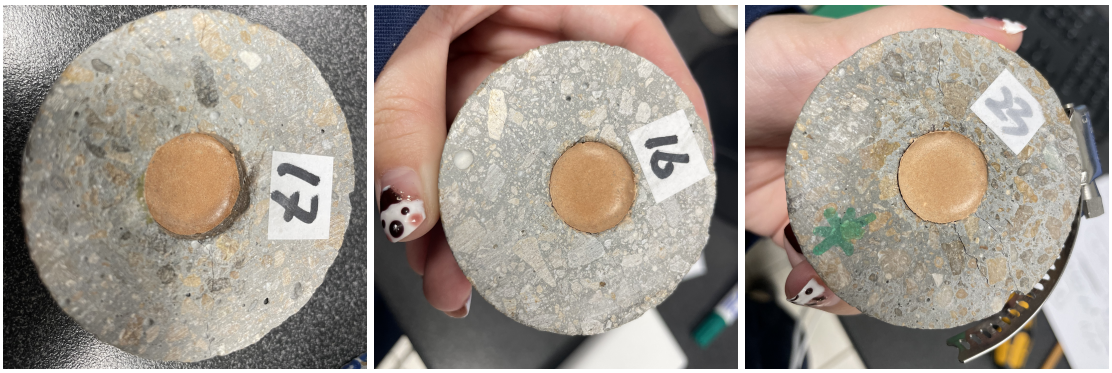

Figure 3.4: Photographs of geo-con specimens with cracks on concrete part following shear testing

2.4 Conclusion and adjustments

The results indicate that the geo-con interface can achieve substantial bonding strength, supporting its potential application in structural repair contexts. However, several limitations were identified in the experimental approach. The occurrence of cracks within the concrete matrix may have led to an underestimation of the true interfacial shear strength. Additionally, the absence of confining pressure in the current setup limits the generalizability of the findings to field conditions where such constraints are present.

Future work should focus on refining the experimental protocol to address these limitations, including the incorporation of confining pressure and the use of non-destructive evaluation techniques to monitor crack initiation and propagation during testing.

3 Hydro-mechanical behaviour under shear loading

To better replicate field-relevant conditions and overcome the limitations identified in the unconfined tests—such as premature failure in the concrete matrix and lack of permeability control—a modified direct shear testing setup was developed. This setup allows for simultaneous monitoring of shear strength and fluid permeability under a constant confining pressure of 3 MPa.

The experimental campaign presented in this chapter explores how surface roughness and aggregate interlock affect interfacial behavior, and provides a comprehensive analysis of the coupled evolution of shear stress and permeability during loading. The findings serve to deepen the understanding of failure mechanisms and transport characteristics at geo–con interfaces, with direct implications for the durability and reliability of structural repairs.

3.1 Materials and Methods

3.1.1 Materials

(1) Concrete substrates

Two types of ordinary Portland cement (OPC) concrete substrates were used to investigate the effect of aggregate grading on interfacial behavior: one containing fine aggregates only, and the other incorporating coarse aggregates. Both concrete types were cast and cured in large blocks at the Centrale Lille Laboratory under standard conditions.

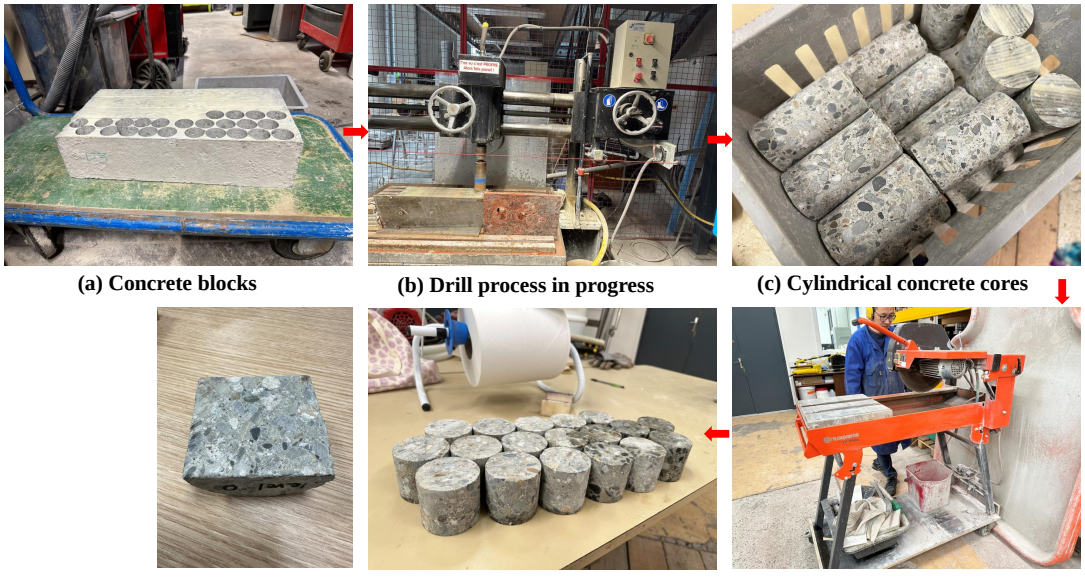

Figure 3.5: Preparation of cylindrical and half-cylindrical concrete specimens from large cast blocks

Cylindrical core specimens with a diameter of 65 mm were extracted from the concrete blocks using a rotary core drilling machine. These cores were then sectioned into

segments of 60 mm height using a precision saw. Depending on the experimental purpose, both full cylindrical and half-cylindrical specimens were prepared: the former were used for standalone concrete control tests, while the latter served as the substrate for geo-con interface formation.

The preparation workflow, including drilling and cutting procedures, is illustrated in Figure 3.5, while Figure 3.6 shows the specimens awaiting shear strength and permeability testing.

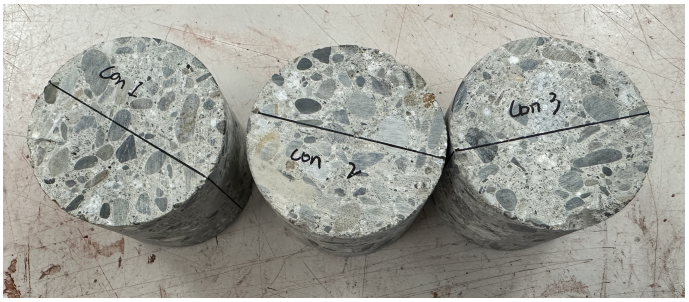

Figure 3.6: Concrete specimens for shear strength and permeability tests

(2) Geopolymer mortar

The material preparation method and the specific formulas have been extensively detailed in **Section 2.1.2**. Following the same procedures, specimens measuring 65 mm in diameter and 60 mm in height were cast. After curing for 14 days in the curing machine under 20°C and 90% relative humidity. After demolding, the ends of the specimens were meticulously leveled using a grinding machine to ensure uniform surface flatness. This standardization is crucial for achieving consistent contact surfaces in subsequent experimental evaluations. The specimens are shown in Figure 3.7.



Figure 3.7: Geopolymer specimens for shear and permeability test

(3) Geopolymer-concrete specimens

Half-cylindrical concrete blocks were strategically placed along the edges within pre-prepared molds, designated for casting geopolymer mortar into the remaining half-cylindrical voids. After demolding, the ends of these composite specimens were carefully leveled using a grinding machine to ensure uniformity of the contact surfaces. The specimens were then cured for 14 days before testing. Each specimen maintained a diameter of 65 mm and a height of approximately 60 mm, comprising one geopolymer-concrete interface. The preparation process is illustrated in the accompanying Figure 3.8, providing a visual representation of each step.



(a) Smooth surface of concrete cylinder (b) Specimens' preparation (c) Specimens to be sheared after grinding

Figure 3.8: Processes involved in preparing concrete specimens

3.1.2 Roughness and quantification

(1) Interface category

To investigate the influence of surface morphology on the interfacial behavior between geopolymer and concrete, four levels of surface roughness were introduced on

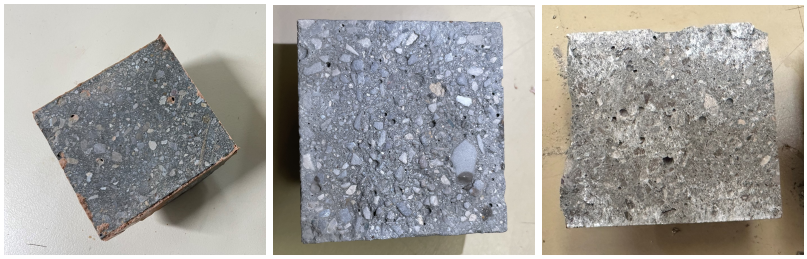

(a) Smooth **(b)** Rough Level 1 **(c)** Rough level 3

Figure 3.9: Fine aggregate concrete half-cylinder specimens with different roughness

half-cylindrical concrete specimens prior to casting the geopolymer. These levels were applied to both fine and coarse aggregate concrete substrates and are classified as follows:

Smooth Level 0 (L0). The reference interface was obtained by cutting full cylindrical concrete cores into half-cylindrical specimens using a precision saw. The freshly cut surfaces were used directly for geopolymer casting without additional surface treatment, representing a smooth, baseline condition with minimal mechanical interlock.

Rough Level 1 (L1). A light sandblasting technique was applied to the cut surfaces of the half-cylindrical specimens to induce moderate surface texture. This treatment aimed to simulate a controlled increase in roughness while maintaining overall surface integrity.

Rough Level 2 (L2). A more aggressive sandblasting procedure was employed to generate higher levels of surface asperity, representing a coarse-textured interface. This level is expected to enhance mechanical interlocking and alter the stress distribution along the interface.

Rough Level 3 (L3). The highest roughness level was obtained by subjecting full cylindrical concrete specimens to direct shear loading, causing failure along the mid-plane. The resulting fracture surfaces were irregular and highly textured, thus representing a mechanically generated rough interface with random morphology.

Figure 3.9 shows representative images of the four roughness levels on fine aggregate concrete, while Figure 3.10 presents the corresponding textures for coarse aggregate concrete substrates.

(2) Roughness quantification

In this study, the surface roughness of the geopolymer–concrete interface was quantified through 3D scanning using the Alicona Imaging System. Focus was placed on coarse



(a) Smooth **(b)** Rough Level 1 **(c)** Rough level 2 **(d)** Rough level 3

Figure 3.10: Coarse aggregate concrete half-cylinder specimens with different roughness

aggregate concrete surfaces, as these specimens provided more pronounced texture suitable for interfacial characterization.

High-resolution 3D surface topography scans were acquired on selected concrete specimens, as shown in Figure 3.11. These scans allowed for visualization and analysis of microstructural features such as aggregate exposure, surface pits, and ridges, all of which influence the mechanical interlocking and permeability of the interface.

Surface roughness was evaluated using parameters defined by ISO 25178. Among these, the arithmetic mean height (S_a) was used as the representative indicator of surface roughness. The S_a value is defined as the average absolute deviation from the mean surface plane and is commonly used to assess mechanical adhesion potential. As a scale-independent and widely recognized metric, S_a facilitates both comparative evaluation and quantitative correlation with shear and permeability results.

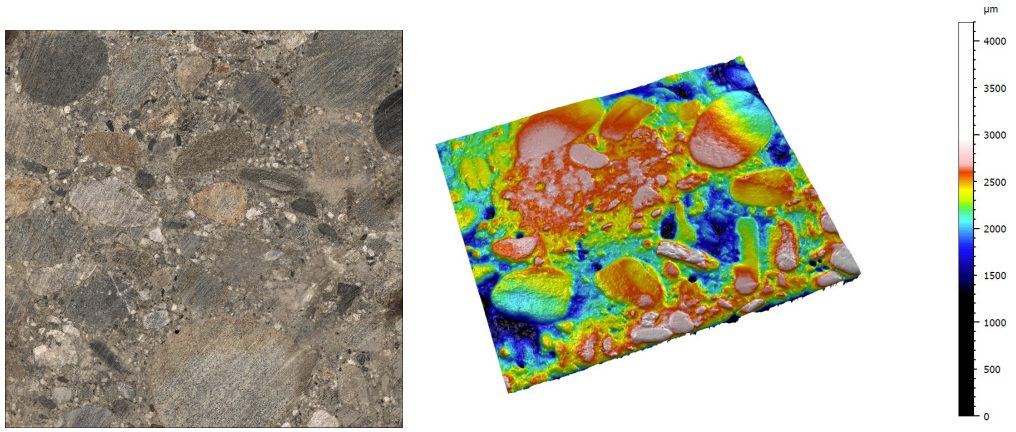

(a) Concrete texture **(b)** 3D topographical map of concrete surface

Figure 3.11: Concrete surface: texture and 3D topographical visualization

3.1.3 Experimental setup

(1) Direct Shear Apparatus

The experimental apparatus consists of four integrated modules designed for coupled shear and permeability testing, as shown in Figure 3.12. The system enables the application of a constant confining pressure of 3 MPa to localize shear at the geopolymer–concrete interface and to facilitate permeability measurements during loading.

The first module is the loading and control system, comprising a materials testing machine, TestControl II electronics, and TestXpert III software. It ensures stable displacement-controlled loading and synchronizes high-resolution acquisition of force and displacement data across all channels.

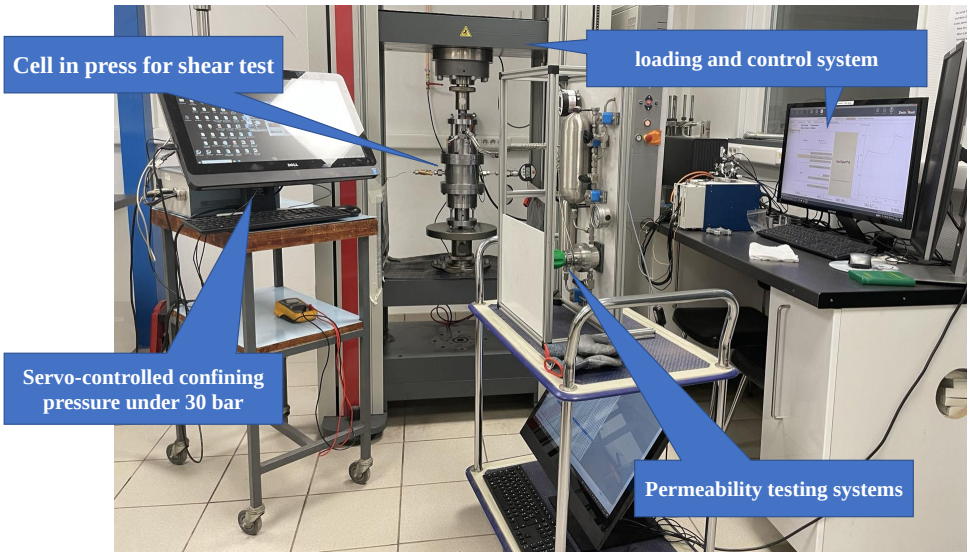

Figure 3.12: Photograph of the shear strength and permeability test apparatus

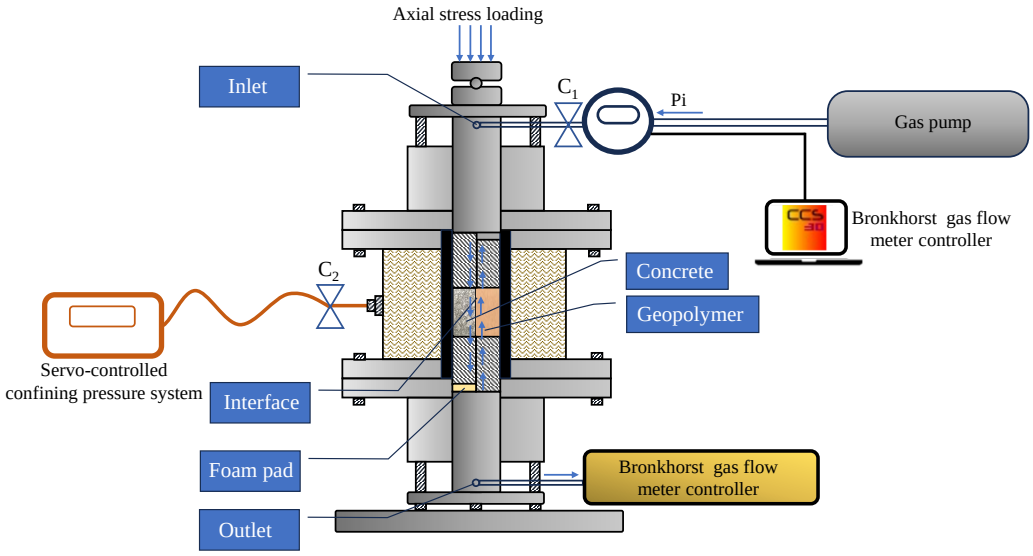

Figure 3.13: Schematic diagram of the shear cell under confining pressure

The second module is the shear cell, illustrated in Figure 3.13, which transmits axial load and ensures interface shearing. Vertical force is applied via stainless steel semi-cylindrical pistons placed above and below the specimen. A compressible foam pad is positioned beneath one side to promote relative sliding, thereby enabling shear concentration at the interface. The specimen is enclosed in a Viton-type EPDM sleeve that ensures sealing and uniform application of confining pressure perpendicular to the axial load.

The third module is a servo-controlled confining pressure system (MiniPompe), which dynamically maintains the confining pressure at 3 MPa throughout the test.

The fourth module integrates a gas permeability testing system. A Bronkhorst flow meter and gas injection circuit allow continuous permeability monitoring during shear. Darcy's law is used to interpret flow behavior, with sealing achieved by aerosol foam to ensure airtight conditions. Permeability is assumed to occur exclusively at the interface, which is the weakest zone in the specimen assembly.

(2) Testing protocol

All experiments were conducted under displacement control with a loading rate of $0.12\,\mathrm{mm/min}$. This rate was selected to ensure quasi-static conditions and minimize

inertial effects during shear loading.

Permeability measurements were carried out at regular displacement intervals of $0.2\,\mathrm{mm}$. Prior to testing, aerosol foam was applied at all critical connections to ensure gas-tight sealing. The confining pressure was established before loading and continuously maintained at 3 MPa using a servo-regulated MiniPompe system.

Permeability data were collected throughout the shear process. Measurements were divided into two stages: before failure, pressure decay at the inlet was monitored over time; after failure, rapid leakage required the use of a Bronkhorst gas flow controller to measure outlet flow rate. These measurements enabled characterization of transport behavior across the interface during the entire deformation process.

3.1.4 Shear stress and permeability calculation

(1) Shear stress calculation

To quantitatively interpret the experimental results obtained from shear tests, the following parameters have been defined: The average tangential stress applied to the interface surface, referred to as shear stress, is denoted by τ. This is calculated by dividing the axial force F exerted by the interface area. Mathematically, it is expressed as:

$$\tau = \frac{F}{A} \tag{3.3}$$

where τ represents the shear stress, F is the axial force, and A is the area of the interface. The shear strength refers to the stress at the point of maximum force during the shearing process. where A is the interfacial area. The area A is determined by the equation:

$$A = D \cdot H \tag{3.4}$$

Here, D represents the diameter and H the height of the cylindrical specimen.

(2) Permeability calculation

Calculation method. The permeability K was calculated using a modified form of Darcy's law for gas flow through the interface. Prior to the onset of interface failure and when permeability is low, the differential air pressure was calculated at the intake.

The barometer was connected to a computer to systematically record the air pressure at each instance using the testXpert III software, with recordings made every second. During the test procedure, the argon gas valve labeled C1 was opened. Once the air pressure stabilized, the system continuously recorded the drop in permeation pressure from P_1 to P_2 at corresponding specimen times t_1 and t_2. Therefore, the initial pressure P_{intial} and the final pressure P_{final} are recorded at atmospheric pressure and calculated according to the following formula.

$$P_{\text{intial}} = P_1 + P_0 \tag{3.5}$$

$$P_{\text{final}} = P_2 + P_0 \tag{3.6}$$

Here, P_0 denotes the atmospheric pressure at the outlet, established at one atmosphere (atm), which serves as the reference pressure for the experiment.

In the experimental setup, the average pressure, denoted as P_{moy}, is calculated by taking the arithmetic mean of the initial and final pressure readings. The formula for calculating P_{moy} is as follows:

$$P_{\text{moy}} = \frac{P_{\text{initial}} + P_{\text{final}}}{2} \tag{3.7}$$

In the experimental context, the variable Q_{moy} represents the flow rate, which is a critical parameter for evaluating fluid dynamics within the system. The flow rate Q_{moy} was then accurately deduced in Equation (3.8).

$$Q_{\text{moy}} = \frac{V\Delta P}{P_{\text{moy}}\Delta t} = \frac{V(P_{\text{initial}} - P_{\text{final}})}{P_{\text{moy}}(t_2 - t_1)} \tag{3.8}$$

Here, ΔP is the pressure differential measured in pascals (Pa). V is the volume of Argon gas affected by the pressure change, measured in cubic meters (m^3). Two distinct volumes for V are employed to adapt to varying permeability conditions. When the permeability is sufficiently high to allow for accurate measurements, a larger volume of 294.94 ml is used. Conversely, when the permeability is too low to be effectively measured with the larger volume, the volume is reduced to 36.81 ml to enhance measurement efficiency. Δt is the time interval over which the pressure change occurs, measured in seconds (s).

Finally, based on the established relationships, the permeability can be expressed as shown in Equation (3.9).

$$K = \frac{\mu \cdot Q_{\text{moy}} \cdot 2 \cdot H \cdot P_{\text{moy}}}{A \cdot ((P_{\text{moy}})^2 - P_0^2)} \tag{3.9}$$

while the variable μ represents the viscosity of the gas, with a value of 2.20×10^{-5} Pa s. The variable H denotes the height of the specimen, measured in meters (m). The variable A represents the interface area of the geo-con, calculated as the product of the specimen's diameter D and height H, effectively encapsulating the contact surface area between the geo-con materials and the testing environment.

Direct reading method. During the experiment, after the peak shear stress is achieved and the material failure occurs, significant argon gas permeation is observed. At this point, stable pressure readings within the specified time become unattainable due to the extensive gas flow. To address this challenge and ensure accurate data collection, a flowmeter is installed at the outlet. This setup allows for the direct measurement of the flow rate, denoted as Q_{out}, Simultaneously, the value of the barometer, P_{i}, is recorded. Based on the established relationships, the permeability can be expressed as shown in Equation (3.10).

$$K = \frac{\mu \cdot Q_{\text{out}} \cdot 2 \cdot H \cdot P_{\text{in}}}{A \cdot ((P_{\text{in}})^2 - P_0^2)} \tag{3.10}$$

Here, P_{in} represents the inlet pressure, calculated using the formula under atmospheric conditions:

$$P_{\text{in}} = P_{\text{i}} + P_0 \tag{3.11}$$

3.1.5 Testing program

To investigate the influence of surface roughness and substrate composition on the hydro-mechanical behavior of geopolymer–concrete interfaces, a comprehensive experimental matrix was established, as summarized in Table 3.1.

The testing program comprises three main groups:

- **Group 1 – Fine aggregate concrete + geopolymer (Geo-con interface):** This group includes specimens with three levels of interface roughness: smooth (L0), sandblasted (L1), and shear-induced (L3), each bonded to geopolymer. All specimens are formed by bonding a half-cylinder of fine aggregate concrete with a half-cylinder of geopolymer mortar.

- **Group 2 – Coarse aggregate concrete + geopolymer (Geo-con interface):** This group includes four roughness levels (L0 to L3), with three replicates each (except L3 with two replicates). Similar to Group 1, all specimens were prepared by bonding geopolymer onto the surface of coarse aggregate concrete.
- **Group 3 – Monolithic reference materials (No interface):** This group serves as control. It includes complete cylindrical specimens made solely of fine aggregate concrete (F-CON), coarse aggregate concrete (C-CON), and geopolymer mortar (G-GEO), without any bonded interface.

Table 3.1
Experimental matrix for shear and permeability tests at geopolymer–concrete interfaces

Group	Specimen ID	Number	Roughness	Materials	Interface
1	F-L0	1	L0	Fine aggregate concrete + geopolymer	Geo-con
	F-L1	1	L1		
	F-L3	1	L3		
2	C-L0	3	L0	Coarse aggregate concrete + geopolymer	Geo-con
	C-L1	3	L1		
	C-L2	3	L2		
	C-L3	2	L3		
3	F-CON	1	–	Fine aggregate concrete	No interface
	C-CON	3	–	Coarse aggregate concrete	
	G-GEO	3	–	Geopolymer	

This matrix allows systematic evaluation of the coupled shear–permeability response at geopolymer–concrete interfaces, accounting for both the nature of the substrate (fine vs. coarse aggregates) and the interface surface morphology.

3.2 Results

3.2.1 Surface roughness characterization

To evaluate the interfacial morphology of geopolymer–concrete interfaces, the surface roughness of the concrete substrates was quantified using a 3D optical scanning method. The roughness of each specimen was expressed by the arithmetic mean height (S_a) parameter in accordance with ISO 25178. Concrete substrates were prepared with three levels of surface roughness: smooth (L0), sandblasted (L1 and L2), and shear-induced (L3).

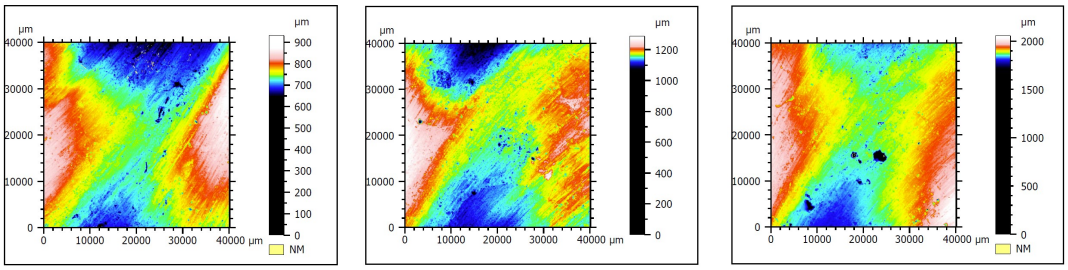

(a) C-L0-1: 60.20 µm **(b)** C-L0-2: 26.44 µm **(c)** C-L0-3: 38.56 µm

Figure 3.14: 3D roughness scans of smooth coarse aggregate concrete surfaces (L0)

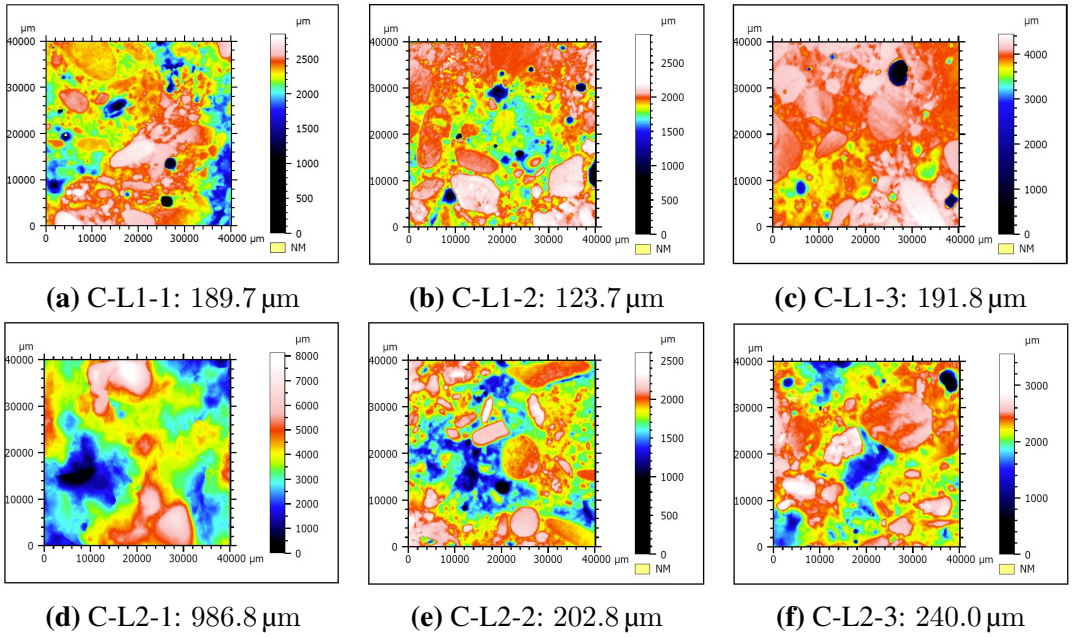

(a) C-L1-1: 189.7 µm **(b)** C-L1-2: 123.7 µm **(c)** C-L1-3: 191.8 µm

(d) C-L2-1: 986.8 µm **(e)** C-L2-2: 202.8 µm **(f)** C-L2-3: 240.0 µm

Figure 3.15: 3D roughness scans of sandblasted concrete surfaces (L1 and L2)

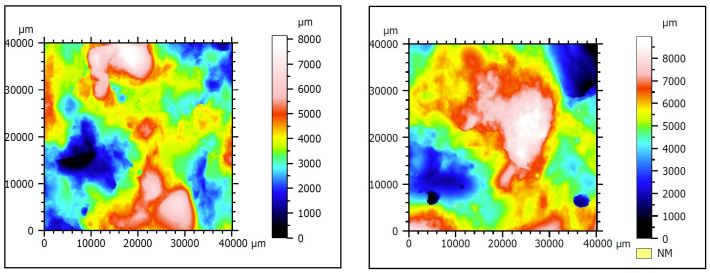

(a) C-L3-1: 1270 µm **(b)** C-L3-2: 979.6 µm

Figure 3.16: 3D roughness scans of shear-fractured concrete surfaces (L3)

Figure 3.14 presents the 3D topographical maps of smooth coarse aggregate concrete surfaces (Level 0). The measured S_a values range from $26.44\,\mu\text{m}$ to $60.20\,\mu\text{m}$, indicating minimal surface asperities and nearly planar bonding areas.

Figure 3.15 shows the 3D roughness scans of concrete surfaces subjected to two levels of sandblasting. The specimens of Level 1 (L1) display S_a values ranging from $123.7\,\mu\text{m}$ to $191.8\,\mu\text{m}$, while Level 2 (L2) surfaces exhibit higher variability, with S_a values from $202.8\,\mu\text{m}$ to $986.8\,\mu\text{m}$. These results indicate increased asperity and surface complexity compared to L0.

Finally, Figure 3.16 displays surfaces formed through shear-induced fracture (L3). These interfaces exhibit the highest roughness, with S_a values up to $1270\,\mu\text{m}$, reflecting pronounced macro-asperities and a highly irregular profile due to mechanical splitting.

3.2.2 Interface shear and permeability response

This section presents and analyzes the results of coupled shear and gas permeability tests performed on geopolymer–concrete interfaces. For each specimen, the left panel in the figures shows the evolution of shear stress and gas permeability (K) with increasing displacement under constant confining pressure, while the right panel displays photographs of the specimen's fractured cross-section after testing.

Based on the concrete substrate type and interface characteristics, the results are grouped into three main interface categories:

(1) Fine aggregate con–geo interfaces (F-L0, F-L1, F-L3)

Figure 3.17 presents the coupled evolution of shear stress and gas permeability (K) for fine aggregate concrete–geopolymer interface specimens with different surface roughness levels. Each subplot displays the shear response (left) and post-failure interface morphology (right) for F-L0 (smooth), F-L1 (moderately rough), and F-L3 (highly roughened).

The smooth interface (F-L0) exhibited the lowest peak shear strength at $4.81\,\mathrm{MPa}$, followed by gradual post-peak softening. In comparison, F-L1 with sandblasted roughness reached a higher strength of $5.76\,\mathrm{MPa}$. The F-L3 specimen, prepared via shear preloading, showed the highest peak strength of $10.41\,\mathrm{MPa}$.

Permeability behavior also varied with roughness. F-L0 and F-L1 showed a sudden rise in K shortly after peak stress, indicating early decohesion and gas pathway formation. For F-L3, the K increase was delayed and occurred during the post-peak stage, suggesting that rougher surfaces enhance mechanical interlock and postpone permeability transitions.

These results highlight the reinforcing effect of surface roughness on interfacial shear strength and indicate a strong coupling between damage evolution and gas permeability in fine aggregate-based geopolymer–concrete interfaces.

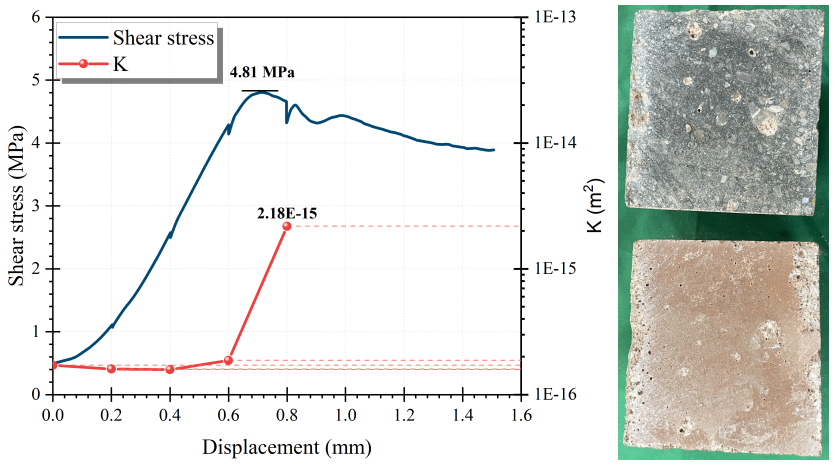

(a) Shear stress and K of F-L0

(b) F-L0

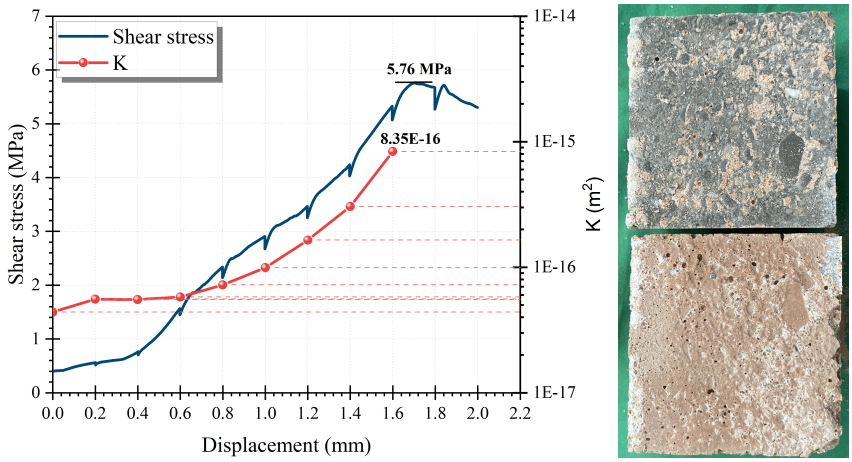

(c) Shear stress and K of F-L1

(d) F-L1

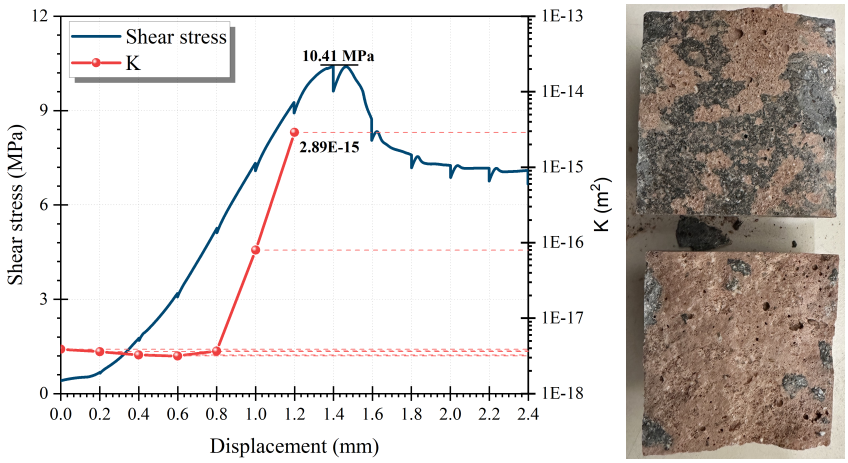

(e) Shear stress and K of F-L3

(f) F-L3

Figure 3.17: Coupled evolution of shear stress and permeability for fine aggregate geo-con interfaces with different surface roughness levels

(2) Coarse aggregate con–geo interfaces (C-L0, C-L1, C-L2, and C-L3)

Figure 3.18, Figure 3.19, Figure 3.20, and Figure 3.21 illustrate the mechanical and permeability responses of coarse aggregate concrete–geopolymer (con–geo) interfaces under shear. The left panels in each figure depict the evolution of shear stress and gas permeability (K) with displacement, while the right panels display the post-failure cross-sectional morphologies.

The C-L0 specimens, featuring smooth interfaces, demonstrate relatively low peak shear strength values ranging from 5.49 MPa to 6.68 MPa. The permeability increase initiates early and evolves progressively during loading, often prior to peak stress. This indicates a weak interfacial bond and limited mechanical interlock, leading to rapid crack initiation and gas pathway formation.

In comparison, the sandblasted interfaces (C-L1 and C-L2) show enhanced bonding performance. For C-L1, the peak shear strength rises to the range of 6.86–7.32 MPa, accompanied by a delayed and more gradual increase in K, suggesting improved resistance to debonding. The C-L2 specimens perform even better, with peak stresses of 7.02–9.03 MPa and lower post-peak permeability. The curves exhibit broader peaks and smoother transitions, indicating more energy dissipation and crack bridging due to higher roughness.

For the most heavily roughened interfaces (C-L3), the maximum shear strength reaches 12.11 MPa, the highest among all specimens. However, the permeability rises sharply post-peak, as observed in C-L3-1 and C-L3-2, implying that while peak strength is maximized, crack networks through the geopolymer matrix develop more prominently.

In summary, increasing surface roughness significantly improves interfacial shear strength and delays permeability onset, especially from smooth (C-L0) to moderately rough (C-L2) conditions. However, overly rough surfaces (C-L3) may promote post-peak cracking into the geopolymer body, causing abrupt increases in permeability.

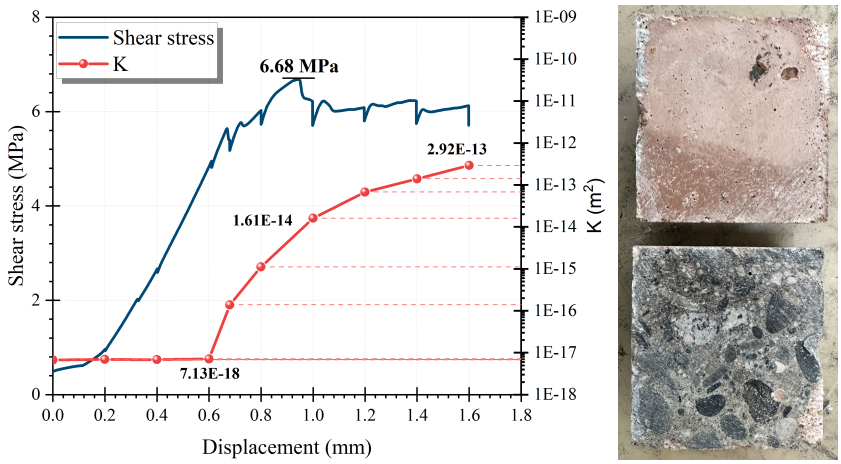

(a) Shear stress and K of C-L0-1

(b) C-L0-1

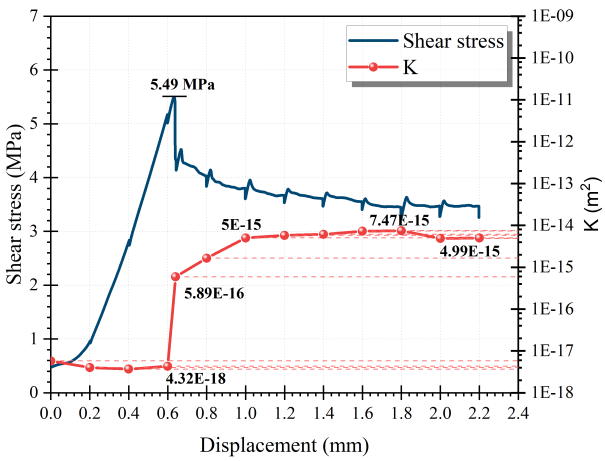

(c) Shear stress and K of C-L0-2

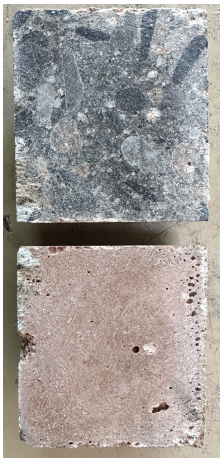

(d) C-L0-2

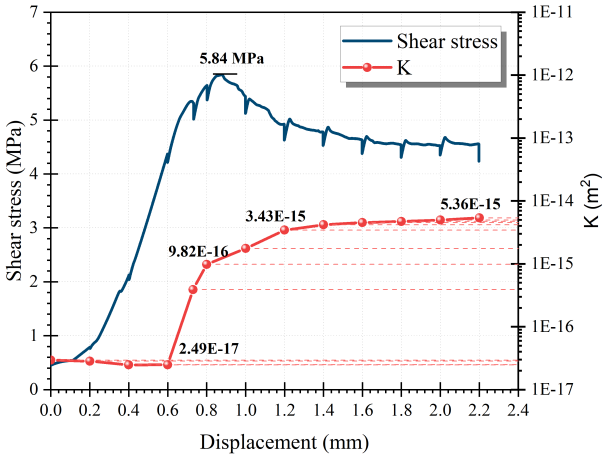

(e) Shear stress and K of C-L0-3

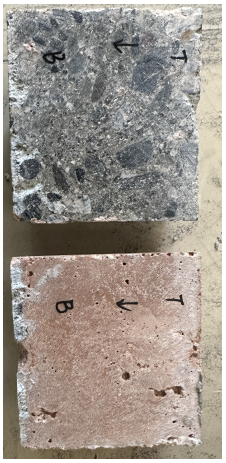

(f) C-L0-3

Figure 3.18: Coupled shear stress and permeability responses of C-L0 coarse aggregate geo-con smooth interfaces

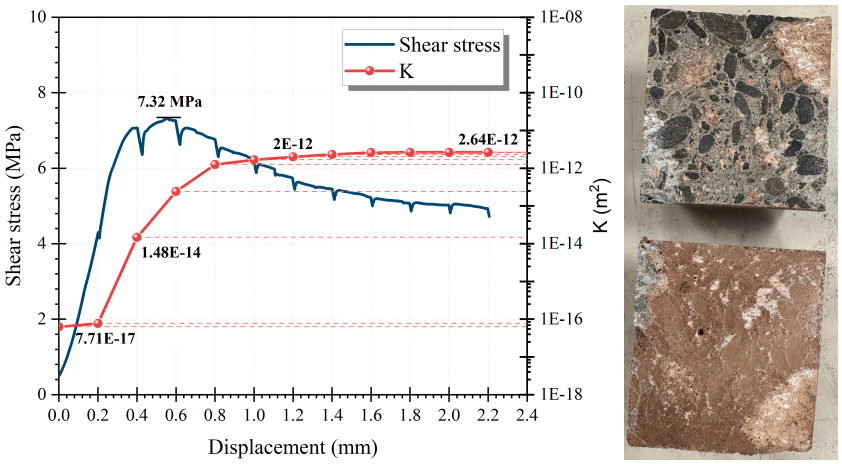

(a) Shear stress and K of C-L1-1

(b) C-L1-1

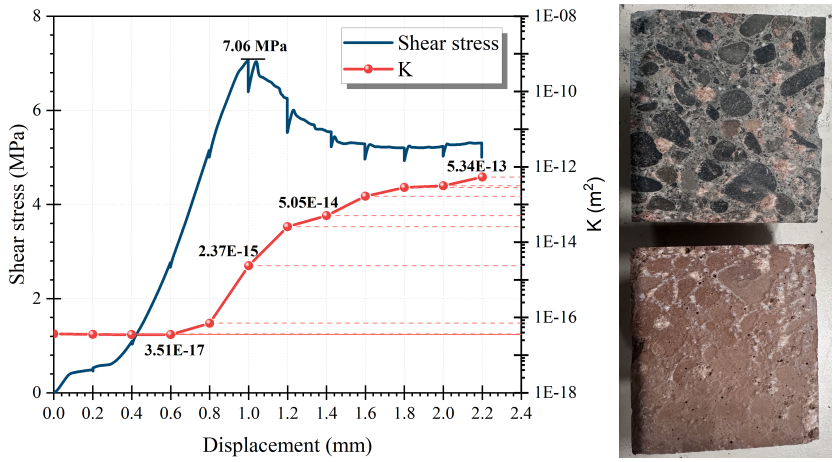

(c) Shear stress and K of C-L1-2

(d) C-L1-2

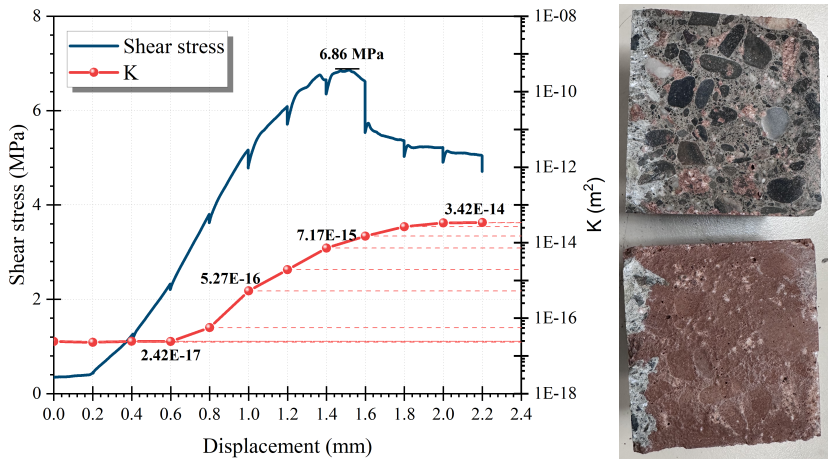

(e) Shear stress and K of C-L1-3

(f) C-L1-3

Figure 3.19: Coupled shear stress and permeability responses of C-L1 coarse aggregate geo-con interfaces

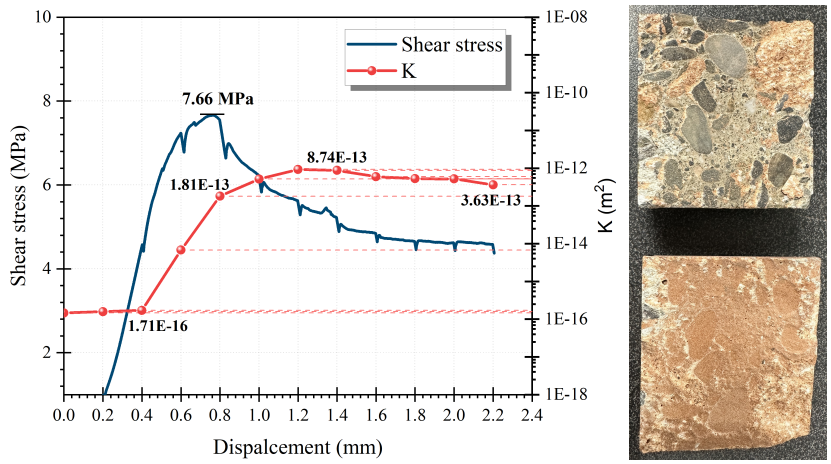

(a) Shear stress and K of C-L2-1 **(b)** C-L2-1

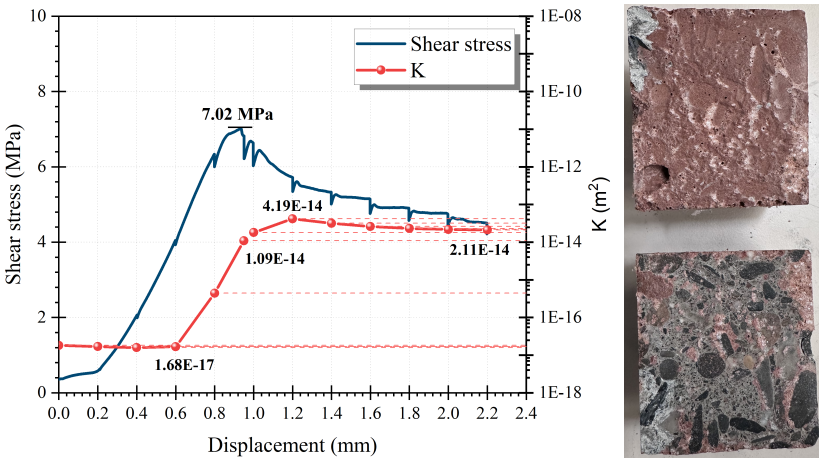

(c) Shear stress and K of C-L2-2 **(d)** C-L2-2

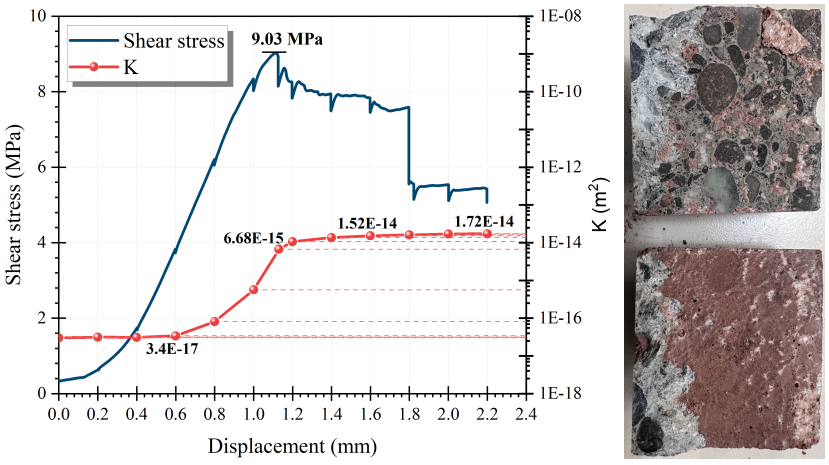

(e) Shear stress and K of C-L2-3 **(f)** C-L2-3

Figure 3.20: Coupled shear stress and permeability responses of C-L2 coarse aggregate geo-con interfaces

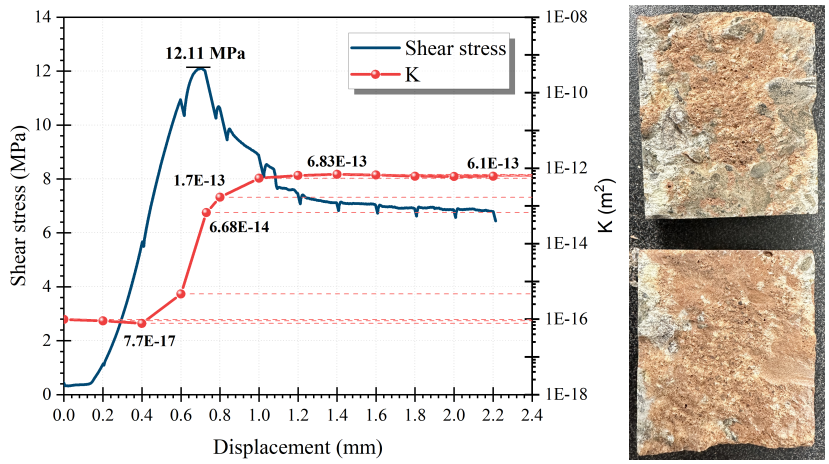

(a) Shear stress and K of C-L3-1

(b) C-L3-1

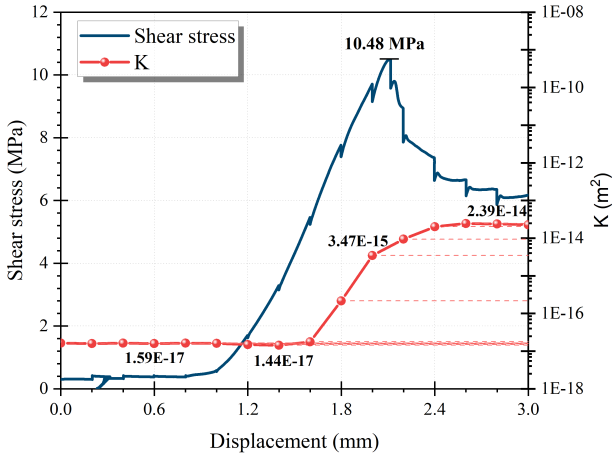

(c) Shear stress and K of C-L3-2



(d) C-L3-2

Figure 3.21: Coupled shear stress and permeability responses of C-L3 coarse aggregate geo-con interfaces

3.2.3 Monolithic specimen comparison

To evaluate the intrinsic mechanical and permeability behaviors of each base material, monolithic specimens of fine aggregate concrete, coarse aggregate concrete, and geopolymer were tested under the same shear-permeability protocol.

The F-CON specimen, shown in Figure 3.22, reached a peak shear strength of 11.29 MPa, with a moderate increase in gas permeability (K) occurring after peak loading. This indicates a dense internal matrix and gradual crack development.

The C-CON series, as shown in Figure 3.23, exhibited the highest peak strengths

(12.76–15.09 MPa). However, K rose significantly during the post-peak stage, implying that microcracks propagated rapidly in the heterogeneous matrix of coarse aggregate concrete.

In comparison, the G-GEO specimens in Figure 3.24 achieved slightly lower but consistent peak shear strengths (10.65–11.15 MPa). Their permeability increased smoothly with displacement and showed no abrupt jumps, reflecting a stable, homogeneous microstructure.

These results confirm that coarse aggregate concrete has the highest load-bearing capacity, while geopolymer exhibits more stable transport behavior. The findings serve as a reference baseline for evaluating bonded interface performance in geopolymer repair applications.

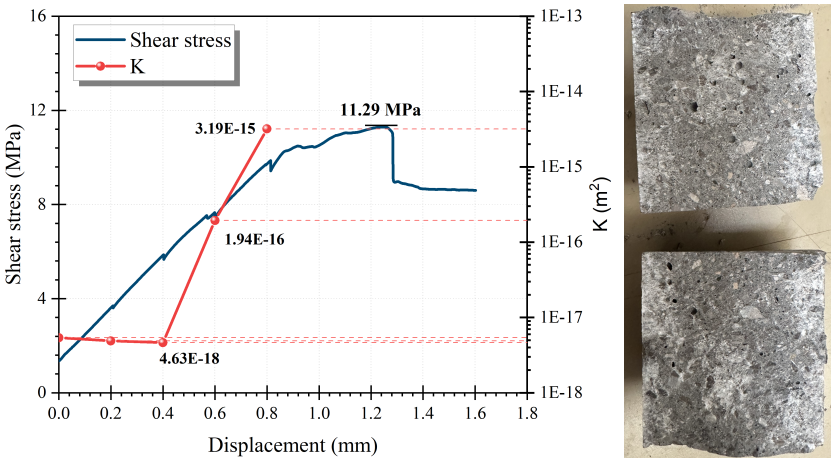

(a) Shear stress and K of F-L0 **(b)** F-CON

Figure 3.22: Coupled shear stress and permeability responses of F-CON whole specimen

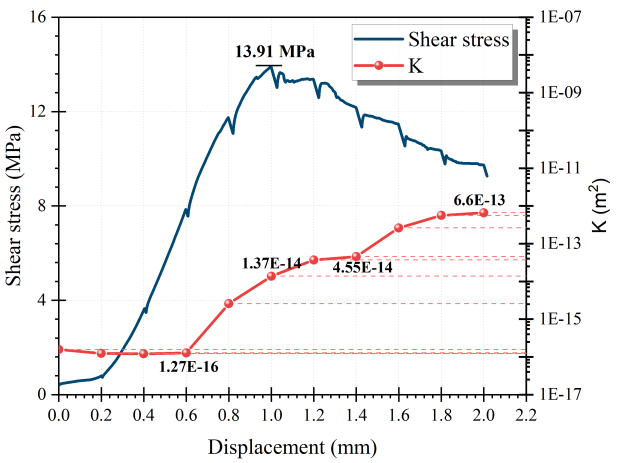

(a) Shear stress and K of C-CON-1



(b) C-CON-1

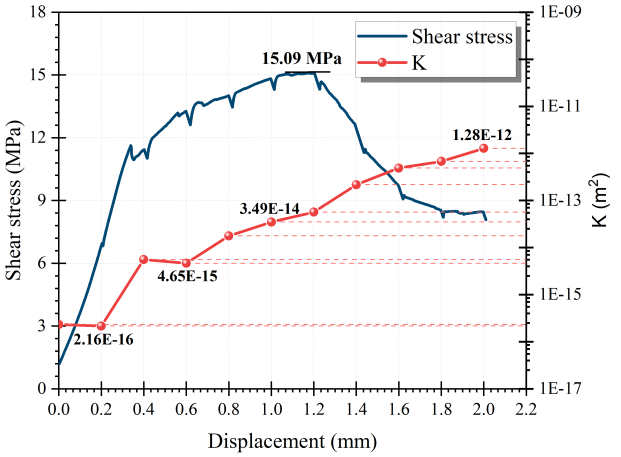

(c) Shear stress and K of C-CON-2



(d) C-CON-2

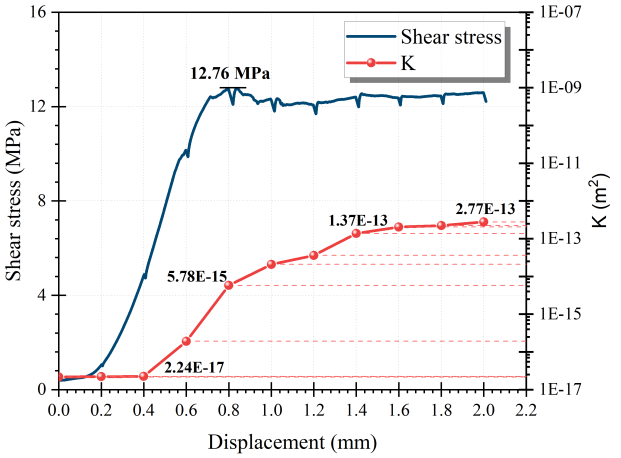

(e) Shear stress and K of C-CON-3



(f) C-CON-3

Figure 3.23: Coupled shear stress and permeability responses of C-CON whole specimens

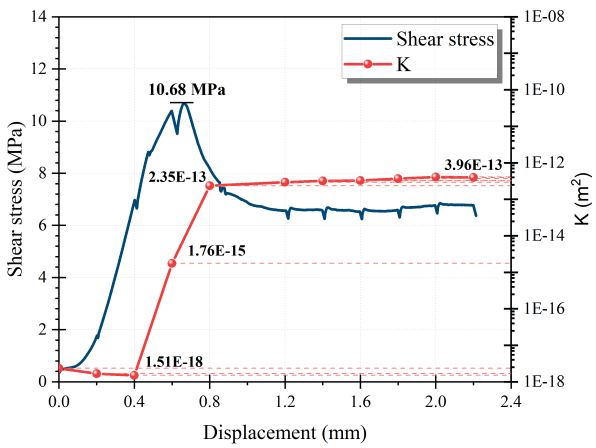

(a) Shear stress and K of G-GEO-1

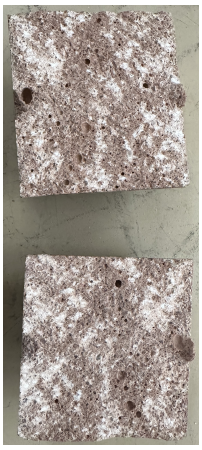

(b) G-GEO-1

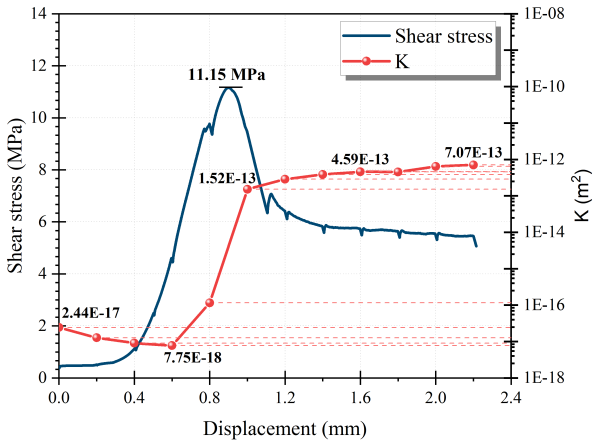

(c) Shear stress and K of G-GEO-2



(d) G-GEO-2

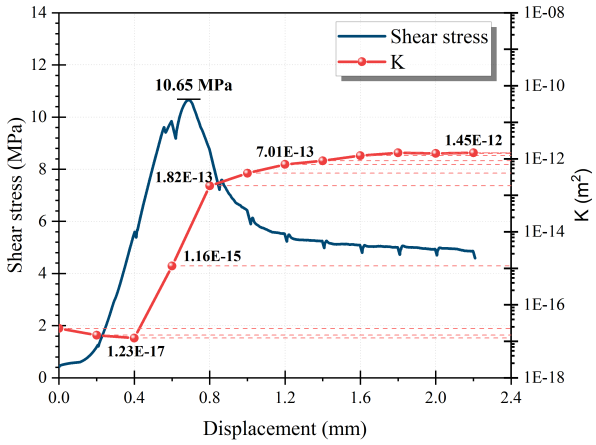

(e) Shear stress and K of G-GEO-3



(f) G-GEO-3

Figure 3.24: Coupled shear stress and permeability responses of G-GEO whole specimens

3.2.4 Summarizes the results

While Figure 3.25 displays the initial and final permeability (K) results for a range of specimens composed of concrete, geopolymer, and geo-con interfaces. The color coding in the graph facilitates easy comparison between initial and final permeability values across different material types. Purple bars represent the initial permeability (K-initial) for each specimen, while orange bars depict the final permeability (K-final) measured after the test procedures.

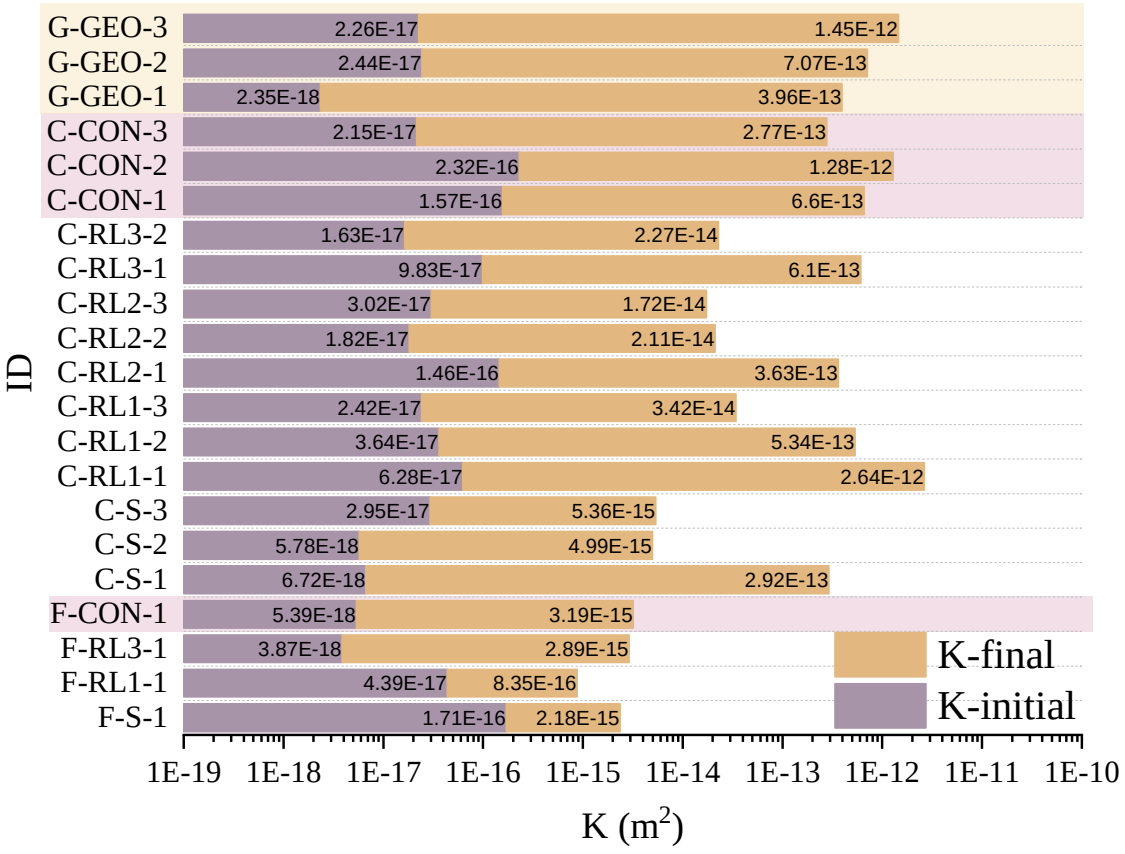

Figure 3.25: Initial and final permeability (K) results for concrete, geopolymer, and geo-con interface

Table 3.2 provides a comprehensive summary of all interface and monolithic specimens tested under coupled shear–permeability conditions. The table consolidates key parameters including roughness (S_a), peak shear strength ($\tau_{\max}$), displacement and strain at peak ($\Delta u_{\tau_{\max}}, \gamma_{\tau_{\max}}$), and average strength for each subgroup ($\bar{\tau}_{\max}$).

Table 3.2
Summary of interface roughness, peak shear strength, and deformation characteristics of all specimens

Group	ID	S_a	$\tau_{\max}$	$\Delta u_{\tau_{\max}}$	$\gamma_{\tau_{\max}}$	$\overline{\tau}_{\max}$
1	F-L0-1	–	4.81 MPa	0.713 mm	0.119	4.81 MPa
	F-L1-1	–	5.76 MPa	1.703 mm	0.028	5.76 MPa
	F-L3-1	–	10.41 MPa	1.399 mm	0.023	10.41 MPa
2	C-L0-1	60.20 μm	6.68 MPa	0.943 mm	0.016	6.00 MPa
	C-L0-2	26.44 μm	5.49 MPa	0.632 mm	0.011	
	C-L0-3	38.56 μm	5.84 MPa	0.879 mm	0.015	
	C-L1-1	189.7 μm	7.32 MPa	0.554 mm	0.009	7.08 MPa
	C-L1-2	123.7 μm	7.06 MPa	0.997 mm	0.017	
	C-L1-3	191.8 μm	6.86 MPa	1.516 mm	0.025	
	C-L2-1	986.8 μm	7.66 MPa	0.767 mm	0.013	7.90 MPa
	C-L2-2	202.8 μm	7.02 MPa	0.934 mm	0.016	
	C-L2-3	240.0 μm	9.03 MPa	1.118 mm	0.019	
	C-L3-1	1270 μm	12.11 MPa	0.707 mm	0.012	11.29 MPa
	C-L3-2	979.6 μm	10.48 MPa	2.112 mm	0.035	
3	F-CON-1	–	11.29 MPa	1.240 mm	0.021	11.29 MPa
	C-CON-1	–	13.91 MPa	0.998 mm	0.017	13.92 MPa
	C-CON-2	–	15.09 MPa	1.174 mm	0.020	
	C-CON-3	–	12.76 MPa	0.835 mm	0.014	
	G-GEO-1	–	10.68 MPa	0.664 mm	0.011	10.83 MPa
	G-GEO-2	–	11.15 MPa	0.900 mm	0.015	
	G-GEO-3	–	10.65 MPa	0.689 mm	0.011	

3.3 Discussion

3.3.1 Hydro-mechanical performance of geopolymer-concrete interfaces under shear loading

Shear strength. The results demonstrate that geopolymer mortar exhibits good bonding performance when used as a repair material with concrete. Even on cut, smooth interfaces, the shear strength between geopolymer and fine aggregate concrete was 4.81 MPa, which constitutes 42.6% of the full concrete cylinder's shear strength. In the case of geopolymer with coarse aggregate concrete, the shear strength reached 6.00 MPa, representing 43.1% of the full concrete cylinder's shear strength.

The presence of roughness significantly enhances the effectiveness of repairs demonstrating the potential applicability of geopolymer-based overlays in repair scenarios, subject to further validation at structural scale. When treated with shear loading, the rough interface between fine aggregate concrete and geopolymers exhibits an interfacial shear strength of 10.41 MPa, representing 92.2% of the strength of intact concrete. Meanwhile, the average shear strength at the interface between coarse aggregate concrete and geopolymers reaches 11.29 MPa, accounting for 81.1% of the full strength of a concrete cylinder.

Permeability (K). The results indicate that the permeability of the concrete, post-repair with geopolymer mortar, did not significantly increase, suggesting that the repair material was highly effective. Additionally, under certain initial load-bearing conditions, there appears to be a trend of reduced permeability, possibly due to the closure of micro-voids within the material.

For fine aggregate concrete, the repaired specimens exhibited a potential trend where the initial permeability of smooth surfaces was higher than that of rough surfaces, particularly after shear loading treatment, with permeability values even lower than those of intact concrete cylinders. In contrast, for coarse aggregate concrete, the initial permeability of the repaired specimens did not show a clear pattern, with some repaired specimens even exhibiting lower permeability than the concrete cylinders. This variation can be attributed not only to individual differences but also to the intrinsic lower permeability of fine aggregate concrete compared to coarse aggregate concrete used in the experiments.

3.3.2 Description of the shear evolution

According to the results presented in Section 3.4, the shear stress-displacement curves for all specimens were smooth and continuous, exhibiting a consistent trend. This observed trend aligns with the typical shear load-displacement characteristic curves reported in other studies conducted under confining pressure (Yang et al., 2024; Yu et al., 2018; Yang et al., 2023). The trend can be categorized into three distinct stages. For instance, the curve for specimen CS-3 exemplifies this behavior, as shown in the Figure 3.26.

Ascending phase (I): In the initial phase, characterized as the elastic-plastic stage, the shear stress-displacement curve exhibits a gradual rise. Upon reaching the full load, the curve transitions into a linear increase. At this phase, the ratio of the change in shear stress (ΔF) to the displacement change (ΔD) is denoted as G. As the loading phase shifts to the plastic stage, the curve begins to flatten. The shear stress in the elastic-plastic stage is primarily generated by the chemical bonds and van der Waals forces at the interface between the geopolymer mortar and concrete. Additionally, the mechanical interlocking and friction at the interface contributed to a portion of the shear force.

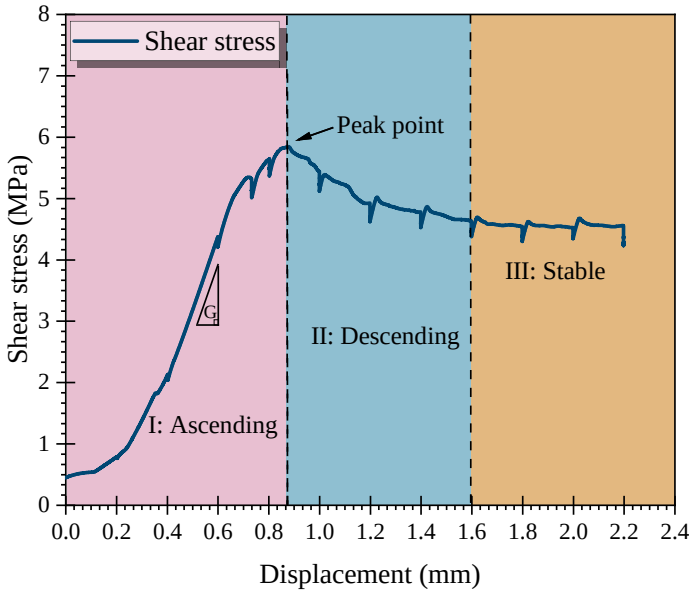

Figure 3.26: Typical shear load-displacement characteristic curves (Yang et al., 2024)

Descending phase (II): The testing machine continued to impose displacement at a speed of 0.12 mm/s, and the curve entered a declining trend, indicating the plastic phase. During this phase, the chemical bonding forces decreased, and the van der Waals forces

sharply declined to almost negligible levels as the displacement increased. In the plastic phase, the shear forces were primarily exerted by the mechanical interlocking and friction at the interface.

Stable phase (III): As the displacement continued to increase, the shear stress curve declined and eventually tended towards an equilibrium, entering the residual stress phase. At this stage, the specimen had undergone significant damage. The primary contributors to the shear stress during this phase were the frictional forces at the interface between the geopolymer and concrete.

3.3.3 Shear strength components

The peak shear strength of concrete comprises three components: bond strength, mechanical interlocking, and contact friction (Waseem and Singh, 2016; Yang et al., 2024, 2023). Under shear stress, parts of the concrete exhibit expansion. This occurs because, under confined shear loading, the interface on either side resists expansion through relative sliding. As the shear displacement increases, particles at the interface rotate and shift, significantly enhancing the shear strength of the interface. Consequently, the shear strength, denoted as τ_p, can be described by the following equation.

$$\tau_p = \tau_c + \tau_f + \tau_d \tag{3.12}$$

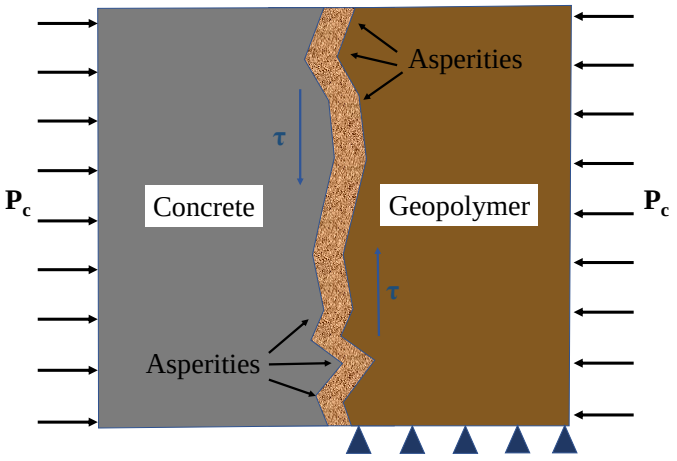

Figure 3.27: Mechanism of relative sliding of the geopolymer and concrete specimen.

While, τ_p represents the peak shear strength at the interface between geopolymer mor-

tar and concrete. τ_c is the sum of the chemical bonding forces and van der Waals forces, collectively referred to as the bond strength. τ_f refers to the frictional force generated when relative displacement occurs at the interface. τ_d denotes the stress required to resist expansion when concrete and geopolymer undergo relative motion. The contribution of chemical bonding, frictional resistance, and dilatancy to the overall shear strength is schematically illustrated in the Figure 3.27.

To simplify the analysis, it is assumed that the residual strength in the stable phase of the shear stress-displacement curve is solely provided by the frictional strength of the contact surfaces. Consequently, it is possible to derive several important characteristic values from the curves, as shown in Table 3.3.

Table 3.3
Characteristic values from the shear stress displacement curves

Group	ID	Shear strength (MPa)	G	τ_f (MPa)	τ_c + τ_d (MPa)
1	F-L0-1	4.81	8.68	3.89	0.92
	F-L1-1	5.76	2.71	–	–
	F-L3-1	10.41	10.62	7.06	3.35
2	C-L0-1	6.68	11.03	6.06	0.62
	C-L0-2	5.49	10.63	3.48	2.01
	C-L0-3	5.84	11.72	4.54	1.30
	C-L1-1	7.32	23.06	5.05	2.27
	C-L1-2	7.06	10.44	5.21	1.85
	C-L1-3	6.86	7.35	5.23	1.63
	C-L2-1	7.66	19.17	4.63	3.03
	C-L2-2	7.02	11.45	4.77	2.25
	C-L2-3	9.03	11.60	5.51	3.52
	C-L3-1	12.11	28.84	6.92	5.19
	C-L3-2	10.48	11.77	5.51	3.52
3	F-CON-1	11.29	10.67	8.63	2.66
	C-CON-1	13.91	22.10	9.80	4.11
	C-CON-2	15.09	34.64	8.40	6.69
	C-CON-3	12.76	26.46	12.14	0.62
	G-GEO-1	10.68	27.31	6.75	3.93
	G-GEO-2	11.15	26.37	5.57	5.58
	G-GEO-3	10.65	25.67	4.98	5.67

As evident from the table, under a confining pressure of 3 MPa, the shear strength, specifically the contact friction strength (τ_f), predominantly influences both the whole concrete specimens and geopolymer specimens, as well as the interface between the geopolymer and concrete. However, the cohesive strength (τ_c) and shear expansion strength (τ_d) also play significant roles.

3.3.4 Hydro-mechanical coupling shear stages

According to Section 3.4, the permeability (K), as represented in the displacement line plots, exhibits continuous curves that consistently follow the same trend across all datasets. These permeability curves correlate with the phases observed in the shear stress versus displacement curve. The variations in K are categorized into four distinct stages, corresponding to changes in shear stress, as illustrated in the Figure 3.28. This analysis primarily uses the specimen CS-3, which features a smooth interface between the geopolymer and coarse aggregate concrete, as an example.

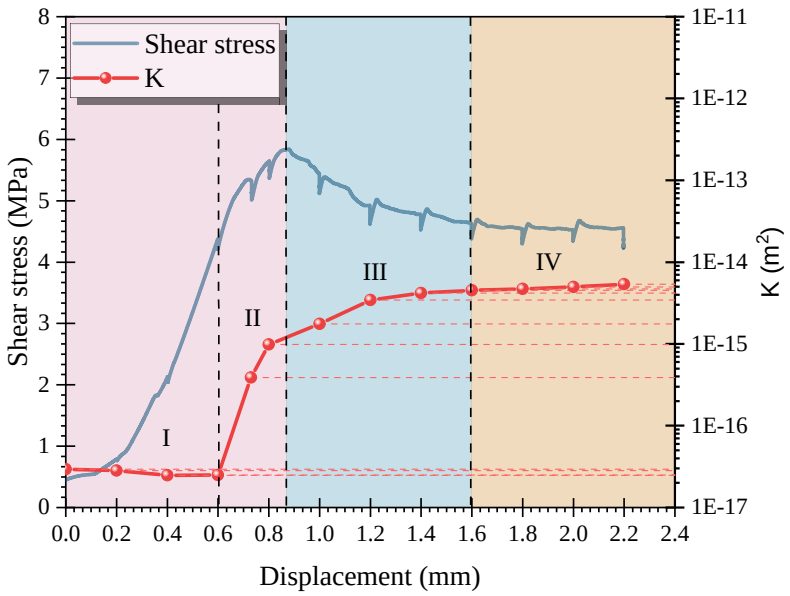

Figure 3.28: Typical shear permeability-displacement characteristic curves

Descending phase (I). Initially, the permeability (K) experiences a slight decrease, which may be attributed to the compaction of the material under the initial load and the closure of micro-voids. This indicates an initial resistance within the material's structure, preventing significant changes in gas transport pathways at low levels of shear stress.

Rapid ascending phase (II). As displacement continues and shear stress begins to increase, new micro-channels and fractures develop within the material, leading to a marked increase in permeability. This stage reflects the formation of new pathways that facilitate a higher volume of gas flow due to the widening and interconnecting of cracks.

Gradual ascending phase (III). This stage corresponds with the peak and subsequent decrease in shear stress. The permeability continues to rise even as the shear stress begins to decline, indicating that the material's internal structure is now dominated by the newly formed channels and cracks, which remain open despite a reduction in applied stress.

Stable phase (IV). After reaching the peak in shear stress, the permeability shows a trend toward stabilization or slight reduction. This behavior indicates that the material may undergo microstructural rearrangement, such as partial closure of previously formed cracks or reorientation of particles that partially obstruct gas flow. These mechanisms could lead to a reduction in permeability, even under continued displacement. However, since the permeability does not significantly decrease in most cases—and in some instances continues to increase slightly—this response cannot be attributed to self-healing. Further analysis, including the estimation of error bars for permeability values, would help to clarify the significance and consistency of this trend.

3.3.5 Comparative evaluation of the peak shear strength at geopolymer–concrete interfaces with fine and coarse aggregate concrete

The shear performance of geopolymer-repaired interfaces reveals a notable distinction between fine and coarse aggregate concretes. Specimens with fine aggregate concrete (Group 1) exhibited variable interfacial shear strengths depending on the surface roughness. The highest peak shear strength reached 10.41 MPa for the L3-treated interface (F-L3-1). In comparison, the coarse aggregate concrete specimens (Group 2) generally achieved higher peak values across corresponding surface preparations, with the maximum strength observed at 12.11 MPa under identical L3 roughness conditions (C-L3-1).

Moreover, intact specimens without a bonded interface (C-CON) reached the highest average shear strength of 13.92 MPa, underscoring the superior load-carrying capacity of unaltered coarse aggregate concrete. This contrast highlights the influence of aggregate type on interfacial behavior.

The enhanced performance of coarse aggregate specimens may be attributed to more pronounced interlocking at the interface, potentially facilitated by increased surface asperities and irregularities inherent to larger aggregates. This hypothesis aligns with roughness parameters such as S_a and S_q, which are known to influence bond strength through mechanical interlocking and dilatancy effects. However, a precise correlation between aggregate size and surface morphology requires further quantitative surface analysis.

Overall, these results underscore the importance of aggregate characteristics and surface treatment in governing the interfacial shear resistance of geopolymer–concrete systems. While fine aggregates may offer advantages in workability or aesthetics, coarse aggregates appear more favorable in terms of mechanical performance under shear loading.

3.3.6 Influence of roughness on geopolymer-concrete interface hydro-mechanical behavior

(1) Roughness influence on shear strength

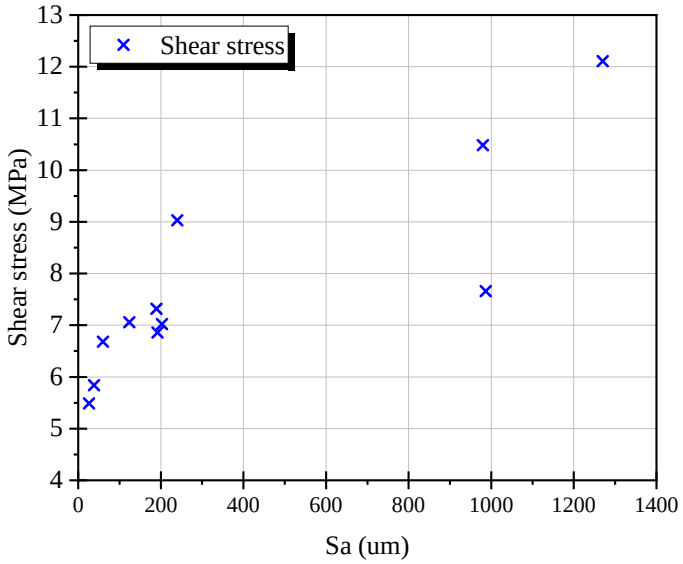

Figure 3.29: Scatter plot of shear modulus (MPa) and Sa (um)

For con-geo specimens with interfaces repaired using geopolymer mortar, variations in surface roughness significantly influence the shear strength. To examine this relationship, a scatter plot was created that illustrates the correlation between shear strength (expressed in MPa) and surface roughness (Sa, measured in micrometers). Figure 3.29 dis-

plays this correlation, highlighting a clear trend where increases in roughness correspond to increases in shear strength.

The scatter plot reveals that the data points are predominantly distributed along an upward sloping trajectory, further substantiating the positive correlation between the variables. This correlation likely illustrates the influence of surface roughness on the shear transfer capabilities of material interfaces; a rougher interface tends to enhance the shear strength of materials.

The Pearson correlation coefficient, a statistical measure of the strength and direction of a linear relationship between two variables, ranges from -1 to +1. A coefficient of +1 indicates a perfect positive correlation, -1 a perfect negative correlation, and 0 no correlation. The formula for the Pearson correlation coefficient is:

$$r = \frac{n(\sum xy) - (\sum x)(\sum y)}{\sqrt{[n\sum x^2 - (\sum x)^2][n\sum y^2 - (\sum y)^2]}} \tag{3.13}$$

where x and y are the variables, n is the number of data points, $\sum xy$ is the sum of the products of corresponding values, $\sum x$ and $\sum y$ are the sums of the values, and $\sum x^2$ and $\sum y^2$ are the sums of the squares of the values.

Our calculation yields a coefficient of 0.814, indicating a strong positive correlation. Considering the Equation (3.12), where τ_p represents the total shear strength and τ_c, τ_f, and τ_d signify the contributions from chemical bonding, frictional resistance, and mechanical interlocking, respectively, the impact of surface roughness on the interface between geopolymer mortar and concrete under confining pressure can be further elucidated. As surface roughness increases, not only does mechanical interlocking (τ_d) enhance due to the greater interfacial engagement, but the area available for chemical bonding (τ_c) also increases. Rough surfaces provide more micro-contact points, which promote chemical interactions and strengthen the bond at the interface. Thus, increasing surface roughness not only mechanically augments shear strength but also effectively improves the overall structural performance through enhanced chemical bonding. This synergistic effect ensures that the repaired structure is better equipped to withstand stresses and loads.

(2) Roughness influence on shear modulus G

Figure 3.30 presents two datasets: Surface Roughness (Sa, measured in micrometers, μm) and Shear Modulus (G, measured in MPa). Visually, the peaks and troughs in the data for "G" appear to correlate with the trends observed in the "Sa" dataset, particularly of

specimens of C-RL1-1, C-RL2-1, and C-RL3-1. This visual analysis suggests a potential relationship between the surface roughness and the shear modulus, which may indicate that variations in the roughness of the interface influence its mechanical response under shear stress.

Using Pearson's correlation coefficient as Equation (3.13), the calculated result is $r \approx 0.646$. This indicates a moderate positive correlation between surface roughness (Sa) and shear modulus (G), suggesting that as the roughness of the interface increases, the shear modulus also tends to increase.

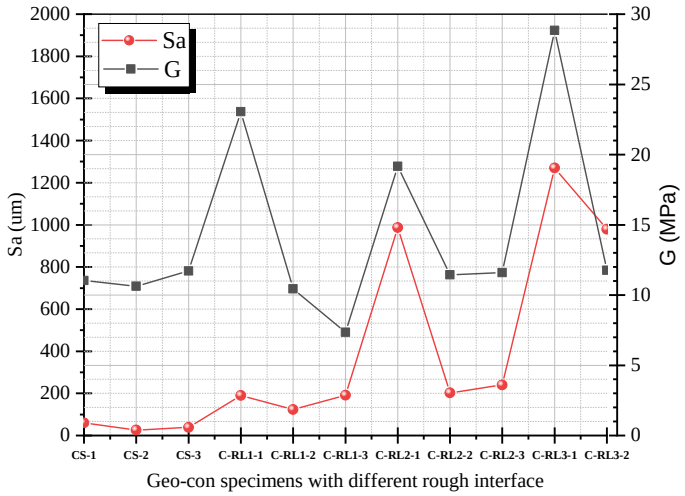

Figure 3.30: Scatter plot of shear stress (MPa) and Sa (um)

In our observations of the shear modulus, we noted an increasing trend in correlation with the enhancement of interface roughness. This indicates that interfaces with higher roughness can more effectively transmit forces under the same shear stress, thereby enhancing the structural shear stiffness. The interaction between the microstructures of geopolymer and concrete under high confining pressure and shear loading may influence the performance of the interface. Factors such as the development of micro-cracks, changes in porosity, and the chemical bonding between materials are likely to impact the shear modulus.

3.4 Roughness before shear tests and after shear tests

Based on the post-shear test photographs presented in Section 3.4.2, it is evident that different levels of roughness result in noticeable material delamination from the opposite

part on both the semicylindrical sides of the geopolymer mortar and concrete. Consequently, a detailed roughness scan was conducted on the interfaces of specimens with the highest roughness, identified as C-RL3-1 and C-RL3-2, as illustrated in the Figure 3.31. The photograph of the specimen, post-testing, is shown in Figure 3.21.

In this study, the surfaces of concrete specimens C-RL3-1 and C-RL3-2 were initially scanned for roughness, recording Sa values of 1270 µm and 979.6 µm, respectively. A layer of geopolymer mortar was then applied, and the specimens underwent shear testing under a confining pressure of 3 MPa. Post-shear testing roughness scans, as shown in Figure 3.36, indicated reduced Sa values of 894.8 µm and 840.3 µm respectively. Photographs post-testing, as depicted in the attached images, show the physical state of the surfaces.

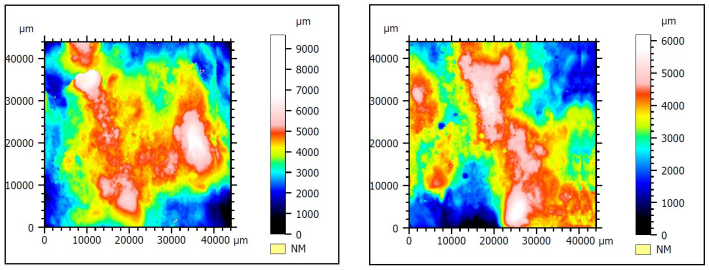

(a) C-RL3-1: 894.8 um **(b)** C-RL3-2: 840.3 um

Figure 3.31: Roughness scanning images and results after shear tests

The reduction in roughness can primarily be attributed to the shear forces during testing which likely caused abrasion and smoothing of the concrete surfaces. This mechanical interaction may have led to the displacement and redistribution of finer particles within the geopolymer mortar, filling in the micro-voids and thus reducing the overall surface roughness. These changes suggest an improved interfacial bond between the concrete and the geopolymer mortar.

4 Conclusion

This chapter presented an extensive experimental investigation on the coupled hydro-mechanical behavior of geopolymer-concrete interfaces. The chapter's key conclusions derived from detailed tests and analyses are as follows:

1. **Experimental Methodology:** Initial shear tests under unconfined conditions identified critical limitations, notably concrete substrate fracture rather than interface debonding. This issue was successfully addressed by developing a direct shear apparatus with a constant confining pressure of 30 bar, effectively localizing shear at the geo-con interface.

2. **Shear Strength:** Interfacial shear strengths of geopolymer-concrete specimens significantly depended on aggregate type and surface roughness. Fine aggregate interfaces reached a peak strength of 10.41 MPa, approximately 92.2% of intact concrete strength, whereas coarse aggregate interfaces achieved strengths of 12.11 MPa, representing 87.0% of intact concrete strength. Smooth interfaces showed substantially reduced shear strengths of 4.81 MPa (fine) and 6.00 MPa (coarse).

3. **Permeability Characteristics:** Permeability coefficients (K) remained low (below 10^{-16} m^2) until peak shear was reached, after which significant increases (up to 10^{-13} m^2) were observed, indicating post-failure crack propagation. Notably, certain repaired fine-aggregate interfaces demonstrated final permeability values lower than intact concrete, highlighting effective sealing capability.

4. **Surface Roughness Impact:** The experimental data showed a strong positive correlation (Pearson coefficient $r = 0.814$) between surface roughness (S_a) and peak shear strength. Moreover, roughness moderately correlated ($r = 0.646$) with the initial shear modulus, suggesting enhanced stiffness and bonding effectiveness with increased roughness.

5. **Shear Resistance Components:** Analysis revealed that frictional resistance predominantly influenced post-peak shear behavior. The combined contribution of cohesive bonding and dilatancy reached up to 5.67 MPa in highly roughened interfaces, demonstrating significant mechanical interlocking and chemical adhesion effects.

These results confirm the necessity of proper surface preparation and reliable experimental setups for accurately assessing geopolymer mortars as structural repair materials. The insights gained in this chapter provide a comprehensive understanding of interfacial behaviors crucial for developing effective and durable geopolymer-based repair strategies.

CHAPTER 4

Numerical simulations

1 Introduction

This chapter presents the validation of a finite element model aimed at simulating the shear behavior of geopolymer–concrete interfaces under confining pressure. Building upon the experimental observations detailed in Chapter 3, the numerical approach adopted here seeks to reproduce and interpret the observed interface responses using a calibrated modeling framework. The simulation program is implemented using **Abaqus/Standard**, a finite element software known for its robustness in handling nonlinear material behavior, contact interactions, and large deformations.

The numerical model's constitutive law replicates the phenomena occurring at the interfaces between concrete and geopolymer, primarily governed by the geo-con bond strength. The combined effects of normal stress, surface roughness, and the chemical-mechanical bonding between the two materials dictate the comprehensive shear behavior at the interface. This behavior can be delineated into three distinct stages, as illustrated in Figure 4.1, following the conceptual framework initially proposed by Saiang et al. (Saiang et al., 2005). These stages include the initial elastic phase, the progressive mobilization of interface friction, and the final post-peak softening response.

The experimental data used for numerical calibration and validation are those presented in Chapter 3, which examine the shear performance of geopolymer–concrete interfaces subjected to varying confinement. The focus is restricted to the interface between geopolymer mortar and coarse aggregate concrete, as introduced in Chapter 2. Four dis-

tinct interface roughness levels are considered. The L0 interface represents a smooth contact formed without any surface treatment. L1 and L2 are prepared by sandblasting the concrete surface, introducing controlled degrees of surface texture. The highest roughness, denoted as L3, is obtained by shearing concrete cylinders to expose a highly irregular aggregate surface. These graded roughness levels provide a systematic basis for assessing how interface texture influences bond strength and shear resistance under different confinement levels.

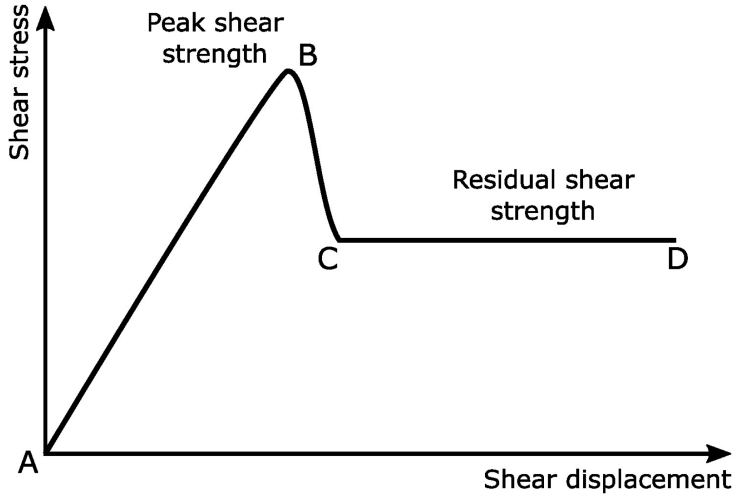

Figure 4.1: Main stages of the shear evolution of interfaces under low normal loading. (Badika et al., 2022)

2 Construction of numerical model

This section defines the architecture of the finite element model developed to simulate the shear behavior of geo-con interfaces under confining pressure. The numerical model is implemented and incorporates detailed definitions of software selection, geometry, meshing strategy, and constitutive laws for all involved materials and interfaces.

2.1 Software Selection and Justification

Abaqus/Standard was selected as the finite element platform for its robust capabilities in modeling nonlinear material behavior, contact interactions, and large-deformation responses. Importantly, it supports user-defined subroutines (UMAT/VUMAT), which offer

flexibility for implementing complex material and interface behavior laws (Dassault Systèmes,, 2016). These features are critical to accurately reproduce the shear-slip evolution and pressure-dependent frictional behavior observed at geo-con interfaces.

The choice of Abaqus/Standard over other platforms (e.g., Abaqus/Explicit or ANSYS) is also motivated by its efficient handling of quasi-static simulations involving cohesive zone modeling (CZM), frictional contact, and damage evolution (Turon et al., 2006; Needleman, 1987; Pietruszczak and Mroz, 2001). This ensures convergence reliability, particularly for simulations involving localized interface degradation and multistage failure.

2.2 Model geometry and mesh sensitivity

To accurately replicate the experimental setup, a full 3D numerical model was employed despite the axisymmetric geometry of the specimen. This choice was made to capture non-uniform stress states and complex interfacial behavior, which cannot be reliably represented by axisymmetric simplifications. The model includes three material domains: concrete, geopolymer mortar, and a surrounding rubber sleeve that exerts a uniform radial pressure of $3.0\,\mathrm{MPa}$ to simulate confinement.

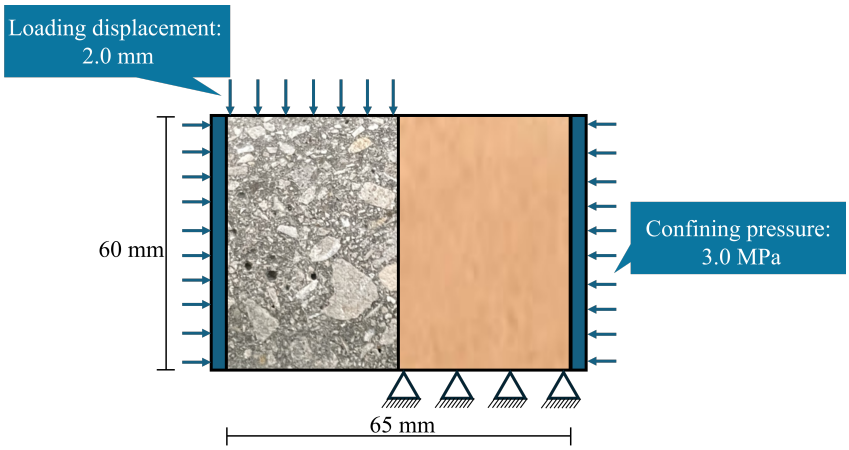

Figure 4.2: 2D schematic view of the direct shear test configuration.

Note: A confining pressure of $3.0\,\mathrm{MPa}$ is applied radially through a surrounding rubber layer. A horizontal displacement of $2.0\,\mathrm{mm}$ is imposed on the top concrete section, while the geopolymer base remains fixed. The bonded interface is located at the horizontal mid-plane between the two materials.

To induce interfacial shear, a horizontal displacement of $2.0\,\mathrm{mm}$ is applied to the top concrete portion, while the bottom surface of the geopolymer block is fully constrained to prevent rigid body motion. The interface response is monitored at the bonded region between the two materials.

The simulation is performed using a structured hexahedral mesh composed of C3D8R elements. To ensure accuracy in the shear-critical interface zone, a finer mesh (element size of $4\,\mathrm{mm}$) is applied in the geopolymer region, while coarser elements ($5\,\mathrm{mm}$) are used in the concrete and rubber domains. Mesh continuity is maintained across all interfaces to ensure smooth stress transfer and avoid artificial stress concentrations.

A mesh sensitivity analysis was conducted by comparing results with element sizes of 3 mm, 4 mm, and 5 mm in the geopolymer region. The variation in peak shear stress was found to be less than 2% between 3 mm and 4 mm configurations, confirming mesh convergence. Therefore, the 4 mm mesh was adopted for all subsequent simulations to achieve an optimal balance between computational cost and accuracy.

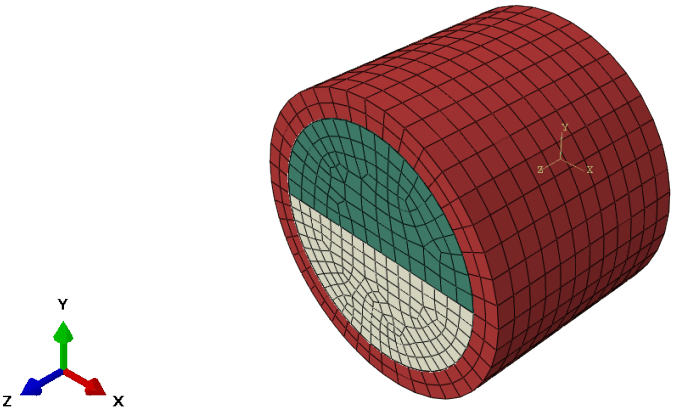

Figure 4.3: Structured mesh distribution used in the geopolymer–concrete model.

Note: Green = concrete, Yellow = geopolymer mortar, Red = rubber confinement. A magnified view of the mesh at the interface is provided in Appendix X.

2.3 Constitutive models for studied materials

Representing the mechanical behavior of the constituents is essential for simulating the interfacial shear response of geopolymer–concrete systems under confinement.

The geopolymer and concrete are modeled as pressure-dependent brittle materials

governed by the Mohr–Coulomb plasticity criterion. Although the full determination of Mohr–Coulomb parameters ideally requires multiaxial testing, in this study they were approximated from uniaxial compression tests by assuming a friction angle based on literature values and computing the cohesion from the peak uniaxial compressive strength. This approach, while simplified, provides reasonable input values for simulating brittle materials under confined shear conditions.

The surrounding rubber layer, responsible for imposing lateral confinement during shear, is simulated using a hyperelastic Mooney–Rivlin formulation (Kumar and Rao, 2016; Yeoh, 1997), allowing for large, reversible deformations. Finally, the interfacial behavior is described using a cohesive–frictional law that combines traction–separation relations, damage evolution, and frictional sliding, enabling the numerical model to capture the full range of interfacial failure stages observed experimentally.

The following subsections describe the constitutive laws and material parameters used for each domain in detail.

2.4 Constitutive models for studied materials

Accurately representing the mechanical behavior of the constituents is essential for simulating the interfacial shear response of geopolymer–concrete systems under confinement. In this study, three categories of materials are involved: the bulk materials (geopolymer mortar and concrete), the rubber confining layer, and the geopolymer–concrete interface.

The geopolymer and concrete are modeled as pressure-dependent brittle materials governed by the Mohr–Coulomb plasticity criterion, calibrated from uniaxial compression tests. The surrounding rubber layer, responsible for imposing lateral confinement during shear, is simulated using a hyperelastic Mooney–Rivlin formulation (Kumar and Rao, 2016; Yeoh, 1997), allowing for large, reversible deformations. Finally, the interfacial behavior is described using a cohesive–frictional law that combines traction–separation relations, damage evolution, and frictional sliding, enabling the numerical model to capture the full range of interfacial failure stages observed experimentally.

The following subsections describe the constitutive laws and material parameters used for each domain in detail.

2.4.1 Concrete and geopolymer: Mohr–Coulomb model

The mechanical behavior of concrete and geopolymer mortar was modeled using the Mohr–Coulomb plasticity model, which is commonly used for brittle materials such as rocks, concrete, and cementitious composites. This model accounts for shear failure under pressure-dependent conditions, defined by the material's internal friction angle and cohesion.

The Mohr–Coulomb yield criterion is defined as:

$$\tau = c + \sigma \tan \phi \tag{4.1}$$

where τ is the shear stress at failure, σ is the normal stress, c is the cohesion, and ϕ is the internal friction angle.

This model includes an associated or non-associated flow rule and can represent dilatancy behavior through a separate dilation angle ψ, allowing volumetric expansion under shear. In this study, the dilation angle is assumed equal to or smaller than the friction angle for convergence purposes.

Material properties were determined from uniaxial compression tests, and the elastic properties are presented in Table 4.1. Compared to concrete, the geopolymer mortar exhibits a lower elastic modulus and a higher Poisson's ratio, indicating greater deformability under axial loading.

Note that Young's modulus E and Poisson's ratio ν define the linear elastic behavior prior to yielding. These parameters are independent of the Mohr–Coulomb failure criterion but are essential for calculating the initial stiffness and stress distribution.

While cohesion c and friction angle ϕ are independent parameters in the Mohr–Coulomb criterion, both contribute to the shear strength envelope. They can be estimated independently from different experimental conditions—e.g., c from unconfined compression and ϕ from triaxial or direct shear tests—but in simplified calibration (e.g., from uniaxial tests), assumptions are often made to estimate one from the other.

Both concrete and geopolymer domains were meshed using 8-node linear brick elements with reduced integration (C3D8R) in *Abaqus/Standard*, ensuring efficiency in nonlinear simulations involving shear localization and interface interactions.

Table 4.1
Linear elastic properties of geopolymer and concrete used for Mohr–Coulomb model

Material	Density (kg/m^3)	Young's modulus (MPa)	Poisson's ratio
Geopolymer	2302×10^{-9}	9800	0.25
Concrete	2321×10^{-9}	35500	0.18

2.4.2 Rubber layer: Mooney–Rivlin hyperelastic model

To simulate the confinement condition applied in the direct shear tests, a hyperelastic rubber layer is introduced in the finite element model. This rubber sleeve replicates the function of the experimental membrane used to impose radial pressure on the cylindrical specimen.

The rubber material is modeled using the Mooney–Rivlin hyperelastic model in its compressible form, which is suitable for modeling elastomers with small but nonzero volumetric changes. Although rubber is typically considered nearly incompressible, a finite compressibility parameter D_1 is introduced to ensure numerical stability in the finite element implementation. This model defines the strain energy potential W as a function of the invariants of the right Cauchy–Green deformation tensor:

$$W = C_{10}(I_1 - 3) + C_{01}(I_2 - 3) + \frac{1}{D_1}(J_{\text{el}} - 1)^2 \tag{4.2}$$

where:

- C_{10} and C_{01} are material constants defining deviatoric deformation,
- D_1 controls volumetric compressibility,
- I_1, I_2 are the first and second invariants of the deviatoric strain tensor,
- J_{el} is the elastic volume ratio.

This formulation allows the rubber to undergo large, reversible strains, maintaining radial confinement on the geopolymer–concrete interface during shear loading (Shahzad et al., 2015; Yamashita et al., 2023). The values of C_{10}, C_{01}, and D_1 are selected based on typical elastomer properties used in confined loading tests, as summarized in Table 4.2.

Table 4.2
Mooney–Rivlin hyperelastic parameters for rubber material

Material	C_{10}	C_{01}	D_1
Rubber	0.69	0.173	0.0124

In the numerical simulation, the rubber region is meshed using reduced-integration elements (C3D8R) compatible with large strain formulations. Contact interactions are defined between the rubber and the surrounding concrete and geopolymer domains, using hard contact in the normal direction and low-penalty friction ($\mu = 0.0001$) in the tangential direction. This ensures stable confinement while avoiding significant shear transfer at the rubber–solid interfaces.

2.4.3 Geo–con interface: Cohesive–Frictional model

The geopolymer–concrete interface was modeled using zero-thickness cohesive elements (COH3D8) inserted between bonded surfaces. These elements combine a traction–separation law with a damage-modulated friction model, allowing for both progressive bond degradation and post-debonding sliding resistance.

Elastic behavior The linear elastic response is represented by the stress vector, calculated by multiplying the stiffness matrix with the displacement vector as shown in Equation (4.3). This formulation remains effective until initial damage occurs at the bond interface. The equation can be expressed as:

$$t = \begin{bmatrix} t_n \\ t_s \\ t_t \end{bmatrix} = \begin{bmatrix} K_n & 0 & 0 \\ 0 & K_s & 0 \\ 0 & 0 & K_t \end{bmatrix} \begin{bmatrix} \delta_n \\ \delta_s \\ \delta_t \end{bmatrix} \tag{4.3}$$

In this equation:

- t_n, t_s, t_t are normal and shear tractions.
- K_n, K_s, K_t represent the stiffness in normal and shear directions, respectively.
- $\delta_n, \delta_s, \delta_t$ are the displacements in the normal and shear directions.

This method applies individually to each bond between concrete and geopolymer, effectively modeling the shear behavior of geo-con interfaces before reaching peak stress conditions.

Damage initiation and evolution Damage initiates once the nominal stress in any direction exceeds its critical threshold. The criterion of maximum stress, as defined in Equation (4.4), marks the initiation of damage within the numerical model. When satisfied within a concrete-rock bond, this criterion signals a decline in stiffness according to a predefined damage evolution law, rendering the linear elastic model described in Equation (4.3) inapplicable.

$$\max\left(\frac{\langle t_n\rangle}{t_n^0}, \frac{t_s}{t_s^0}, \frac{t_t}{t_t^0}\right) = 1 \tag{4.4}$$

This equation reflects the point at which the stress resistances, denoted by t_n^o, t_s^o, and t_t^o, exceed the thresholds leading to damage. The Macaulay brackets in $\langle t_n\rangle$ indicate that only positive values of t_n affect the outcome, emphasizing that normal compressive stresses do not induce separation. These stress components, t_n, t_s, and t_t, are essential for accurately modeling the stresses experienced by the concrete-rock bond during shearing processes.

Upon confirming damage initiation at the geo-con interface, the contributions to stress are derived from the traction-separation law, modified by the damage parameter D. This parameter transitions from zero, prior to any reduction in stiffness, to one upon the complete failure of the bond. The following expression, Equation (4.5), elucidates how the stress vector components are computed:

$$\begin{aligned} t_n &= \begin{cases} (1-D)\bar{t}_n & \bar{t}_n \geq 0 \\ \bar{t}_n \end{cases}, \\ t_s &= (1-D)\bar{t}_s, \\ t_t &= (1-D)\bar{t}_t, \end{aligned} \tag{4.5}$$

where $\bar{t}_n$, $\bar{t}_s$, and $\bar{t}_t$ are the initial stress components derived from Equation (4.3). The term $\vec{t}_{traction}(\bar{t}_n, \bar{t}_s, \bar{t}_t)$ represents the traction's contribution according to the separation law. Equation (4.6) is utilized in the Abaqus simulation tool to model an exponential decay in stress following damage initiation, effectively portraying the gradual deterioration of the bond at the geo-con interface.

Following the onset of damage at the geo-con interface, as indicated by Equation (4.4), the damage parameter D calculates the influence on stress using the traction–separation approach. The parameter D evolves from zero, representing undamaged stiffness, to one, indicating complete bond failure. The post-initiation degradation is modeled by an exponential damage function, as defined in Equation (4.6), which is adapted from the cohesive zone modeling framework implemented in Abaqus (**?**) and originally proposed by Ortiz and Pandolfi (1999).

The post-initiation degradation is modeled by an exponential damage function Equation (4.6):

$$D = 1 - \left(\frac{\delta_m^o}{\delta_m^{max}}\right)\left[\frac{1 - \exp\left(-\alpha\left(\frac{\delta_m^{max} - \delta_m^o}{\delta_m^f - \delta_m^o}\right)\right)}{1 - \exp(-\alpha)}\right] \tag{4.6}$$

In this formula, δ_m^o represents the initial separation at damage, while δ_m^f denotes the separation at bond failure, and δ_m^{max} is the peak separation observed. The parameter α is a dimensionless factor dictating the rate of damage progression. The term $\delta_m^f - \delta_m^o$ is defined as plastic displacement, serving as a key model parameter for describing the damage evolution at the geo-con interface.

Frictional response Following the confirmation of damage initiation at the geo-con interface, as described by Equation (4.5), the resultant stress is governed by the traction-separation law and the progressive engagement of frictional forces. This integrated approach is termed the cohesive frictional model. The frictional response is determined by the Coulomb friction law, presented in Equation (4.7):

$$t_{\text{friction}} = \begin{bmatrix} t_n \\ D\mu t_n \\ D\mu t_n \end{bmatrix} \tag{4.7}$$

where μ represents the friction coefficient. This equation models the frictional forces acting upon the geo-con interface, taking into account the damage level represented by D and the normal stress t_n.

Combined interface law The integration of behavioral laws into a unified expression is accomplished with Equation (2.6), which combines the effects of traction and friction at the geo-con interface:

$$t = t_{\text{traction}} + t_{\text{friction}} \tag{4.8}$$

Here, t_{traction} is determined as per Equation (4.5), and t_{friction} follows the methodology described in Equation (4.7). Equation (4.8) encapsulates the complete stress response of a geo-con bond under shear forces, synthesizing linear elastic responses, damage progression, and frictional effects into a comprehensive stress history model.

The methodology for selecting and integrating these behaviors into our model is rigorously informed by a critical analysis of existing experimental research. Notably, the studies conducted by El Merabi (2018) and Badika et al. (2022) have been instrumental in shaping our approach to the mechanical interactions at the interface.

3 Simulation of interface behavior

The simulation framework was established based on the calibrated constitutive models, and includes detailed boundary conditions, interface behavior, and parameter calibration procedures.

This section presents the numerical implementation of the loading process, the treatment of interface roughness, and the validation of simulated responses against experimental results. The aim is to reproduce the key stages of interfacial failure—namely elastic bonding, progressive degradation, and frictional sliding—and to analyze how interface characteristics influence shear resistance.

3.1 Boundary conditions and loading steps

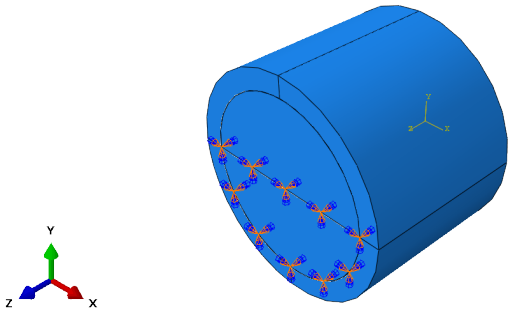

(a) Boundary conditions applied during the initial step

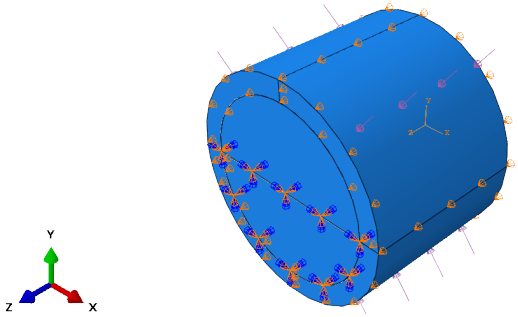

(b) Confining pressure application during the second step

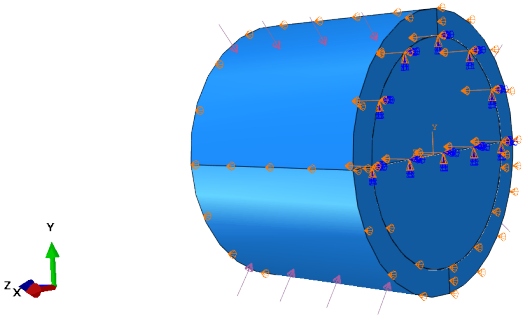

(c) Shear loading application during the third step

Figure 4.4: Boundary conditions and loading steps

The boundary conditions and loading steps in the numerical simulation are designed to replicate the experimental configuration of the direct shear test under a confining pressure of $3\,\mathrm{MPa}$. The model setup is illustrated in Figure 4.4.

The specimen consists of a bonded interface between two cylindrical materials: concrete and geopolymer mortar. A horizontal displacement of $2.0\,\mathrm{mm}$ is imposed on the top surface of the geopolymer, while the bottom surface of the concrete remains fixed. Note

that the positioning of concrete and geopolymer in the upper and lower halves is arbitrary from a mechanical modeling perspective—the key condition is the relative motion across the bonded interface. The displacement is applied to one end (here: top of geopolymer), while the other (bottom of concrete) is fixed.

Initially, displacement constraints are imposed to prevent rigid body motion. Both axial and lateral displacements are restricted on appropriate surfaces, and rotational degrees of freedom are restrained as necessary to maintain equilibrium.

In the second step, a uniform radial pressure of $3.0\,\mathrm{MPa}$ is applied to the lateral surface of the cylinder to simulate the constant normal loading (CNL) condition. This pressure is maintained throughout the subsequent loading.

In the final step, a shear displacement is applied along the z-axis to the top surface of the geopolymer. The fixed concrete base and the applied relative displacement promote shear slip at the interface mid-plane, enabling the development of interfacial failure representative of the experimental setup.

3.2 Incorporation of surface roughness

The shear behavior of geo–con interfaces is strongly influenced by surface roughness. In this study, four levels of interface roughness were defined in the experimental program: L0 (as-cast smooth), L1 (light sandblasting), L2 (medium sandblasting), and L3 (mechanically roughened via shearing). These roughness levels were introduced on the concrete surface before geopolymer casting to simulate practical surface preparation conditions.

In the numerical model, the geometric roughness features were not explicitly meshed. Instead, the influence of surface roughness was incorporated by adjusting key parameters in the cohesive–frictional interface model, following a strategy commonly used in previous studies (Badika et al., 2022; El Merabi, 2018). The following modeling assumptions were adopted:

- **Friction coefficient** μ: Increased with roughness level to simulate enhanced interlocking and post-debonding resistance. The empirical relation $\mu \propto \frac{R_p^0 A}{R_{pm}}$ was used as a guideline, where R_{pm} denotes the mean peak-to-valley surface roughness commonly used to characterize interface roughness.

- **Shear stiffness** K_s: Slightly increased with roughness to reflect higher contact area

and micro-asperity resistance.

- **Shear strength thresholds**: Calibrated to match the experimental peak shear stress for each roughness level.

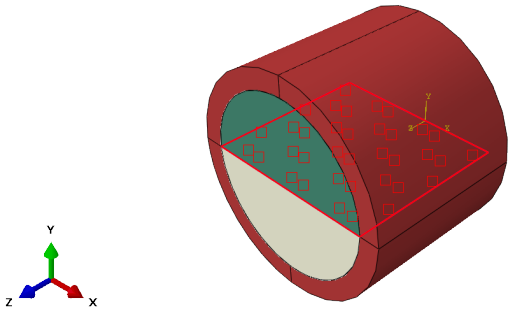

(a) Con-geo interface (in red)

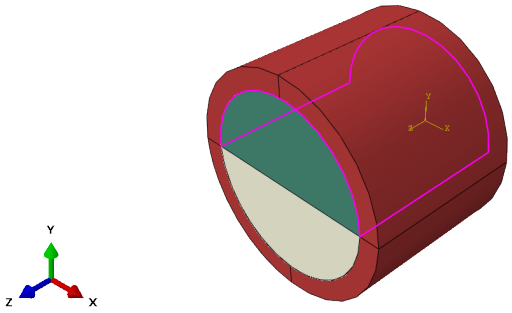

(b) Con-rubber interface (in pink)

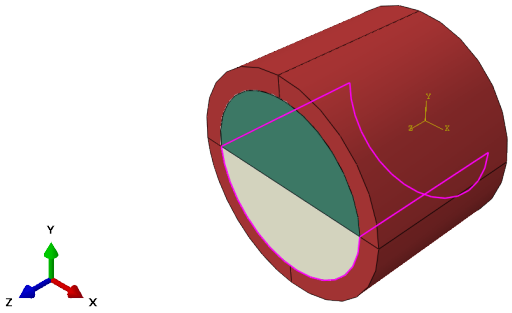

(c) Geo-rubber interface (in pink)

Figure 4.5: Configuration of interfaces in the geopolymer–concrete model

Figure 4.5 illustrates the three types of interfaces modeled in the simulation: (a) the geo–con interface, which is the primary focus; (b) the con–rubber interface; and (c) the geo–rubber interface. The latter two were included to apply radial confinement and avoid

stress concentration at the boundaries. A simple frictional contact model with a low penalty coefficient was applied to the rubber interfaces to allow nearly frictionless sliding.

The roughness effects were modeled by calibrating the shear stress–displacement curves for each roughness level using experimental results. The smooth interface was taken as the baseline, and incremental increases in μ, K_s, and strength thresholds were applied for rougher surfaces.This approach allows the model to replicate the strengthening effect of surface roughness without adding geometric complexity to the finite element mesh.

3.3 Model calibration and parameter validation

The parameter calibration followed a two-step strategy: (i) initial parameter identification based on the smooth interface (L0), and (ii) roughness-dependent parameter adjustment for rough interfaces (L1–L3).

3.3.1 Smooth Interface (L0)

As illustrated in Figure 4.6, the simulation curve "Model-L0" shows good agreement with the experimental data from three repeated direct shear tests (C-L0-1, C-L0-2, and C-L0-3) performed on smooth geopolymer–concrete interfaces. The key mechanical stages captured by the model include:

- **Initial elastic response:** The stiffness parameters ($K_n = 20\ \mathrm{GPa/m}$; $K_{ss} = K_{tt} = 9\ \mathrm{GPa/m}$) were calibrated using the linear portion of the experimental load–displacement curves. To ensure accuracy, the initial compaction phase (typically below 0.05 mm) was excluded, and the fitting was performed over the range where a stable linear slope could be observed, representing the true elastic response of the interface.

- **Peak shear strength:** The maximum shear stress was well captured with a damage initiation threshold of $5.8\ \mathrm{MPa}$, corresponding closely to the peak loads observed in all three tests.

- **Post-peak softening:** The descending branch of the response was modeled using an exponential damage evolution law with a softening parameter $\alpha = 5$, along with

a friction penalty coefficient of 1. This combination reproduced the gradual strength degradation and the residual shear capacity observed experimentally.

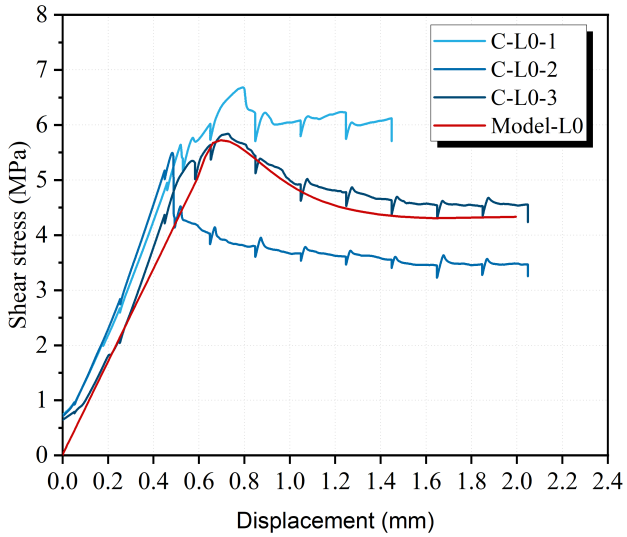

Figure 4.6: Model prediction and experimental results for smooth interface (L0)

Note: Experimental curves C-L0-1, C-L0-2, and C-L0-3 correspond to three replicate direct shear tests on smooth geo–con interfaces. The red line (Model-L0) represents the numerical simulation using calibrated parameters. The elastic stiffness was obtained by fitting the linear portion of the experimental curves after removing the initial compaction stage.

The calibrated parameters for the L0 interface are summarized in Table 4.3, which also includes values for the con–rubber and geo–rubber interfaces.

Table 4.3
Calibrated parameters for smooth interface and rubber interfaces

Interface Type	Behavior Law	Parameter	Value
Geo-con (L0)	Cohesive behavior	K_n (GPa/m)	20
		K_{ss}, K_{tt} (GPa/m)	9
	Damage initiation	Normal damage initiation (MPa)	1
		Shear 1 damage initiation (MPa)	5.8
		Shear 2 damage initiation (MPa)	5.8
	Damage evolution	Plastic displacement (mm)	1
		Exponential parameter	5
	Tangential behavior	Friction penalty	1
		Normal behavior	Hard contact
Con-rubber	Tangential behavior	Friction penalty	0.0001
		Normal behavior	Hard contact
Geo-rubber	Tangential behavior	Friction penalty	0.0001
		Normal behavior	Hard contact

3.3.2 Rough Interfaces (L1, L2, L3)

To simulate the influence of surface roughness, the cohesive parameters calibrated for the smooth interface (L0) were systematically adjusted. The modifications reflect the enhanced stiffness, bond strength, and brittleness observed in experiments. The comparison between simulations and experimental data is shown in Figures 4.7 to 4.9.

The parameters were calibrated using representative experimental curves from each group. For instance, in L3, the simulation is based on C-L3-3, which demonstrated average peak strength and a typical post-peak trend. This choice ensures a meaningful fit without overfitting to one specific outlier. Only the stable elastic region (excluding the initial compaction phase below 0.05 mm) was used for calibrating tangential stiffness. Damage evolution parameters were tuned to match the post-peak descending slope.

Key observations include:

- **L1:** Slight increase in tangential stiffness ($K_{ss} = K_{tt} = 11\ \mathrm{MPa/mm}$) and initiation strength ($\tau_s^0 = 6.5\ \mathrm{MPa}$) yielded higher initial slope and peak stress than

L0.

- **L2:** Increased strength (7.3 MPa) and stiffness (12 MPa/mm) reproduced the sharper post-peak descent, still governed by moderate damage evolution rate ($\alpha = 5$).

- **L3:** To capture the brittle behavior with a pronounced post-peak drop, the softening rate α was reduced to 1, meaning damage accumulates more rapidly once initiated. This represents a more fragile interfacial failure as roughness enhances mechanical interlock but leads to sudden strength loss once damaged.

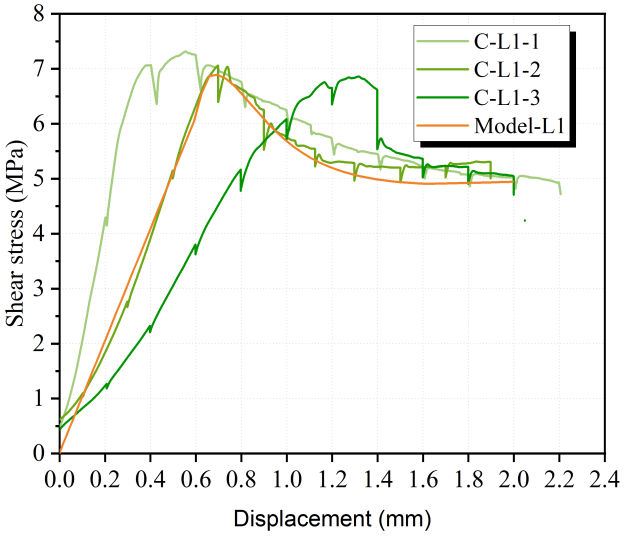

Figure 4.7: Model prediction and experimental results for rough interface L1

Note: C-L1-1, C-L1-2, and C-L1-3 represent experimental results of geo-con interfaces with roughness level L1. The orange line (Model-L1) denotes the numerical prediction using adjusted stiffness and damage parameters specific to L1.

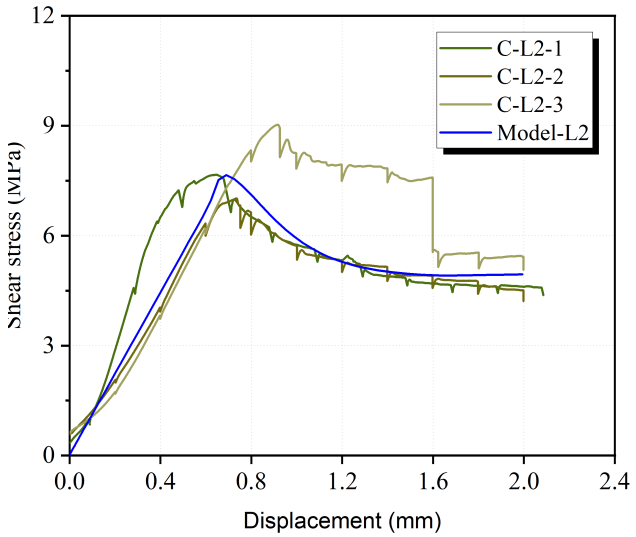

Figure 4.8: Model prediction and experimental results for rough interface L2

Note: Experimental results from three samples (C-L2-1 to C-L2-3) represent direct shear tests on geo-con interfaces with roughness level L2. The dark line (Model-L2) is the simulated shear response based on optimized interface parameters for L2.

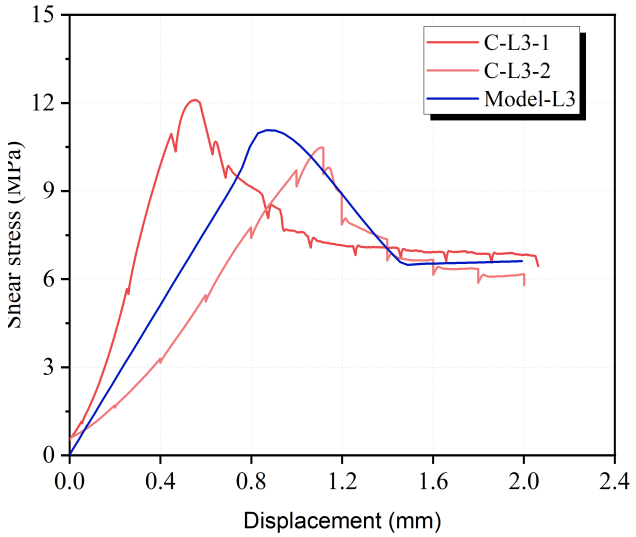

Figure 4.9: Model prediction and experimental results for rough interface L3

Note: C-L3-1 and C-L3-2 are experimental shear stress–displacement curves for geo-con interfaces with the highest roughness (L3). Model-L3 is calibrated based on C-L3-3, capturing its typical peak and post-peak behavior.

Table 4.4
Interface model parameters for the geo–con interface under different roughness levels

Behavior law	**Parameter**	**L0**	**L1**	**L2**	**L3**
Cohesive behavior	K_{nn} (MPa/mm)	20	20	20	20
	K_{ss} (MPa/mm)	9	11	12	14
	K_{tt} (MPa/mm)	9	11	12	14
Damage initiation	σ_n^0 (MPa)	1.0	1.0	1.0	1.0
	τ_{s1}^0 (MPa)	5.8	6.5	7.3	10.5
	τ_{s2}^0 (MPa)	5.8	6.5	7.3	10.5
Damage evolution	$\delta^f - \delta^0$ (mm)	1.0	1.0	1.0	0.7
	α	5	5	5	1
Tangential behavior	Friction penalty	1.0	1.1	1.1	1.35
	Normal behavior	Hard contact	Hard contact	Hard contact	Hard contact

These results collectively demonstrate that increased surface roughness significantly enhances the interfacial shear strength and initial stiffness due to improved mechanical interlocking and bond effectiveness. However, this enhancement also leads to a more abrupt post-peak response, especially for the L3 group, indicating a transition toward more brittle failure modes. The calibrated model successfully captures these trends by adjusting the damage initiation thresholds, tangential stiffness, and the exponential softening parameter α. This supports the suitability of the cohesive–frictional interface model in simulating various roughness conditions observed in geopolymer–concrete shear interfaces.

4 Numerical results and analysis

This section presents and interprets the numerical simulation results to gain deeper insights into the shear behavior at the geopolymer–concrete (geo–con) interface. Particular attention is paid to the evolution of interfacial stress and displacement, as well as the influence of key parameters such as interface roughness, bond strength, and confining pressure on the failure mechanisms. The results provide valuable understanding of the interaction between cohesive bonding and frictional sliding, which governs the overall mechanical response of the interface under shear loading.

4.1 Stages of shear behavior

The simulated shear response of the geo–con interface reveals three distinct stages of interfacial mechanical behavior, which are schematically summarized as follows:

- **Stage I – Elastic deformation:** At the initial stage of loading, the interface exhibits a linear elastic response governed by the intact cohesive bond between the geopolymer mortar and concrete substrate. This stage is characterized by a steep linear rise in the shear stress–displacement curve, controlled by the normal and tangential stiffness parameters K_n, K_{ss}, and K_{tt}.
- **Stage II – Progressive debonding:** Once the interfacial stress reaches the bond strength threshold, damage initiates and gradually evolves according to the exponential damage law defined in the cohesive interface model. This stage is accompanied by a reduction in slope and subsequent softening in the shear curve, reflecting

the degradation of adhesive strength. The shear stress may peak and then begin to drop as localized debonding progresses along the interface.

- **Stage III – Frictional sliding:** After substantial bond degradation, the mechanical response becomes dominated by frictional resistance. At this stage, the residual shear strength is sustained primarily by roughness-induced interlocking and frictional contact under normal pressure. The magnitude of this residual strength depends on the interface roughness level and the applied confining pressure (σ_n). A higher roughness leads to increased post-peak resistance and energy dissipation.

To further understand the evolution of contact pressure during the shear process, the normal stress distribution (CPRESS) on both sides of the interface was extracted and visualized at three representative loading stages: (a) prior to confinement application, (b) after the confinement is fully applied but before shear loading, and (c) after the completion of shear displacement (2 mm). This analysis aimed to verify whether the actual normal stress developed at the interface corresponds to the externally applied confining pressure, and whether this normal contact stress is uniformly distributed.

The results are presented in Figure 4.10 for the geopolymer side and Figure 4.11 for the concrete side.

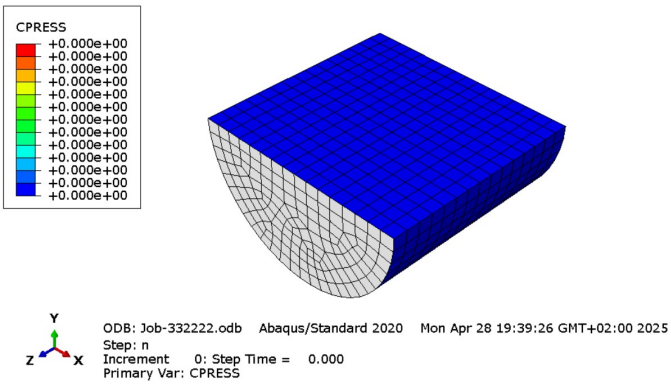

(a) Initial stage (no confinement applied)

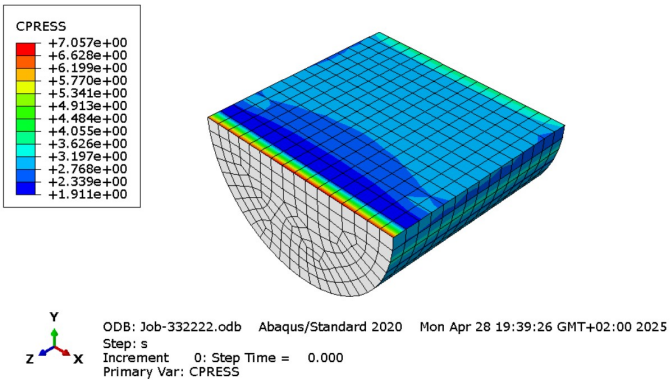

(b) Confinement applied, prior to shear

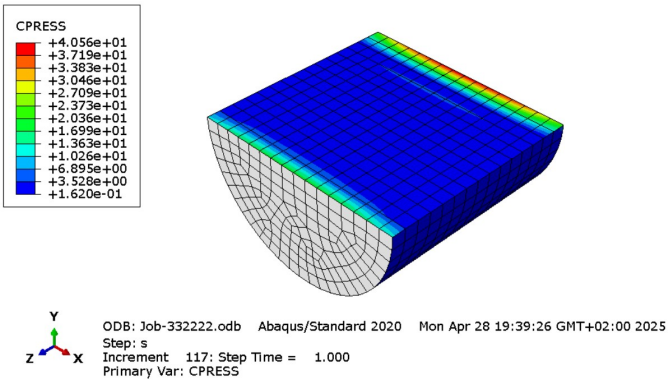

(c) Post-shear stage (2 mm displacement)

Figure 4.10: Normal contact stress (CPRESS) distribution on the geopolymer side at different loading stages

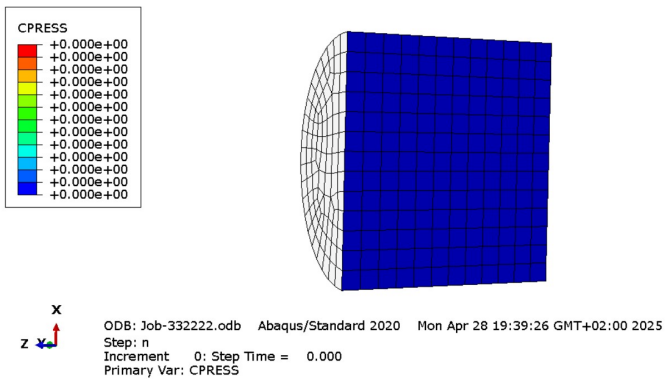

(a) Initial stage (no confinement applied)

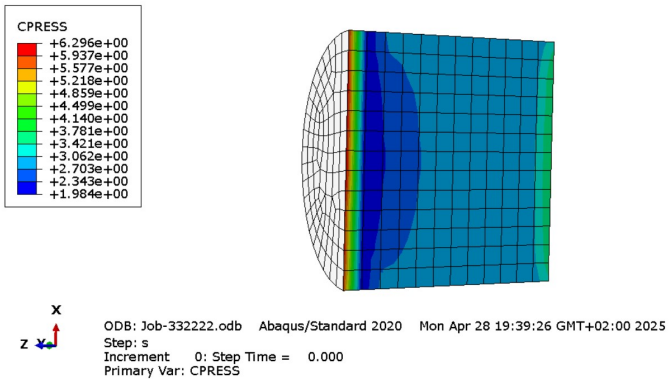

(b) Confinement applied, prior to shear

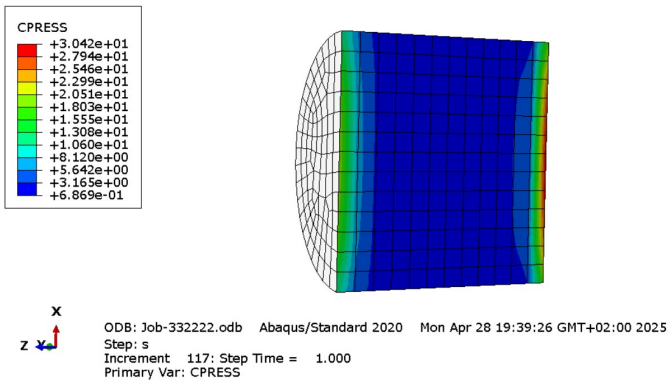

(c) Post-shear stage (2 mm displacement)

Figure 4.11: Normal contact stress (CPRESS) distribution on the concrete side at different loading stages

The results show that before confinement (Figure 4.10(a) and Figure 4.11(a)), no contact stress is transmitted across the interface. Once the normal confinement is applied (Figure 4.10(b) and Figure 4.11(b)), CPRESS increases significantly, indicating full contact. During shear displacement, the CPRESS field becomes redistributed (Figure 4.10(c)

and Figure 4.11(c)), especially at the edge zones, due to frictional sliding and partial separation. This evolution confirms that the interface remains mostly in contact during shear and validates the implementation of frictional contact mechanics in the numerical model.

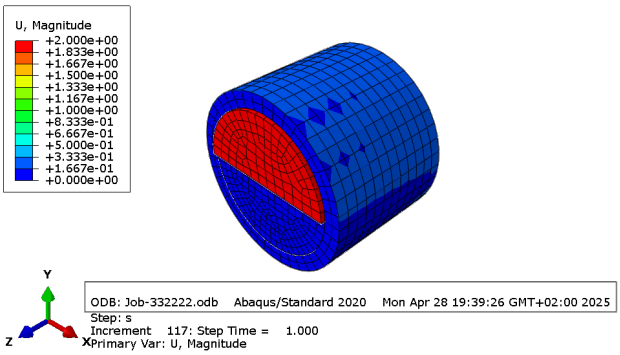

(a) Displacement field (U = 2 mm, Magnitude)

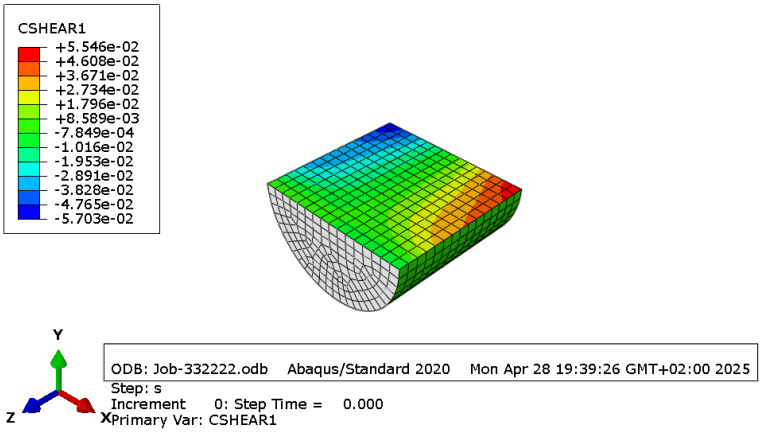

(b) Shear strain (CSHEAR1) on the geopolymer side at intermediate loading stage

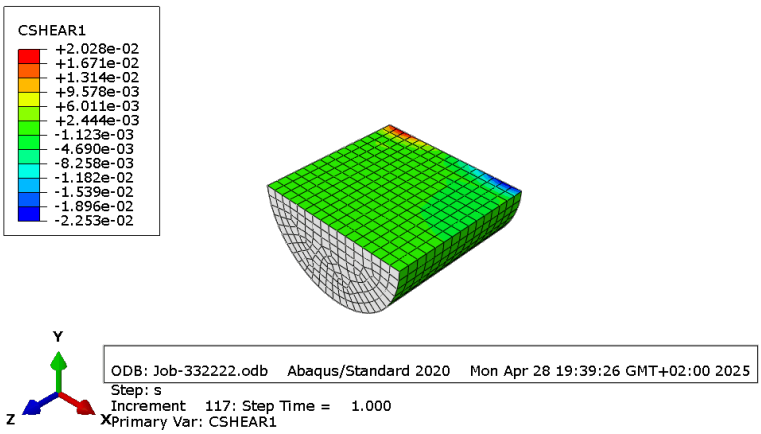

(c) Shear strain (CSHEAR1) on the geopolymer side at final loading stage

Figure 4.12: Evolution of displacement and interfacial shear strain (geopolymer side) in the numerical simulation of smooth geo–con interface under shear loading

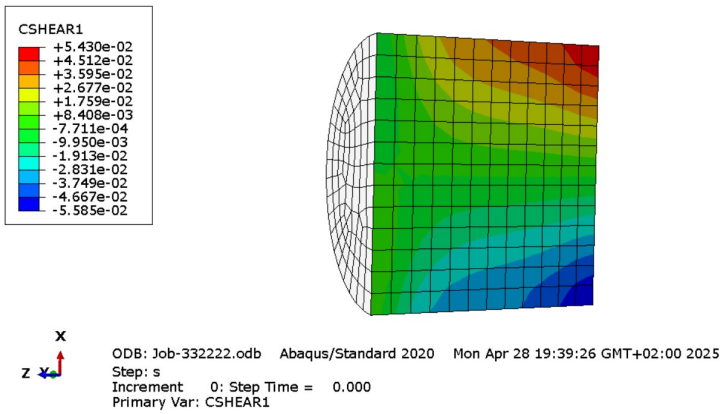

(a) Shear strain (CSHEAR1) on the concrete side at intermediate loading stage

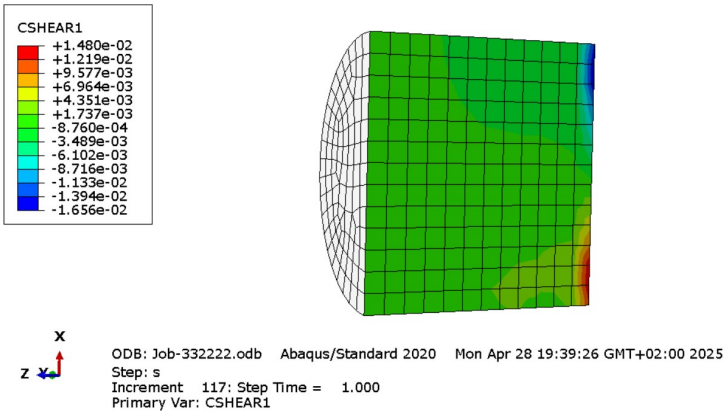

(b) Shear strain (CSHEAR1) on the concrete side at final loading stage

Figure 4.13: Shear strain evolution on the concrete side in the numerical simulation of smooth geo–con interface under shear loading

These three stages—elastic deformation, cohesive debonding, and frictional sliding—are consistent with the experimental observations and the theoretical framework proposed by Saiang et al. (2005), indicating the reliability of the current numerical model in simulating the coupled bond–frictional behavior at geomaterial interfaces.

Post-processing of the finite element simulation was performed to visualize deformation and strain distribution. As shown in Figure 4.12(a), the displacement field demonstrates a nearly uniform relative motion concentrated along the interface, consistent with the prescribed shear displacement, validating the correct kinematic implementation of the loading condition.

In addition, Figure 4.12(b) presents the shear strain distribution (CSHEAR1) on the geopolymer side at an intermediate loading stage. The strain concentration is clearly

localized at the interface region, while the surrounding concrete and geopolymer domains remain mostly unaffected, confirming that the deformation is dominantly governed by interfacial behavior rather than bulk material failure.

At the final stage of loading, Figure 4.12(c) illustrates that the shear strain on the geopolymer side remains continuous and bounded, with no signs of severe localization or damage propagation into the adjoining materials. This observation aligns with the cohesive zone model results and supports the assumption of a smooth interface without macro-interlocking, where shear resistance is predominantly controlled by interfacial bonding and minor frictional contributions.

To provide a complete view of the interface behavior, the shear strain fields on the concrete side are also plotted separately in Figures 4.13(a) and 4.13(b). These plots confirm that strain distribution on the concrete side mirrors the trends observed in the geopolymer region, with localization concentrated near the interface and limited propagation into the bulk. The similarity in strain profiles across both materials supports the validity of the interfacial modeling assumptions and further enhances confidence in the numerical simulation results.

4.2 Parametric studies with interface roughness

Building on the surface roughness analysis presented in Section 3.4.4 of Chapter 3, the arithmetic mean height S_a was selected as the quantitative descriptor of surface roughness for different concrete surface treatments. As a standardized roughness index, S_a enables comparative analysis across smooth, sandblasted, and shear-damaged surfaces.

A correlation analysis was conducted between the interface parameters calibrated in Table 4.4 and the average surface roughness values S_a. Four roughness categories were considered: L0 ($S_a = 41.73$ μm), L1 ($S_a = 168.4$ μm), L2 ($S_a = 476.83$ μm), and L3 ($S_a = 1124.8$ μm), as summarized in Figure 3.14, Figure 3.15, and Figure 3.16.

The key parameters were grouped into three categories: (i) normalized damage initiation strengths τ_{s1}^0, τ_{s2}^0, which reflect the peak shear capacity; (ii) damage evolution parameters $(\delta^f - \delta^0)$ and α, related to post-peak degradation and energy dissipation; and (iii) friction penalty, which governs residual shear resistance.

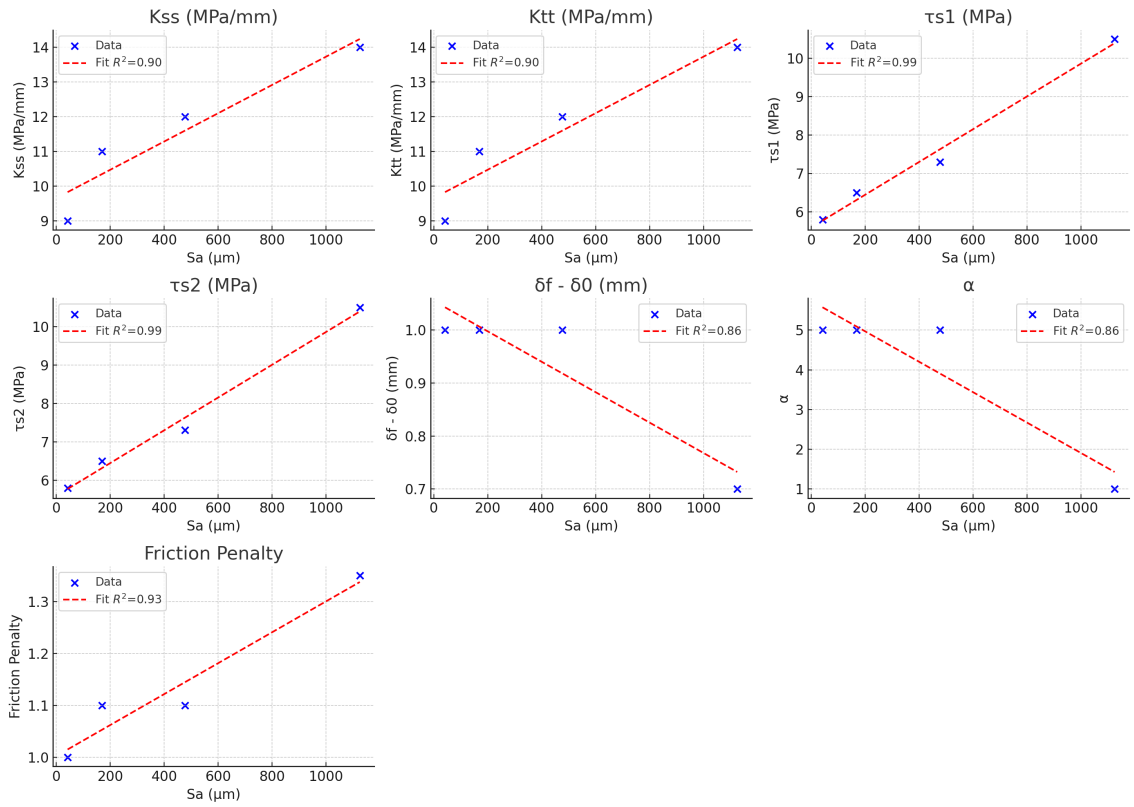

Figure 4.14: Correlation between interface parameters and interface roughness(Sa)

Figure 4.14 shows the scatter plots between each interface parameter and the corresponding S_a value, with linear regression fits. A clear positive correlation was observed between S_a and the stiffness/strength parameters K_{ss}, K_{tt}, τ_{s1}^0, and τ_{s2}^0, with coefficients of determination R^2 ranging from 0.90 to 0.99. This indicates that surface roughness enhances mechanical interlocking, thereby increasing the shear capacity of the interface.

A decreasing trend was also observed for the post-peak damage evolution parameters $\delta^f - \delta^0$ and α with increasing S_a ($R^2 = 0.86$). Although based on a limited number of fitted parameter sets, this trend suggests that rougher interfaces may undergo sharper softening and faster energy dissipation, consistent with reduced cohesion and enhanced frictional sliding.

These findings suggest a transition in interface behavior from bond-dominated to friction-dominated shear mechanisms as surface roughness increases, and highlight the strong interdependence between surface morphology and interface constitutive behavior.

4.3 Prediction of the shear response of concentric cell shear

To explore interface behavior under conditions closer to triaxial confinement and radial stress conditions, a concentric cell shear configuration was adopted. This geometry mimics structural conditions encountered in cylindrical repairs and composite interfaces, and allows uniform confinement application while minimizing edge effects.

In order to further evaluate the applicability of the calibrated interface model under modified structural configurations, a new shear loading scenario—referred to as concentric cell shear—was simulated. This setup retains the same materials, interface models, and mesh strategies as those applied in previous shear simulations. In particular, the cohesive–frictional model for the geo-con interface is maintained as calibrated.

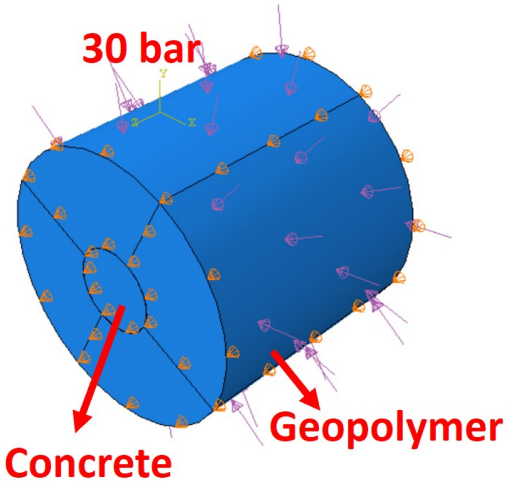

Figure 4.15: Boundary condition of the shear response of concentric cell shear

The major distinction lies in the geometry of the specimen: unlike the previous configuration where the concrete and geopolymer are positioned side-by-side, the concentric model features a concrete core embedded within an outer geopolymer cylinder (Figure 4.15). A confining pressure of 30 bar is applied uniformly around the external boundary to replicate the triaxial compression conditions. Shear loading is introduced via an axial displacement of 2 mm applied on the internal concrete core, while the external geopolymer boundary remains fixed.

4.3.1 Influence of confining pressure

To investigate the effect of confining pressure on the shear response of the concentric cell configuration, a series of numerical simulations were conducted under varying confinement levels. In this setup, the inner concrete core is surrounded by geopolymer, and the interface is modeled as a smooth geo–con surface, consistent with previous calibration. Material properties and mesh discretization remain identical to those used in the half-cylinder shear simulations.

A constant radial pressure of 3, 10, 20, or 30 bar was applied to the outer geopolymer layer. A 2 mm axial displacement was imposed on the concrete core to induce interfacial shear. The simulated shear stress–displacement responses under different confining pressures are shown in Figure 4.16.

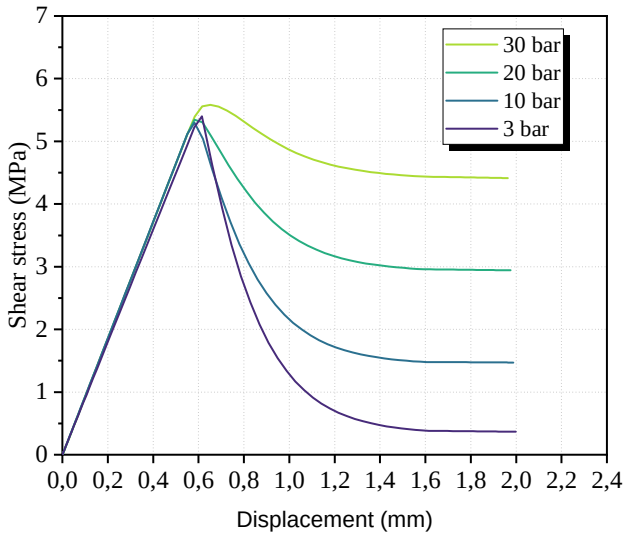

Figure 4.16: Shear stress–displacement response of the concentric geo–con interface under different confining pressures

The results demonstrate a clear trend: increasing confining pressure leads to moderately higher peak shear stress and significantly elevated residual strength. This enhancement arises from greater normal compression at the interface, which increases frictional resistance and delays separation. The simulation under 30 bar exhibits a smoother post-peak decay, indicating enhanced frictional engagement.

Note that the reported shear stress values represent total reaction force divided by the bonded interface area, accounting for geometry variation.

4.3.2 Influence of cell diameter

To examine the effect of concrete core size on the interface behavior, simulations were performed with varying inner core diameters (10 mm, 15 mm, 20 mm, 30 mm), while keeping the outer diameter fixed at 65 mm. A constant confining pressure of 30 bar was applied, and all interfaces were assumed smooth.

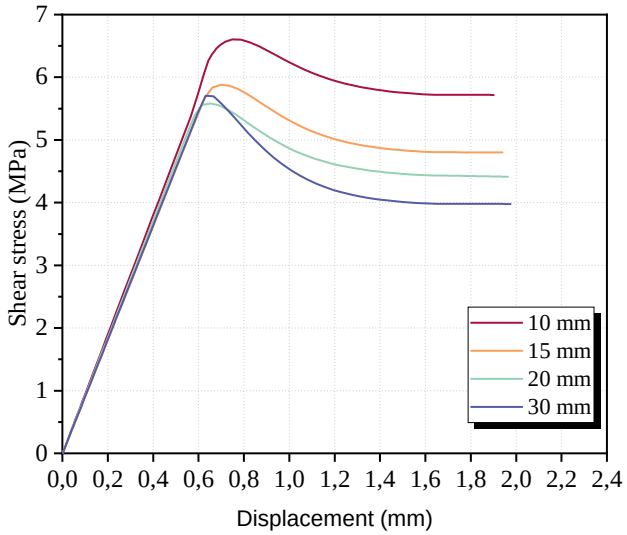

Figure 4.17: Shear stress–displacement response of geo–con interfaces with various concrete core diameters under 30 bar confinement

As shown in Figure 4.17, smaller core diameters result in higher peak shear stress. This trend stems from the increased confinement effectiveness provided by the surrounding geopolymer ring on a smaller core, which intensifies interface pressure and friction. Consequently, reduced diameters also lead to greater energy dissipation and delayed degradation.

Future analysis may consider the influence of dilation angle on stress transfer and volumetric interaction during interfacial sliding.

4.3.3 Influence of roughness

To explore the role of surface morphology on interface shear behavior, a parametric analysis was conducted under constant confining pressure of 30 bar and a concrete core diameter of 20 mm. The simulations were performed using three different interface conditions: L0, L1, and L2.

Figure 4.18 shows the resulting shear stress–displacement responses. It is evident that increasing surface roughness significantly enhances the interface peak shear strength. Specifically, the interface with roughness L2 exhibits the highest shear strength, followed by L1 and the smooth interface. This trend can be attributed to increased mechanical interlocking and frictional mobilization induced by surface asperities under high confining pressure.

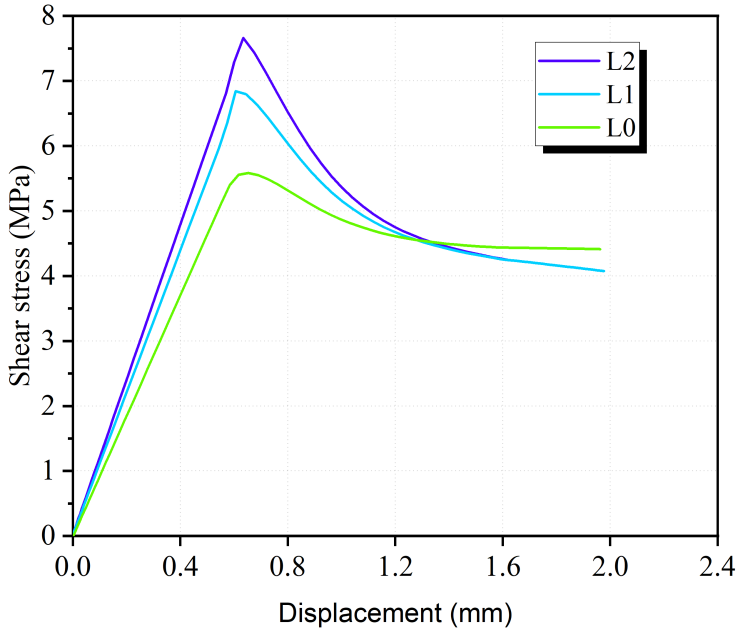

Figure 4.18: Shear stress–displacement response of geo-con interfaces with various roughness under 30 bar confinement

4.4 Evolution of displacement and strain fields

To gain further insight into the deformation mechanisms at the geo–con interface during shear loading, the displacement and shear strain (CSHEAR1) fields were extracted from the numerical simulation of the concentric cell shear test. The interface used in this analysis corresponds to a smooth concrete–geopolymer configuration, subjected to 30 bar confining pressure and a 2 mm horizontal displacement imposed on the concrete core.

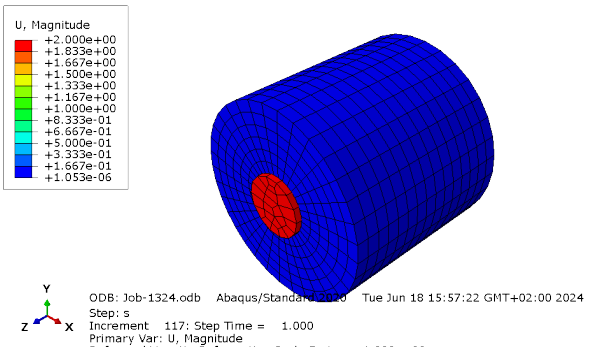

(a) Displacement field (U = 2 mm, Magnitude)

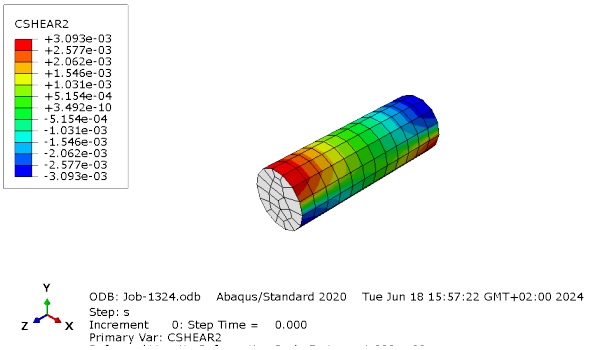

(b) Shear strain (CSHEAR1) distribution at intermediate loading stage

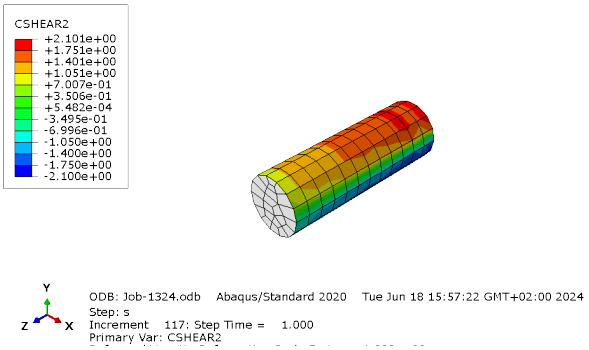

(c) Shear strain (CSHEAR1) distribution at the final loading stage

Figure 4.19: Evolution of displacement and shear strain fields in the concentric cell shear numerical simulation of smooth geo–con interface

Figure 4.19 illustrates the spatial distribution of displacement and shear strain at selected loading stages. The displacement field shown in Figure 4.19(a) confirms that the primary deformation is concentrated near the interface region, with maximum displacement occurring at the outer edge of the geopolymer ring. This distribution indicates effective confinement of the central concrete by the surrounding geopolymer.

Notably, the CSHEAR1 distributions in Figures 4.19(b) and 4.19(c) exhibit non-symmetric

strain localization patterns. This asymmetry likely results from small mesh distortions or numerical perturbations accumulated during large deformation steps. Although the geometry and boundary conditions were axisymmetric, the explicit breaking of symmetry is often observed in nonlinear shear simulations due to progressive damage or convergence sensitivity.

Shear strain maps at intermediate and final loading stages, shown in Figure 4.19(b) and Figure 4.19(c), reveal a progressive accumulation of shear deformation. The intermediate stage exhibits strain concentration along part of the interface perimeter, while the final stage displays a more extensive strain band spanning the entire interface region. This evolution suggests that damage initiates locally and propagates asymmetrically along the interface with increasing shear displacement, which is consistent with typical post-peak softening behavior and interface sliding observed in experimental tests.

5 Conclusion

This chapter presented a numerical investigation of the hydro-mechanical behavior of geo-con interfaces subjected to shear loading under confining pressure. A cohesive–frictional interface model was used and calibrated based on experimental shear test results. The model was able to accurately reproduce the shear stress–displacement responses for various surface conditions, including smooth and rough interfaces.

For smooth interfaces, numerical simulations revealed excellent agreement with experimental data in terms of initial stiffness, peak strength, and post-peak softening behavior. Strain field analysis further confirmed localized deformation near the interface, consistent with experimental observations.

For rough interfaces, parametric calibration was conducted for three distinct roughness levels. A correlation analysis between interface parameters and surface roughness (quantified by S_a) demonstrated that increasing roughness leads to higher shear stiffness and strength, while reducing softening displacement and increasing frictional contribution. This indicates a transition from bond-dominated to friction-dominated failure mechanisms as roughness increases.

Moreover, concentric cell shear simulations were conducted to evaluate the influence of geometric and loading parameters. Results showed that both confining pressure and

cell diameter significantly affect the shear strength and deformation behavior. Higher confining pressure and smaller cell diameter enhance confinement and interfacial strength. Increased roughness in the concentric configuration also led to pronounced improvements in shear resistance.

The validated model captures multiscale geopolymer-concrete interface mechanics under confinement. By integrating numerical and experimental results, this study advances understanding of interfacial shear behavior. Future work will address cyclic loading and environmental degradation effects.

CHAPTER 5

Experimental investigation of Geopolymer-steel Interfaces

1 Introduction

This chapter investigates the coupled hydro-mechanical behavior at the interface between geopolymer mortar and steel. Initial shear tests revealed that premature debonding frequently occurred due to shrinkage-induced cracking of the geopolymer, making it difficult to obtain reliable measurements of interfacial strength or permeability. Surface treatments and adhesive improvements were found to be insufficient in resolving this problem.

To overcome these limitations, a new concentric cell configuration was developed. In this design, the steel substrate is embedded centrally within the geopolymer matrix, allowing for symmetric loading and direct interface activation. The modified setup successfully eliminated steel-to-steel load transfer and made it possible to evaluate shear and permeability behaviors under controlled boundary conditions.

Following the validation of this improved method, further experiments were conducted to examine the influence of a phosphatic additive on the geopolymer–steel interface. The effect on bonding strength and permeability evolution was evaluated and compared to the reference system.

2 Trial tests on geopolymer-steel specimens

A series of preliminary trial tests were conducted to explore the feasibility of bonding geopolymer mortar to steel substrates and to develop a suitable testing methodology for evaluating interfacial performance. These exploratory experiments were inspired by earlier work on geo-concrete interfaces and aimed to assess whether a similar two-part casting configuration could be applied to geo-steel systems. In these trials, various strategies were explored, including modifying the steel surface roughness, adjusting the precursor composition of the geopolymer, and incorporating chemical additives, with the goal of improving interface compatibility and mechanical interaction.

2.1 Specimen preparation for geopolymer-steel interface testing



(a) Semi-cylindrical steel blocks with different surface textures

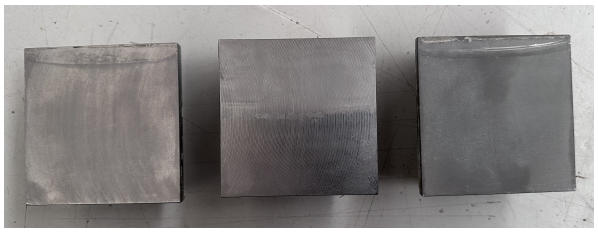

(b) Views of flat steel substrates exhibiting different surface roughness

Figure 5.1: Steel substrates with varying surface roughness for Geo-steel interface preparation

The preparation of geo-steel interface specimens followed a two-part casting approach to replicate controlled bonding conditions. As shown in Figure 5.1, three types of steel substrates were first machined into semi-cylindrical shapes with varying surface roughness levels: Very Smooth (VS), Smooth (S), and Rough (R). These prepared surfaces served as bonding templates for the geopolymer mortar.

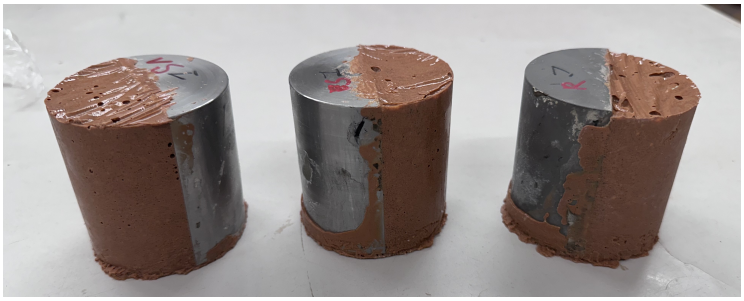

Figure 5.2: Cylindrical geo-Steel specimens after demolding

Subsequently, geopolymer mortar was freshly mixed and cast onto the exposed flat surface of each steel semi-cylinder. After curing and demolding, the specimens were demolded to obtain full cylindrical samples composed of half steel and half geopolymer. The final bonded specimens are displayed in Figure 5.2, clearly illustrating the continuity and integrity of the interface. This half-cylinder configuration provides a well-defined and repeatable geometry for subsequent mechanical tests focused on interfacial shear and fracture behaviors.

2.2 Specimen behavior after curing

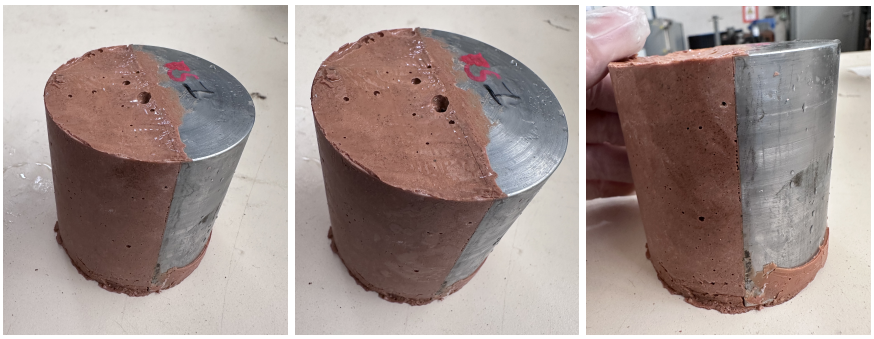

(a) VS surface **(b)** S surface **(c)** R surface

Figure 5.3: Geo-steel interface specimens after curing, showing different steel surface roughness levels

After casting and curing, the geo-steel interface specimens were demolded to evaluate the initial bonding condition between geopolymer mortar and the steel substrates. As shown in Figure 5.3, the external appearance of the specimens suggested that full contact was achieved during casting, with no visible macro-gaps between the geopolymer and the

steel half-cylinders across all roughness conditions. The geopolymer surfaces appeared continuous and well-formed on all specimens.

However, during handling and transfer, it was observed that most specimens exhibited spontaneous interface separation. As illustrated in Figure 5.4, the geopolymer and steel segments detached cleanly along the bonded surface, with no visible mechanical interlocking or cohesive failure. This behavior indicates that the bonding achieved under the initial trial conditions was insufficient to withstand even minimal external disturbances.



Figure 5.4: Debonded geo-steel interface specimens after curing

2.3 Discussion and adjustment

The observations from the preliminary casting and curing tests indicate that the initial geo-steel interface configuration was not sufficient to ensure effective bonding. Although the specimens appeared intact after demolding, the consistent debonding behavior suggests a lack of both chemical and mechanical adhesion under the original conditions. These results highlight the necessity for further adjustments in both material formulation and interface design. Therefore, in the following section, several targeted strategies are introduced to improve the bonding performance of the geopolymer-steel system, including surface treatment, precursor modification, and additive incorporation.

3 Methods to improve geo-steel binder

Based on the initial results discussed, it became evident that modifications were required to enhance the interfacial performance between geopolymer mortar and steel sub-

strates. The improvement strategies focused on three key aspects: (1) optimizing the surface characteristics of the steel substrate to promote better mechanical interlocking (Nguyen et al., 2018; Yang et al., 2022b; Boopalan et al., 2018); (2) adjusting the geopolymer precursor formulation to improve chemical compatibility and reduce shrinkage-induced detachment (Zhang et al., 2024b; Liu et al., 2023); and (3) incorporating additives aimed at enhancing interfacial adhesion or modifying the rheology of the fresh mix (Bhardwaj et al., 2020).

3.1 Surface treatments

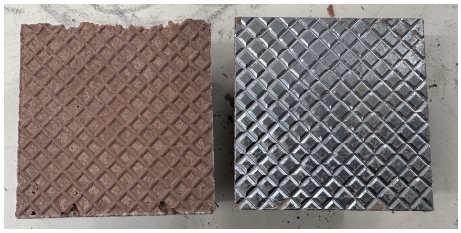

(a) Debonding after curing – mechanically carved steel

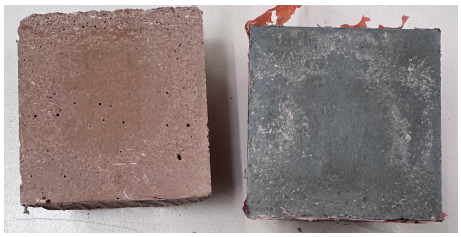

(b) Debonding after curing – chemically treated steel

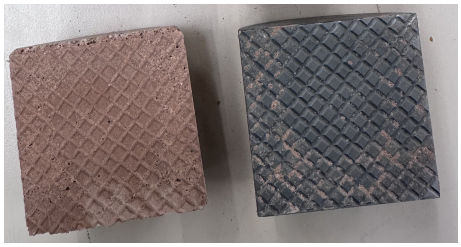

(c) Preloading failure – carved and sandblasted steel

Figure 5.5: Debonded geo-steel specimens with different steel surface treatments

In an effort to enhance the mechanical interlocking at the geo-steel interface, several surface treatment techniques were applied to the steel substrates. The treatments aimed to increase surface roughness and facilitate stronger physical bonding between the steel

and the geopolymer mortar. However, despite the implementation of these strategies, the results indicated that interface integrity remained inadequate.

Three types of surface treatment were investigated:

- **Mechanical carving**, in which a cross-hatched pattern was engraved onto the steel surface (Figure 5.5(a));
- **Chemical etching**, using acid to generate micro-scale surface roughness (Figure 5.5(b));
- **Combined carving and sandblasting**, intended to produce both macro- and micro-textured topographies (Figure 5.5(c)).

After casting and curing, specimens from both the mechanically carved and chemically treated groups (Figure 5.5(a) and Figure 5.5(b)) exhibited immediate debonding—separating cleanly upon demolding or handling, without any applied mechanical load. The combined treatment group (Figure 5.5(c)) showed relatively improved bonding, but still failed at the very initial stage of shear test setup. In these cases, the bond failed even before any displacement or load was applied, as evidenced by a sudden increase in permeability readings and post-test inspection showing complete interface separation at zero displacement.

These outcomes demonstrated that surface treatment alone, even when combining multiple roughening techniques, was insufficient to establish a stable geo-steel interface.

3.2 Using phosphatic additive

To investigate the potential of additive-assisted geopolymer systems for improving interface bonding, a phosphatic additive was incorporated at 2% by mass of metakaolin (MK), as illustrated in Figure 5.6(a). The additive was added during dry blending with MK and standard sand prior to casting.



(a) Mixing with phosphatic additive



(b) Crack (sandblasted)



(c) Crack (sandblasted)



(d) Debonding specimen (sandblasted)



(e) Bonding area



(f) Before setup

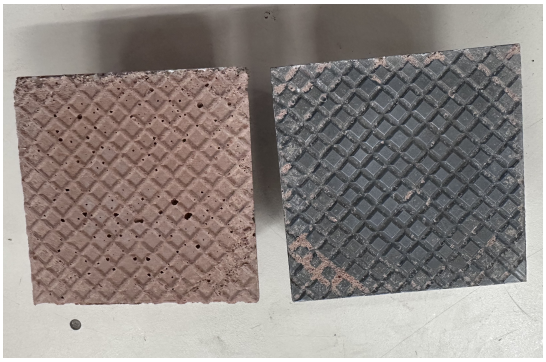

(g) Debonding specimen (carved + sandblasted)

Figure 5.6: Debonding behavior of geo-steel specimens with 2% phosphatic additive

Two interface configurations were tested. In the first group, the mix was cast against **sandblasted steel surfaces**. As shown in Figure 5.6(b), Figure 5.6(c), and Figure 5.6(c), visible cracks appeared within a few days of curing, followed by spontaneous debonding at the interface. These specimens showed poor adhesion, failing even without mechanical loading.

In the second group, the same geopolymer formulation was cast onto **carved and sandblasted steel surfaces**. The specimens appeared visually intact during curing (Figure 5.6(e)), but debonding occurred prematurely during test setup, even before any load

was applied (Figure 5.6(f) and Figure 5.6(g)).

These results demonstrate that the addition of 2% phosphatic additive was not sufficient to ensure stable geopolymer-steel bonding, regardless of surface condition. While early cracking was reduced in the carved group, the bond strength remained too weak for practical mechanical testing.

3.3 Using silicon-rich MK

In this test series, a new metakaolin (MK) with high silicon content was employed, produced by flash calcination technology. The chemical composition of this silicon-rich MK is presented in Table 5.1, showing a significantly elevated SiO_2 content of over 72%, along with moderate levels of Al_2O_3 and minor oxides. The same geopolymer formulation as in previous trials was used, ensuring that any performance change could be attributed to the precursor itself.

Table 5.1
Chemical composition of the silicon-rich metakaolin

New MK	%	CaO	SiO_2	Al_2O_3	Fe_2O_3	K_2O	MgO	SO_3	TiO_2	ZrO_2
		2.52	72.15	14.88	5.17	0.66	0.23	0.10	1.00	0.09

As illustrated in Figure 5.7(a), Figure 5.7(b), and Figure 5.7(c), the use of silicon-rich MK significantly reduced the occurrence of early-age cracks. No visible cracking or delamination was observed during curing, and the specimens remained intact under handling and preparation. This allowed the shear interface testing to proceed smoothly, including simultaneous permeability monitoring under confined loading conditions. A confining pressure of 30 bar was applied throughout the test.

The specimen maintained structural integrity during fixture assembly and shear loading, and the permeability test was successfully conducted. However, the post-failure appearance (Figure 5.7(d), Figure 5.7(e), and Figure 5.7(f)) revealed a relatively low cohesive strength of the geopolymer matrix. This suggests that while the silicon-rich MK improved early interface stability, further optimization of the binder system is still needed to enhance bulk strength and fracture resistance.

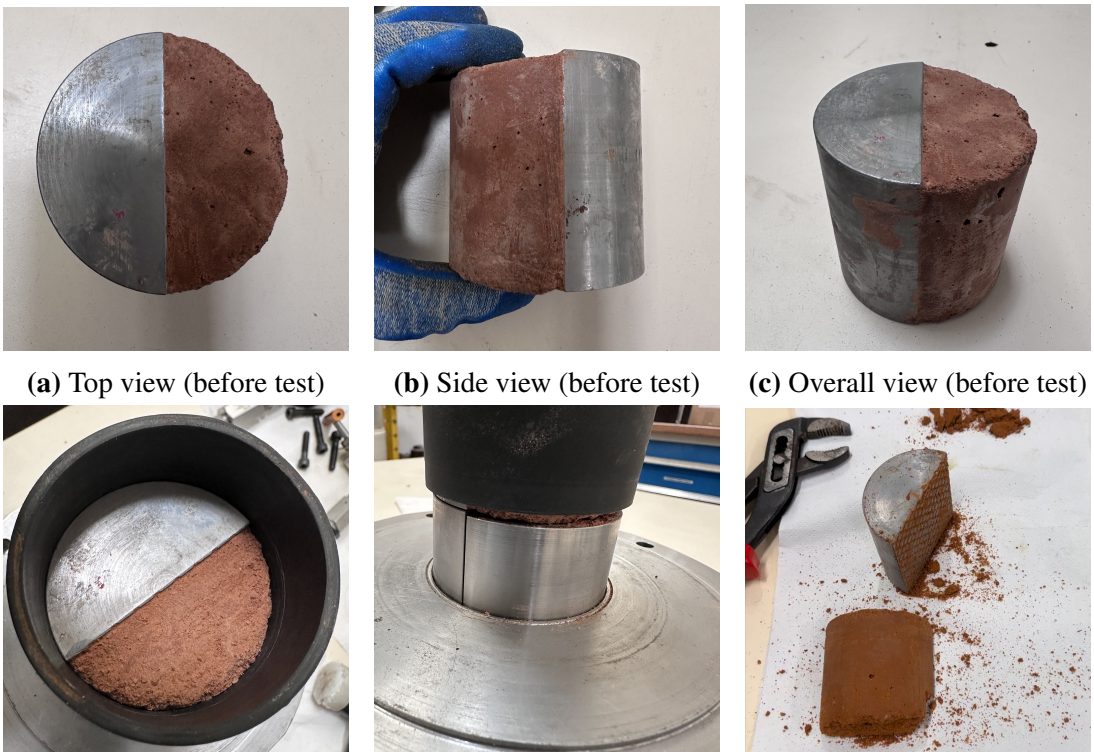

(a) Top view (before test) **(b)** Side view (before test) **(c)** Overall view (before test)

(d) In fixture (after test) **(e)** Removing rubber sleeve **(f)** Failure surface after testing

Figure 5.7: Shear test performance of geo-steel specimens made with silicon-rich MK

The results of the shear-permeability test using the silicon-rich geopolymer are presented in Figure 5.8. Initially, the shear stress increased gradually with displacement, while the permeability coefficient (K) exhibited a decreasing trend. This behavior is consistent with progressive interface mobilization, indicating that the geopolymer matrix was engaged and undergoing shear deformation.

However, after approximately 1.4 mm of displacement, a marked increase in shear stress was observed, while the permeability values remained relatively stable and low (around 2.23×10^{-15} m^2). This decoupling of stress and permeability response suggests a shift in the load transfer mechanism. It is inferred that beyond this point, the geopolymer interface had likely failed, and the applied load was being increasingly supported by the rigid steel component. The stiffer nature of steel, in contrast to the geopolymer, accounts for the sudden rise in measured shear resistance without corresponding permeability changes.

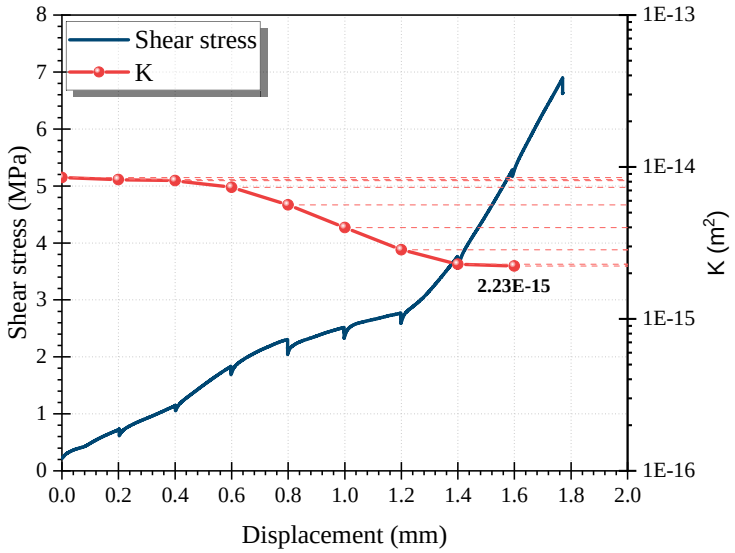

Figure 5.8: Shear stress and permeability results of new MK geopolymer

This behavior implies that while the silicon-rich geopolymer allowed for successful interface testing and permeability capture under confinement, its low cohesive strength limits its contribution in the later stages of deformation. Post-peak resistance was largely governed by the mechanical engagement of the steel substrate, rather than continued bonding at the geo-steel interface.

3.4 Conclusion and adjustments

The trial shear tests discussed consistently exhibited interfacial debonding between the geopolymer mortar and steel substrates. While surface treatments and chemical additives were applied to improve adhesion, these measures failed to prevent early failure. This suggests that the problem does not stem from poor intrinsic bonding, but from a more fundamental incompatibility at the interface.

The primary cause of failure is attributed to differential shrinkage. As the geopolymer undergoes volumetric contraction during curing, the adjacent steel remains dimensionally stable. This mismatch induces tensile stresses at the interface, leading to crack initiation and subsequent debonding. As a result, improvements in adhesion alone—whether through increased surface roughness or chemical interaction—cannot prevent failure if shrinkage remains unaddressed.

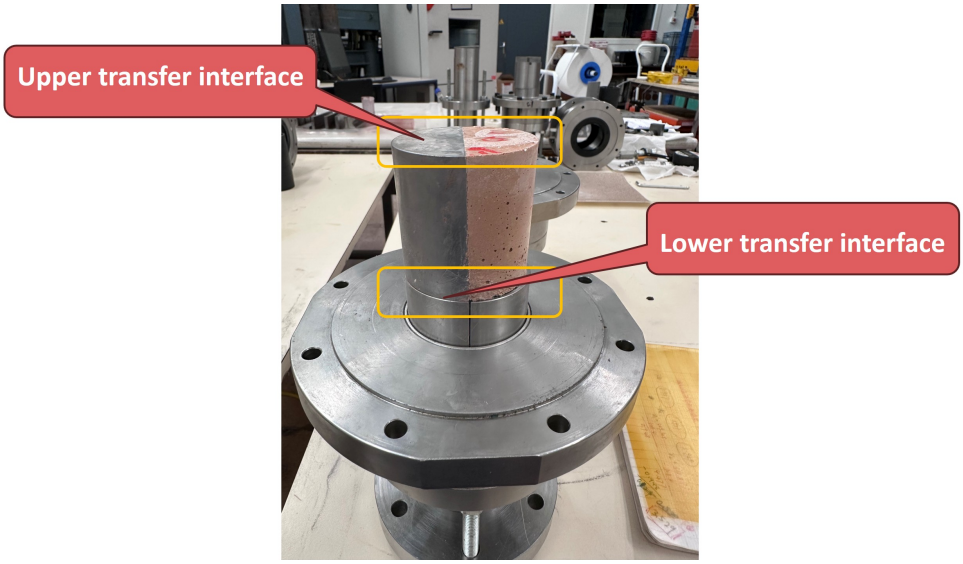

Figure 5.9: Load transfer interfaces in the shear testing setup

Even in specimens where shrinkage-induced damage was minimized, limitations of the testing apparatus introduced further complications. As illustrated in Figure 5.9, the shear test setup relies on perfect alignment between the upper and lower steel–steel transfer interfaces. In practice, however, minor misalignments or imperfections in interface contact often cause part of the load to be transferred directly through the steel components. This unintended load bypass masks the actual response of the geopolymer–steel interface and severely compromises the accuracy of the test results.

Given these observations, the previous tests are regarded as exploratory trials, primarily aimed at identifying interface failure mechanisms and evaluating specimen preparation methods. In the next chapter, a concentric cell testing strategy is introduced to overcome these challenges.

4 Concentric cell testing

To overcome the limitations identified in the preliminary shear interface tests, a concentric cell testing approach was developed. In this configuration, the steel substrate is embedded centrally within a geopolymer matrix, and the entire assembly is subjected to axial loading. Unlike previous methods where load was transferred through external steel-to-steel interfaces, this setup enables direct and symmetric activation of the geo-steel

interface under controlled boundary conditions.

4.1 Test design and cell setup

The overall test system used for the concentric cell experiments was consistent with that employed in the previous geo-con interface trials, including the axial loading system, the confining pressure system (operating under 30 bar), and the gas flow control and data acquisition units. Only the internal test cell was redesigned to enable central loading and more reliable shear path control.

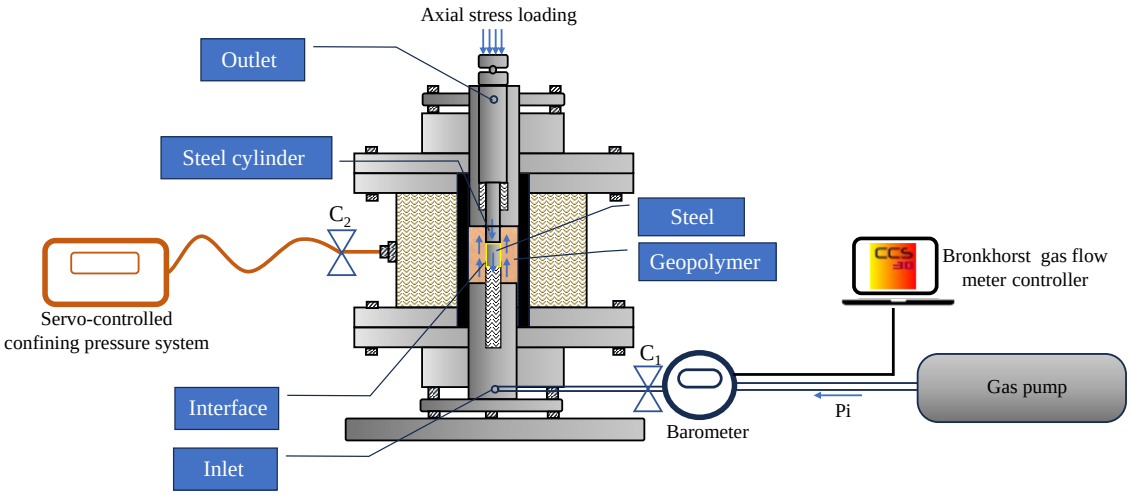

Figure 5.10: Schematic diagram cell under press for concentric cell shear and permeability test

As shown in Figure 5.10, the modified cell adopts a concentric geometry where a cylindrical steel rod is embedded symmetrically within a geopolymer matrix. The steel insert, with a diameter of 20 mm and a height of 30 mm, serves as the core substrate. It is concentrically surrounded by a geopolymer cylinder with a diameter of 65 mm and a height of approximately 60 mm. This configuration ensures uniform circumferential confinement and accurate activation of the steel–geopolymer interface under axial compression.

The axial load is applied vertically onto the top face of the steel insert, while the surrounding geopolymer is confined by a servo-controlled lateral pressure system. Gas flow is introduced from the bottom inlet, allowing measurement of interface permeability throughout the shear test. This revised setup guarantees clear boundary conditions and

eliminates steel-to-steel load transfer paths, thus ensuring the test response is governed solely by the interface mechanics.

4.2 Shear test with permeability measure of geopolymer-steel interface

Before analyzing the shear and permeability behavior, it is essential to assess the physical condition of the tested specimen. As shown in Figure 5.11, the post-test geo–steel sample exhibited no visible cracks or damage on any surface—top, bottom, or side. This intact appearance indicates that the shear deformation occurred without inducing macroscopic failure in the geopolymer or interfacial delamination. The absence of cracks confirms that the recorded shear strength values are reliable and reflect the genuine mechanical performance of the interface. Moreover, it ensures that the measured permeability was not biased by through-crack gas pathways, thereby validating the subsequent analysis of coupled hydro-mechanical behavior.



(a) Top view after testing **(b)** Bottom view after testing **(c)** Side view after testing

Figure 5.11: Post-test appearance of geo-steel specimen showing no visible cracks, confirming the validity of shear strength results

The results obtained from the concentric cell testing are presented in Figure 5.12, where the evolution of shear stress and gas permeability with respect to axial displacement is plotted. The specimen exhibited stable mechanical behavior with a gradual increase in shear stress up to a peak value of $17.34\,\mathrm{MPa}$ at a displacement of approximately $1.68\,\mathrm{mm}$. This peak indicates the mobilization of interfacial frictional resistance under the applied load.

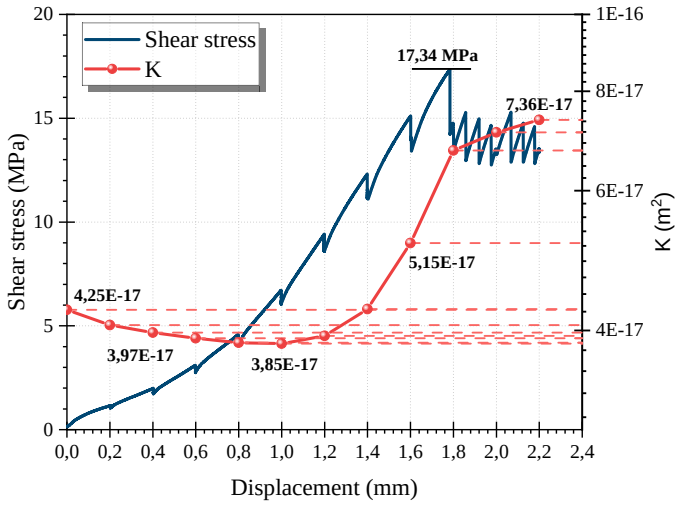

Figure 5.12: Shear stress and permeability results of geo-steel specimen concentric cell testing

The gas permeability (K) showed a distinct two-phase response. Initially, the permeability decreased slightly from $4.25 \times 10^{-17}\,\mathrm{m}^2$ to $3.85 \times 10^{-17}\,\mathrm{m}^2$, suggesting a compaction effect that may have improved the sealing of *microvoids* near the interface. However, after the onset of significant shear displacement (>$1.5\,\mathrm{mm}$), a pronounced increase in permeability was observed, reaching a maximum of $7.36 \times 10^{-17}\,\mathrm{m}^2$. This increase is likely due to the initiation of interface opening or *microcrack* development, which enhanced gas flow pathways.

The simultaneous measurement of mechanical and transport parameters confirms the reliability of the concentric setup and highlights the strong coupling between interface damage and permeability evolution. These findings demonstrate that the failure process of the geo-steel interface is progressive, involving both frictional sliding and structural degradation at the contact zone.

It is also worth noting that the initial gas permeability ($K \approx 4.25 \times 10^{-17}\ \mathrm{m}^2$) was relatively high even before the onset of significant shear displacement. This may be attributed to microcracks or interfacial voids generated during the early curing stage due to autogenous shrinkage of the geopolymer matrix. Although no visible cracks were observed after testing (Figure 5.11), such early-age defects could have created preferential gas pathways, thereby explaining the elevated initial permeability. This hypothesis is consistent with the known shrinkage behavior of geopolymer materials and suggests that sealing capacity at the interface may be partially compromised prior to mechanical load-

ing. Further microstructural investigations, such as SEM or X-ray CT, are recommended to validate the presence and morphology of shrinkage-induced microcracks.

4.3 Using phosphatic additive to improve geopolymer-steel bonding

4.3.1 Compressive and flexural strength of phosphatic geopolymer mortar

The mechanical performance of the phosphatic geopolymer mortar was characterized through standardized flexural and compressive strength tests. All procedures were conducted in accordance with EN 12390-3 (2019) and EN 12390-5 (2019), following the methodology outlined in Chapter 2.

Flexural strength was assessed using three prismatic specimens ($40\,\mathrm{mm} \times 40\,\mathrm{mm} \times 160\,\mathrm{mm}$). The measured failure loads were 2954 N, 2717 N, and 2888 N, corresponding to flexural strengths of 8.08 MPa, 7.44 MPa, and 7.90 MPa, respectively. The average flexural strength was determined to be **7.81 MPa**, which is comparable to the reference value of 7.86 MPa obtained from the unmodified geopolymer system. This result indicates that the incorporation of the phosphatic additive does not adversely affect flexural performance.

Compressive strength was evaluated using the six fractured halves resulting from the flexural tests. The recorded compressive strengths were 55.7 MPa, 53.7 MPa, 53.3 MPa, 53.5 MPa, 49.4 MPa, and 49.2 MPa. The corresponding average compressive strength was **52.15 MPa**, which represents a slight increase compared to the control mixture (49.82 MPa). This improvement may be attributed to enhanced matrix densification or better interface cohesion induced by the 2 wt% phosphatic additive.

In summary, the phosphatic geopolymer mortar exhibits improved compressive strength without compromising flexural capacity, highlighting its potential for structural applications where enhanced load-bearing performance is required.

4.3.2 Shear test with permeability measure of phosphatic geo-steel interface



(a) Top view after testing **(b)** Bottom view after testing **(c)** Side view after testing

Figure 5.13: Post-test appearance of phosphatic geo-steel specimen showing no visible cracks, confirming the validity of shear strength results

The reliability of the shear test results was first confirmed by the post-test condition of the specimens. As shown in Figure 5.13, the geopolymer-steel composite remained intact after the test, with no visible cracks observed on the top, bottom, or lateral surfaces. This confirms that the shear strength values obtained during the experiment were not influenced by premature failure or macrocrack development, and thus represent the actual interfacial bonding performance.

Based on this validation, a concentric shear-permeability test was performed on a geopolymer specimen with a phosphatic additive, added at $2\,\%$ by mass of metakaolin. The formulation and test setup remained consistent with previous tests. As shown in Figure 5.14, the specimen reached a peak shear strength of $18.26\,\mathrm{MPa}$, representing a slight improvement in mechanical performance compared to the reference without additive.

Regarding permeability, the measured values ranged between $6.14 \times 10^{-19}\,\mathrm{m}^2$ and $2.03 \times 10^{-18}\,\mathrm{m}^2$, with relatively mild fluctuations throughout the shear loading. The initial permeability of $1.06 \times 10^{-18}\,\mathrm{m}^2$ decreased slightly in the early stages, then remained stable or increased marginally. This behavior indicates no significant interface opening or cracking, suggesting that the phosphatic additive may contribute to enhanced interfacial sealing or reduced shrinkage-induced damage.

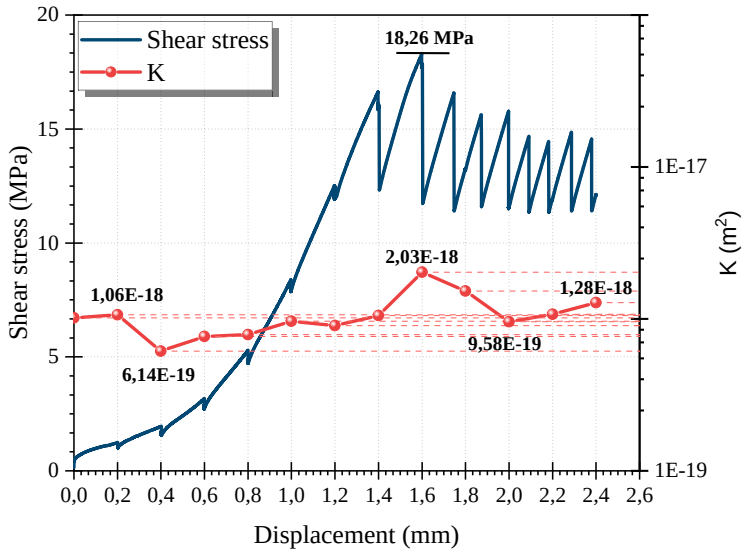

Figure 5.14: Shear stress and permeability results of geo-steel specimen concentric cell testing

Notably, the average permeability observed in this test is significantly lower than that of the geopolymer reference system without additive, which typically exhibited permeability values above $1.00 \times 10^{-18}\,\mathrm{m}^2$ under similar loading conditions. This marked reduction implies that the addition of phosphatic compounds promotes a denser interfacial microstructure, possibly through chemical densification or improved matrix continuity. The results support the hypothesis that phosphatic modification not only enhances compressive strength but also contributes to interface impermeability, which is essential in durability-critical applications such as structural repair and containment.

This reduction in permeability highlights the significant influence of the phosphatic additive on interfacial transport properties. Beyond mechanical performance, the observed densification effect may be attributed to the formation of secondary reaction products at the geopolymer–steel interface, which can reduce micro-defects and hinder fluid migration pathways. Such improvements are critical for geopolymer applications exposed to aggressive environments, where reduced permeability directly translates into enhanced durability and chemical resistance.

It is noteworthy that the initial gas permeability ($K \approx 1.06 \times 10^{-18}\ \mathrm{m}^2$) measured in this test appears higher than expected compared to the reference system (Figure 5.12). This discrepancy may arise from local heterogeneities during casting or interface preparation, such as imperfect contact or entrapped air pockets at the steel–geopolymer interface.

Alternatively, the sample might have undergone minor early-age shrinkage that was not fully mitigated by the phosphatic additive. While the additive is generally associated with enhanced densification and reduced permeability, the initial value observed here suggests that localized effects may still govern the early-stage permeability response. Further replicate tests and microstructural observations are recommended to verify the repeatability of this behavior and isolate the underlying cause.

5 Conclusion

This chapter investigated the interfacial behavior between geopolymer mortar and steel substrates under coupled shear and permeability conditions. Initial trial tests revealed severe bonding deficiencies, primarily driven by shrinkage-induced cracking and interface incompatibility. Various surface treatments and additive strategies were explored to address these challenges, but most failed to prevent spontaneous debonding during curing or preloading stages.

To overcome these limitations, a concentric cell testing system was developed. This modified configuration eliminated steel-to-steel load transfer, ensured uniform confinement, and enabled direct activation of the geo-steel interface under controlled shear conditions. The concentric setup successfully resolved the issues of misalignment and premature failure, allowing for accurate measurement of both shear strength and gas permeability.

The reference geopolymer specimen exhibited a peak shear strength of $17.34\,\mathrm{MPa}$, with permeability decreasing during early loading due to compaction and subsequently increasing post-failure due to microcrack formation. The phosphatic geopolymer specimen demonstrated slightly improved mechanical performance, achieving a peak shear strength of $18.26\,\mathrm{MPa}$, while maintaining a relatively low and stable permeability range of 6.14×10^{-19} to $2.03 \times 10^{-18}\,\mathrm{m}^2$. These results suggest that the phosphatic additive enhances both sealing capacity and mechanical integrity at the interface.

Complementary flexural and compressive strength tests further confirmed the efficacy of the phosphatic additive, showing slight improvements in bulk properties without compromising matrix workability or cohesion.

Post-test inspection confirmed the absence of macroscopic cracks in all concentric cell

specimens, validating the reliability of the measured hydro-mechanical responses. Nevertheless, the unexpectedly high initial permeability in the phosphatic specimen suggests that localized imperfections or minor shrinkage effects may still influence early-stage transport behavior. This highlights the need for further optimization of mix design and microstructural refinement.

In conclusion, the concentric cell methodology proved to be a robust approach for evaluating geo-steel interface performance, and the incorporation of phosphatic additives demonstrated clear benefits in improving interfacial durability. These findings provide a promising foundation for the design of geopolymer-based repair systems in steel-reinforced infrastructures.

CHAPTER 6

Large-Scale Validation: Application on Repaired Beams

1 Introduction

Previous chapters have comprehensively explored the mechanical properties and interface bonding behavior of geopolymer repair materials through material-scale tests and shear interface analysis. While these studies provided fundamental insights into the physical characteristics and interaction mechanisms of geopolymer–concrete systems, further verification at the structural level remains necessary to assess their practical viability in real-world repair scenarios.

This chapter aims to extend the research from interface-scale to structural application scale, by evaluating the performance of geopolymer mortar in the repair of damaged reinforced concrete (RC) beams, a common and critical component in civil infrastructure. RC beams are selected as test specimens due to their representative structural behavior under flexural loading, well-established failure modes, and compatibility with both mechanical testing and DIC-based strain field analysis. Furthermore, they provide a robust platform for directly comparing the influence of repair materials and interface preparation methods on global structural responses such as stiffness, load capacity, ductility, and crack development.

In this context, a total of twelve RC beams were designed, pre-damaged, and subsequently repaired using either geopolymer mortar or commercial cementitious repair products, under two interface conditions: smooth (as-cast) and rough (mechanically treated).

Four experimental groups were established:

- CON (unrepaired control beams),
- GEO-S (geopolymer repair with smooth interface),
- GEO-R (geopolymer repair with rough interface), and
- P-S (commercial product repair with smooth interface).

All specimens were subjected to four-point bending tests, and their behavior was analyzed in terms of load–displacement response, stiffness, ultimate load, and crack evolution. Advanced Digital Image Correlation (DIC) was employed to capture full-field strain distributions and monitor crack propagation in real time. This enabled a quantitative comparison of repair effectiveness not only through global force–displacement curves but also through detailed crack pattern tracking and localized strain fields.

The primary objective of this chapter is to evaluate whether geopolymer mortar, when applied under realistic structural conditions, can provide comparable or superior repair performance to commercial products, and to identify the role of interface roughness in influencing failure modes and long-term durability. The results offer practical insights for the deployment of geopolymer-based repair strategies in field applications.

2 Design and fabrication of damaged beams

2.1 Reinforced concrete beams geometry

The first group consists of 3 unmodified concrete beams serving as the control group. 6 beams repaired with geopolymer mortar are divided into two groups: the second group includes 3 beams with smooth interfaces, and the third group comprises 3 beams with rough interfaces to investigate the impact of surface roughness on the repair efficacy. The final group consists of 3 beams repaired using a commercial repair material, which serves to compare with the performance of similar products currently available on the market.

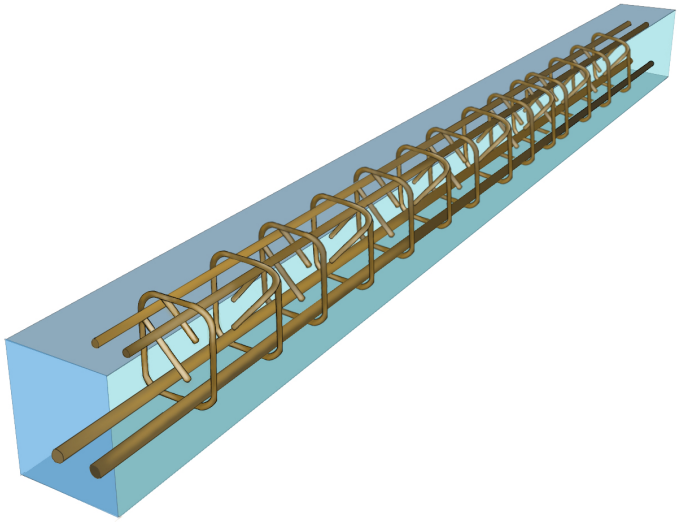

Figure 6.1: Stereoscopic image of a beam

The beam utilized is a rectangular reinforced concrete element with a total length of 1.5 meters and a cross section measuring 120 mm in height and 100 mm in width. As shown in Figure 6.1, the reinforcement layout includes two bottom longitudinal bars serving as the primary flexural reinforcement, and shorter top bars that were included mainly for constructability and to hold the steel cage during casting. Transverse stirrups are uniformly distributed along the beam to maintain bar positioning and control cracking during handling and early loading stages, rather than serving a major structural role in shear resistance.

The illustrated beam corresponds to a typical laboratory-scale specimen for single-span structures. Its internal reinforcement design follows standard pedagogical practices adopted in civil engineering experiments, providing a representative configuration for assessing the performance of repair materials under flexural loading.

The reinforcement layout of the beam is shown in detail in Figure 6.2, including the elevation and cross-sectional views. Two HA8 bars are placed at the bottom to resist flexural tension, while two HA6 bars are arranged at the top primarily for geometric balance and cage stability. Fourteen stirrups (HA6, spaced at 6–9 cm) are uniformly distributed along the span, with closer spacing in the central region to reduce variability and ensure specimen consistency during loading.

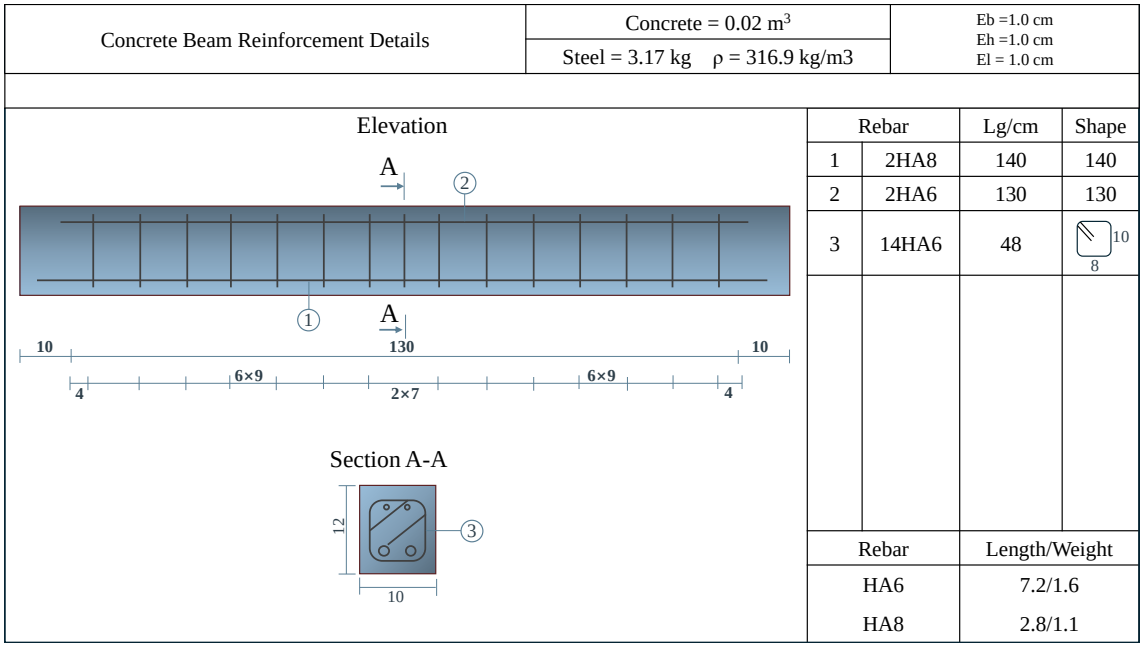

Figure 6.2: Concrete beam reinforcement details (Unit:mm)

This configuration follows standard laboratory practice for small-scale flexural beam specimens and ensures mechanical integrity during both casting and testing. The stirrups are not designed to carry shear loads but help maintain bar alignment and confinement during handling. This reinforcement pattern was kept consistent across all specimens to isolate the influence of repair materials in subsequent sections.

As shown in Figure 6.3, the repairs were carried out in the bottom tension zone of the beams, where the longitudinal rebars are subjected to maximum tensile stress under flexural loading. The repair thickness was approximately 4 cm, ensuring direct contact with both the existing concrete and the reinforcing steel.

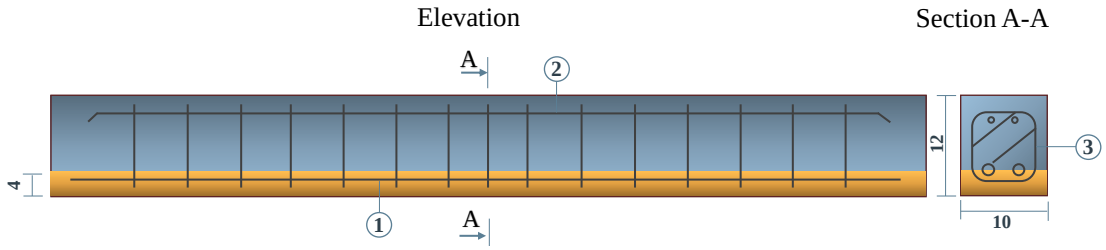

Figure 6.3: Concrete beam reinforcement details with repair materials (Unit:mm)

This configuration was selected to simulate realistic damage scenarios and to evaluate

the bonding performance of the repair material under tension-dominated conditions. In such cases, rebar slip at the repair–steel interface is a common failure mode, particularly in the absence of sufficient mechanical anchorage or chemical adhesion. Therefore, the test setup is intended to assess the effectiveness of the repair materials in preventing interface debonding and ensuring strain transfer continuity between the substrate and the reinforcement.

2.2 Materials and repair materials properties

2.2.1 Concrete

The mix was designed to achieve a target compressive strength of 25 MPa, with an actual average value of 29.44 MPa based on six cube specimens tested according to BS EN 12390-3.

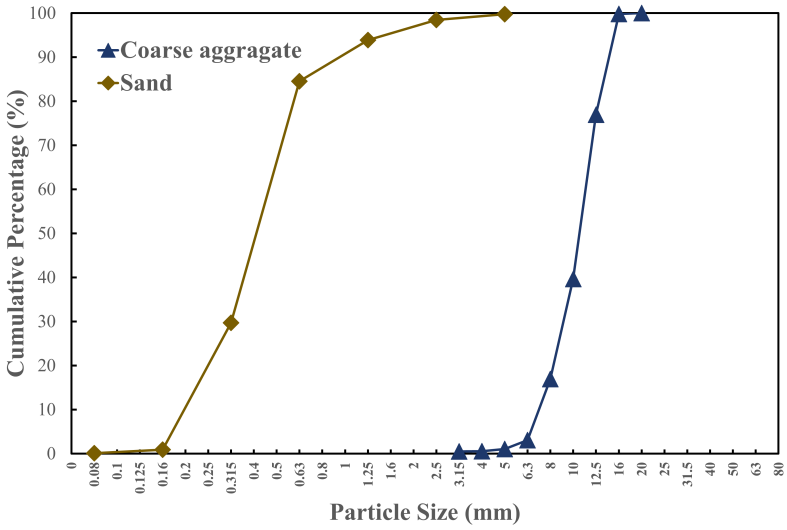

Figure 6.4: The particle size distribution for sand and coarse aggregate

The experiments were conducted using a commonly employed multi-purpose cement conforming to the EN 197-1, suitable for general construction applications. Both the sand and coarse aggregate used were sourced from standard laboratory stock materials. The sand had a fineness modulus of 1.94, indicating a medium-fine grading appropriate for mortar consistency. The particle size distribution for these aggregates is illustrated in Figure 6.4.

2.2.2 Repair materials: geopolymer mortar and commercial repair product

Geopolymer mortar. When utilizing geopolymer mortar as a repair material, the mix proportions and preparation methods referenced in Section 2.1 of Chapter 2 were adopted. However, due to the substantial quantity required for repairing reinforced concrete beams, a larger mixing vessel typically used for preparing concrete in the laboratory was employed.

Commercial repair product. In the comparative analysis of repair materials, the commercial product utilized was "Rapide". The selection of Rapide was based on its classification as an R4 repair mortar according to EN 1504-3, offering a benchmark for high-performance commercial solutions in structural rehabilitation. It is specifically formulated for civil engineering and architectural works, offering excellent adhesion, thickness retention, and a very high compression strength. This comparison aims to evaluate the performance differences between the commercial 'weber.rep rapide' and the experimentally developed geopolymer mortar used in the study.

2.3 Specimens fabrication and repair

In Section 2.1, the study delineates four groups of repaired beams. The first group, labeled as CON-1, CON-2, and CON-3, comprises intact reinforced concrete beams serving as the control group. The second group, named GEO-S-1, GEO-S-2, and GEO-S-3, consists of beams repaired with geopolymer mortar without any surface roughness treatment, categorized as smooth. The third group, designated as GEO-R-1, GEO-R-2, and GEO-R-3, features beams repaired with geopolymer mortar and subjected to a surface roughening process to create a rough geo-con interface. The fourth group, identified as P-S-1, P-S-2, and P-S-3, includes beams repaired with a commercial repair product, also treated as smooth due to the absence of surface roughness treatment. These categorizations facilitate a comprehensive comparison of the impact of surface treatments and material types on the structural performance of repaired beams.

I will now describe, step by step, how these beams were fabricated.

2.3.1 Rebar cages fabrication

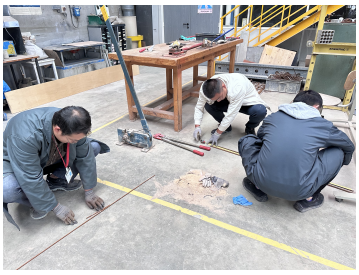

(a) Cutting rebar to size



(b) Stirrup fabrication



(c) Stirrups ready for use



(d) Rebar binding in progress



(e) Rebar cages ready for use

Figure 6.5: Rebar cages fabrication progress

The fabrication of rebar cages was conducted to ensure consistent reinforcement layout and mechanical performance across all specimens. Figure 6.5 illustrates the systematic process of fabricating rebar cages, essential for reinforcing concrete structures. The sequence began with cutting the rebar to precise dimensions Figure 6.5(a), ensuring that each piece meets the specifications required for the stirrups. Subsequently, the stirrup fabrication Figure 6.5(b) involved bending and shaping the rebar to form the necessary loops and hooks. Once the stirrups were prepared, they were organized and laid out as shown in Figure 6.5(c), ready for integration into larger assemblies. The process continued with the rebar binding Figure 6.5(d), where the prepared stirrups were meticulously tied together using wire ties to form a stable framework. Finally, the completed rebar cages Figure 6.5(e) are shown, fully assembled and ready for implementation into the construction site.

2.3.2 Fabrication of complete reinforced concrete beams and reinforced concrete beams for repair

The prepared rebar cages were first installed on supports to ensure a protective layer thickness of 1 cm before being placed into the beam molds. To ensure the repair zone aligns with the tensile region under bending, the beam forms were oriented upside-down during the casting process of repairable beams. This inversion ensures that the concrete for the repair beams is cast first and allowed to solidify before the repair material is added. To maintain consistency, the rebar cages for the complete reinforced concrete beams, which do not require repairs, are placed in the same manner.



(a) Concrete in mixing drum **(b)** Vibrating slurry **(c)** Fresh concrete beams

(d) Beams covered with film **(e)** Demolded CON beams

Figure 6.6: Fabrication of complete reinforced concrete beams

Figure 6.6 depicts the systematic fabrication of complete reinforced concrete beams. The process commenced with the sequential addition of coarse aggregates, sand, cement, and water into the mixing drum, as shown in panel Figure 6.6(a). This mixture was then agitated to ensure a homogenous slurry, illustrated in panel Figure 6.6(b). Once the slurry reached the desired consistency, it was poured into molds, as seen in panel Figure 6.6(c).

To eliminate entrapped air and ensure full compaction, a handheld poker vibrator was applied immediately after pouring. The vibrator was systematically inserted along the beam length to facilitate aggregate settlement and reduce internal voids.

After vibration, the surface of the freshly cast beams was smoothed to achieve a flat finish. The beams were then covered with a protective film to prevent premature drying and to ensure proper curing conditions, demonstrated in panel Figure 6.6(d). Following adequate curing, the beams were demolded, revealing the finished structures ready for use in construction, depicted in panel Figure 6.6(e).

The procedure for preparing reinforced concrete beams that require repair differs mainly in the casting stage of the concrete slurry. Specifically, two bottom bars and upper space were reserved, as shown in Figure 6.7, due to the beams being cast in an inverted orientation. After casting, the beams were covered with a protective film to facilitate curing and to ensure the concrete sets properly.



(a) Vibrating slurry **(b)** Fresh concrete beams **(c)** Beams covered with film

Figure 6.7: Fabrication of reinforced concrete beams for repair

After final setting of concrete part, the upper part of the beams was ready to be cast using repair materials.

2.3.3 Rough concrete surface treatment

In the experimental procedure aimed at creating a rough interface on geo-concrete surfaces, a specific treatment was applied to enhance the bond between geopolymer mortar and concrete. As illustrated in Figure 6.8(a), the surface of the concrete beam was first treated with a surface retarder (SikaCem® Désactivant 4-6), meticulously applied following the manufacturer's instructions. This product is specifically designed to delay the concrete setting on the surface and was used some time after the concrete was cast but before it began to set, ensuring a uniform effect. This retarder delays surface hydration, allowing selective removal of cement paste and exposure of aggregates, thereby enhancing mechanical interlocking at the interface.

Following the application of the surface retarder, the concrete surface underwent a thorough washing using a high-pressure water jet, as depicted in Figure 6.8(b). This step was crucial to remove the thin layer of cement paste and expose the rougher aggregate beneath, which is essential for achieving the desired rough texture.

The final appearance of the treated concrete surface, shown in Figure Figure 6.8(c), demonstrates the effectiveness of this method. The exposed aggregate provides a significantly increased surface roughness, which is critical for enhancing the mechanical interlock at the geo-concrete interface.



(a) Applying surface retarder **(b)** High-pressure water **(c)** Finished rough surface

Figure 6.8: Fabrication of reinforced concrete beams with rough surface for repair

2.3.4 Repairing smooth and rough concrete beams with geopolymer mortar

Figure 6.9 illustrates the methodological approach adopted for the repair of reinforced concrete beams using geopolymer mortar. The preparation commenced 24 hours prior to application with the preparation of an alkali activated solution. This solution, along with metakaolin and standard sand, was then added to a mixing drum, as shown in Figure 6.9(a), to create a homogeneous geopolymer slurry (Figure 6.9(b)). The meticulous mixing process ensured a consistent and workable slurry that was essential for effective application on the beams.



(a) Geopolymer in mix drum **(b)** Geopolymer slurry **(c)** Fresh GEO-S beams



(d) Fresh GEO-R beams **(e)** Demolded GEO-S beams **(f)** Demolded GEO-R beams

Figure 6.9: Fabrication of beams repaired with geopolymer mortar

The beams, referred to as GEO-S and GEO-R, underwent repair with the geopolymer mortar tailored to their respective surface conditions. GEO-S beams, with unroughened interfaces, and GEO-R beams, with roughened interfaces as treated according to section 2.3.3, are shown in Figure 6.9(c) and Figure 6.9(d) respectively. Immediately after casting, a handheld poker vibrator was used to compact the geopolymer mortar. The vibrator was carefully applied along the repair zone to eliminate entrapped air and ensure intimate contact between the fresh geopolymer and the substrate surface, especially in roughened interface conditions. This step was essential to promote proper bonding and minimize the risk of void formation at the repair interface. Post-application, the beams were covered to prevent premature drying and to maintain optimal curing conditions. Demolding of the beams (Figure 6.9(e) and Figure 6.9(f)) was conducted once the geopolymer mortar achieved sufficient set and strength. This stage revealed the effective adhesion and compatibility of the geopolymer mortar with both smooth and rough textures of the beams.

2.3.5 Repairing smooth concrete beams with commercial products

The experimental process illustrated in Figure 6.10 aimed to evaluate the effectiveness of structural repairs using commercial products, Weber.rep rapide, in comparison to geopolymer mortar.



(a) Commercial products



(b) Products slurry



(c) Fresh P-S beams



(d) Demolded P-S beams

Figure 6.10: Fabrication of beams repaired with commercial products

The preparation phase involved thoroughly wetting the substrate, followed by a slight drying period to optimize the adhesive properties of the mortar. According to the manufacturer's guidelines, approximately 3.6 liters of water per 25 kg bag of Weber.rep rapide were added. The components were mixed mechanically to form a homogeneous and workable slurry, as depicted in Figure 6.10(b).

Immediately after pouring, a handheld poker vibrator was used to compact the commercial repair mortar. Careful vibration was applied along the repair area to eliminate entrapped air and ensure full penetration into surface voids, particularly along the interface between the mortar and the original concrete substrate.

This slurry was then meticulously applied to smooth-surfaced beams (denoted as P-S), ensuring that the application thickness met the repair requirements, as shown in Figure 6.10(c). The beams were subsequently covered to prevent rapid drying and to ensure an effective curing process. After the final setting period, the beams were demolded, revealing the fully restored surfaces, which are displayed in Figure 6.10(d).

3 Testing setup and methods

3.1 Loading method

To comprehensively evaluate the flexural behavior of intact and repaired beams, four-point bending tests were conducted, as illustrated in Figure 6.11. This method was specifically selected for its ability to uniformly apply bending moments within a controlled segment of the beam, crucial for accurately assessing the mechanical properties of the beam material.

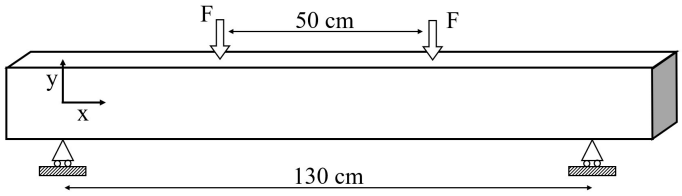

Figure 6.11: Diagram of the beam subjected to four-point bending test

In the depicted setup, the beam is supported at two points, 130 cm apart, which defines the overall span. The load is applied at two points, each 50 cm away from the respective closest support point, resulting in a pure bending zone of 50 cm at midspan, where shear effects are minimized and bending-induced deformations dominate. This configuration ensures that the region between the loads is subjected to a uniform bending moment, minimizing the influence of shear forces which are typically higher near the support points. This particular arrangement of the load points facilitates the isolation of the beam's bending behavior, focusing stress within the middle third of the span, where the material properties and effects of any repairs are most pronounced. The constant moment area is ideal for testing the intrinsic properties of the beam, including any enhancements or weaknesses introduced by repair materials.

To replicate the loading conditions depicted in Figure 6.11 for the four-point bending test, a single 500 kN hydraulic jack was employed, exerting force through a steel loading beam, as shown in Figure 6.12. The hydraulic jack is centrally positioned above the specimen to ensure that the load is uniformly distributed across the loading points. The specimen, positioned within the frame, is supported by sliding supports that allow for mi-

nor adjustments and alignment during the test to accommodate any shifts or deformation. The load cell, placed directly above the specimen between the hydraulic jack and the steel loading beam, is used to measure the exact force being applied.

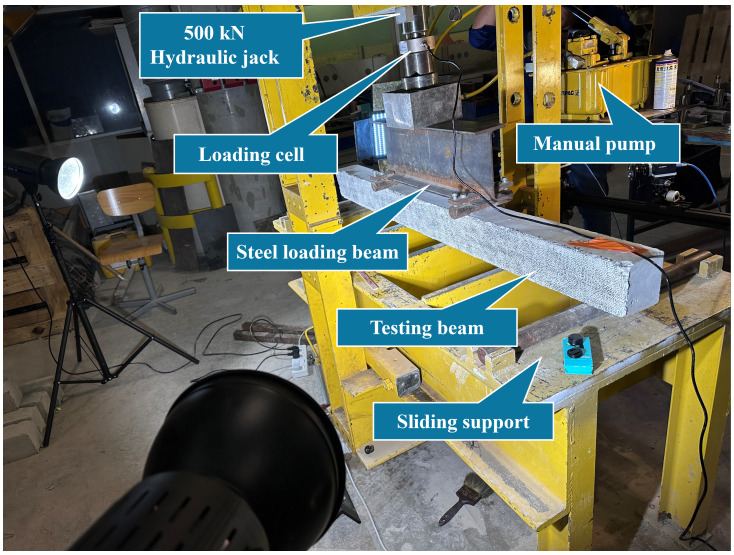

Figure 6.12: Loading apparatus

3.2 Measurement items and methods

In this study, primary measured parameters include applied load, vertical displacement, surface strain distribution, and crack development characteristics (initiation and width). The jack loading was quantified using an attached load cell. Displacement, strain, and crack measurements were facilitated by two sets of Digital Image Correlation (DIC) 3D systems strategically placed on either side of the beam to capture comprehensive data across the specimen's surface. DIC is a non-contact, three-dimensional displacement and widely used non-contact optical method for full-field displacement and strain measurement (Sutton et al., 2009; Schreier et al., 2009). Each DIC system comprises two cameras that employ a stereoscopic method to measure displacement at every position on the specimen's surface. In this experiment, two DIC systems, totaling four cameras, were used, each with a resolution of 960 w pixels.

Synchronization of force and displacement data is achieved by recording the DIC computer interface's index and the load cell data displayed on the computer.

3.2.1 DIC set up

The setup of the loading apparatus posed significant challenges in obtaining an unobstructed view of the entire beam during the loading process due to its influence on the DIC system's line of sight. Numerous trials were conducted to circumvent this issue, which initially hindered our ability to monitor the beam's behavior comprehensively under load. After extensive experimentation, a dual DIC system configuration was adopted to enhance data collection. This arrangement allowed for capturing detailed displacement and strain data from multiple angles, ensuring that no critical deformations were missed during the testing phases.

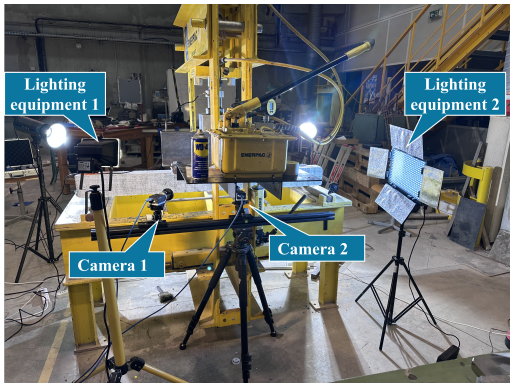

(a) DIC Setup – Midspan (Group 1)

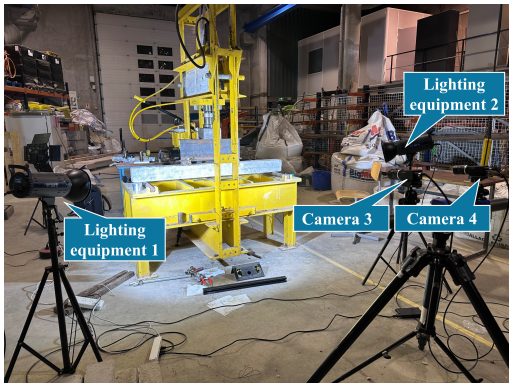

(b) DIC Setup – Full Beam (Group 2)

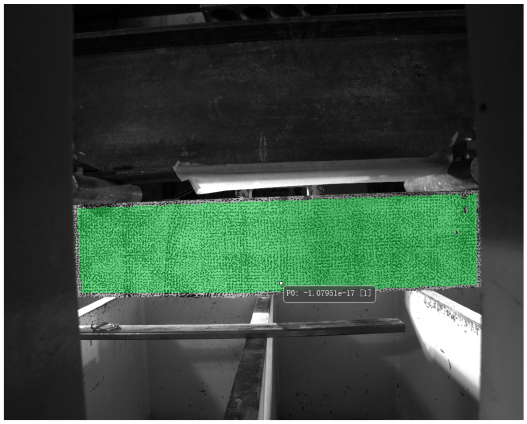

(c) Field of View – Midspan (Group 1)

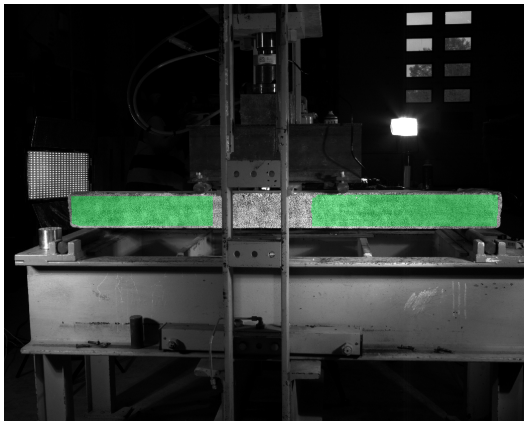

(d) Field of View – Full Beam (Group 2)

Figure 6.13: Digital Image Correlation (DIC) configuration and observation zones

Notes: (a) and (b) show the physical setup of two stereoscopic DIC systems targeting the midspan and full beam regions, respectively; (c) and (d) illustrate the corresponding fields of view for each group.

As shown in Figure 6.13, the final Digital Image Correlation (DIC) system was strategically configured to overcome visual obstructions caused by the loading frame and to ensure accurate, full-field strain measurements during the four-point bending test. Two sets of stereo-DIC systems were positioned symmetrically on either side of the beam. This dual configuration enabled comprehensive coverage of both localized and global deformations throughout the loading process.

This setup significantly enhanced data reliability by enabling cross-verification of results between different observation zones. Moreover, the combination of focused and global views provided a robust basis for analyzing fracture initiation, crack propagation, and post-peak softening behaviors across the entire specimen.

Group 1 – Midspan monitoring. As illustrated in Figure 6.13(a) and Figure 6.13(c), the first DIC group was dedicated to observing the midspan region, which corresponds to the constant moment zone. This area is most susceptible to flexural failure, and thus, Group 1's configuration prioritized spatial resolution and measurement precision. By focusing on the central 50 cm zone, this system was capable of capturing the detailed evolution of localized strain concentrations and the earliest signs of crack initiation. The use of high-resolution optics in this critical region ensured accurate monitoring of deformation patterns under increasing load.

Group 2 – Full-span observation. As shown in Figure 6.13(b) and Figure 6.13(d), Group 2 was configured to monitor the entire span of the beam. This broader view complemented the midspan-focused Group 1 by enabling detection of distributed displacement and strain patterns along the entire length of the specimen. This setup proved essential for capturing peripheral damage, delocalized cracking, or progressive failure mechanisms that may not be evident at the midspan.

Combined measurement strategy. The integration of both DIC systems produced a comprehensive dataset combining high-resolution, localized deformation data with global structural response information. This dual-scale approach facilitated robust analysis of load-induced behavior, allowing correlation between local strain localization and global flexural performance. The resulting data provided a solid foundation for assessing the effectiveness of repair techniques and evaluating the structural integrity of repaired beams.

3.3 Experimental procedure

Preparation of beam surfaces. Prior to testing, beam surfaces were coated with a uniform layer of matte white paint to enhance speckle contrast. Black speckles were subsequently applied using a textured roller.

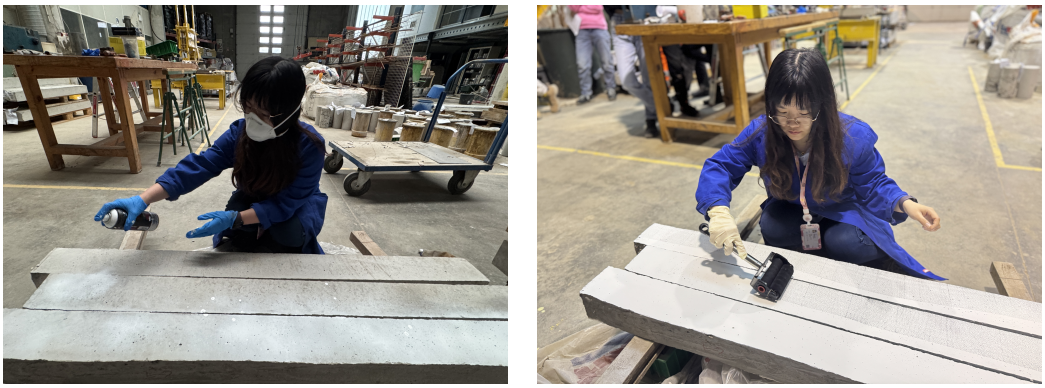

(a) Surface preparation – white matte coating

(b) Speckle pattern application – black dot spraying

Figure 6.14: Surface preparation procedure for DIC measurement

Calibration of DIC systems. Prior to the actual tests, the DIC systems were carefully calibrated to ensure accurate measurements. Calibration involved setting up the cameras to focus clearly on the beams' surfaces where the black dots were visible.

Execution of four-point bending tests. Manual loading was conducted using a hand-operated hydraulic pump, which applied precise and controlled forces at designated points along the beams to induce bending.

4 Results and discussion

4.1 Failure modes based on full-field strain visualization

To investigate the structural failure of both unrepaired and repaired beams, full-field strain maps were obtained using 3D-DIC. Among various strain components derived from the measured displacement fields, the maximum principal strain (ε_1) was selected as the most representative indicator for crack development analysis. This measure captures the

local maximum tensile strain, which is particularly relevant in concrete fracture, where failure is predominantly governed by tension (Gencturk et al., 2014; Destrebecq et al., 2011; Paschalis et al., 2018).

For each beam, two DIC visualizations were extracted at the final stage of loading: a central view focusing on the constant-moment region and a full-span view encompassing the entire beam. The center view highlights localized damage in the high-bending zone, while the whole-beam view reflects the overall deformation pattern, including the development of shear cracks and interface-related responses. These two perspectives offer complementary insights into failure mechanisms, enabling a more comprehensive understanding of how different repair strategies affect structural performance.

The color distribution in the DIC strain maps corresponds to the magnitude of ε_1, with cool colors (e.g., blue and purple) indicating low tensile strain and warm colors (e.g., red and orange) indicating regions of high tensile concentration, often corresponding to crack initiation and propagation zones. These visualized ε_1 fields are interpreted qualitatively in this section, focusing on the initiation, direction, and evolution of strain localization across different specimen groups.

4.1.1 Unrepaired concrete beams (CON)

Figure 6.15 presents the full-field maximum principal strain (ε_1) maps of three nominally identical reinforced concrete beams (CON-1, CON-2, and CON-3) obtained via Digital Image Correlation (DIC) at the final loading stage. For each specimen, two perspectives are displayed: a localized view focusing on the mid-span region and a full-span view capturing the overall deformation behavior. These complementary views enable the assessment of both local strain concentration and global crack propagation patterns.

Under controlled loading and identical reinforcement layouts, all three beams were expected to exhibit similar flexural-to-shear transition behavior. However, subtle variations in cracking intensity and damage mode were observed.

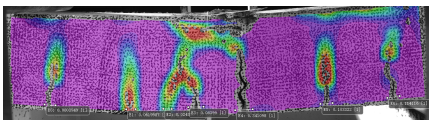

(a) CON-1: Center region strain map

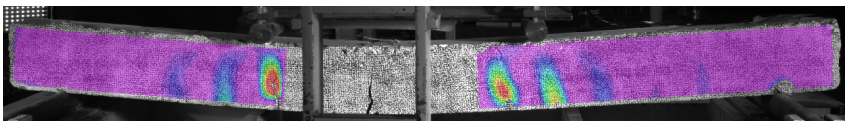

(b) CON-1: Full-span strain map

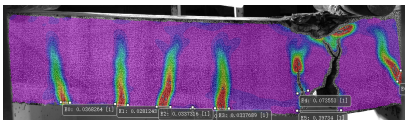

(c) CON-2: Center region strain map

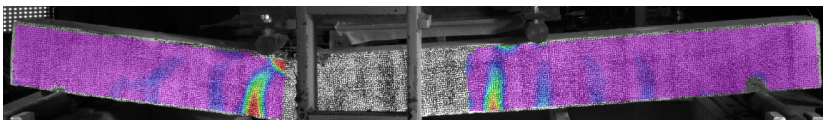

(d) CON-2: Full-span strain map

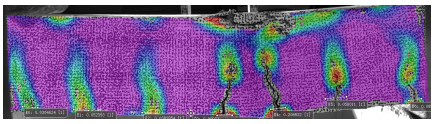

(e) CON-3: Center region strain map

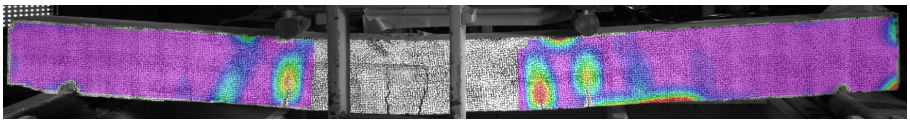

(f) CON-3: Full-span strain map

Figure 6.15: Full-field maximum principal strain (ε_1) distribution of reinforced concrete beams at final loading stage (CON-1 to CON-3)

CON-1 shows the initiation of vertical flexural cracks near the mid-span, evolving gradually into inclined shear cracks. The distribution suggests a mixed-mode failure involving both flexure and shear, yet without dominant rupture.

CON-2 exhibits a more severe failure mode. A major vertical crack extends from the tensile to the compressive zone, accompanied by audible reinforcement fracture. The strain field displays prominent diagonal cracking across the shear span, indicating a shear-dominated failure. The symmetry and intensity of the strain zones suggest critical damage localization and internal force redistribution prior to collapse.

CON-3 demonstrates the most extensive failure. Diagonal cracks are more distributed and deeper across both shear spans, as shown in the full-span map. The higher principal

strain values and wider cracking suggest earlier shear cracking onset and faster degradation of structural integrity.

These observations highlight that even under identical geometric and loading conditions, reinforced concrete beams can exhibit variability in damage progression due to microstructural or boundary inconsistencies. Nonetheless, all three specimens reflect a transition from flexural cracking to diagonal shear failure, underscoring the vulnerability of beams subjected to combined bending and shear actions.

4.1.2 Geopolymer-repaired beams with smooth interfaces (GEO-S)

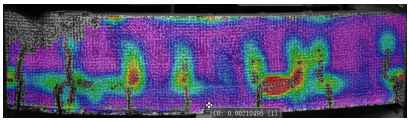

(a) GEO-S-1: Center region strain map

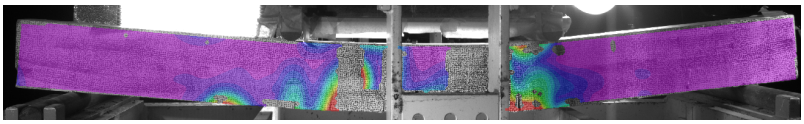

(b) GEO-S-1: Full-span strain map

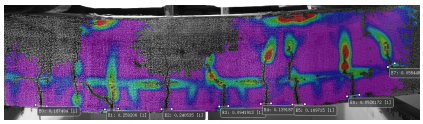

(c) GEO-S-2: Center region strain map

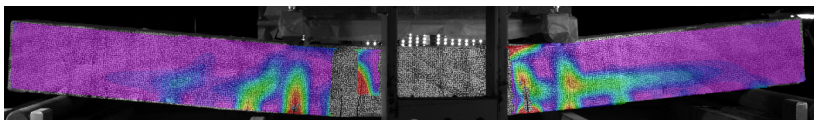

(d) GEO-S-2: Full-span strain map

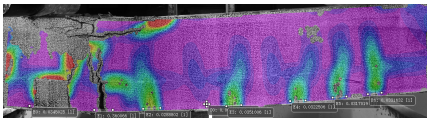

(e) GEO-S-3: Center region strain map

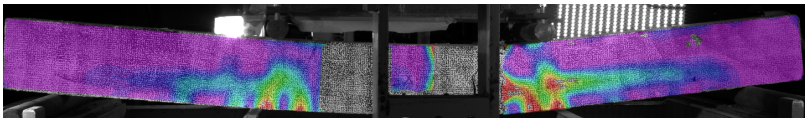

(f) GEO-S-3: Full-span strain map

Figure 6.16: Full-field maximum principal strain (ε_1) distribution of beams repaired with geopolymer mortar on smooth interfaces

Figure 6.16 illustrates the failure characteristics of beams repaired using geopolymer mortar directly applied to untreated concrete surfaces, representing smooth geo-con interfaces. In this configuration, no surface roughening or mechanical treatment was introduced prior to the repair, aiming to assess the bond performance under minimally prepared conditions.

GEO-S-1: Both the center and full-span strain maps reveal localized strain concentrations near the interface region, indicating insufficient mechanical integration between the geopolymer mortar and the original concrete. While the repair initially offers structural continuity, failure initiates at the material interface, manifesting as crack formation and propagation across the tension zone.

GEO-S-2: Displays more extensive cracking patterns throughout the beam. The strain distribution suggests that the bond at the interface is critically weak, as cracks not only initiate near the repaired zone but propagate longitudinally along the span. This behavior reflects the inability of the geopolymer to effectively distribute tensile stresses and resist delamination.

GEO-S-3: Exhibits the most severe damage among the specimens in this group, with large-scale strain fields and continuous crack propagation across the entire tensile face. The poor adhesion to the smooth substrate leads to premature failure, indicating that the repair layer fails to function as a structural continuum under load.

These observations emphasize the importance of surface preparation in geopolymer-based repairs. The smooth interfaces hinder effective mechanical interlock and chemical bonding, resulting in localized stress concentrations and brittle failure modes. Without appropriate surface treatment, the geopolymer layer is prone to early delamination, compromising both the load-bearing capacity and durability of the repaired beams. These findings are consistent with interface behavior studies in similar systems (Bissonnette et al., 2011; Manawadu et al., 2023; Feng et al., 2020).

4.1.3 Geopolymer-repaired beams with rough interfaces (GEO-R)

Figure 6.17 showcases the failure phenomena observed in three reinforced concrete beams—GEO-R-1, GEO-R-2, and GEO-R-3—repaired with geopolymer mortar applied over mechanically roughened interfaces and tested under four-point bending. This interface treatment aimed to enhance the bond performance between the geopolymer repair

layer and the original concrete substrate, thereby influencing the load distribution and failure mechanisms.

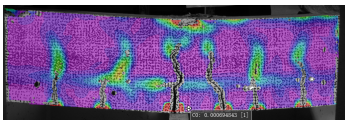

(a) GEO-R-1: Center region strain map



(b) GEO-R-1: Full-span strain map

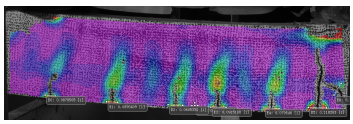

(c) GEO-R-2: Center region strain map

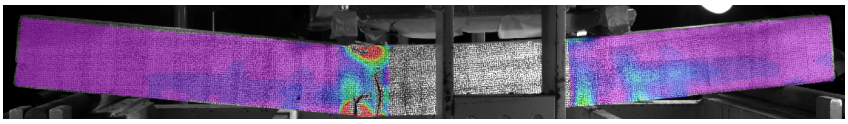

(d) GEO-R-2: Full-span strain map

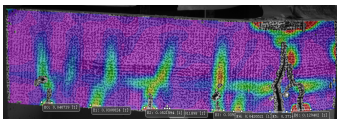

(e) GEO-R-3: Center region strain map

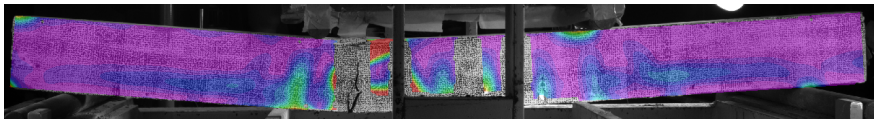

(f) GEO-R-3: Full-span strain map

Figure 6.17: Full-field maximum principal strain (ε_1) distribution of beams repaired with geopolymer mortar on rough interfaces

GEO-R-1: The DIC strain maps show moderately improved stress transfer in the central region, where strain concentrations are notably reduced compared to the smooth-interface cases. This suggests that the surface roughening promoted improved micromechanical interlocking, which delayed crack initiation. Nevertheless, the full-span view still reveals prominent diagonal cracks, indicating that while bonding was enhanced, the repair material remained susceptible to shear-induced failure under high loading.

GEO-R-2: Compared to GEO-R-1, this specimen demonstrates more favorable structural response. The center region exhibits reduced strain localization, while the full-span

map shows more distributed and less severe cracking. These observations indicate that the roughened interface enabled more uniform load transfer and effectively restrained the development of major failure zones.

GEO-R-3: This beam shows the most favorable performance among the three. Both the center and full-span images reveal minimal strain accumulation and virtually no major cracking. The results imply that the rough interface achieved a strong interfacial bond, enabling the geopolymer mortar to act cohesively with the original substrate throughout loading. The failure was less severe and more ductile in nature, reflecting a well-integrated repair system.

Overall, the use of roughened interfaces significantly enhanced the effectiveness of geopolymer repairs. The improvement is attributed to increased mechanical interlocking and improved interfacial friction, both of which facilitate better stress transfer and delay the onset of fracture. These findings underscore the importance of surface preparation in repair design and align with previous studies advocating for mechanical surface treatment to improve bond performance (Gadri and Guettala, 2017; Pacheco-Torgal et al., 2017).

4.1.4 Commercial repair beams with smooth interfaces (P-S)

Figure 6.18 illustrates the failure behavior of beams repaired using commercial repair mortars directly applied to untreated, smooth concrete interfaces. The three specimens—P-S-1, P-S-2, and P-S-3—were subjected to four-point bending tests. Their failure modes were captured using full-field Digital Image Correlation (DIC), allowing visualization of principal strain distributions and crack development across the repaired regions.

P-S-1: The strain field in the center region reveals localized concentration near the repair zone, indicating partial load transfer and insufficient interfacial integration. While the repair material initially offered some mechanical support, the full-span view shows the emergence of extensive cracking along the repair boundary. This suggests a premature failure caused by poor adhesion and abrupt stress discontinuities at the interface.

P-S-2: The strain distribution is more dispersed, with elevated strain values observed both in the midspan and near the supports. The propagation of diagonal cracks across the span indicates that the commercial product failed to ensure effective stress redistribution. This inadequate bonding to the smooth interface severely impaired the global structural performance.

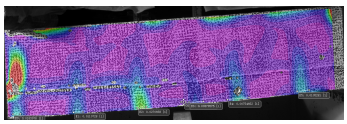

(a) P-S-1: Center region strain map

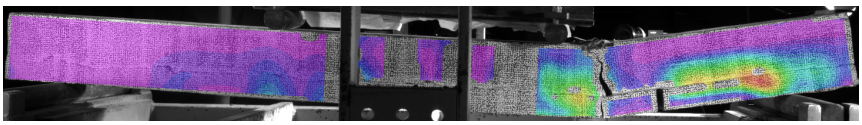

(b) P-S-1: Full-span strain map

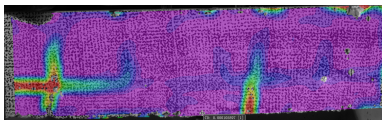

(c) P-S-2: Center region strain map



(d) P-S-2: Full-span strain map

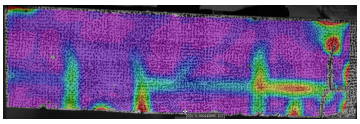

(e) P-S-3: Center region strain map



(f) P-S-3: Full-span strain map

Figure 6.18: Full-field maximum principal strain (ε_1) distribution of beams repaired with commercial repair mortar on smooth interfaces

P-S-3: Among the three specimens, P-S-3 exhibited the most critical failure response. DIC results show widespread, high-magnitude strain concentrations, accompanied by pervasive cracking throughout the entire beam length. The failure mechanism is characterized by poor load transfer, interfacial debonding, and fracture of the repair zone, indicating that the commercial mortar lacked sufficient toughness and ductility.

These findings underscore the inadequate performance of commercial repair products under bending loads when applied to existing concrete with minimal interface enhancement. While surface smoothness may contribute to weak bonding, other factors such as the rheological compatibility of the repair mortar, mismatch in stiffness and shrinkage behavior, improper thickness application, and the intrinsic brittleness of the material also

likely influenced the structural response. The strain localization and extensive cracking observed across all specimens suggest that the commercial repair system, in its current implementation, may not be well-suited for structural rehabilitation applications requiring high deformability and durable load transfer. Future applications should consider not only surface preparation, but also repair material selection, mechanical compatibility, and execution quality to improve structural outcomes.

4.1.5 Comparative discussion of observed failure patterns

The full-field strain visualizations presented in this section reveal distinct failure characteristics across different beam groups, shaped by the repair strategy and interface condition.

Unrepaired beams (CON group) exhibited classic flexural behavior followed by diagonal cracking, with localized strain concentrations near midspan. These results align with typical behavior of reinforced concrete under four-point bending, dominated by combined bending and shear.

In contrast, beams repaired with geopolymer mortar over smooth interfaces (GEO-S) showed premature cracking at the repair boundary and widespread strain fields, reflecting insufficient bonding and discontinuous stress transfer. This confirms the critical role of interface quality in repair durability.

Beams with roughened geopolymer-concrete interfaces (GEO-R) demonstrated improved structural integrity, with more evenly distributed strain and delayed crack propagation. The enhanced mechanical interlock at rough interfaces effectively mitigated strain localization, confirming the benefit of surface preparation.

Commercially repaired beams (P-S), despite using industrial-grade R4-class products, exhibited poor failure resistance. This may be due to insufficient bonding on smooth surfaces, or incompatibility in stiffness, thickness, or shrinkage behavior with the substrate concrete.

Overall, the strain-based visual assessment provides strong experimental evidence that interface conditions and repair material properties jointly govern failure mechanisms. These findings highlight the necessity for targeted interface design and material selection in durable structural repair.

4.2 Force–displacement response of the tested beams

To evaluate the mechanical performance of the repaired and unrepaired beams under flexural loading, the force–displacement (F–δ) response of each specimen was recorded during the four-point bending tests. This response offers valuable insight into the global structural behavior, particularly in terms of flexural stiffness, load-bearing capacity, and deformation tolerance.

The initial linear segment of the F–δ curve corresponds to the elastic regime, from which the flexural stiffness of the beam can be inferred. The peak load defines the ultimate load-bearing capacity, while the displacement at failure reflects the ductility of the system. Moreover, the area under the force–displacement curve up to peak or failure point provides a reliable measure of the energy absorption capacity and structural toughness (Tashan, 2022; Hussein et al., 2012).

In the context of structural repair, force–displacement curves are essential for evaluating how different repair materials and interface conditions affect load transfer efficiency and failure evolution. Comparative interpretation of these responses among beam groups offers a quantitative basis for assessing the effectiveness and limitations of each repair strategy.

4.2.1 Unrepaired concrete beams (CON)

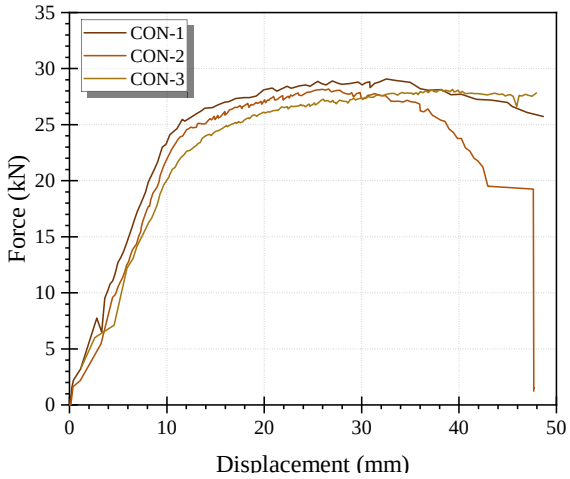

Figure 6.19: Force–displacement (F–δ) response curves of unrepaired reinforced concrete beams (CON-1 to CON-3)

The force–displacement (F–δ) curves of the unrepaired reinforced concrete beams (CON-1 to CON-3), shown in Figure 6.19, reveal distinct flexural responses under four-point bending. These curves are supported by corresponding DIC strain field results (Figure 6.15) and demonstrate the inherent variability in failure modes among identical concrete members.

CON-1 exhibited a steadily increasing force with displacement, followed by a peak load and a mild post-peak descending branch. This gradual softening suggests moderate ductility and some residual load-carrying capacity after initial cracking. The DIC images confirm multiple crack formations distributed along the span, enabling stress redistribution and contributing to the relatively stable post-peak response.

CON-2 presented a similar ascending response but experienced a more pronounced force drop immediately after the peak. This sharp degradation indicates a relatively brittle behavior, with limited capacity for stress redistribution. The corresponding DIC maps highlight a dominant through-crack near midspan and a reduction in strain localization zones, signaling a rapid collapse mechanism.

CON-3 achieved the highest peak force among the three specimens, indicating superior initial stiffness and load-bearing capacity. However, its post-peak behavior was characterized by an abrupt decline in force, pointing to a sudden failure. The extensive strain concentrations observed in the DIC results are consistent with a pronounced diagonal cracking pattern, which undermined the beam's residual strength.

Overall, the unrepaired beams display typical characteristics of reinforced concrete under flexural loading, including elastic behavior prior to cracking, followed by crack propagation and eventual failure. Despite having the same geometry and reinforcement, variations in casting quality, curing conditions, or minor heterogeneities in the concrete matrix may have contributed to the differences in post-peak performance.

4.2.2 Geopolymer-repaired beams with smooth interfaces (GEO-S)

Figure 6.20(a) illustrates the force–displacement (F–δ) responses of beams GEO-S-1, GEO-S-2, and GEO-S-3, each repaired using geopolymer mortar applied over smooth concrete surfaces.

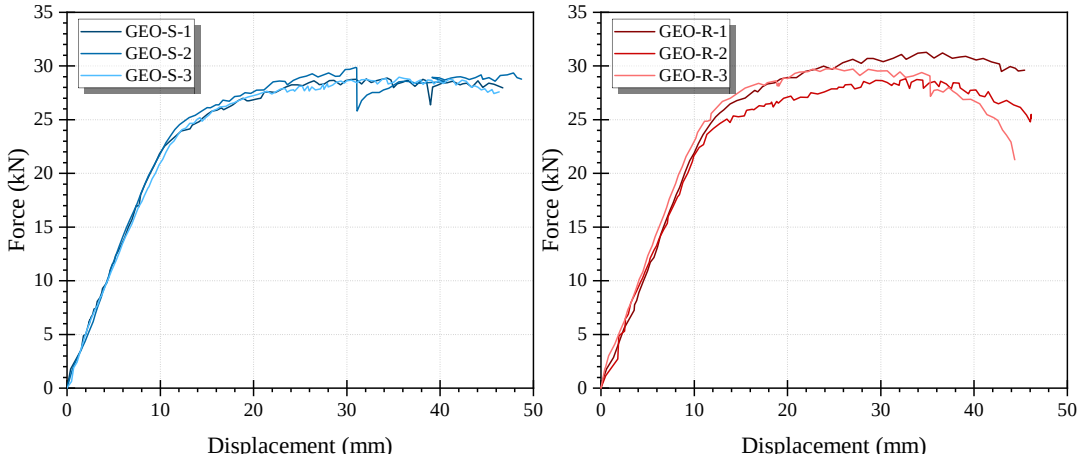

(a) GEO-S beams: Smooth geo–con interfaces

(b) GEO-R beams: Rough geo–con interfaces

Figure 6.20: Force–displacement (F–δ) response curves of reinforced concrete beams repaired with geopolymer mortar (GEO-S and GEO-R)

All three specimens exhibit comparable initial stiffness, as evidenced by the nearly parallel slopes of their ascending branches up to approximately $20\,\mathrm{mm}$ displacement. This consistency suggests that the geopolymer mortar achieved uniform bonding performance in the early elastic stage. The maximum load capacities range from approximately $28\,\mathrm{kN}$ to $30\,\mathrm{kN}$, reflecting the ability of the repaired beams to carry flexural loads effectively, albeit slightly lower than the unrepaired reference beams shown in Figure 6.19.

Beyond peak loading, GEO-S-2 and GEO-S-3 demonstrate minor fluctuations and local drops in load, which can be attributed to crack propagation and interfacial debonding between the geopolymer and the original concrete substrate. These fluctuations highlight the limitations of smooth interfaces in maintaining post-peak integrity under flexural stresses.

These curves are supported by the corresponding DIC strain field results (Figure 6.16), which visualize crack formation and strain localization. Together, they reveal the variability in failure progression even among nominally identical specimens, confirming the sensitivity of the repair performance to local interface conditions and inherent material heterogeneity.

4.2.3 Geopolymer-repaired beams with rough interfaces (GEO-R)

Figure 6.20(b) presents the force–displacement (F–δ) response curves of beams GEO-R-1, GEO-R-2, and GEO-R-3, repaired with geopolymer mortar applied over roughened concrete interfaces.

Compared to the smooth interface group, the GEO-R specimens show slightly higher peak loads, reaching up to approximately 31 kN, particularly in GEO-R-3. The ascending branches of the three curves exhibit a nearly linear increase in force, indicating consistent initial stiffness and elastic behavior. This trend suggests that the rough interface treatment contributed to an improved mechanical interlock at the geo–con interface, enhancing early-stage stress transfer.

The post-peak behavior varies among the specimens. GEO-R-1 and GEO-R-3 maintain relatively stable load-bearing capacity beyond peak load, with only moderate decreases, indicating better crack bridging and load redistribution. In contrast, GEO-R-2 exhibits a more sudden decline, suggesting localized interfacial failure or insufficient bonding in that specimen.

These interpretations are further supported by DIC strain field observations shown in Figure 6.17, which reveal distributed diagonal cracking and reduced strain localization compared to the GEO-S group. Notably, the extent of delamination and crack propagation appears less severe, implying a more efficient stress transfer across the roughened interfaces.

Overall, the integration of rough interfaces enhances the peak load and post-peak stability of geopolymer-repaired beams, although the stiffness and failure patterns remain broadly similar to those with smooth interfaces. These findings align with prior research emphasizing the role of surface roughness in improving bond strength and structural response in concrete repair systems.

4.2.4 Commercial repair beams (P-S)

The force–displacement (F–δ) curves for the reinforced concrete beams repaired with commercial products are presented in Figure 6.21. These specimens, labeled P-S-1 through P-S-3, were repaired over untreated, smooth concrete interfaces. All three beams exhibit a comparable ascending phase, characterized by a rapid increase in load-bearing capacity, followed by a relatively low peak force and a pronounced post-peak decline.

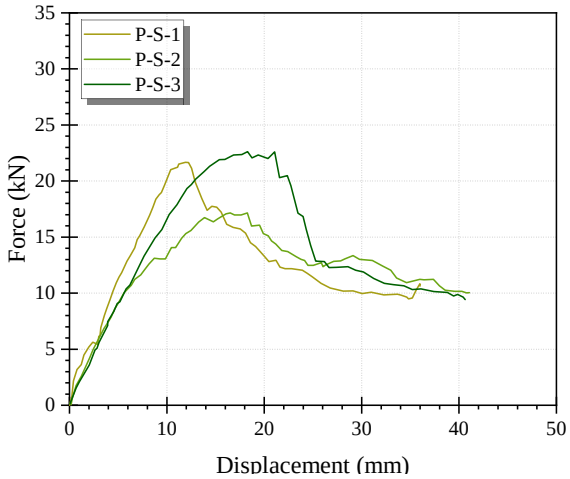

Figure 6.21: Force–displacement (F–δ) response curves of reinforced concrete beams repaired with commercial repair products (P-S-1 to P-S-3)

The initial slopes of the curves reflect moderate stiffness levels, indicating that the commercial products provided some degree of early-age bonding effectiveness. However, the sudden force drops observed after peak loading suggest limited energy absorption capacity and poor ductility, characteristic of brittle fracture modes. These brittle responses imply that the repair products were unable to develop sufficient interfacial compatibility or toughness to sustain large deformations after cracking onset.

This mechanical behavior is further substantiated by the DIC strain field images shown in Figure 6.18, where intense strain localization and abrupt crack formation are evident, particularly in the tension zones near the midspan. Cracks tend to initiate at the interface between the repair layer and the original concrete and propagate rapidly, leading to premature structural failure. The combination of F–δ responses and full-field strain maps highlights the limited effectiveness of commercial repair materials under smooth interface conditions and emphasizes the importance of interfacial engineering in achieving durable repair performance.

4.2.5 Summary comparison across all beams

Figure 6.22 illustrates the force–displacement (F–δ) responses of all tested beam specimens, enabling a direct comparison of the structural performance under different repair strategies and interface conditions. This aggregated view highlights the influence of both repair material type (commercial products vs. geopolymer mortar) and surface

treatment (smooth vs. rough interfaces) on flexural behavior.

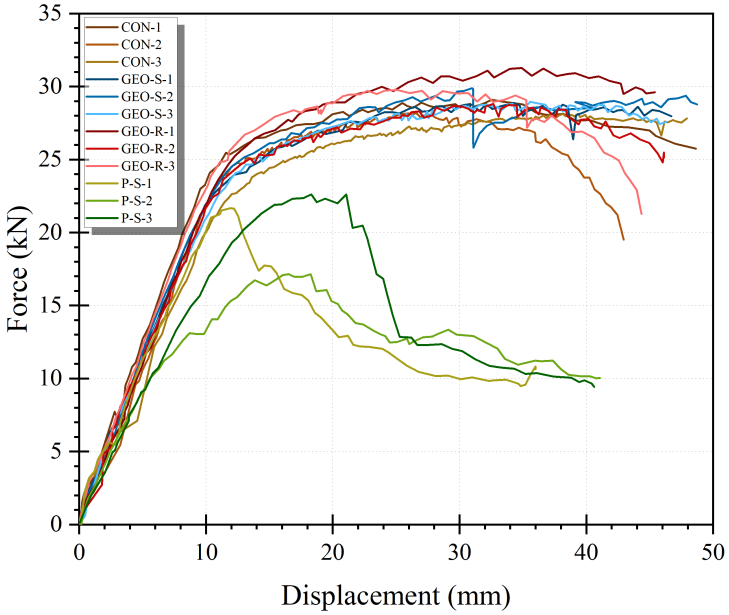

Figure 6.22: Comparative force–displacement (F–δ) curves of all beam specimens, including unrepaired, geopolymer-repaired, and commercially repaired groups

Quantitative data summarizing flexural stiffness and peak load are provided in Table 6.1, offering further insight into the mechanical properties of each beam group.

The comparison reveals that beams repaired with geopolymer mortar (GEO-S and GEO-R) consistently outperform those repaired with commercial products (P-S), both in stiffness and peak force. Among these, the GEO-R group—featuring roughened interfaces—achieved the highest average peak load, indicating that interface roughening can enhance bond quality and load transfer capacity.

While the average stiffness of the GEO-S and GEO-R beams is comparable to that of the original (CON) beams, the commercial product group (P-S) displayed markedly lower values. This suggests that geopolymer mortar not only provides improved structural continuity but is also more resilient under flexural stress conditions.

Table 6.1
Flexural stiffness and peak load results from four-point bending tests on all beam specimens

Group	Specimen ID	Stiffness (kN/mm)	Average	Peak force (kN)	Average
CON	CON-1	2.34		29.16	
	CON-2	2.20		28.23	
	CON-3	1.99	2.18	28.18	28.52
GEO-S	GEO-S-1	2.15		28.88	
	GEO-S-2	2.16		29.90	
	GEO-S-3	2.07	2.13	28.96	29.25
GEO-R	GEO-R-1	2.18		31.40	
	GEO-R-2	2.13		28.84	
	GEO-R-3	2.29	2.20	29.84	30.03
P-S	P-S-1	2.02		21.85	
	P-S-2	1.33		17.39	
	P-S-3	1.66	1.67	22.84	20.69

In summary, the combined evidence from force–displacement curves and quantitative performance metrics strongly supports the use of geopolymer mortar—particularly in combination with surface roughening—as a promising strategy for the rehabilitation of damaged reinforced concrete beams.

4.2.6 CON: Crack evolution and failure behavior

The crack initiation and propagation behavior of unrepaired concrete beams (CON-1, CON-2, and CON-3) under four-point bending is investigated through full-field DIC strain patterns and corresponding crack evolution curves, as shown in Figure 6.23. These results are essential for identifying the fracture mechanisms of control specimens and serve as a baseline for evaluating repair performance.

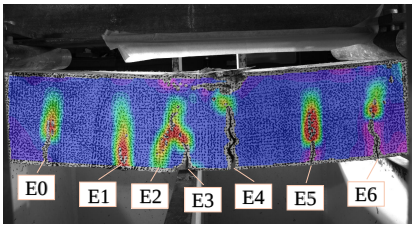

(a) DIC crack pattern of CON-1

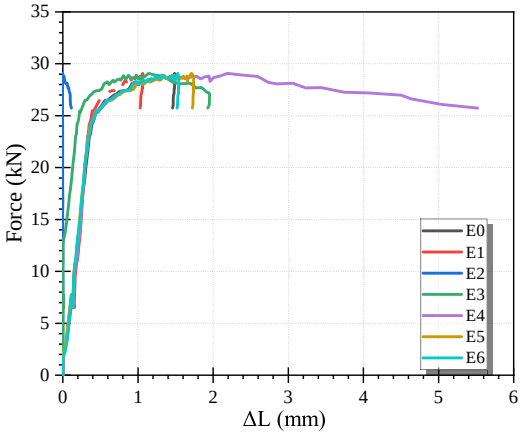

(b) Crack evolution curve of CON-1

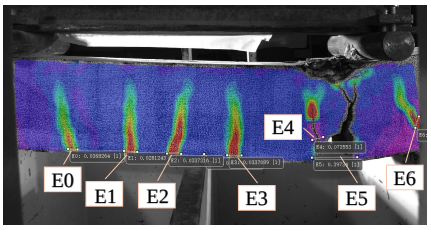

(c) DIC crack pattern of CON-2

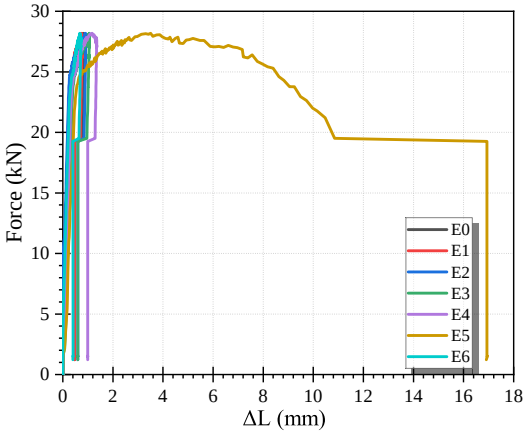

(d) Crack evolution curve of CON-2

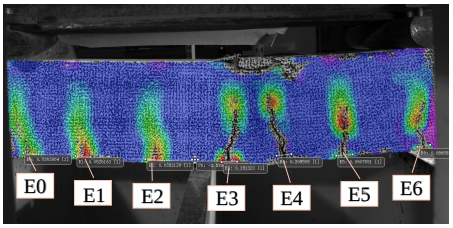

(e) DIC crack pattern of CON-3

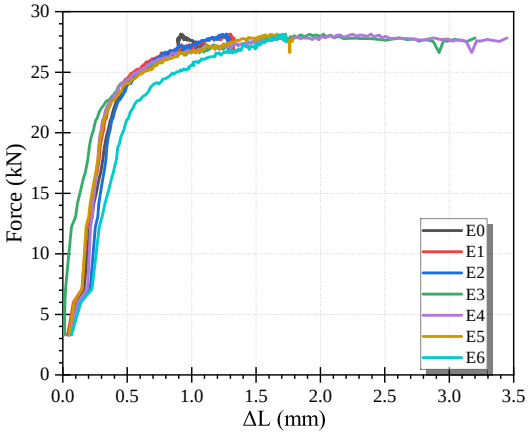

(f) Crack evolution curve of CON-3

Figure 6.23: Crack patterns and evolution curves of unrepaired reinforced concrete beams (CON-1 to CON-3)

Crack pattern characteristics. As shown in the DIC strain maps (Figure 6.23(a)–6.23(e)), all beams developed multiple vertical bending cracks in the mid-span tension zone. In CON-1, approximately six to seven cracks were observed, with relatively uniform strain localization and controlled crack width evolution. In CON-2, crack propagation was more severe, especially at E4, which exhibited extensive opening and possible crushing at the compression zone, suggesting reduced post-cracking integrity. In contrast, CON-3 exhibited a more evenly distributed crack field with lower peak strain intensities, indicating a ductile failure mode without a dominant critical crack.

Crack evolution behavior. The force–crack opening curves (ΔL) provide further insight into the fracture development of each specimen. In CON-1 (Figure 6.23(b)), most cracks stabilized after reaching the peak load, indicating residual load-bearing capacity and controlled failure. In CON-2 (Figure 6.23(d)), the peak was followed by a rapid drop, where crack E4 dominated the failure process, suggesting a brittle response. Meanwhile, CON-3 (Figure 6.23(f)) maintained a relatively flat curve after the peak, suggesting a more ductile behavior with distributed damage and gradual stiffness degradation.

Despite having identical material and geometric parameters, the three control beams exhibited significant variability in crack evolution and failure modes. This highlights the influence of inherent material heterogeneity and possible local defects. The DIC-assisted tracking of crack development offers a precise visualization of failure processes, establishing a reliable benchmark for subsequent analysis of repaired specimens.

4.2.7 GEO-S: Crack evolution and patterns

Figure 6.24 presents the DIC strain maps and corresponding crack evolution curves for three beams (GEO-S-1 to GEO-S-3) repaired with geopolymer mortar on smooth interfaces. These results are critical in evaluating the effectiveness of the geopolymer repair strategy in terms of strain distribution, crack control, and post-repair flexural performance.

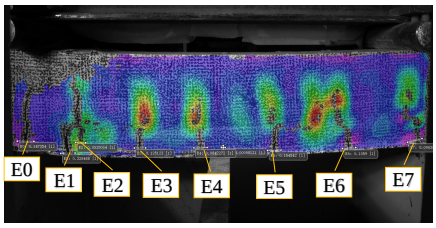

(a) DIC crack pattern of GEO-S-1

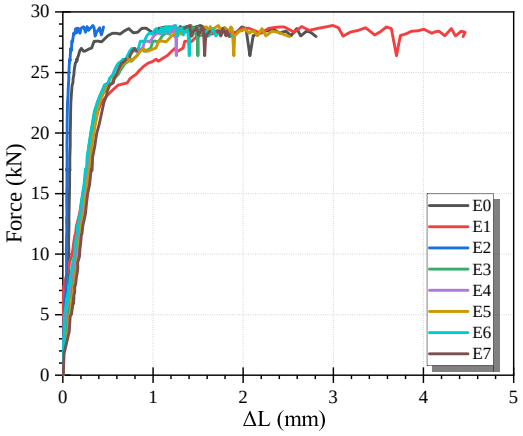

(b) Crack evolution curve of GEO-S-1

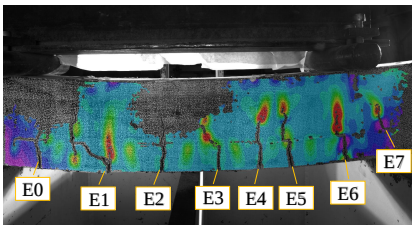

(c) DIC crack pattern of GEO-S-2

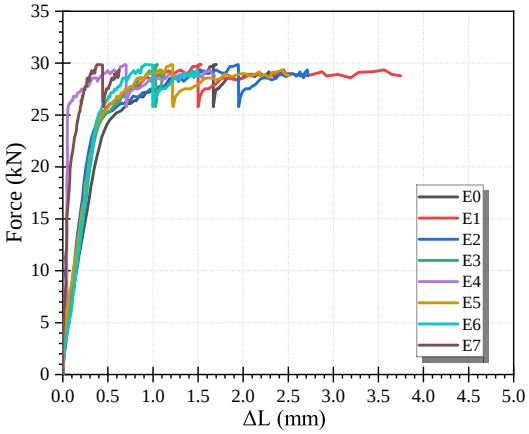

(d) Crack evolution curve of GEO-S-2

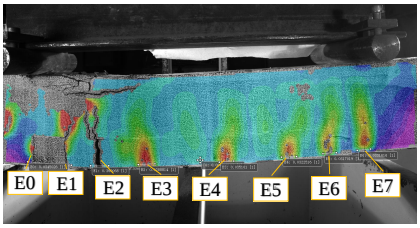

(e) DIC crack pattern of GEO-S-3

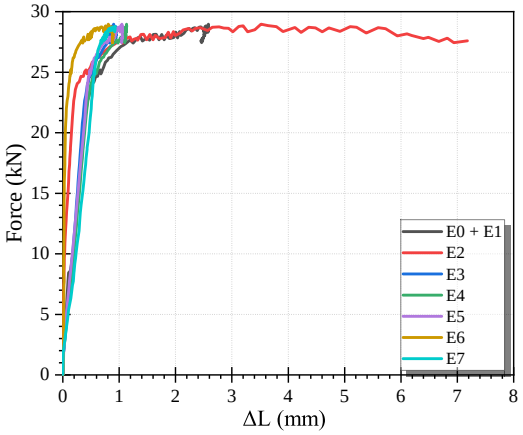

(f) Crack evolution curve of GEO-S-3

Figure 6.24: Crack patterns and evolution curves of beams repaired with geopolymer mortar on smooth interfaces (GEO-S-1 to GEO-S-3)

Crack pattern analysis. The DIC strain fields of beams GEO-S-1 to GEO-S-3 reveal localized crack formations concentrated along the geopolymer-concrete interfaces and tensile zones. In GEO-S-1 (Figure 6.24(a)), a series of distinct cracks are visible with strong strain localization, indicating a relatively uniform stress distribution across the repaired region. GEO-S-2 (Figure 6.24(c)) and GEO-S-3 (Figure 6.24(e)) exhibit more widely distributed cracks, with several cracks initiating near the mid-span and progressing toward the loading points. These patterns suggest that while the smooth interface may limit mechanical interlock, the geopolymer still ensures a degree of crack control through chemical adhesion.

Crack evolution analysis. The crack opening displacement curves (Figure 6.24(b) – Figure 6.24(f)) reflect a stable crack propagation behavior. After an initial elastic stage, multiple cracks begin to open simultaneously as the applied force approaches the peak value. Compared to the unrepaired control group, these beams show more gradual post-peak softening, with less abrupt load drops, indicative of enhanced ductility and energy dissipation capacity provided by the geopolymer mortar. Notably, the evolution curves are relatively consistent among the three specimens, suggesting good reproducibility of the repair performance.

These findings demonstrate that geopolymer mortar, even without surface roughening, can restore considerable structural performance in flexural members, offering a viable and sustainable alternative to conventional repair strategies for RC structures.

4.2.8 GEO-R: Crack evolution and patterns

Figure 6.25 presents the DIC crack strain fields and corresponding crack evolution curves for beams GEO-R-1, GEO-R-2, and GEO-R-3, all of which were repaired with geopolymer mortar applied to roughened interfaces. These figures provide valuable insight into the influence of mechanical interlocking on post-repair cracking behavior.

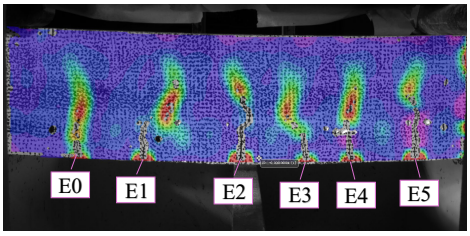

(a) DIC crack pattern of GEO-R-1

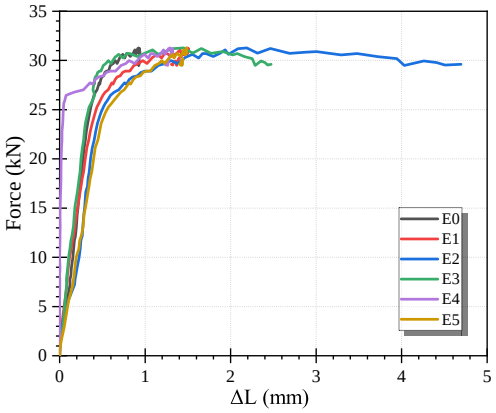

(b) Crack evolution curve of GEO-R-1

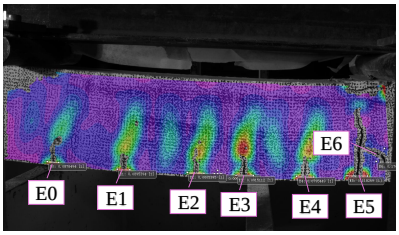

(c) DIC crack pattern of GEO-R-2

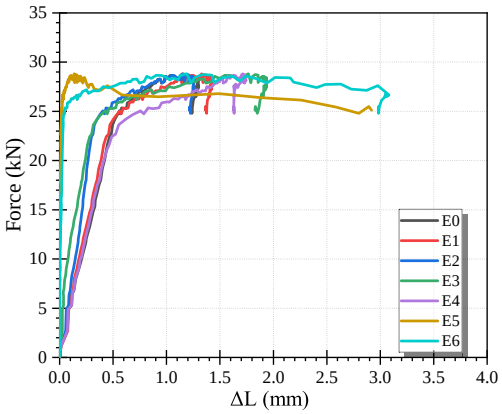

(d) Crack evolution curve of GEO-R-2

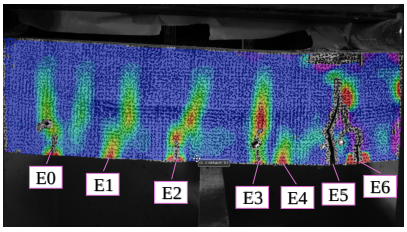

(e) DIC crack pattern of GEO-R-3

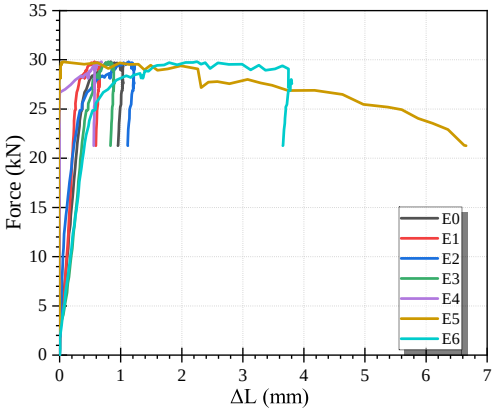

(f) Crack evolution curve of GEO-R-3

Figure 6.25: Crack patterns and evolution curves of beams repaired with geopolymer mortar on rough interfaces (GEO-R-1 to GEO-R-3)

Crack pattern analysis. As shown in the DIC strain fields (Figure 6.25(a), Figure 6.25(c), and Figure 6.25(e)), the roughened interface resulted in distinct and well-distributed crack

patterns in all three specimens. GEO-R-1 and GEO-R-3 exhibited pronounced strain localization in the interface zones, indicating stress concentration along the repair joints. This suggests a partial mismatch in stiffness or imperfect interfacial bonding under increasing flexural loading. Nevertheless, the crack development appears more controlled and distributed than in the smooth-interface repair cases.

Crack evolution analysis. The corresponding force–displacement curves (Figure 6.25(b), Figure 6.25(d), and Figure 6.25(f)) demonstrate high initial stiffness and extended load-bearing capacity in all three beams. GEO-R-1 exhibited a long plateau region before a gradual decline in force, while GEO-R-2 and GEO-R-3 maintained stable loads over relatively large displacements. This behavior is indicative of a quasi-ductile failure mode enabled by the mechanical interlock at the rough interface.

These results highlight the advantages of surface roughening in improving the bond performance of geopolymer repair systems. Although localized failure still occurs near the interface, the delayed and distributed nature of crack propagation supports the use of mechanical interlocking to extend service life and enhance residual strength in repaired members.

4.2.9 P-S: Crack evolution and patterns

Figure 6.26 presents the crack development behavior of P-S-1 to P-S-3 beams, which were repaired using commercial products applied over smooth interfaces. The DIC strain maps and corresponding force–displacement responses offer insights into the failure mechanisms and interface performance under flexural loading.

Crack pattern analysis. As illustrated in Figure 6.26(a), Figure 6.26(c), Figure 6.26(e), the strain localization fields of all three specimens reveal significantly less distributed strain zones compared to geopolymer-repaired specimens. In particular, cracks are more concentrated and fewer in number, indicating limited crack-bridging or stress diffusion effects. This localized behavior suggests weaker mechanical compatibility between the repair material and the host concrete.

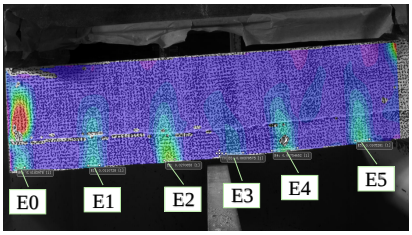

(a) DIC crack pattern of P-S-1

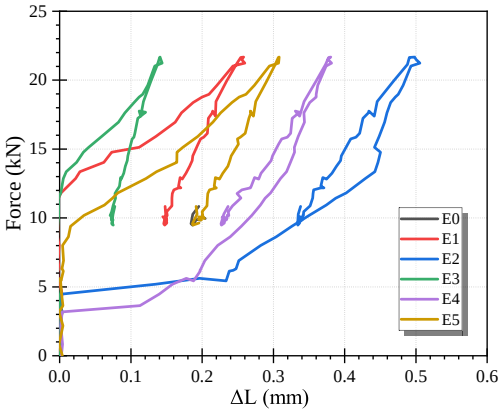

(b) Crack evolution curve of P-S-1

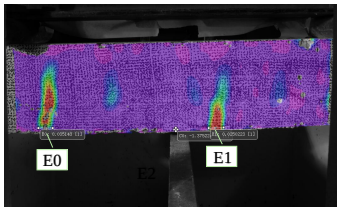

(c) DIC crack pattern of P-S-2

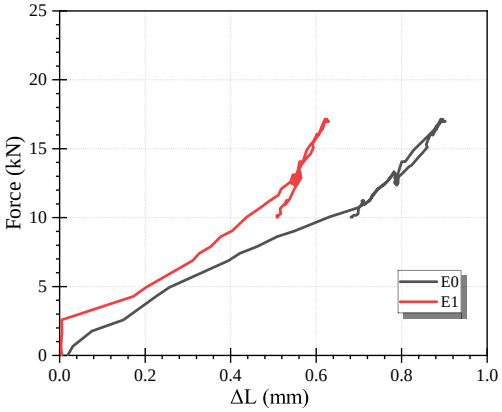

(d) Crack evolution curve of P-S-2

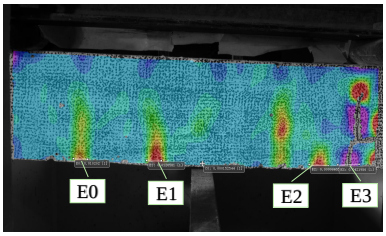

(e) DIC crack pattern of P-S-3

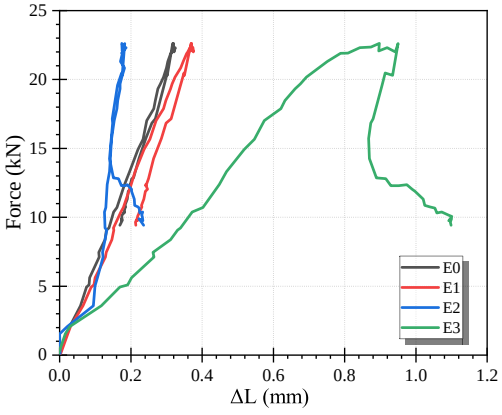

(f) Crack evolution curve of P-S-3

Figure 6.26: Crack patterns and evolution curves of beams repaired with commercial repair materials (P-S-1 to P-S-3)

Crack evolution analysis. The force–displacement curves in Figure 6.26(b), Figure 6.26(d), Figure 6.26(f) are characterized by abrupt slope changes and early crack opening. While

the initial loading phase demonstrates some stiffness, the rapid force drop upon crack propagation reflects brittle behavior. Notably, the crack opening displacements are significantly smaller than those observed in GEO-S and GEO-R groups, suggesting inadequate energy dissipation capacity.

Delamination mechanism. In several cases (e.g., P-S-1 and P-S-3), a distinctive increase and then decrease in the crack opening force is observed. This phenomenon is likely attributed to interface delamination, whereby the loss of bond between the commercial product and the original concrete restricts further stress transfer. The limited interfacial roughness and insufficient adhesive performance of commercial mortars exacerbate this effect, leading to premature failure at lower deformation levels.

These observations collectively underscore the limitations of commercial repair mortars when applied over smooth concrete interfaces. Compared to geopolymer repairs, the P-S group exhibits inferior crack control, lower deformation tolerance, and reduced bonding integrity under flexural loading.

4.2.10 Comparison of crack numbers across groups

Table 6.2 summarizes the number of visible cracks observed in each beam after testing.

CON Group: All control beams exhibited 7 cracks, indicating stable and repeatable fracture behavior.

GEO-S Group: All smooth-interface geopolymer-repaired beams showed 8 cracks, suggesting enhanced crack dispersion due to strain localization in the geopolymer matrix.

GEO-R Group: Beams with roughened interfaces averaged 6.67 cracks, slightly fewer than the other groups, implying improved stress redistribution through mechanical interlock.

P-S Group: The commercial repair group showed the highest variability (2–6 cracks, avg. 4.00), reflecting poor bonding and potential delamination.

Table 6.2
Observed number of cracks in each beam specimen after testing

Group	Specimen ID	Number of Cracks	Average
CON	CON-1	7	
	CON-2	7	
	CON-3	7	7.00
GEO-S	GEO-S-1	8	
	GEO-S-2	8	
	GEO-S-3	8	8.00
GEO-R	GEO-R-1	6	
	GEO-R-2	7	
	GEO-R-3	7	6.67
P-S	P-S-1	6	
	P-S-2	2	
	P-S-3	4	4.00

Summary: The geopolymer repair groups—particularly with rough interfaces—exhibit comparable or improved cracking performance relative to the control beams. In contrast, the P-S group shows unpredictable crack formation, raising concerns about the long-term reliability of commercial repair systems under structural loading.

5 Conclusion

This chapter presented a comprehensive investigation into the flexural behavior and crack development of reinforced concrete beams repaired with geopolymer mortar and commercial products. Four-point bending tests were performed on unrepaired beams (CON), beams repaired with geopolymer on smooth interfaces (GEO-S), geopolymer on rough interfaces (GEO-R), and beams repaired using a commercial material (P-S). Key findings are as follows:

The force–displacement response revealed that geopolymer repair substantially enhanced the structural performance of damaged beams. The GEO-R group exhibited the highest average peak load ($30.03\,\mathrm{kN}$), followed closely by GEO-S ($29.25\,\mathrm{kN}$), both of which surpassed or matched the control group (CON, $28.52\,\mathrm{kN}$). In contrast, the P-S group displayed a significantly lower peak load, averaging only $20.69\,\mathrm{kN}$, indicating limited reinforcement effectiveness.

Flexural stiffness showed a similar trend: GEO-R had an average stiffness of $2.20\,\mathrm{kN/mm}$, GEO-S $2.13\,\mathrm{kN/mm}$, and CON $2.18\,\mathrm{kN/mm}$. The P-S group, however, recorded the lowest average stiffness at $1.67\,\mathrm{kN/mm}$, highlighting weaker interfacial load transfer and compatibility.

DIC-based strain field analysis revealed distinct crack initiation and propagation patterns among the groups. The CON group exhibited multiple evenly distributed cracks at midspan, showing a ductile failure mode. GEO-S and GEO-R displayed finer and more distributed cracks, with GEO-R exhibiting better crack restraint due to enhanced mechanical interlock provided by the rough interface. In contrast, P-S beams showed fewer but wider cracks, along with visible delamination and interfacial debonding, reflecting a brittle failure mode with steep load drops.

Crack number statistics support these observations: the CON group averaged 7 cracks; GEO-S, 8 cracks, indicating distributed damage and energy dissipation; GEO-R, 6.67 cracks, reflecting reduced cracking due to interfacial confinement; and P-S, only 4 cracks on average, with high variability, implying potential cohesive or adhesive failure modes.

In conclusion, geopolymer mortar—particularly when combined with rough surface preparation—demonstrates superior structural restoration capability compared to commercial repair materials. It not only restores flexural strength and stiffness but also improves crack control and damage tolerance. These results support the adoption of geopolymer systems as a sustainable and high-performance solution for rehabilitating damaged reinforced concrete elements in civil infrastructure.

CONCLUSIONS AND PERSPECTIVES

Conclusions

This thesis has systematically investigated the mechanical, hydro-mechanical, and structural performance of geopolymer mortar as a sustainable repair material for reinforced concrete structures. The major conclusions drawn from the six chapters are summarized as follows:

- **Chapter 1** provided a critical review of conventional OPC-based repair systems and highlighted the advantages of geopolymer mortars in terms of CO_2 reduction, mechanical performance, and durability. The research gap on interface behavior under realistic loading and environmental conditions was clearly identified.
- **Chapter 2** presented an extensive experimental characterization of the geopolymer mortar used in this study. The material exhibited favorable fresh-state workability and notable hardened-state performance, achieving compressive strength above 49 MPa and flowability exceeding 120 mm. Digital Image Correlation revealed significant early-age shrinkage, underscoring the importance of plastic deformation control during application.
- **Chapter 3** focused on the shear and permeability response of geopolymer–concrete interfaces under constant confining pressure. The interfacial shear strength was significantly influenced by surface roughness and substrate composition. Coarse aggregate rough interfaces reached shear strength values up to 12.11 MPa, and permeability increased sharply after peak load, confirming crack-driven transport. A strong positive correlation ($r = 0.814$) was found between roughness and shear strength.
- **Chapter 4** developed a calibrated finite element model using a cohesive–frictional law to simulate interface shear behavior. The numerical results aligned closely with experimental observations, capturing the three distinct stages of shear evolution and replicating crack propagation patterns observed in DIC strain fields.
- **Chapter 5** investigated the geopolymer–steel interface using a novel concentric cell setup. The results showed enhanced bonding and reduced permeability with

phosphatic additives. Shear strength reached 18.26 MPa, and no visible interfacial cracks were observed after testing, confirming mechanical integrity.

- **Chapter 6** validated the previous findings at structural scale. Full-scale repaired beams showed that geopolymer mortar—especially under rough interface conditions—not only restored stiffness and peak load but also improved crack control compared to commercial products. The DIC strain maps confirmed distributed cracking and ductile failure modes in geopolymer-repaired beams.

In sum, the research demonstrates that geopolymer mortars are effective, robust, and environmentally favorable materials for structural repair, offering both mechanical resilience and interfacial compatibility.

Perspectives

Several future directions are proposed to advance the development and application of geopolymer repair systems:

- **Ambient curing optimization**: Develop mix formulations capable of maintaining high performance under ambient or mild curing conditions, to better suit field application without the need for elevated temperatures.
- **Long-term performance tracking**: Evaluate durability under cyclic loading, freeze-thaw, carbonation, and chloride exposure to assess service performance over extended periods.
- **Multi-scale modeling**: Incorporate micromechanical and meso-scale models to simulate shrinkage evolution, interfacial cracking, and permeability with higher physical fidelity.
- **Structural design guidelines**: Establish performance-based criteria and design recommendations for geopolymer-based repair under fatigue and seismic actions.
- **Life-cycle assessment (LCA)**: Assess the environmental and economic benefits of geopolymer systems through cradle-to-grave analysis for sustainable asset management.

- **Field trials and pilot applications**: Collaborate with industry to implement field-scale repair cases, enabling in-situ validation and practical refinement of geopolymer repair techniques.

These directions aim to bridge the gap between laboratory validation and real-world implementation, supporting the broader adoption of geopolymer technologies in sustainable infrastructure maintenance.

REFERENCES

Abbas, A., Carcasses, M., Ollivier, J.P., 1999. Gas permeability of concrete in relation to its degree of saturation. Materials and structures 32, 3–8.

Abdul Rashid, M.K., Ramli Sulong, N.H., Alengaram, U.J., 2020. Fire resistance performance of composite coating with geopolymer-based bio-fillers for lightweight panel application. Journal of Applied Polymer Science 137, 49558.

Aggelis, D.G., 2011. Classification of cracking mode in concrete by acoustic emission parameters. Mechanics Research Communications 38, 153–157. URL: https://www.sciencedirect.com/science/article/pii/S0093641311000620, doi:https://doi.org/10.1016/j.mechrescom.2011.03.007.

Aguirre-Guerrero, A.M., Robayo-Salazar, R.A., de Gutiérrez, R.M., 2017. A novel geopolymer application: Coatings to protect reinforced concrete against corrosion. Applied Clay Science 135, 437–446.

Ahmad, S., Elahi, A., Barbhuiya, S., Farid, Y., 2012. Use of polymer modified mortar in controlling cracks in reinforced concrete beams. Construction and building materials 27, 91–96.

Ahmad Zailani, W.W., Bouaissi, A., Abdullah, M.M.A.B., Abd Razak, R., Yoriya, S., Mohd Salleh, M.A.A., Rozainy MAZ, M.R., Fansuri, H., 2020. Bonding strength characteristics of fa-based geopolymer paste as a repair material when applied on opc substrate. Applied Sciences 10, 3321.

Ahmed, H.U., Mohammed, A.A., Rafiq, S., Mohammed, A.S., Mosavi, A., Sor, N.H., Qaidi, S.M., 2021. Compressive strength of sustainable geopolymer concrete composites: a state-of-the-art review. Sustainability 13, 13502.

Ahmed, H.U., Mohammed, A.S., Qaidi, S.M., Faraj, R.H., Hamah Sor, N., Mohammed, A.A., 2023. Compressive strength of geopolymer concrete composites: a systematic comprehensive review, analysis and modeling. European Journal of Environmental and Civil Engineering 27, 1383–1428.

Al Bakri, M.M., Mohammed, H., Kamarudin, H., Niza, I.K., Zarina, Y., 2011. Review on fly ash-based geopolymer concrete without portland cement. Journal of engineering and technology research 3, 1–4.

Al-Fasih, M.Y., Mohamad, M., Ibrahim, I., Ahmad, Y., Ariffin, M.M., Sarbini, N., Mohamed, R., Kueh, A., 2021. Experimental and numerical evaluations of composite concrete-to-concrete interfacial shear strength under horizontal and normal stresses. Plos one 16, e0252050.

Al-Jabri, R.A., Al-Maamari, R.S., Wilson, O.B., 2015. Klinkenberg-corrected gas permeability correlation for shuaiba carbonate formation. Journal of Petroleum Science and Engineering 131, 172–176.

Al-Majidi, M.H., Lampropoulos, A., Cundy, A., Meikle, S., 2016. Development of geopolymer mortar under ambient temperature for in situ applications. Construction and Building Materials 120, 198–211.

Al-Zahrani, M., Maslehuddin, M., Al-Dulaijan, S., Ibrahim, M., 2003. Mechanical properties and durability characteristics of polymer-and cement-based repair materials. Cement and Concrete Composites 25, 527–537.

Alanazi, H., Yang, M., Zhang, D., Gao, Z.J., 2016. Bond strength of pcc pavement repairs using metakaolin-based geopolymer mortar. Cement and Concrete Composites 65, 75–82.

Aldahdooh, M., Bunnori, N.M., Johari, M.M., Jamrah, A., Alnuaimi, A., 2016. Retrofitting of damaged reinforced concrete beams with a new green cementitious composites material. Composite structures 142, 27–34.

Aleem, M.A., Arumairaj, P., 2012. Geopolymer concrete–a review. International journal of engineering sciences & emerging technologies 1, 118–122.

Alekseev, V., Vasiliev, S., Ivanov, M., 2018. The porosity determination of dispersion medium by the method of expansion of pore air into vacuum (on the example of the main soil types in the chuvash republic), in: IOP Conference Series: Materials Science and Engineering, IOP Publishing. p. 012001.

Alfano, G., Sacco, E., 2006. Combining interface damage and friction in a cohesive-zone model. International Journal for Numerical Methods in Engineering 68, 542–582.

Almutairi, A.L., Tayeh, B.A., Adesina, A., Isleem, H.F., Zeyad, A.M., 2021. Potential applications of geopolymer concrete in construction: A review. Case Studies in Construction Materials 15, e00733.

Alnahhal, A.M., Alengaram, U.J., Ibrahim, M.S.I., Yusoff, S., Metselaar, H.S.C., Johnson, P.G., 2022. Synthesis of ternary binders and sand-binder ratio on the mechanical and microstructural properties of geopolymer foamed concrete. Construction and Building Materials 349, 128682.

Amran, M., Huang, S.S., Debbarma, S., Rashid, R.S., 2022. Fire resistance of geopolymer concrete: A critical review. Construction and Building Materials 324, 126722.

Anburuvel, A., 2023. Deployment perspectives of precursors in geopolymer synthesization: a review from their utilization prospects. Innovative Infrastructure Solutions 8, 264.

Andrade, C., Alonso, C., Molina, F., 1993. Cover cracking as a function of bar corrosion: Part i-experimental test. Materials and structures 26, 453–464.

Andrew, R.M., 2018. Global co 2 emissions from cement production. Earth System Science Data 10, 195–217.

Archez, J., Farges, R., Gharzouni, A., Rossignol, S., 2021. Influence of the geopolymer formulation on the endogeneous shrinkage. Construction and Building Materials 298, 123813. URL: https://www.sciencedirect.com/science/article/pii/S0950061821015737, doi:https://doi.org/10.1016/j.conbuildmat.2021.123813.

Ariyadasa, P.W., Manalo, A.C., Lokuge, W., Aravinthan, V., Pasupathy, K., Gerdes, A., 2024. Bond performance of fly ash-based geopolymer mortar in simulated concrete sewer substrate. Construction and Building Materials 446, 137927.

Arora, A., Singh, B., Kaur, P., 2019. Novel material ie magnesium phosphate cement (mpc) as repairing material in roads and buildings. Materials Today: Proceedings 17, 70–76.

Assaad, J.J., 2018. Development and use of polymer-modified cement for adhesive and repair applications. Construction and Building Materials 163, 139–148.

ASTM International, 2020. ASTM C1437-20 - standard test method for flow of hydraulic cement mortar. DOI: 10.1520/C1437-20.

ASTM International, 2021. ASTM C1579-21: Standard Test Method for Evaluating Plastic Shrinkage Cracking of Restrained Fiber Reinforced Concrete (Using a Steel Form Insert). ASTM International, West Conshohocken, PA. DOI: https://doi.org/10.1520/C1579-21.

Badika, M., Capdevielle, S., Saletti, D., Briffaut, M., 2024. Investigation of the influence of roughness on the shear resistance of concrete-rock interfaces using random field simulations, numerical simulations, and neural network modeling: Proposition of two approaches for the estimation of the peak shear strength. Rock Mechanics and Rock Engineering 57, 9511–9537.

Badika, M., El Merabi, B., Capdevielle, S., Dufour, F., Saletti, D., Briffaut, M., 2022. Influence of concrete–rock bonds and roughness on the shear behavior of concrete–rock interfaces under low normal loading, experimental and numerical analysis. Applied Sciences 12, 5643.

Bai, M., Ding, T., Zhao, Y., Zhao, Y., 2024. Shear performance of new-to-old concrete interface based on various surface preparation techniques and roughness. Case Studies in Construction Materials 21, e03549.

Bakharev, T., 2005. Resistance of geopolymer materials to acid attack. Cement and concrete research 35, 658–670.

Bakharev, T., Sanjayan, J., Cheng, Y.B., 1999. Effect of elevated temperature curing on properties of alkali-activated slag concrete. Cement and Concrete Research 29, 1619–1625. URL: https://www.sciencedirect.com/science/article/pii/S000888469900143X, doi:https://doi.org/10.1016/S0008-8846(99)00143-X.

Bataille, C., Åhman, M., Neuhoff, K., Nilsson, L.J., Fischedick, M., Lechtenböhmer, S., Solano-Rodriquez, B., Denis-Ryan, A., Stiebert, S., Waisman, H., et al., 2018. A review of technology and policy deep decarbonization pathway options for making energy-intensive industry production consistent with the paris agreement. Journal of Cleaner Production 187, 960–973.

Bear, J., 2013. Dynamics of fluids in porous media. Courier Corporation.

Bernal, S.A., Provis, J.L., 2014. Durability of alkali-activated materials: progress and perspectives. Journal of the American Ceramic Society 97, 997–1008.

Bhardwaj, P., Gupta, R., Mishra, D., Sanghi, S., Verma, S., Amritphale, S.S., 2020. Corrosion and fire protective behavior of advanced phosphatic geopolymeric coating on mild steel substrate. Silicon 12, 487–500.

Bhutta, A., Farooq, M., Banthia, N., 2019. Performance characteristics of micro fiber-reinforced geopolymer mortars for repair. Construction and Building Materials 215, 605–612.

Bhutta, A., Farooq, M., Zanotti, C., Banthia, N., 2017. Pull-out behavior of different fibers in geopolymer mortars: effects of alkaline solution concentration and curing. Materials and Structures 50, 1–13.

Bissonnette, B., Courard, L., Fowler, D.W., Granju, J.L., 2011. Bonded Cement-based Material Overlays for the Repair, the Lining or the Strengthening of Slabs or Pavements: State-of-the-art Report of the RILEM Technical Committee 193-RLS. volume 3. Springer Science & Business Media.

Blum, J.D., Wasserburg, G., Hutcheon, I.D., Beckett, J.R., Stolper, E.M., 1988. 'domestic'origin of opaque assemblages in refractory inclusions in meteorites. Nature 331, 405–409.

Bondar, D., Lynsdale, C., Milestone, N.B., Hassani, N., Ramezanianpour, A.A., 2011. Effect of type, form, and dosage of activators on strength of alkali-activated natural pozzolans. Cement and Concrete Composites 33, 251–260.

Boopalan, C., Rajamane, N., Jeyalakshmi, R., 2018. Studies on adhesive bond strength of steel reinforcing bars with fly ash based-ambient cured geopolymer concrete, in: AIP Conference Proceedings, AIP Publishing.

Briffaut, M., Duan, Z., Nicolas, G., 2024. Effect of thermal aging on shear strength of concrete-epoxy interface in extreme moisture conditions. Academic Journal of Civil Engineering 42, 619–628.

British Standards Institution, 2002. BS EN 12617-4:2002. Products and systems for the protection and repair of concrete structures - Test methods - Determination of shrinkage and expansion. Standard.

BS EN 12390-3, 2019. BS EN 12390-3:2019. Testing hardened concrete – Part 3: Compressive strength of test specimens. British Standards Institution. London, UK. Standard No. BS EN 12390-3:2019.

Bu, Y., Spragg, R., Weiss, W., 2014. Comparison of the pore volume in concrete as determined using astm c642 and vacuum saturation. Advances in Civil Engineering Materials 3, 308–315.

Cabrera, J., Al-Hasan, A., 1997. Performance properties of concrete repair materials. Construction and Building Materials 11, 283–290.

Cai, Y., Yu, L., Yang, Y., Gao, Y., Yang, C., 2019. Effect of early age-curing methods on drying shrinkage of alkali-activated slag concrete. Materials 12, 1633.

Caliskan, S., Karihaloo, B.L., Barr, B., 2002. Study of rock–mortar interfaces. part i: surface roughness of rock aggregates and microstructural characteristics of interface. Magazine of Concrete Research 54, 449–461.

Castel, A., 2016. Bond between steel reinforcement and geopolymer concrete. Handbook of low carbon concrete , 375.

Castel, A., Foster, S.J., 2015. Bond strength between blended slag and class f fly ash geopolymer concrete with steel reinforcement. Cement and Concrete Research 72, 48–53.

Castillo, H., Collado, H., Droguett, T., Sánchez, S., Vesely, M., Garrido, P., Palma, S., 2021. Factors affecting the compressive strength of geopolymers: A review. Minerals 11, 1317.

Çelik, A.İ., Özbayrak, A., Şener, A., Acar, M.C., 2022. Numerical analysis of flexural and shear behaviors of geopolymer concrete beams. Journal of Sustainable Construction Materials and Technologies 7, 70–80.

Chandra, N., Li, H., Shet, C., Ghonem, H., 2002. Some issues in the application of cohesive zone models for metal–ceramic interfaces. International Journal of Solids and Structures 39, 2827–2855.

Chen, C., Shenoy, S., Sasaki, K., Zhang, H., Tian, Q., 2024. Influence of liquid-to-solid ratios on properties and microstructure of coal gasification slag-based one-part geopolymer. Case Studies in Construction Materials 20, e02924.

Chen, K., Wu, D., Yi, M., Cai, Q., Zhang, Z., 2021a. Mechanical and durability properties of metakaolin blended with slag geopolymer mortars used for pavement repair. Construction and Building Materials 281, 122566.

Chen, W., Li, B., Wang, J., Thom, N., 2021b. Effects of alkali dosage and silicate modulus on autogenous shrinkage of alkali-activated slag cement paste. Cement and Concrete Research 141, 106322. URL: https://www.sciencedirect.com/science/article/pii/S0008884620316021, doi:https://doi.org/10.1016/j.cemconres.2020.106322.

Chen, X., Zhang, J., Xiao, Y., Li, J., 2015. Effect of roughness on shear behavior of red clay–concrete interface in large-scale direct shear tests. Canadian Geotechnical Journal 52, 1122–1135.

Chen, Y., Wei, J., Huang, H., Jin, W., Yu, Q., 2018. Application of 3d-dic to characterize the effect of aggregate size and volume on non-uniform shrinkage strain distribution in concrete. Cement and Concrete Composites 86, 178–189. URL: https://www.sciencedirect.com/science/article/pii/S0958946516307624, doi:https://doi.org/10.1016/j.cemconcomp.2017.11.005.

China, S., James, D.E., 2012. Comparison of laser-based and sand patch measurements of pavement surface macrotexture. Journal of Transportation Engineering 138, 176–181.

Chindaprasirt, P., Rattanasak, U., 2016. Improvement of durability of cement pipe with high calcium fly ash geopolymer covering. Construction and Building Materials 112, 956–961.

Chithambaram, S.J., Kumar, S., Prasad, M.M., Adak, D., 2018. Effect of parameters on the compressive strength of fly ash based geopolymer concrete. Structural Concrete 19, 1202–1209.

Collins, F., Sanjayan, J., 1999. Workability and mechanical properties of alkali activated slag concrete. Cement and Concrete Research 29, 455–458. URL: https://www.sciencedirect.com/science/article/pii/S0008884698002361, doi:https://doi.org/10.1016/S0008-8846(98)00236-1.

Collins, F., Sanjayan, J., 2000. Effect of pore size distribution on drying shrinking of alkali-activated slag concrete. Cement and Concrete Research 30, 1401–1406. URL: https://www.sciencedirect.com/science/article/pii/S0008884600003276, doi:https://doi.org/10.1016/S0008-8846(00)00327-6.

Conde Silva, J., Serra, C., 2022. A review on cement-based materials and practices for rehabilitation, retrofitting, and strengthening of hydraulic structures. Practice Periodical on Structural Design and Construction 27, 03122002.

Cong, P., Cheng, Y., 2021. Advances in geopolymer materials: A comprehensive review. Journal of Traffic and Transportation Engineering (English Edition) 8, 283–314.

Cong, P., Du, R., Gao, H., Chen, Z., 2024. Comparison and assessment of carbon dioxide emissions between alkali-activated materials and opc cement concrete. Journal of Traffic and Transportation Engineering (English Edition) .

Dahou, Z., Castel, A., Noushini, A., 2016. Prediction of the steel-concrete bond strength from the compressive strength of portland cement and geopolymer concretes. Construction and Building Materials 119, 329–342.

Dan, H., Ma, Z., Li, M., Ma, S., Tan, J., 2023. Early performance and bonding mechanism of metakaolin (mk)-ground granulated blast furnace slag (ggbs) based geopolymer road repair mortar. International Journal of Pavement Engineering 24, 2252156.

Dassault Systèmes,, 2016. Abaqus 6.14 Documentation. Dassault Systèmes. https://www.3ds.com/products-services/simulia/products/abaqus/.

Dassekpo, J.B.M., Feng, W., Miao, L., Dong, Z., 2021. Effect of alkali activators on loess geopolymer: potential waterproof repair material. Journal of Materials in Civil Engineering 33, 04021247.

Davidovits, J., 1991a. Geopolymers. Journal of Thermal Analysis 37, 1633–1656.

Davidovits, J., 1991b. Geopolymers: inorganic polymeric new materials. Journal of Thermal Analysis and calorimetry 37, 1633–1656.

Deb, P.S., Nath, P., Sarker, P.K., 2014. The effects of ground granulated blast-furnace slag blending with fly ash and activator content on the workability and strength properties of geopolymer concrete cured at ambient temperature. Materials & Design (1980-2015) 62, 32–39.

Destrebecq, J.F., Toussaint, E., Ferrier, E., 2011. Analysis of cracks and deformations in a full scale reinforced concrete beam using a digital image correlation technique. Experimental Mechanics 51, 879–890.

van Deventer, J.S., Provis, J.L., Duxson, P., Brice, D.G., 2010. Chemical research and climate change as drivers in the commercial adoption of alkali activated materials. Waste and biomass valorization 1, 145–155.

Ding, T., et al., 2022. Concrete-to-concrete interfaces: Behaviour and modelling .

Ding, Y., Dai, J.G., Shi, C.J., 2016. Mechanical properties of alkali-activated concrete: A state-of-the-art review. Construction and Building Materials 127, 68–79.

Dong, X., Karrech, A., Elchalakani, M., Qi, C., Manca, M., 2020. 3d bolted cohesive element for the modelling of bolt-reinforced rough rock-shotcrete interfaces. Computers and Geotechnics 125, 103659.

Dudziak, S., Jackiewicz-Rek, W., Kozyra, Z., 2021. On the calibration of a numerical model for concrete-to-concrete interface. Materials 14, 7204.

Duran Atiş, C., Bilim, C., Özlem Çelik, Karahan, O., 2009. Influence of activator on the strength and drying shrinkage of alkali-activated slag mortar. Construction and Building Materials 23, 548–555. URL: https://www.sciencedirect.com/science/article/pii/S0950061807002486, doi:https://doi.org/10.1016/j.conbuildmat.2007.10.011.

Duxson, P., Fernández-Jiménez, A., Provis, J.L., Lukey, G.C., Palomo, A., van Deventer, J.S., 2007a. Geopolymer technology: the current state of the art. Journal of materials science 42, 2917–2933.

Duxson, P., Provis, J.L., 2008. Designing precursors for geopolymer cements. Journal of the american ceramic society 91, 3864–3869.

Duxson, P., Provis, J.L., Lukey, G.C., Van Deventer, J.S., 2007b. The role of inorganic polymer technology in the development of 'green concrete'. cement and concrete research 37, 1590–1597.

Ekaputri, J.J., Indriyantho, B.R., Han, A., Gan, B.S., et al., 2022. Shear-bond behavior of self-compacting geopolymer concrete to conventional concrete. Construction and Building Materials 321, 126167.

El Dandachy, M.E., AlMohamad, D., Briffaut, M., El-Mir, A., Assaad, J.J., El-Hassan, H., 2024a. Assessment of concrete-to-concrete shear bond behavior using 3-d direct shear testing. Results in Engineering 24, 103000.

El Dandachy, M.E., Briffaut, M., Dufour, F., 2024b. Experimental investigation of the transfer properties of ribbed and round steel rebars concrete interfaces under shear loading and after unloading. Construction and Building Materials 451, 138746.

El Merabi, B., 2018. Mechanical behavior of cohesive concrete-rock joints at the dam-foundation interface: geometrical and mechanical influence of asperities. Ph.D. thesis. Université Grenoble Alpes.

EN 1015-3, 2007. Methods of test for mortar for masonry – Part 3: Determination of consistence of fresh mortar (by flow table). CEN, Brussels.

EN 12390-3, 2019. Testing hardened concrete – Part 3: Compressive strength of test specimens. CEN, Brussels.

EN 12390-5, 2019. Testing hardened concrete – Part 5: Flexural strength of test specimens. CEN, Brussels.

EN 1504-3, 2005. EN 1504-3:2005. Products and systems for the protection and repair of concrete structures – Definitions, requirements, quality control and evaluation of conformity – Part 3: Structural and non-structural repair. European Committee for Standardization. Brussels, Belgium. Standard No. EN 1504-3.

EN 196-3, 2016. Methods of testing cement – Part 3: Determination of setting times and soundness. CEN, Brussels.

EN 197-1, 2011. EN 197-1:2011. Cement – Part 1: Composition, specifications and conformity criteria for common cements. European Committee for Standardization. Brussels, Belgium. Standard No. EN 197-1.

Farhan, K.Z., Johari, M.A.M., Demirboğa, R., 2021. Impact of fiber reinforcements on properties of geopolymer composites: A review. Journal of Building Engineering 44, 102628.

Feng, S., Xiao, H., Li, H., 2020. Comparative studies of the effect of ultrahigh-performance concrete and normal concrete as repair materials on interfacial bond properties and microstructure. Engineering Structures 222, 111122.

Firdous, R., Stephan, D., 2019. Effect of silica modulus on the geopolymerization activity of natural pozzolans. Construction and Building Materials 219, 31–43.

Fu, C., Ye, H., Jin, X., Yan, D., Jin, N., Peng, Z., 2016. Chloride penetration into concrete damaged by uniaxial tensile fatigue loading. Construction and Building Materials 125, 714–723. URL: https://www.sciencedirect.com/science/article/pii/S0950061816313599, doi:https://doi.org/10.1016/j.conbuildmat.2016.08.096.

Gadri, K., Guettala, A., 2017. Evaluation of bond strength between sand concrete as new repair material and ordinary concrete substrate (the surface roughness effect). Construction and Building Materials 157, 1133–1144.

Ganeshan, M., Venkataraman, S., 2022. Interface shear strength evaluation of self compacting geopolymer concrete using push-off test. Journal of King Saud University-Engineering Sciences 34, 98–107.

Gao, H., Zhai, Y., 2022. Numerical investigation of the concrete–rock combined body influence of inclined interface on dynamic characteristics and failure behaviors. Arabian Journal of Geosciences 15, 435.

Gao, Z., Zhang, P., Wang, J., Wang, K., Zhang, T., 2022. Interfacial properties of geopolymer mortar and concrete substrate: Effect of polyvinyl alcohol fiber and nano-sio2 contents. Construction and Building Materials 315, 125735.

Gebregziabiher, B.S., Thomas, R., Peethamparan, S., 2015. Very early-age reaction kinetics and microstructural development in alkali-activated slag. Cement and concrete composites 55, 91–102.

Gelli, R., Ridi, F., 2023. An overview of magnesium-phosphate-based cements as bone repair materials. Journal of Functional Biomaterials 14, 424.

Gencturk, B., Hossain, K., Kapadia, A., Labib, E., Mo, Y.L., 2014. Use of digital image correlation technique in full-scale testing of prestressed concrete structures. Measurement 47, 505–515.

Ghosh, K., Ghosh, P., 2012. Effect of synthesizing parameters on compressive strength of flyash based geopolymer paste. Int J Struct Civ Eng 1, 1–11.

Grengg, C., Müller, B., Staudinger, C., Mittermayr, F., Breininger, J., Ungerböck, B., Borisov, S.M., Mayr, T., Dietzel, M., 2019. High-resolution optical ph imaging of concrete exposed to chemically corrosive environments. Cement and Concrete Research 116, 231–237. URL: https://www.sciencedirect.com/science/article/pii/S0008884618307051, doi:https://doi.org/10.1016/j.cemconres.2018.10.027.

Guo, S.Y., Zhang, X., Chen, J.Z., Mou, B., Shang, H.S., Wang, P., Zhang, L., Ren, J., 2020. Mechanical and interface bonding properties of epoxy resin reinforced portland cement repairing mortar. Construction and Building Materials 264, 120715.

Guo, X., Shi, H., Dick, W.A., 2010. Compressive strength and microstructural characteristics of class c fly ash geopolymer. Cement and concrete composites 32, 142–147.

Gutiérrez-Ch, J., Senent, S., Melentijevic, S., Jimenez, R., 2018. Distinct element method simulations of rock-concrete interfaces under different boundary conditions. Engineering Geology 240, 123–139.

Guzmán-Carrillo, H., Gasca-Tirado, J., López-Romero, J., Luis, M.A.C., Eric, M.R.M., Pineda-Piñón, J., Pérez-Bueno, J., Feregrino-Montes, C., López-Naranjo, E., Manzano-Ramírez, A., 2021. Encapsulation of toxic heavy metals from waste crt using calcined kaolin base-geopolymer. Materials Chemistry and Physics 257, 123745.

Habert, G., De Lacaillerie, J.D., Roussel, N., 2011. An environmental evaluation of geopolymer based concrete production: reviewing current research trends. Journal of cleaner production 19, 1229–1238.

Hachem, A.A., Khatib, J.M., Ezzedine El Dandachy, M., 2024. Assessment of interfacial mortar-mortar bond and pure shear strength of metakaolin-based geopolymer. International Journal of Building Pathology and Adaptation .

Hadi, M.N., Al-Azzawi, M., Yu, T., 2018. Effects of fly ash characteristics and alkaline activator components on compressive strength of fly ash-based geopolymer mortar. Construction and Building Materials 175, 41–54.

Haha, M.B., Le Saout, G., Winnefeld, F., Lothenbach, B., 2011. Influence of activator type on hydration kinetics, hydrate assemblage and microstructural development of alkali activated blast-furnace slags. Cement and Concrete Research 41, 301–310.

Haque, M.A., Chen, B., 2019. Research progresses on magnesium phosphate cement: A review. Construction and building materials 211, 885–898.

Hasanbeigi, A., Price, L., Lin, E., 2012. Emerging energy-efficiency and co2 emission-reduction technologies for cement and concrete production: A technical review. Renewable and Sustainable Energy Reviews 16, 6220–6238.

Hashmi, A.F., Khan, M., Bilal, M., Shariq, M., Baqi, A., 2022. Green concrete: an eco-friendly alternative to the opc concrete. Construction 2, 93–103.

Hassan, A., Arif, M., Shariq, M., 2020. A review of properties and behaviour of reinforced geopolymer concrete structural elements-a clean technology option for sustainable development. Journal of Cleaner Production 245, 118762.

Hassan, K., Brooks, J., Al-Alawi, L., 2001. Compatibility of repair mortars with concrete in a hot-dry environment. Cement and concrete composites 23, 93–101.

He, Y., Zhang, X., Hooton, R., Zhang, X., 2017. Effects of interface roughness and interface adhesion on new-to-old concrete bonding. Construction and Building Materials 151, 582–590.

Hills, T., Florin, N., Fennell, P.S., 2016. Decarbonising the cement sector: a bottom-up model for optimising carbon capture application in the uk. Journal of cleaner production 139, 1351–1361.

Hong, L., Gu, X., Lin, F., 2014. Influence of aggregate surface roughness on mechanical properties of interface and concrete. Construction and Building Materials 65, 338–349.

Hossain, M.M., Karim, M.R., Hossain, M., Islam, M.N., Zain, M., 2015. Durability of mortar and concrete containing alkali-activated binder with pozzolans: A review. Construction and Building Materials 93, 95–109.

Hu, D., Zhou, H., Hu, Q., Shao, J., Feng, X., Xiao, H., 2012. A hydro-mechanical-chemical coupling model for geomaterial with both mechanical and chemical damages considered. Acta Mechanica Solida Sinica 25, 361–376.

Huang, D., Liu, Z., Lin, C., Lu, Y., Li, S., 2024. Effects and mechanisms of component ratio and cross-scale fibers on drying shrinkage of geopolymer mortar. Construction and Building Materials 411, 134299. URL: https://www.sciencedirect.com/

science/article/pii/S0950061823040175, doi:https://doi.org/10.1016/j.conbuildmat.2023.134299.

Huang, Q.w., Wang, L.p., Wang, J.y., 2014. Mechanical properties of artificial materials for bone repair. Journal of Shanghai Jiaotong University (Science) 19, 675–680.

Huang, Y., Ye, H., Fu, C., Jin, N., 2017. Modeling moisture transport at the surface layer of fatigue-damaged concrete. Construction and Building Materials 151, 196–207. URL: https://www.sciencedirect.com/science/article/pii/S0950061817311789, doi:https://doi.org/10.1016/j.conbuildmat.2017.06.038.

Hubbert, M.K., 1956. Darcy's law and the field equations of the flow of underground fluids. Transactions of the AIME 207, 222–239.

Huseien, G.F., Mirza, J., Ismail, M., Ghoshal, S., Ariffin, M.A.M., 2018. Effect of metakaolin replaced granulated blast furnace slag on fresh and early strength properties of geopolymer mortar. Ain Shams Engineering Journal 9, 1557–1566.

Huseien, G.F., Mirza, J., Ismail, M., Ghoshal, S., Hussein, A.A., 2017. Geopolymer mortars as sustainable repair material: A comprehensive review. Renewable and Sustainable Energy Reviews 80, 54–74.

Hussein, M., Kunieda, M., Nakamura, H., 2012. Strength and ductility of rc beams strengthened with steel-reinforced strain hardening cementitious composites. Cement and Concrete Composites 34, 1061–1066.

Immel, K., Duong, T.X., Nguyen, V.H., Haiat, G., Sauer, R.A., 2020. A modified coulomb's law for the tangential debonding of osseointegrated implants. Biomechanics and modeling in mechanobiology 19, 1091–1108.

International Energy Agency, 2024. Cement – analysis and key findings. https://www.iea.org/energy-system/industry/cement. Available at: https://www.iea.org/energy-system/industry/cement.

International Energy Agency (IEA), 2021. Net zero by 2050. https://www.iea.org/reports/net-zero-by-2050. License: CC BY 4.0.

International Organization for Standardization, 2003. ISO 15105–2:2003: Plastics — Film and sheeting — Determination of gas transmission rate — Part 2: Equal-pressure method. https://www.iso.org/standard/36148.html. Standard.

ISO 25178, 2012. ISO 25178-2:2012 – Geometrical Product Specifications (GPS) – Surface texture: Areal – Part 2: Terms, definitions and surface texture parameters. https://www.iso.org/standard/42785.html. International Organization for Standardization.

Jaya, N.A., Yun-Ming, L., Cheng-Yong, H., Abdullah, M.M.A.B., Hussin, K., 2020. Correlation between pore structure, compressive strength and thermal conductivity of porous metakaolin geopolymer. Construction and Building Materials 247, 118641.

Jumaat, M.Z., Kabir, M., Obaydullah, M., 2006. A review of the repair of reinforced concrete beams. Journal of Applied Science Research 2, 317–326.

Karadumpa, C.S., Pancharathi, R.K., 2024. Study on energy use and carbon emission from manufacturing of opc and blended cements in india. Environmental Science and Pollution Research 31, 5364–5383.

Karami, A., Stead, D., 2008. Asperity degradation and damage in the direct shear test: a hybrid fem/dem approach. Rock mechanics and rock engineering 41, 229–266.

Karuppaiyan, J., Jeyalakshmi, R., 2024. Dielectric response of alkali aluminosilicate hydrate and silico alumino phosphate network present in metakaolin–graphene oxide geopolymer: A comparative study. Inorganic Chemistry Communications 161, 112036.

Kaur, K., Singh, J., Kaur, M., 2018. Compressive strength of rice husk ash based geopolymer: The effect of alkaline activator. Construction and Building Materials 169, 188–192.

Kaze, C.R., Djobo, J.N.Y., Nana, A., Tchakoute, H.K., Kamseu, E., Melo, U.C., Leonelli, C., Rahier, H., 2018. Effect of silicate modulus on the setting, mechanical strength and microstructure of iron-rich aluminosilicate (laterite) based-geopolymer cured at room temperature. Ceramics International 44, 21442–21450.

Khale, D., Chaudhary, R., 2007. Mechanism of geopolymerization and factors influencing its development: a review. Journal of materials science 42, 729–746.

Khan, I., Xu, T., Castel, A., Gilbert, R.I., Babaee, M., 2019. Risk of early age cracking in geopolymer concrete due to restrained shrinkage. Construction and Building Materials 229, 116840. URL: https://www.sciencedirect.com/science/article/pii/S0950061819322767, doi:https://doi.org/10.1016/j.conbuildmat.2019.116840.

Khan, M.Z.N., Shaikh, F.U.A., Hao, Y., Hao, H., 2018. Effects of curing conditions and sand-to-binder ratios on compressive strength development of fly ash geopolymer. Journal of Materials in Civil Engineering 30, 04017267.

Kim, G.W., Oh, T., Lee, S.K., Banthia, N., Yoo, D.Y., 2023. Development of ca-rich slag-based ultra-high-performance fiber-reinforced geopolymer concrete (uhp-frgc): Effect of sand-to-binder ratio. Construction and Building Materials 370, 130630.

Krizan, D., Zivanovic, B., 2002. Effects of dosage and modulus of water glass on early hydration of alkali–slag cements. Cement and Concrete Research 32, 1181–1188. URL: https://www.sciencedirect.com/science/

article/pii/S0008884601007177, doi:https://doi.org/10.1016/S0008-8846(01)00717-7.

Kumar, N., Rao, V.V., 2016. Hyperelastic mooney-rivlin model: determination and physical interpretation of material constants. Parameters 2, 01.

Lahoti, M., Tan, K.H., Yang, E.H., 2019. A critical review of geopolymer properties for structural fire-resistance applications. Construction and Building Materials 221, 514–526.

Lee, N., Kim, E., Lee, H.K., 2016. Mechanical properties and setting characteristics of geopolymer mortar using styrene-butadiene (sb) latex. Construction and Building Materials 113, 264–272.

Leong, H.Y., Ong, D.E.L., Sanjayan, J.G., Nazari, A., 2016. The effect of different na2o and k2o ratios of alkali activator on compressive strength of fly ash based-geopolymer. Construction and Building Materials 106, 500–511.

Li, C.Q., 2003. Life-cycle modeling of corrosion-affected concrete structures: Propagation. Journal of Structural Engineering 129, 753–761.

Li, C.Q., 2005. Time dependent reliability analysis of the serviceability of corrosion affected concrete structures. International Journal of Materials & Structural Reliability 3, 105–116.

Li, H., Chandra, N., 2003. Analysis of crack growth and crack-tip plasticity in ductile materials using cohesive zone models. International Journal of Plasticity 19, 849–882.

Li, S., Ma, W., Chen, D., Lu, Y., Liu, Z., 2024. Bonding characteristics between existing concrete substrate and high ductility geopolymer overlays under direct shear loading. Engineering Structures 315, 118324.

Li, V., Mishra, D., Wu, H., 1995. Matrix design for pseudo-strain-hardening fibre reinforced cementitious composites. Materials and Structures 28, 586–595. doi:10.1007/BF02473191.

Li, W., Lemougna, P.N., Wang, K., He, Y., Tong, Z., Cui, X., 2017. Effect of vacuum dehydration on gel structure and properties of metakaolin-based geopolymers. Ceramics International 43, 14340–14346.

Li, X., Sun, Q., Li, J., Liu, Y., Sun, H., Zhang, C., 2025. Experimental study on the shear performance of the bonding interface between geopolymer concrete and cement concrete. Journal of Building Engineering 103, 112193.

Ling, Y., Wang, K., Fu, C., 2019. Shrinkage behavior of fly ash based geopolymer pastes with and without shrinkage reducing admixture. Cement and Concrete Composites 98, 74–82.

Liu, J., Deng, X., Ma, Z., Liu, H., 2023. Effect of alternative silicon sources on alkali-activated carbon steel slag binder and silicon sources substitution mechanism. Results in Engineering 19, 101322.

Loosveldt, H., Lafhaj, Z., Skoczylas, F., 2002. Experimental study of gas and liquid permeability of a mortar. Cement and concrete research 32, 1357–1363.

Luhar, S., Luhar, I., Shaikh, F.U.A., 2021a. Review on performance evaluation of autonomous healing of geopolymer composites. Infrastructures 6, 94.

Luhar, S., Nicolaides, D., Luhar, I., 2021b. Fire resistance behaviour of geopolymer concrete: An overview. Buildings 11, 82.

Luo, P.F., Chao, Y.J., Sutton, M.A., 1994. Application of stereo vision to three-dimensional deformation analyses in fracture experiments. Optical engineering 33, 981–990.

Luo, Y., Zhang, Q., Wang, D., Yang, L., Gao, X., Liu, Y., Xue, G., 2023. Mechanical and microstructural properties of mk-fa-ggbfs-based self-compacting geopolymer concrete composites. Journal of Building Engineering 77, 107452.

Maaze, M.R., Shrivastava, S., 2023. Process parameter design approach for pressed fly ash geopolymer brick using box–behnken design: Influence of forming pressure, sand-to-precursor ratio and liquid-to-solid content. Innovative Infrastructure Solutions 8, 116.

Majidi, B., 2009. Geopolymer technology, from fundamentals to advanced applications: a review. Materials Technology 24, 79–87.

Manawadu, A., Qiao, P., Wen, H., 2023. Characterization of substrate-to-overlay interface bond in concrete repairs: a review. Construction and Building Materials 373, 130828.

Mangat, P., Limbachiya, M., 1997. Repair material properties for effective structural application. Cement and concrete research 27, 601–617.

Maras, M.M., 2021. Characterization of performable geopolymer mortars for use as repair material. Structural Concrete 22, 3173–3188.

Markandeya, A., Mapa, D., Fincan, M., Shanahan, N., Stetsko, Y., Riding, K., Zayed, A., 2019. Chemical shrinkage and cracking resilience of metakaolin concrete. ACI Materials Journal 116.

Markets, Markets, 2021. Concrete repair mortar market report. URL: https://www.marketsandmarkets.com.

Mastali, M., Kinnunen, P., Dalvand, A., Mohammadi Firouz, R., Illikainen, M., 2018. Drying shrinkage in alkali-activated binders – a critical review. Construction and Building Materials 190, 533–550. URL: https://www.sciencedirect.com/science/article/pii/S0950061818323043, doi:https://doi.org/10.1016/j.conbuildmat.2018.09.125.

McLellan, B.C., Williams, R.P., Lay, J., Van Riessen, A., Corder, G.D., 2011. Costs and carbon emissions for geopolymer pastes in comparison to ordinary portland cement. Journal of cleaner production 19, 1080–1090.

Menes Badika Kiyedi, J.M., 2023. Comportement mécanique et hydrique d'une interface béton-milieu granulaire sous sollicitation tangentielle. Ph.d. thesis. Université Gustave Eiffel. Champs-sur-Marne, France. URL: https://theses.hal.science/tel-04438344. available online at HAL: tel-04438344.

Meyer, D., Combrinck, R., 2022. Utilising microct scanning technology as a method for testing and analysing plastic shrinkage cracks in concrete. Construction and Building Materials 317, 125895.

Min, G., Fukuda, D., Oh, S., Kim, G., Ko, Y., Liu, H., Chung, M., Cho, S., 2020. Three-dimensional combined finite-discrete element modeling of shear fracture process in direct shearing of rough concrete–rock joints. Applied Sciences 10, 8033.

Minoru, K., Toshiro, K., Yuichi, U., Keitetsu, R., 2001. Evaluation of bond properties in concrete repair materials. Journal of materials in civil engineering 13, 98–105.

Mirza, J., Durand, B., Bhutta, A.R., Tahir, M.M., 2014. Preferred test methods to select suitable surface repair materials in severe climates. Construction and Building Materials 50, 692–698.

Moccia, F., Ruiz, M.F., Muttoni, A., 2021. Spalling of concrete cover induced by reinforcement. Engineering Structures 237, 112188.

Mohammed, A.S.S.K., Géber, R., 2025. Effect of liquid-solid ratio on metakaolin-based geopolymer binder properties. Pollack Periodica 20, 110–116.

Morgan, D., 1996. Compatibility of concrete repair materials and systems. Construction and building materials 10, 57–67.

Mouzannar, H., Bost, M., Leroux, M., Virely, D., 2017. Experimental study of the shear strength of bonded concrete–rock interfaces: surface morphology and scale effect. Rock Mechanics and Rock Engineering 50, 2601–2625.

Muñiz-Villarreal, M., Manzano-Ramírez, A., Sampieri-Bulbarela, S., Gasca-Tirado, J.R., Reyes-Araiza, J.L., Rubio-Ávalos, J.C., Pérez-Bueno, J., Apatiga, L., Zaldivar-Cadena, A., Amigó-Borrás, V., 2011. The effect of temperature on the geopolymerization process of a metakaolin-based geopolymer. Materials Letters 65, 995–998.

Murali, A.K., Tran, K.M., Haque, A., Bui, H.H., 2022. Experimental and numerical investigation of the load-bearing mechanisms of piles socketed in soft rocks. Rock Mechanics and Rock Engineering 55, 5555–5576.

Muthu, M., Sadowski, Ł., 2023. Performance of permeable concrete mixes based on cement and geopolymer in aggressive aqueous environments. Journal of Building Engineering 76, 107143.

Nasvi, M.M., Gamage, R.P., Jay, S., 2012. Geopolymer as well cement and the variation of its mechanical behavior with curing temperature. Greenhouse gases: science and technology 2, 46–58.

Natali, A., Manzi, S., Bignozzi, M., 2011. Novel fiber-reinforced composite materials based on sustainable geopolymer matrix. Procedia engineering 21, 1124–1131.

Nath, P., Sarker, P.K., 2014. Effect of ggbfs on setting, workability and early strength properties of fly ash geopolymer concrete cured in ambient condition. Construction and Building materials 66, 163–171.

Nath, P., Sarker, P.K., 2015. Use of opc to improve setting and early strength properties of low calcium fly ash geopolymer concrete cured at room temperature. Cement and concrete composites 55, 205–214.

Nath, P., Sarker, P.K., 2017. Flexural strength and elastic modulus of ambient-cured blended low-calcium fly ash geopolymer concrete. Construction and Building Materials 130, 22–31.

Needleman, A., 1987. A continuum model for void nucleation by inclusion debonding .

Nematollahi, B., Sanjayan, J., Shaikh, F., 2016. Matrix design of strain hardening fiber reinforced engineered geopolymer composite. Composites Part B: Engineering 89, 253–265. doi:10.1016/j.compositesb.2015.11.002.

Ng, C., Alengaram, U.J., Wong, L.S., Mo, K.H., Jumaat, M.Z., Ramesh, S., 2018. A review on microstructural study and compressive strength of geopolymer mortar, paste and concrete. Construction and Building Materials 186, 550–576.

Nguyen, K.T., Le, T.A., Lee, K., 2018. Evaluation of the mechanical properties of sea sand-based geopolymer concrete and the corrosion of embedded steel bar. Construction and Building Materials 169, 462–472.

Nian, G., Li, Q., Xu, Q., Qu, S., 2018. A cohesive zone model incorporating a coulomb friction law for fiber-reinforced composites. Composites Science and Technology 157, 195–201.

Nie, S., Zhou, J., Yang, F., Lan, M., Li, J., Zhang, Z., Chen, Z., Xu, M., Li, H., Sanjayan, J.G., 2022. Analysis of theoretical carbon dioxide emissions from cement production: Methodology and application. Journal of Cleaner Production 334, 130270.

Novais, R.M., Pullar, R.C., Labrincha, J.A., 2020. Geopolymer foams: An overview of recent advancements. Progress in Materials Science 109, 100621.

Oelkers, E.H., 2001. General kinetic description of multioxide silicate mineral and glass dissolution. Geochimica et Cosmochimica Acta 65, 3703–3719.

Ohama, Y., Ramachandran, V., 1996. Polymer-modified mortars and concretes, in: Concrete admixtures handbook. Elsevier, pp. 558–656.

Orteu, J.J., 2009. 3-d computer vision in experimental mechanics. Optics and lasers in engineering 47, 282–291.

Orteu, J.J., Cutard, T., Garcia, D., Cailleux, E., Robert, L., 2007. Application of stereovision to the mechanical characterisation of ceramic refractories reinforced with metallic fibres. Strain 43, 96–108.

Ortiz, M., Pandolfi, A., 1999. Finite-deformation irreversible cohesive elements for three-dimensional crack-propagation analysis. International journal for numerical methods in engineering 44, 1267–1282.

Ostrowski, N., Roy, A., Kumta, P.N., 2016. Magnesium phosphate cement systems for hard tissue applications: A review. ACS Biomaterials Science & Engineering 2, 1067–1083.

Otsuki, N., Miyazato, S.i., Diola, N.B., Suzuki, H., 2000. Influences of bending crack and water-cement ratio on chloride-induced corrosion of main reinforcing bars and stirrups. Materials Journal 97, 454–464.

Pacheco-Torgal, F., Labrincha, J., Leonelli, C., Palomo, A., Chindaprasit, P., 2014. Handbook of alkali-activated cements, mortars and concretes. Elsevier.

Pacheco-Torgal, F., Melchers, R.E., Shi, X., De Belie, N., Van Tittelboom, K., Perez, A.S., 2017. Eco-efficient repair and rehabilitation of concrete infrastructures. Woodhead Publishing.

Palacios, M., Puertas, F., 2005. Effect of superplasticizer and shrinkage-reducing admixtures on alkali-activated slag pastes and mortars. Cement and concrete research 35, 1358–1367.

Panda, B., Paul, S.C., Mohamed, N.A.N., Tay, Y.W.D., Tan, M.J., 2018. Measurement of tensile bond strength of 3d printed geopolymer mortar. Measurement 113, 108–116.

Pantazopoulou, S.J., Papoulia, K., 2001. Modeling cover-cracking due to reinforcement corrosion in rc structures. Journal of engineering mechanics 127, 342–351.

Papa, E., Landi, E., Miccio, F., Medri, V., 2022. K2o-metakaolin-based geopolymer foams: production, porosity characterization and permeability test. Materials 15, 1008.

Park, J.W., Song, J.J., 2009. Numerical simulation of a direct shear test on a rock joint using a bonded-particle model. International Journal of Rock Mechanics and Mining Sciences 46, 1315–1328.

Paschalis, S.A., Lampropoulos, A.P., Tsioulou, O., 2018. Experimental and numerical study of the performance of ultra high performance fiber reinforced concrete for the flexural strengthening of full scale reinforced concrete members. Construction and building materials 186, 351–366.

Pawelec, K.M., White, A.A., Best, S.M., 2019. Properties and characterization of bone repair materials, in: Bone Repair Biomaterials. Elsevier, pp. 65–102.

Peng, K.D., Huang, B.T., Xu, L.Y., Hu, R.L., Dai, J.G., 2022a. Flexural strengthening of reinforced concrete beams using geopolymer-bonded small-diameter cfrp bars. Engineering Structures 256, 113992.

Peng, K.D., Zeng, J.J., Huang, B.T., Huang, J.Q., Zhuge, Y., Dai, J.G., 2022b. Bond performance of frp bars in plain and fiber-reinforced geopolymer under pull-out loading. Journal of Building Engineering 57, 104893.

Phoo-ngernkham, T., Maegawa, A., Mishima, N., Hatanaka, S., Chindaprasirt, P., 2015. Effects of sodium hydroxide and sodium silicate solutions on compressive and shear bond strengths of fa–gbfs geopolymer. Construction and Building Materials 91, 1–8.

Pietruszczak, S., Mroz, Z., 2001. On failure criteria for anisotropic cohesive-frictional materials. International journal for numerical and analytical methods in geomechanics 25, 509–524.

Pradhan, J., Panda, S., Dwibedy, S., Pradhan, P., Panigrahi, S.K., 2024. Production of durable high-strength self-compacting geopolymer concrete with ggbfs as a precursor. Journal of Material Cycles and Waste Management 26, 529–551.

Prieto, M., Tanner, P., Andrade, C., 2011. Bond response in structural concrete with corroded steel bars. experimental results, in: Modelling of Corroding Concrete Structures: Proceedings of the Joint fib-RILEM Workshop held in Madrid, Spain, 22–23 November 2010, Springer. pp. 231–241.

Provis, J.L., Bernal, S.A., 2014. Geopolymers and related alkali-activated materials. Annual Review of Materials Research 44, 299–327.

Prusty, J.K., Pradhan, B., 2022. Investigation on effect of precursor materials and sand-to-binder ratio on strength development, acid resistance and microstructure evolution of geopolymer mortar. Construction and Building Materials 346, 128501.

Qaidi, S., Najm, H.M., Abed, S.M., Ahmed, H.U., Al Dughaishi, H., Al Lawati, J., Sabri, M.M., Alkhatib, F., Milad, A., 2022. Fly ash-based geopolymer composites: A review of the compressive strength and microstructure analysis. Materials 15, 7098.

Qi, X., Gay, N., Carlier, J.p., Jia, Y., Briffaut, M., 2024. Experimental investigation of coupled hydro-mechanical behavior of geomaterials interfaces. Academic Journal of Civil Engineering 42, 284–296.

Quelennec, B., Duan, Z., Delannoy, R., Gay, N., Briffaut, M., Tognetti, V., Delpouve, N., Delbreilh, L., Bredif, L., Duthoit, A., et al., 2023. Effect of physical and chemical ageing on barrier properties of epoxy coating. Construction and Building Materials 409, 133908.

Rahman, M.M., Akhtarul Islam, M., 2022. Application of epoxy resins in building materials: progress and prospects. Polymer Bulletin 79, 1949–1975.

Rashad, A.M., 2013. Metakaolin as cementitious material: History, scours, production and composition–a comprehensive overview. Construction and building materials 41, 303–318.

Renaud, S., Bouaanani, N., Miquel, B., 2021. Experimental, analytical, and finite element assessment of the shear strength of concrete-rock interfaces at different scales. International Journal for Numerical and Analytical Methods in Geomechanics 45, 1238–1259.

Research, G.V., 2023. Concrete restoration market report. URL: https://www.grandviewresearch.com.

Roe, K., Siegmund, T., 2003. An irreversible cohesive zone model for interface fatigue crack growth simulation. Engineering fracture mechanics 70, 209–232.

Rooses, A., Steins, P., Dannoux-Papin, A., Lambertin, D., Poulesquen, A., Frizon, F., 2013. Encapsulation of mg–zr alloy in metakaolin-based geopolymer. Applied clay science 73, 86–92.

Rovnaník, P., 2010. Effect of curing temperature on the development of hard structure of metakaolin-based geopolymer. Construction and building materials 24, 1176–1183.

Rudnicki, T., Boroński, J., Stałowski, P., Kaczmarek, P., Witkowski, P., 2023. Modern repair system for concrete pavement based on fast-setting concrete mixes, in: Proceedings of the 14th International Symposium on Concrete Roads, Kraków, Poland, pp. 25–28.

Safiuddin, M., Hearn, N., 2005. Comparison of astm saturation techniques for measuring the permeable porosity of concrete. Cement and Concrete Research 35, 1008–1013.

Saiang, D., Malmgren, L., Nordlund, E., 2005. Laboratory tests on shotcrete-rock joints in direct shear, tension and compression. Rock mechanics and rock engineering 38, 275–297.

Samson, G., Cyr, M., Gao, X.X., 2017. Formulation and characterization of blended alkali-activated materials based on flash-calcined metakaolin, fly ash and ggbs. Construction and Building Materials 144, 50–64.

Santos, P.M., Júlio, E.N., 2013. A state-of-the-art review on roughness quantification methods for concrete surfaces. Construction and Building Materials 38, 912–923.

Sarker, P., 2011. Bond strengths of geopolymer and cement concretes. Advances in Science and Technology 69, 143–151.

Satpute Manesh, B., Wakchaure Madhukar, R., Patankar Subhash, V., 2012. Effect of duration and temperature of curing on compressive strength of geopolymer concrete. Int. J. Eng. Innov. Technol 1, 152–155.

Schreier, H., Orteu, J.J., Sutton, M.A., 2009. Image correlation for shape, motion and deformation measurements: Basic concepts, theory and applications. Image Correlation for Shape, Motion and Deformation Measurements .

Seidel, J.P., Haberfield, C.M., 2002. Laboratory testing of concrete-rock joints in constant normal stiffness direct shear. Geotechnical Testing Journal 25, 391–404.

Sekkal, W., Izadifar, M., Zaoui, A., Ukrainczyk, N., Koenders, E., 2023. Theoretical investigation of protective graphene-coated metakaolin geopolymer interface under moisture and chemical composition effects. Powder Technology 430, 119007.

Serpieri, R., Alfano, G., Sacco, E., 2015. A mixed-mode cohesive-zone model accounting for finite dilation and asperity degradation. International Journal of Solids and Structures 67, 102–115.

Shahedan, N.F., Hadibarata, T., Abdullah, M.M.A.B., Jusoh, M.N.H., Abd Rahim, S.Z., Isia, I., Bras, A.A., Bouaissi, A., Juwono, F.H., 2024. Potential of fly ash geopolymer concrete as repairing and retrofitting solutions for marine infrastructure: A review. Case Studies in Construction Materials , e03214.

Shaheen, F., Pradhan, B., 2017. Influence of sulfate ion and associated cation type on steel reinforcement corrosion in concrete powder aqueous solution in the presence of chloride ions. Cement and Concrete Research 91, 73–86.

Shahi, S., Fakhri, E., Yavari, H., Maleki Dizaj, S., Salatin, S., Khezri, K., 2022. Portland cement: an overview as a root repair material. BioMed Research International 2022, 3314912.

Shahzad, M., Kamran, A., Siddiqui, M.Z., Farhan, M., 2015. Mechanical characterization and fe modelling of a hyperelastic material. Materials research 18, 918–924.

Shen, Y., Wang, Y., Yang, Y., Sun, Q., Luo, T., Zhang, H., 2019. Influence of surface roughness and hydrophilicity on bonding strength of concrete-rock interface. Construction and Building Materials 213, 156–166.

Shi, C., 1996. Strength, pore structure and permeability of alkali-activated slag mortars. Cement and concrete research 26, 1789–1799.

Shi, C., Zou, X., Yang, L., Wang, P., Niu, M., 2020. Influence of humidity on the mechanical properties of polymer-modified cement-based repair materials. Construction and Building Materials 261, 119928.

Sikora, S., Gapys, E., Michalowski, B., Horbanowicz, T., Hynowski, M., 2018. Geopolymer coating as a protection of concrete against chemical attack and corrosion, in: E3S Web of Conferences, EDP Sciences. p. 00101.

Sivasakthi, M., Jeyalakshmi, R., et al., 2021. Effect of change in the silica modulus of sodium silicate solution on the microstructure of fly ash geopolymers. Journal of Building Engineering 44, 102939.

Sofi, M., Van Deventer, J., Mendis, P., Lukey, G., 2007. Engineering properties of inorganic polymer concretes (ipcs). Cement and concrete research 37, 251–257.

Song, X., Song, X., Liu, H., Huang, H., Anvarovna, K.G., Ugli, N.A.D., Huang, Y., Hu, J., Wei, J., Yu, Q., 2022. Cement-based repair materials and the interface with concrete substrates: Characterization, evaluation and improvement. Polymers 14, 1485.

Stengel, T., Reger, J., Heinz, D., 2009. Life cycle assessment of geopolymer concrete–what is the environmental benefit. Concrete Solutions 9.

Sutton, M.A., Orteu, J.J., Schreier, H., 2009. Image correlation for shape, motion and deformation measurements: basic concepts, theory and applications. Springer Science & Business Media.

Swathi, B., Vidjeapriya, R., 2023. Influence of precursor materials and molar ratios on normal, high, and ultra-high performance geopolymer concrete–a state of art review. Construction and Building Materials 392, 132006.

Tan, J., Dan, H., Ma, Z., 2022. Metakaolin based geopolymer mortar as concrete repairs: Bond strength and degradation when subjected to aggressive environments. Ceramics International 48, 23559–23570.

Tanikawa, W., Shimamoto, T., 2009. Comparison of klinkenberg-corrected gas permeability and water permeability in sedimentary rocks. International Journal of Rock Mechanics and Mining Sciences 46, 229–238.

Tashan, J., 2022. Flexural behavior evaluation of repaired high strength geopolymer concrete. Composite Structures 300, 116144.

Tayeh, B.A., Zeyad, A.M., Agwa, I.S., Amin, M., 2021. Effect of elevated temperatures on mechanical properties of lightweight geopolymer concrete. Case Studies in Construction Materials 15, e00673.

Temuujin, J., Minjigmaa, A., Lee, M., Chen-Tan, N., Van Riessen, A., 2011a. Characterisation of class f fly ash geopolymer pastes immersed in acid and alkaline solutions. Cement and concrete composites 33, 1086–1091.

Temuujin, J., Rickard, W., Lee, M., van Riessen, A., 2011b. Preparation and thermal properties of fire resistant metakaolin-based geopolymer-type coatings. Journal of non-crystalline solids 357, 1399–1404.

Temuujin, J., Van Riessen, A., Williams, R., 2009. Influence of calcium compounds on the mechanical properties of fly ash geopolymer pastes. Journal of hazardous materials 167, 82–88.

Tennakoon, C., Shayan, A., Sanjayan, J.G., Xu, A., 2017. Chloride ingress and steel corrosion in geopolymer concrete based on long term tests. Materials & design 116, 287–299.

Tepfers, R., 1973. A theory of bond applied to overlapped tensile reinforcement splices for deformed bars. Division of concrete structures .

Tian, Y., Liu, Q., Liu, D., Kang, Y., Deng, P., He, F., 2018. Updates to grasselli's peak shear strength model. Rock Mechanics and Rock Engineering 51, 2115–2133.

Tomkins, B.W., 2011. Chemical resistance of geopolymer concrete against h2so4 & naoh .

Turner, L.K., Collins, F.G., 2013. Carbon dioxide equivalent (co2-e) emissions: A comparison between geopolymer and opc cement concrete. Construction and building materials 43, 125–130.

Turon, A., Camanho, P.P., Costa, J., Dávila, C., 2006. A damage model for the simulation of delamination in advanced composites under variable-mode loading. Mechanics of materials 38, 1072–1089.

Ueng, T.H., Lyu, S.J., Chu, H.W., Lee, H.H., Wang, T.T., 2012. Adhesion at interface of geopolymer and cement mortar under compression: An experimental study. Construction and Building Materials 35, 204–210.

Valikhani, A., Jahromi, A.J., Mantawy, I.M., Azizinamini, A., 2020. Experimental evaluation of concrete-to-uhpc bond strength with correlation to surface roughness for repair application. Construction and Building Materials 238, 117753.

Vanitha, N., Revathi, T., Sivasakthi, M., Jeyalakshmi, R., 2022. Microstructure properties of poly (phospho-siloxo) geopolymeric network with metakaolin as sole binder reinforced with n-sio2 and n-al2o3. Journal of Solid State Chemistry 312, 123188.

Varga, C., 2015. Cementos activados alcalinamente: Comportamiento reológico y durable en medio ácido. PhD Tesis, UNED Madrid, Spain .

Vasconcelos, E., Fernandes, S., de Aguiar, B., Pacheco-Torgal, F., 2013. Concrete retrofitting using cfrp and geopolymer mortars, in: Materials science forum, Trans Tech Publ. pp. 427–432.

Verma, N., Rao, M., Kumar, S., 2022. Effect of curing regime on compressive strength of geopolymer concrete, in: IOP Conference Series: Earth and Environmental Science, IOP Publishing. p. 012031.

Volokh, K.Y., 2004. Comparison between cohesive zone models. Communications in Numerical Methods in Engineering 20, 845–856.

Vora, P.R., Dave, U.V., 2013. Parametric studies on compressive strength of geopolymer concrete. Procedia Engineering 51, 210–219.

Walther, J.V., 1996. Relation between rates of aluminosilicate mineral dissolution, ph, temperature, and surface charge. American Journal of Science 296, 693–728.

Wang, K., Le, H., 2023. The development of cement-based, intumescent and geopolymer fire-retardation coatings for metal structures: a review. Coatings 13, 495.

Wang, L., Wang, L., Yang, Y., Zhu, X., Zhang, D., Gao, X., 2022. Discrete element modeling of rock-concrete bi-material discs under dynamic tensile loading. Construction and Building Materials 327, 126962.

Wang, S., Xue, Q., Zhu, Y., Li, G., Wu, Z., Zhao, K., 2021a. Experimental study on material ratio and strength performance of geopolymer-improved soil. Construction and Building Materials 267, 120469.

Wang, Y., Peng, K., Alrefaei, Y., Dai, J., 2021b. The bond between geopolymer repair mortars and opc concrete substrate: Strength and microscopic interactions. Cement and Concrete Composites 117, 103899. doi:10.1016/j.cemconcomp.2020.103899.

Waseem, S.A., Singh, B., 2016. Shear transfer strength of normal and high-strength recycled aggregate concrete–an experimental investigation. Construction and Building Materials 125, 29–40.

Washburn, E.W., Bunting, E.N., 1922. Porosity: Vi. determination of porosity by the method of gas expansion. Journal of the American Ceramic Society 5, 112–130.

Wasim, M., Ngo, T.D., Law, D., 2021. A state-of-the-art review on the durability of geopolymer concrete for sustainable structures and infrastructure. Construction and Building Materials 291, 123381.

Wazien, A.W., Abdullah, M.M.A.B., Razak, R.A., Rozainy, M.M.R., Tahir, M.F.M., Faris, M., Hamzah, H.N., 2016. Review on potential of geopolymer for concrete repair and rehabilitation, in: MATEC Web of Conferences, EDP Sciences. p. 01065.

Williams, B.D., Neeway, J.J., Snyder, M.M., Bowden, M.E., Amonette, J.E., Arey, B.W., Pierce, E.M., Brown, C.F., Qafoku, N.P., 2016. Mineral assemblage transformation of a metakaolin-based waste form after geopolymer encapsulation. Journal of Nuclear Materials 473, 320–332.

Witherspoon, R., Wang, H., Aravinthan, T., Omar, T., 2009. Energy and emissions analysis of fly ash based geopolymers, in: SSEE 2009: Solutions for a Sustainable Planet. Engineers Australia Barton, ACT, pp. 311–321.

Wu, H., Gao, J., Liu, C., Chen, G., 2024. Cementitious properties of sustainable alkali-activated materials with ground ggbs-based geopolymer waste powder as recycled precursor. Journal of Building Engineering 88, 109210.

Wu, L., Farzadnia, N., Shi, C., Zhang, Z., Wang, H., 2017. Autogenous shrinkage of high performance concrete: A review. Construction and Building Materials 149, 62–75.

Wu, Q., An, X., 2014. Development of a mix design method for scc based on the rheological characteristics of paste. Construction and Building Materials 53, 642–651.

Xia, J., Chen, K., Hu, S., Chen, J., Wu, R., Jin, W., 2023. Experimental and numerical study on the microstructure and chloride ion transport behavior of concrete-to-concrete interface. Construction and Building Materials 367, 130317.

Xia, Q., Wen, J., Tang, X., Zhu, Y., Xu, Z., Du, Z., Liu, X., 2021. Optimal preparation and degradation characterization of repair mortar containing waterborne epoxy resin emulsions. Construction and Building Materials 298, 123839.

Xie, T., Ozbakkaloglu, T., 2015. Behavior of low-calcium fly and bottom ash-based geopolymer concrete cured at ambient temperature. Ceramics International 41, 5945–5958.

Xin, L., Jin-yu, X., Weimin, L., Erlei, B., 2014. Effect of alkali-activator types on the dynamic compressive deformation behavior of geopolymer concrete. Materials Letters 124, 310–312.

Xu, F., Kong, F., Xiong, Q., Li, Y., Zhu, J., Sun, T., Peng, C., Lin, J., 2022. Internal interfacial interaction analysis of geopolymer-recycled aggregate pervious concrete based on a infiltration model. Construction and Building Materials 333, 127417.

Yadollahi, M.M., Benli, A., Demirboğa, R., 2015. The effects of silica modulus and aging on compressive strength of pumice-based geopolymer composites. Construction and Building Materials 94, 767–774.

Yamashita, Y., Uematsu, H., Tanoue, S., 2023. Calculation of strain energy density function using ogden model and mooney–rivlin model based on biaxial elongation experiments of silicone rubber. Polymers 15, 2266.

Yang, H., Li, H., Li, C., Li, X., Jiang, J., Gong, M., 2024. Failure criterion and damage evolution of high-strength geopolymer concrete under compression-shear composite loading after high temperatures. Construction and Building Materials 450, 138686. URL: https://www.sciencedirect.com/science/

article/pii/S0950061824038285, doi:https://doi.org/10.1016/j.conbuildmat.2024.138686.

Yang, H., Yang, Q., Luo, J., Jiang, J., Mei, J., Liu, A., 2023. Shear strength and failure criterion of geopolymer coral aggregate concrete under compression-shear loading. Journal of Building Engineering 76, 107241. URL: https://www.sciencedirect.com/science/article/pii/S2352710223014213, doi:https://doi.org/10.1016/j.jobe.2023.107241.

Yang, J., Sun, Z., De Belie, N., Snoeck, D., 2022a. Mitigating plastic shrinkage cracking in alkali-activated slag systems by internal curing with superabsorbent polymers. Cement and Concrete Composites 134, 104784.

Yang, K.H., Song, J.K., 2009. Workability loss and compressive strength development of cementless mortars activated by combination of sodium silicate and sodium hydroxide. Journal of materials in Civil Engineering 21, 119–127.

Yang, K.H., Song, J.K., Ashour, A.F., Lee, E.T., 2008. Properties of cementless mortars activated by sodium silicate. Construction and building materials 22, 1981–1989.

Yang, T., Xu, S., Liu, Z., Li, J., Wu, P., Yang, Y., Wu, C., 2022b. Experimental and numerical investigation of bond behavior between geopolymer based ultra-high-performance concrete and steel bars. Construction and Building Materials 345, 128220.

Yang, T., Zhu, H., Zhang, Z., 2017a. Influence of fly ash on the pore structure and shrinkage characteristics of metakaolin-based geopolymer pastes and mortars. Construction and Building Materials 152, 284–293. doi:10.1016/j.conbuildmat.2017.06.170.

Yang, T., Zhu, H., Zhang, Z., 2017b. Influence of fly ash on the pore structure and shrinkage characteristics of metakaolin-based geopolymer pastes and mortars. Construction and Building Materials 153, 284–293.

Yang, T.R., Chang, T.P., Chen, B.T., Shih, J.Y., Lin, W.L., 2012. Effect of alkaline solutions on engineering properties of alkali-activated ggbfs paste. Journal of Marine Science and Technology 20, 10.

Yang, Z., Brown, H., Huddleston, J., Seger, W., 2016. Performance evaluation of rapid-set prepackaged cementitious materials for rehabilitation of surface distress of concrete transportation structures. PCI Journal 61.

Yeoh, O., 1997. Hyperelastic material models for finite element analysis of rubber. Journal of Natural Rubber Research 12, 142–153.

Yu, Z., Huang, Q., Xie, X., Xiao, N., 2018. Experimental study and failure criterion analysis of plain concrete under combined compression-shear stress. Construction and Building Materials 179, 198–206. URL: https://www.sciencedirect.com/

science/article/pii/S0950061818313278, doi:https://doi.org/10.1016/j.conbuildmat.2018.05.242.

Zanotti, C., Borges, P.H., Bhutta, A., Banthia, N., 2017. Bond strength between concrete substrate and metakaolin geopolymer repair mortar: Effect of curing regime and pva fiber reinforcement. Cement and Concrete Composites 80, 307–316.

Zhang, B., Zhu, H., Chen, J., Yang, O., 2019a. Evaluation of bond performance of corroded steel bars in concrete after high temperature exposure. Engineering Structures 198, 109479. URL: https://www.sciencedirect.com/science/article/pii/S0141029619318395, doi:https://doi.org/10.1016/j.engstruct.2019.109479.

Zhang, C.Y., Han, R., Yu, B., Wei, Y.M., 2018. Accounting process-related co2 emissions from global cement production under shared socioeconomic pathways. Journal of cleaner production 184, 451–465.

Zhang, H.Y., Yan, J., Kodur, V., Cao, L., 2019b. Mechanical behavior of concrete beams shear strengthened with textile reinforced geopolymer mortar. Engineering Structures 196, 109348.

Zhang, J., Wang, H., Awed, A.M., Xie, J., Gu, F., 2024a. Performance evaluation of high early strength micro-expansion geopolymer grout potentially used for sustainable road infrastructure. Transportation Geotechnics 49, 101400.

Zhang, X., Du, M., Fang, H., Shi, M., Zhang, C., Wang, F., 2021. Polymer-modified cement mortars: Their enhanced properties, applications, prospects, and challenges. Construction and Building Materials 299, 124290.

Zhang, Y., Zhang, Z., Jiang, S., Wang, C., Ma, Z., 2024b. Characterization of geopolymer with 100% thermoactivated construction spoil powder: Effects of alkali dosage, silicate modulus and curing temperature. Journal of Building Engineering 98, 111511.

Zhang, Y., Zhou, C., Song, J., Li, J., Gong, Y., 2024c. Foundry waste reutilization: Anti-shrinkage geopolymer based on nano-clay and coal gangue. Construction and Building Materials 434, 136710. URL: https://www.sciencedirect.com/science/article/pii/S0950061824018518, doi:https://doi.org/10.1016/j.conbuildmat.2024.136710.

Zhang, Y., Zhu, P., Liao, Z., Wang, L., 2020. Interfacial bond properties between normal strength concrete substrate and ultra-high performance concrete as a repair material. Construction and Building Materials 235, 117431.

Zhang, Z., Provis, J.L., Reid, A., Wang, H., 2014. Geopolymer foam concrete: An emerging material for sustainable construction. Construction and Building Materials 56, 113–127.

Zhang, Z., Wang, H., Provis, J.L., 2012. Quantitative study of the reactivity of fly ash in geopolymerization by ftir. Journal of Sustainable Cement-Based Materials 1, 154–166.

Zhao, W., Chen, W., Zhao, K., 2018. Laboratory test on foamed concrete-rock joints in direct shear. Construction and Building Materials 173, 69–80.

Zheng, C., Mao, Z., Chen, L., Qian, H., Wang, J., 2023. Development of a novel rapid repairing agent for concrete based on gfrp waste powder/ggbs geopolymer mortars. Journal of Building Engineering 71, 106542.

Zhong, H., Ooi, E.T., Song, C., Ding, T., Lin, G., Li, H., 2014. Experimental and numerical study of the dependency of interface fracture in concrete–rock specimens on mode mixity. Engineering Fracture Mechanics 124, 287–309.

Zhong, Q., Nie, H., Xie, G., Peng, H., 2023. Experimental study on the characteristics, rheological factors, and flowability of mk-ggbfs geopolymer slurry. Journal of Building Engineering 76, 107300.

Zhong, Q., Tian, X., Xie, G., Luo, X., Peng, H., 2022. Investigation of setting time and microstructural and mechanical properties of mk/ggbfs-blended geopolymer pastes. Materials 15, 8431.

Étude expérimentale et numérique du comportement hydromécanique couplé des interfaces des géomatériaux

Cette thèse étudie expérimentalement et numériquement le comportement hydromécanique couplé des interfaces entre un mortier géopolymère à base de potassium et les constituants des structures en béton armé (béton et acier), dans le cadre de la réparation durable. Le mortier présente une bonne ouvrabilité, une résistance à la compression de 49,8 MPa à 14 jours et une faible perméabilité intrinsèque, tandis que la corrélation d'images numériques (DIC) révèle que plus de 70 % du retrait se développe durant les premières 24 heures. Un dispositif original permettant de mesurer simultanément le cisaillement et la perméabilité sous confinement constant (3 MPa) a été développé. Les résultats montrent que l'augmentation de la rugosité de surface améliore fortement la résistance interfaciale (jusqu'à 12 MPa) et retarde l'augmentation de la perméabilité, avec trois phases comportementales identifiées : adhérence initiale, dégradation progressive et glissement frictionnel résiduel. Les interfaces géopolymère–acier, étudiées à l'aide d'un dispositif concentrique symétrique, présentent une adhérence améliorée et une perméabilité réduite grâce à l'ajout d'additifs phosphatés. Un modèle cohésif–frottant implémenté sous Abaqus/Standard reproduit fidèlement les réponses expérimentales. Des essais de flexion en quatre points sur poutres réparées confirment une amélioration de la charge ultime, de la ductilité et de la fissuration. L'ensemble des résultats démontre que le mortier géopolymère constitue une solution performante et durable pour la réparation des structures en béton armé.

Mots-clefs : Mortier géopolymère ; Réparation du béton armé ; Interface béton–géopolymère ; Interface acier–géopolymère ; Comportement hydromécanique ; Modélisation par éléments finis

Experimental and Numerical Investigation of Coupled Hydro-mechanical Behavior of Geomaterials Interfaces

This thesis presents an experimental and numerical investigation of the coupled hydro-mechanical behavior of interfaces between potassium-based geopolymer mortar and reinforced concrete constituents (concrete and steel) for durable repair applications. The geopolymer exhibits good workability, high compressive strength (49.8 MPa at 14 days), and low intrinsic permeability, while Digital Image Correlation (DIC) shows that more than 70% of total shrinkage occurs within the first 24 hours. A novel device enabling simultaneous measurement of shear strength and permeability under constant confinement (3 MPa) was developed. Results demonstrate that increasing surface roughness significantly enhances interfacial strength (up to 12 MPa) and delays permeability growth, with three behavioral stages identified: initial adhesion, progressive degradation, and residual frictional sliding. Geopolymer–steel interfaces tested using a symmetric concentric configuration show improved adhesion and reduced permeability with phosphatic additives. A cohesive–frictional finite element model implemented in Abaqus/Standard accurately reproduces experimental responses. Four-point bending tests on repaired beams confirm improved ultimate load, ductility, and crack distribution. Overall, geopolymer mortar is demonstrated to be a robust and sustainable material for reinforced concrete repair.

Mots-clefs : Geopolymer mortar ; Reinforced concrete repair ; Concrete–geopolymer interface ; Steel–geopolymer interface ; Hydro-mechanical behavior ; Finite element modeling